Solitary waves and wave groups at the shore

Jana Orszaghova

Christ Church

University of Oxford

A thesis submitted for the degree of

Doctor of Philosophy

Trinity 2011

Acknowledgments

First and foremost I would like to thank both of my supervisors, Prof. Alistair Borthwick and Prof. Paul Taylor, for the guidance, support and knowledge they gave to me while I was writing this thesis. They were a fantastic team to work with, their combined expertise covering both offshore and coastal engineering as well as numerical and experimental methods. They allowed me to explore and work in my own way and at my own pace, but also pushed and directed me when it was needed. I could not have asked for more dedicated and knowledgeable supervisors. It has been such an honour to be their student, and it is to them I would like to dedicate this thesis.

I would also like to extend my gratitude to Dr. Alison Hunt-Raby for providing me with, and guiding me through the UKCRF experimental data, and to Prof. Shih-Chun Hsiao and his student Ting-Chieh Lin, who kindly gave me access to the Tainan supertank experiment dataset. The funding from the EPSRC is also gratefully acknowledged.

My family and friends were very supportive throughout this work. I would like to thank my parents for being wonderful role models throughout my life, and for looking after me even while living away from home. A special thank you goes to Gareth and the lovely volleyball girls, who made my DPhil years in Oxford the best time of my life.

Abstract

A significant proportion of the world's population and physical assets are located in low lying coastal zones. Accurate prediction of wave induced run-up and overtopping of sea defences are important in defining the extent and severity of wave action, and in assessing risk to people and property from severe storms and tsunamis.

This thesis describes a one-dimensional numerical model based on the Boussinesq equations of Madsen and Sørensen (1992) and the non-linear shallow water equations. The model is suitable for simulating propagation of weakly non-linear and weakly dispersive waves from intermediate to zero depth, such that any inundation and/or overtopping caused by the incoming waves is also calculated as part of the simulation. Wave breaking is approximated by locally switching to the non-linear shallow water equations, which can model broken waves as bores. A piston paddle wavemaker is incorporated into the model for complete reproduction of laboratory experiments. A domain mapping technique is used in the vicinity of the paddle to transform a time-varying domain into a fixed domain, so that the governing equations can be more readily solved.

First, various aspects of the numerical model are verified against known analytical and newly derived semi-analytical solutions. The complete model is then validated with laboratory measurements of run-up and overtopping involving solitary waves. NewWave focused wave groups, which give the expected shape of extreme wave events in a linear random sea, are used for further validation. Simulations of experiments of wave group run-up on a plane beach yield very good agreement with the measured run-up distances and free surface time series. Wave-by-wave overtopping induced by focused wave groups is also successfully simulated with the model, with satisfactory agreement between the experimental and the predicted overtopping volumes. Repeated simulations, now driven by second order paddle displacement signals, give insight into second order error waves spuriously generated by using paddle signals derived from linear theory. Separation of harmonics reveals that the long error wave is significantly affecting the wave group shape and leading to enhanced runu-up distances and overtopping volumes. An extensive parameter study is carried out using the numerical model investigating the influence on wave group run-up of linear wave amplitude at focus, linear focus location, and wave group phase at focus. For a given amplitude, both the phase and the focus location significantly affect the wave group run-up. It is also found that the peak optimised run-up increases with the wave amplitude, but wave breaking becomes an inhibiting factor for larger waves. This methodology is proposed for extreme storm wave induced run-up analysis.

Contents

Nomenclature

$(x_p)_t$	Paddle velocity
$\boldsymbol{f}$	Vector of mass and momentum fluxes
$\boldsymbol{s}$	Vector of source and sink terms
$\boldsymbol{u}$	Vector of conserved variables η and q
$\Delta\omega$	Angular frequency resolution
Δf	Frequency resolution
Δt	Time stepping interval
Δx	Computational grid resolution
η	Free surface elevation above a prescribed horizontal datum
η_x	Free surface slope
μ	Dispersion parameter
ω_n	Angular frequency of the n^{th} component
ω_p	Peak angular frequency
$\overline{u}$	Depth-averaged velocity
Φ	Velocity potential
ϕ	Phase angle
Ψ	Slope limiter
ρ	Water density
τ_b	Bottom friction

θ_n	Phase function of the n th component, given by $k_n x - \omega_n t$
$\tilde{x}$	Transformed horizontal coordinate (via transformation T)
$\tilde{x}_i$	Location of the i^{th} grid point in the transformed domain
ε	Nonlinearity parameter
$\widetilde{M}$	Number of transformed grid points
ξ	Solitary wave moving ordinate
ζ	Free surface elevation above still water level
ζ_c	Original or crest-focused free surface
ζ_t	Inverted or trough-focused free surface
A	Solitary wave amplitude
A_n	Coefficient for Stokes second order correction
a_n	Wave amplitude of the n^{th} component
$A_{\mathcal{N}}$	NewWave linear focus amplitude
B	Boussinesq linear dispersion enhancement coefficient
b	Bottom elevation
$B^{\pm}_{nm}$	Coefficient for second order sum and difference terms
C	Solitary wave celerity
c_0	Biésel paddle transfer function
C_f	Bottorm friction coefficient
c_n	Wave celerity of the n^{th} component
d	Total water depth
f_n	Frequency of the n^{th} component
$F^{\pm}_{nm}$	Second order paddle transfer function
g	Gravitational acceleration

h	Still water depth
k_n	Wave number of the n^{th} component
L	Computational/physical domain length
M	Total number of grid points and/or grid cells
m	Length of the *paddle domain*
m_0	Location of the end of the *paddle domain*
M_{switch}	Number of grid points governed by the Boussinesq equations
N	Number of Fourier components
q	Horizontal flux
R	Vertical or horizontal run-up
S_n	Energy spectrum (discrete)
T	Domain transformation
t	Time
t_f	Focus time
u	Horizontal velocity component
V	Overtopping volume per unit length of seawall
w	Vertical velocity component
x	Horizontal coordinate
x_f	Focus location
x_i	Location of the i^{th} grid point or location of the centre of i^{th} grid cell
x_p	Paddle displacement
z	Vertical coordinate measured from a prescribed horizontal datum
z^*	Vertical coordinate measured from the still water level

Chapter 1

Introduction and literature review

This chapter provides a brief introduction to the ocean environment, with an emphasis on coastal hydrodynamics. Past and current engineering methods for wave prediction in the coastal zone are then reviewed. Boussinesq-type models are introduced, leading onto the motivation and aim of this work. A synopsis of the thesis is also given.

1.1 Waves in the open ocean

Oceans cover 71 % of the Earth's surface. Ocean hydrodynamic behaviour is dominated by waves and currents. Most surface water waves are wind generated. These **progressive waves** can travel large distances over the sea from the point of origin. A wind generated sea surface can be considered as being composed of many such waves, each with its own frequency and direction of propagation. With Fourier superposition, periodic wave trains combine to form wave groups. Typical periods of ocean waves are in the order of seconds to a few tens of seconds, and the wavelengths of these waves are in the order of tens of meters to a few hundreds of meters. Propagation of wind waves in the open ocean is governed by frequency dispersion, meaning that longer waves travel faster (see the dispersion relation in any textbook covering water wave theory, such as Chapter 4 of Sarpkaya and Isaacson (1981)). **Tides**, on the other hand, are caused by the gravitational influences of the Sun and the Moon, and are characterised by a roughly 12 hour period. **Tsunamis** are generated by a rapid displacement of a large volume of water, and can be triggered by earthquakes, large-scale landslides or volcanic eruptions. In the open ocean tsunami wavelengths can reach hundreds of kilometers, and their wave periods vary from 5 to 60 minutes (according to Chapter 1 of Wright *et al.* (1999)). Tsunamis travel at a great speed (comparable to that of a jet aircraft), and in deep water can often be undetected due to their small wave height, typically less than one meter. Due to their very large

wavelengths, tsunamis can be considered as shallow water waves even in the open ocean. In absolute terms, tsunami waves transport large amounts of water across the ocean due to their immense wavelength, unlike wind generated progressive waves (see Stokes drift in second order Stokes wave theory in any textbook covering water wave theory such as Chapter 10 of Dean and Dalrymple (1991) or Chapter 11 of Tucker and Pitt (2001)). Surface ocean currents are created and maintained by wind circulation in the atmosphere. Currents can affect the wave speed, wave amplitude, and propagation direction. Wave-current interaction is a complex process, and will not be considered in this thesis.

1.2 Waves approaching the shore

Coastal hydrodynamics involves the interaction of ocean dynamics with the coast, whereby the domain boundaries are given by beaches, cliffs, and man-made structures. Coastal zones are characterised by relatively shallow depths. As ocean waves approach the shore, they become transformed by the bed topography and the resulting decreasing water depth. The interaction between waves and the domain boundaries is a two-way process as the incoming waves also continuously shape beach profiles, erode cliffs and impact on coastal structures. Coastal morphodynamic processes will not be considered in this thesis.

Shallow water wave transformation processes include refraction, shoaling, and wave breaking, and these affect the incoming wave characteristics such as wavelength, wave height, wave celerity as well as direction of propagation. **Wave refraction** bends the waves so that the wave crests become increasingly parallel with the bottom contour lines as they come ashore. In general, wave rays (which are lines perpendicular to wave crests indicative of wave propagation direction) converge towards headlands, and diverge in bays. Refraction will not be considered in this thesis as the work carried out is limited to one horizontal dimension.

Shoaling steepens the waves and increases their amplitude and ultimately leads to wave breaking. The section of the beach where breaking takes place is known as the surf zone. **Wave breaking** is a highly complex phenomenon involving dissipation of energy and turbulence, air entrapment, and sediment mixing and transport. Four breaker types have been identified: spilling, plunging, collapsing and surging. Illustrations of their different characteristics can be found in most water waves textbooks, such as Wright *et al.* (1999) or Sarpkaya and Isaacson (1981). The transition

from one breaker type to another is gradual, and changing from spilling to surging waves involves an increase in beach slope and a decrease in wave steepness. The surf similarity parameter, also known as the Iribarren number, is given by $\xi_0 = \frac{\tan\beta}{\sqrt{H_0/L_0}}$ (see Battjes (1974)), where β is the beach slope and the ratio of offshore wave height and wavelength H_0/L_0 is the wave steepness. The surf similarity parameter can be used for breaker type identification with $\xi_0 < 0.5$ corresponding to spilling breakers and $\xi_0 > 3.3$ corresponding to collapsing and surging breaking waves. The surf similarity parameter also correlates with the width of the surf zone; wide surf zones are associated with lower values of the surf similarity parameter, and narrow surf zones with higher values.

Broken waves travel up the shore in the form of bores, and can infiltrate into the underlying porous medium. They eventually run out of momentum and wash down the beach due to gravity. The section of the beach experiencing such up-rush and down-wash of water is known as the swash zone. Following Kobayashi (1999), **wave run-up** in the coastal engineering field is defined as the maximum elevation above the still water level reached by the up-rushing water. It is therefore a vertical measure. In this thesis, horizontal run-up is also used, and refers to the horizontal distance from the still shoreline to the maximum extent of the up-rush. Wave run-up comprises wave setup and swash. Wave setup is the additional elevation of the mean water level within the surf zone associated with breaking waves in decreasing water depths. Dean (2009) gives a detailed account of the phenomenon. Swash represents the oscillating fluctuations above the wave setup associated with advance of individual wave up-rush and the subsequent retreat.

Waves can pose a great threat to coastal communities and valuable housing and infrastructure assets located near the shore. According to McGranahan *et al.* (2007) 10% of the world's population live in the so-called low elevation coastal zone, which is less than 10 meters above sea level. Recent tragic and devastating tsunami events, the 2004 Indian Ocean Sumatra-Andaman earthquake tsunami and the 2011 Japanese Tohoku earthquake tsunami, illustrate the destructive power of these earthquake-triggered waves. According to the U.S. Geological Survey, the death toll from the 2004 tsunami event was around 220 000 lives [1]. The recent Japanese disaster severely damaged part of the country's east coast with over 300 000 destroyed buildings, widespread disruption of electricity, gas and water supplies, and telecommunications and railway service. The estimated total economic damage in Japan at the time of

[1] http://earthquake.usgs.gov/earthquakes/eqinthenews/2004/us2004slav/#summary

writing stands at $ 309 billion, with a death toll of around 20 000 lives [2]. Figure 1.1 depicts the tsunami devastation in Yuriage, a small fishing port near Sendai in Japan.

Figure 1.1: Before and after satellite photographs of destruction in Yuriage, Sendai, Japan caused by Tohoku earthquake tsunami in 2011. Images taken from the National Geographic webpage http://news.nationalgeographic.com/news/2011/03/110316-zoom-satellite-pictures-japan-tsunami-earthquake-world-before-after.

Storm waves can be just as dangerous and damaging. Hurricane Katrina devastated much of New Orleans and other coastal towns in the Gulf of Mexico in the summer of 2005. According to the U.S. National Hurricane Center [3] about 80 % of New Orleans was flooded to varying degrees, with a maximum inundation depth of about 6 m. Figure 1.2 shows photographs of the city before and after hurricane Katrina's land-fall. A combination of environmental forcings, interaction with the relatively wide and shallow continental shelf leading onto the Mississippi and Louisiana coastlines, and the large size of the storm produced a very high storm surge. Storm surge is a rise in the water level (above the usual predicted tidal elevation) associated with storms mainly due to winds pushing the water towards the shore and to a lesser extent due to the low atmospheric pressure. Sections along the Mississippi coast experienced surge elevation of 7-8.5 m. The disaster has been estimated to cause total economic losses of $ 81 billion in the United States . The total number of fatalities, directly or indirectly related to the hurricane, is estimated at around 1800. A special issue of Ocean Engineering (2010, Volume 37, Issue 1) was published on hurricane Katrina, with 13 papers covering laboratory, numerical and theoretical work on the disaster.

[2] http://earthquake.usgs.gov/earthquakes/eqinthenews/2011/usc0001xgp/#summary
[3] http://www.nhc.noaa.gov/pdf/TCR-AL122005_Katrina.pdf

Figure 1.2: Before and after photographs illustrating the extent of flooding in New Orleans, US caused by hurricane Katrina in 2005. Images taken from the Guardian newspaper webpage http://www.guardian.co.uk/world/gallery/2010/aug/26/hurricanekatrina-neworleans.

According to the IPCC (Intergovernmental Panel on Climate Change), coastal areas are very likely to be exposed to increasing risks over coming decades due to climate change and sea-level rise. Anticipated climate-related changes include intensification of tropical and extra-tropical cyclones and larger extreme waves and storm surges [4].

There is a need to improve the understanding of coastal hydrodynamics for safe and effective coastal planning, and functional sea defence design. Numerical modelling is a very valuable and relatively inexpensive tool enabling engineers to predict coastal sea levels, the extent of inundation, and the amount of overtopping. The work presented in this thesis aims to further the knowledge in the field by developing an intermediate and shallow water wave transformation model, which can act as a useful engineering tool for extreme run-up and overtopping analysis and statistics.

1.3 Prediction of wave run-up and overtopping

As already discussed, run-up is defined as the upper limit of the wave up-rush above the still water level (see Kobayashi (1999)). Run-up on a beach therefore describes the extent of the wave action. Run-up on a coastal structure determines whether overtopping takes place. When run-up is above the crest of the structure, water will flow over the crest. This is known as green water overtopping, as opposed to overtopping due to white water, which relates to droplets from breaking waves or spray (see Pullen *et al.* (2007)). In this thesis, only green overtopping is considered.

[4] http://www.ipcc.ch/publications_and_data/ar4/wg2/en/ch6s6-es.html

Kobayashi (1999) provides a detailed and comprehensive review on the knowledge and understanding of, and methods for calculation of run-up and overtopping on beaches and coastal structures. EurOtop (see Pullen *et al.* (2007)) is a more recent manual for wave overtopping of sea defences and related structures. Another useful source of information is the special issue in Coastal Engineering (2009, Volume 56, Issue 2) which is devoted to dissemination of findings from CLASH (Crest Level Assessment of coastal Structures by full scale monitoring, neural network prediction and Hazard analysis on permissible wave overtopping). Three main approaches of wave run-up and overtopping prediction have been identified: empirical formulae, numerical models and physical models. The first two are considered below. Much of the remainder of this section is based on the above sources.

1.3.1 Empirical formulae

Estimation of run-up and overtopping traditionally utilised empirical methods, whereby the run-up/overtopping response is related to the incoming wave and the beach/structure characteristics. Many empirical formulae were non-dimensionalised using the incoming wave height, and certain run-up formulae were expressed using the surf similarity parameter ξ_0. Early studies were aimed at smooth, impermeable beaches/structures and regular waves (see for example the run-up formula of Hunt (1959)). Run-up induced by irregular waves was quantified by van der Meer and Stam (1992) for smooth and rocky structures. Later van der Meer and Janssen (1995) provided overtopping formulae for mean overtopping discharge (per unit length of the structure, measured in l/s/m) and overtopping volume per wave (per unit length of the structure, measured in l/m) together with a number of reduction factors to account for varying structure and wave field characteristics.

The CLASH project gathered a considerable amount of overtopping data (from over 10,000 tests involving irregular waves) into one database in an attempt to develop a generic overtopping tool for structures of complex geometry. Using neural network modelling, the mean overtopping discharge can be estimated from the database for a given input consisting of 3 parameters that define the incoming wave field (related to wave height, period and direction) and 12 parameters that describe the structure. van der Meer *et al.* (2009) provide further details on the database. Clearly there has been considerable progress made in the applicability of empirical relationships. Also, this 'black box' approach is computationally efficient. However, the CLASH database (as well as many empirical relations) utilises input wave field characteristics defined at the toe of the structure, and these values might be difficult to obtain. Also, even

though a very large number of tests is consolidated in the database, for cases outside the permitted parameter range (where the underlying implied empirical relations may no longer hold) an alternative strategy must be applied.

1.3.2 Numerical models

Validated numerical models could be used for run-up and overtopping prediction. Models based on phase-resolving governing equations allow estimation of shoreline motion and of wave-by-wave overtopping (as opposed to only the mean overtopping discharge). Traditionally, the non-linear shallow water equations have been employed for numerical run-up and overtopping studies. With improvements in computer capabilities and resources, models based on Navier-Stokes equations are also being applied in coastal hydrodynamics. The phase-resolving numerical models can be applied to an arbitrary (within the restriction defined by the governing equations) geometry of the beach/structure, and as such are less restrictive than empirical relations, which are valid only for specific configurations.

1.3.2.1 SWE models

Numerical models based on the non-linear shallow water equations have been used by many researchers for run-up and/or overtopping prediction in the inner surf and swash zones (see Hu *et al.* (2000), Hubbard and Dodd (2002), Liang and Borthwick (2009) for example). Many stable and robust (due to there being only first derivatives present in the governing equations), efficient (using staggered and adaptive computational grids), and accurate (thanks to shock-capturing methods) codes have been developed for this equation set. Unfortunately, the equations are only applicable in very shallow water due to their non-dispersive nature.

1.3.2.2 NSE models

Proper flow variation in the vertical coordinate can be described by Navier-Stokes equations. Two main approaches have been identified for applying these equations in the coastal zone. The first one is the Volume of Fluid (VOF) method for tracking the free surface evolution applied to the traditional Eulerian representation of the equations (see Liu *et al.* (1999), Losada *et al.* (2008) for example). The second approach is SPH (Smoothed Particle Hydrodynamics), which is a grid-less Lagrangian particle method (see Dalrymple and Rogers (2006), Shao *et al.* (2006) for example). Both approaches can capture much of the complex physics of wave shoaling, breaking,

run-up and overtopping with good estimates of the velocity and pressure distributions. They are, however, computationally expensive and as yet cannot be applied to large domains or in parameter studies requiring a large number of runs. It should be noted, however, that thanks to code parallelisation and the use of GPUs (computer graphics cards) the run times are being continually shortened.

1.4 Boussinesq models

Numerical models based on Boussinesq-type equations provide a compromise between accuracy and practicality, and are increasingly popular operational predictive tools in coastal engineering. They have been used for simulations of many coastal hydrodynamic phenomena, including wave induced run-up (see for example Kennedy *et al.* (2000) or Fuhrman and Madsen (2008). Application of Boussinesq-type models to prediction of wave overtopping has been rare (apart from two studies found in the literature, by Stansby (2003) and Lynett *et al.* (2010)). Boussinesq models are essentially two dimensional and as such the free surface is no longer a boundary. The vertical coordinate is explicitly eliminated, yet some representation of the vertical flow structure is retained.

The classical Boussinesq equations derived by Peregrine (1967) were limited to weakly non-linear and weakly dispersive waves and assumed $O(\varepsilon) = O(\mu^2)$, whereby the non-linearity parameter ε represents the ratio of wave amplitude to depth, and the dispersion term μ is the ratio of depth to wavelength. Since 1967, there have been considerable attempts made to extend the applicability of Boussinesq equations both onshore and offshore. Comprehensive reviews of the earlier development of the field, including derivations, can be found in Dingemans (1997) and Madsen and Schäffer (1999).

Of the myriad of candidates, the enhanced equation set by Madsen and Sørensen (1992) is $O(\varepsilon, \mu^2)$ accurate, yet has improved dispersion properties thanks to a mathematical manipulation of the dispersive terms. The incorporation of a Padé approximant of the linear dispersion relation into the momentum equations, as suggested by Madsen and Sørensen (1992), results in equations suitable (in terms of linear dispersion characteristics) for relative water depth as deep as $\mu = 0.5$ (approximately equivalent to $kh = 3$, with k representing the wavenumber and h is the still water depth). The vertical profile in the extended deeper region is not properly modelled, due to the underlying assumption of the quadratic vertical variation of the horizontal

velocity, yet the wave propagation in the extended region is captured with reasonable accuracy. Another widely used equation set was derived by Nwogu (1993), and possesses equivalent dispersion properties. Nwogu's equations are formulated in terms of the surface elevation and horizontal velocity at a specific depth chosen to minimise wave propagation errors from linear theory.

Further extensions to the validity of Boussinesq-type equations have been achieved by deriving the so called fully non-linear equations, whereby $O(\varepsilon) = 1$ is assumed, as well as deriving higher order equations which retain $O(\mu^4)$ and equivalent terms (see for example Wei *et al.* (1995), Gobbi *et al.* (2000)). A novel approach for deriving Boussinesq-type equations was proposed by Agnon *et al.* (1999), whereby non-linearity is fully retained by decoupling the problem into first considering the Laplace equation in the undisturbed fluid domain and then solving the nonlinear free surface conditions. Further improvements, in terms of more accurate vertical variation of the velocity field, following the decoupling concept were given by Madsen *et al.* (2002, 2003). The emphasis of much of the above work is to extend the range of applicability of Boussinesq models into deeper water. In contrast, the work carried out in the present thesis focuses on developing a robust Boussinesq-like model appropriate for water depths from intermediate to zero depth.

Boussinesq-type equations cannot model wave breaking, unless they are modified to account for the associated energy dissipation. The most common breaking treatments in the Boussinesq framework are the surface roller concept (see Schäffer *et al.* (1993), Madsen *et al.* (1997)) or the inclusion of artificial viscosity in the momentum equation (see Zelt (1991), Karambas and Koutitas (1992), Kennedy *et al.* (2000)). These have been successful and facilitated the application of solvers to regions further inshore into the surf zone, but at the cost of requiring tunable parameters. However, as discussed earlier, the non-linear shallow water equations are appropriate for modelling broken waves in the surf zone. The overall dissipation of energy is captured physically correctly (see textbooks on shallow water shock conditions, for example Section 2.7 in Johnson (1997)). Due to the lack of frequency dispersion in the non-linear shallow water equations, any waveform modelled by these equations has a tendency to shock up to produce bores or hydraulic jumps, even on a horizontal bottom. For this reason the equations cannot be used pre-breaking, as they would lead to incorrect and premature prediction of wave breaking.

Hybrid numerical models based on the Boussinesq-type equations pre-breaking and the non-linear shallow water equations post-breaking allow modelling of wave

propagation from intermediate to shallow water. In this way appropriate governing equations are applied at all stages of the propagation and wave breaking is handled naturally. This approach is adopted in the present thesis, and the work builds upon that of Borthwick *et al.* (2006). In the present numerical model, the breaking criterion, which triggers a local switch from Boussinesq to the non-linear shallow water equations, is based on local wave steepness. Recently there have been similar hybrid models proposed by Tonelli and Petti (2009) and Bonneton *et al.* (2011) with the breaking trigger related to the wave non-linearity ε and the local energy dissipation respectively.

In order to capture faithfully the propagating bores, an appropriate shock capturing numerical scheme has to be applied to the non-linear shallow water equations. A well-established Godunov-type finite volume method, with data reconstruction, is used in the thesis, following Hu *et al.* (2000), Hubbard and Dodd (2002), Liang and Borthwick (2009) among others. Such methods additionally allow for natural treatment of the moving shoreline, allowing the extension of the model into the swash zone. The shoreline motion is computed as part of the solution, so there is no need for any tracking of the wet/dry front. The model can thus deal with multiple shorelines and splitting of the water mass, as can occur during an overtopping event.

1.5 Aims and objectives

The overall purpose of the thesis is to further the knowledge and understanding of wave induced run-up and overtopping by means of numerical modelling. This work is carried out using a hybrid numerical model based on the Boussinesq equations derived by Madsen and Sørensen (1992) pre-breaking and the non-linear shallow water equations post-breaking. Although the chosen set of Boussinesq equations is relatively unsophisticated and contains less of the physics compared to the newer derivations (see Section 1.4), it has been selected for its simplicity (small number of low order terms) and relative ease for numerical computation.

One novel feature of the present numerical model is the inclusion of a full model for a piston paddle wavemaker. Thus, the scheme allows for complete simulations of shallow water laboratory experiments, including the wave generation process. The problem of the time-varying domain size, due to the paddle movement, is overcome by implementing a domain transformation, so that calculations are performed in a fixed domain. This horizontal transformation has similarities to a σ-transformation

used in the vertical coordinate in three-dimensional free surface flow problems (as an example see Turnbull *et al.* (2003)).

The key objectives of the present work can be summarised as:

1. to develop a numerical model based on Boussinesq equations and the non-linear shallow water equations suitable for intermediate, shallow and zero water depths capable of complete representation of laboratory experiments including wave generation, wave propagation, shoaling and breaking, and interaction with beach/structure and any resulting wave up-rush or overtopping,

2. to reproduce focused wave group run-up and overtopping laboratory experiments of Hunt (2003), and subsequently to numerically investigate error waves spuriously generated by using linear wavemaker theory,

3. to apply the Boussinesq model to prediction of extreme wave run-up induced by storm waves (represented by NewWave focused wave groups), and to lay out a methodology for extreme wave run-up analysis and statistics.

1.6 Thesis outline

The structure of the remainder of the thesis is as follows. **Chapter 2** lays out the mathematical background of the present work, including the derivation of the governing equations. The mathematical treatment of the moving paddle boundary is explained. Wavemaker theory for regular, irregular and solitary waves is also covered. **Chapter 3** describes the numerical methods used to solve the governing equations, the wetting and drying algorithm and the boundary conditions. Special attention is given to the moving grid adjacent to the paddle. **Chapter 4** presents the model verification and validation. A new semi-analytical solitary wave solution is derived, and is used to confirm conservation properties of the model as well as to test the paddle wavemaker implementation. The complete model is validated against experimental measurements involving solitary waves. The material in the first four chapters has been published in an ICCE 2010 (International Conference on Coastal Engineering) conference paper Orszaghova *et al.* (2011) and has been accepted for publication in a JCP (Journal of Computational Physics) paper Orszaghova *et al.* (2012). **Chapter 5** details further validation of the model against run-up and overtopping measurements involving NewWave focused wave groups. Results from repeated runs of these

simulations using second order accurate paddle signals are also presented for comparison, and conclusions are drawn on the importance of second order wavemaker theory. **Chapter 6** features an extensive parameter study of storm wave induced run-up on a plane beach carried out using the numerical model, and presents a methodology for extreme run-up analysis. Lastly, conclusions of the work and recommendations for further research are given in **Chapter 7**.

Chapter 2

Mathematical formulation

In this Chapter a derivation of the classical Boussinesq equations is presented, followed by treatment to enhance their dispersion properties. The non-linear shallow water equations are also introduced. Treatment of wave breaking is considered. Incorporation of the paddle is presented, along with the first and second order wavemaker theory.

2.1 Derivation of the classical Boussinesq equations

The classical low order Boussinesq equations for one horizontal dimension are derived following the work of Madsen and Schäffer (1998, 1999). It is assumed that the fluid is incompressible, inviscid and irrotational. The starting point for the derivation comprises the Laplace equation for velocity potential together with the kinematic bottom boundary condition and kinematic and dynamic free surface boundary conditions. Using non-dimensional variables, the velocity potential is expressed as a power series in the vertical coordinate. Infinite series expressions for the velocity potential and horizontal and vertical velocities, satisfying the Laplace equation, are found in terms of values of these variables at the still water level. Next, the bottom boundary condition is used to find a relationship between the still water level horizontal and vertical velocity components. The kinematic and dynamic free surface boundary conditions give rise to equations for conservation of mass and horizontal linear momentum respectively, expressed in terms of free surface elevation and horizontal velocity at the still water level. Finally the equations are formulated in terms of depth-integrated velocity, retaining terms of order up to $O(\varepsilon, \mu^2)$. The vertical coordinate is thus explicitly eliminated from the Boussinesq equation formulation.

The Laplace equation and associated boundary conditions read as

$$\Phi_{xx} + \Phi_{z^*z^*} = 0, \tag{2.1a}$$

$$\Phi_{z^*} + h_x\Phi_x = 0 \qquad \text{on } z^* = -h, \tag{2.1b}$$

$$\Phi_{z^*} - \zeta_t - \zeta_x\Phi_x = 0 \qquad \text{on } z^* = \zeta, \tag{2.1c}$$

$$\Phi_t + \frac{1}{2}(\Phi_x^2 + \Phi_{z^*}^2) + g\zeta = 0 \qquad \text{on } z^* = \zeta, \tag{2.1d}$$

where Φ is the velocity potential, x is the horizontal coordinate, z^* is the vertical coordinate measured upwards from still water level, t is time, h is the still water depth, ζ the free surface elevation above still water level and g is gravitational acceleration. Figure 2.1 presents a definition sketch.

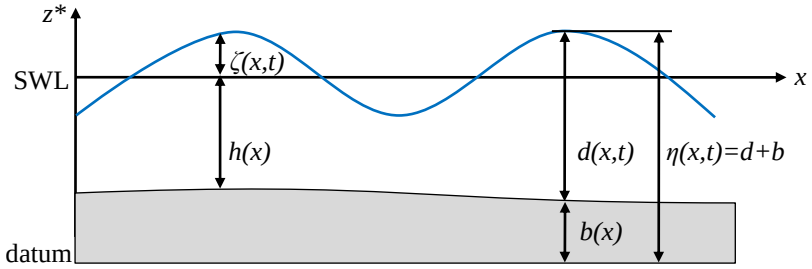

Figure 2.1: Definition sketch.

To express the magnitude of individual terms explicitly, scaling is applied such that

$$x' = \frac{x}{l_0}, \quad z^{*'} = \frac{z^*}{h_0}, \quad \zeta' = \frac{\zeta}{a_0}, \quad h' = \frac{h}{h_0}, \quad t' = \frac{\sqrt{gh_0}}{l_0}t, \quad \Phi' = \frac{h_0}{a_0 l_0\sqrt{gh_0}}\Phi,$$

where the primes denote non-dimensional variables and a_0, h_0, l_0 denote a typical wave amplitude, water depth and wavelength. In non-dimensional form, Equation (2.1) becomes

$$\mu^2\Phi_{xx} + \Phi_{z^*z^*} = 0, \tag{2.2a}$$

$$\Phi_{z^*} + \mu^2 h_x\Phi_x = 0 \qquad \text{on } z^* = -h, \tag{2.2b}$$

$$\Phi_{z^*} - \mu^2\zeta_t - \varepsilon\mu^2\zeta_x\Phi_x = 0 \qquad \text{on } z^* = \varepsilon\zeta, \tag{2.2c}$$

$$\Phi_t + \frac{1}{2}\varepsilon(\Phi_x^2 + \frac{1}{\mu^2}\Phi_{z^*}^2) + \zeta = 0 \qquad \text{on } z^* = \varepsilon\zeta, \tag{2.2d}$$

where the primes have been dropped for convenience. Note that the ratio between the characteristic depth and wavelength, $\mu = \frac{h_0}{l_0}$, is the dispersion or the shallowness parameter, and the ratio between the characteristic wave amplitude and depth, $\varepsilon = \frac{a_0}{h_0}$, is the non-linearity parameter.

Expressing the velocity potential as a power series in the vertical coordinate z^* such that

$$\Phi(x, z^*, t) = \sum_{n=0}^{n=\infty} z^{*n} \Phi^{(n)}(x, t) \tag{2.3}$$

and substituting into (2.2a) leads to

$$\Phi^{(n+2)} = \frac{-\mu^2}{(n+2)(n+1)} \Phi^{(n)}_{xx}. \tag{2.4}$$

By expanding (2.3) about $z^* = 0$ and successively applying the recurrence relation (2.4) it is possible to obtain expressions for Φ and the horizontal and vertical velocity components $u = \Phi_x$ and $w = \Phi_{z^*}$ in terms of variables at the still water level such that

$$\Phi(x, z^*, t) = \sum_{n=0}^{\infty} \frac{(-1)^n}{(2n)!} \mu^{2n} z^{*2n} \frac{\partial^{2n} \hat{\Phi}}{\partial x^{2n}} + \sum_{n=0}^{\infty} \frac{(-1)^n}{(2n+1)!} \mu^{2n+2} z^{*2n+1} \frac{\partial^{2n} \hat{w}}{\partial x^{2n}}, \tag{2.5a}$$

$$u(x, z^*, t) = \sum_{n=0}^{\infty} \frac{(-1)^n}{(2n)!} \mu^{2n} z^{*2n} \frac{\partial^{2n} \hat{u}}{\partial x^{2n}} + \sum_{n=0}^{\infty} \frac{(-1)^n}{(2n+1)!} \mu^{2n+2} z^{*2n+1} \frac{\partial^{2n+1} \hat{w}}{\partial x^{2n+1}}, \tag{2.5b}$$

$$w(x, z^*, t) = \sum_{n=0}^{\infty} \frac{(-1)^{n+1}}{(2n+1)!} \mu^{2n+2} z^{*2n+1} \frac{\partial^{2n+1} \hat{u}}{\partial x^{2n+1}} + \sum_{n=0}^{\infty} \frac{(-1)^n}{(2n)!} \mu^{2n+2} z^{*2n} \frac{\partial^{2n} \hat{w}}{\partial x^{2n}}, \tag{2.5c}$$

where for (2.5b) and (2.5c) differentiation with respect to x and z^* has additionally been performed, and $\hat{\Phi} = \Phi(x, 0, t)$, $\hat{u} = u(x, 0, t) = \Phi_x(x, 0, t) = \hat{\Phi}_x$ and $\hat{w} = \frac{1}{\mu^2} w(x, 0, t) = \frac{1}{\mu^2} \Phi_{z^*}(x, 0, t)$.

Substitution of (2.5b) and (2.5c) into the bottom boundary condition (2.2b) gives an exact relationship between the still water level velocity components as follows:

$$\hat{w} + \sum_{n=0}^{\infty} \frac{(-1)^n}{(2n+1)!} \mu^{2n} \frac{\partial}{\partial x} \Big(h^{2n+1} \frac{\partial^{2n} \hat{u}}{\partial x^{2n}} \Big) - \sum_{n=0}^{\infty} \frac{(-1)^n}{(2n+2)!} \mu^{2n+2} \frac{\partial}{\partial x} \Big(h^{2n+2} \frac{\partial^{2n+1} \hat{w}}{\partial x^{2n+1}} \Big) = 0. \tag{2.6}$$

One can derive an approximate explicit expression for $\hat{w}$, to a given order in μ, by substituting (2.6) into itself and retaining the appropriate terms. Such an expression to order $O(\mu^2)$ is given by

$$\hat{w} = -(h\hat{u})_x + \mu^2 \Big(\frac{h^3}{6} \hat{u}_{xx} - \frac{h^2}{2} (h\hat{u})_{xx} \Big)_x + O(\mu^4). \tag{2.7}$$

The velocity components at the free surface are defined as $\tilde{u} = u(x, \varepsilon\zeta, t) = \Phi_x(x, \varepsilon\zeta, t)$ and $\tilde{w} = \frac{1}{\mu^2} w(x, \varepsilon\zeta, t) = \frac{1}{\mu^2} \Phi_{z^*}(x, \varepsilon\zeta, t)$. Using (2.5b) and (2.5c), $\tilde{u}$ and $\tilde{w}$

can be expressed in terms of $\hat{u}$ and $\hat{w}$ as

$$\tilde{u} = \sum_{n=0}^{\infty} \frac{(-1)^n}{(2n)!} \mu^{2n} \varepsilon^{2n} \zeta^{2n} \frac{\partial^{2n} \hat{u}}{\partial x^{2n}} + \sum_{n=0}^{\infty} \frac{(-1)^n}{(2n+1)!} \mu^{2n+2} \varepsilon^{2n+1} \zeta^{2n+1} \frac{\partial^{2n+1} \hat{w}}{\partial x^{2n+1}}, \tag{2.8a}$$

$$\tilde{w} = \sum_{n=0}^{\infty} \frac{(-1)^{n+1}}{(2n+1)!} \mu^{2n} \varepsilon^{2n+1} \zeta^{2n+1} \frac{\partial^{2n+1} \hat{u}}{\partial x^{2n+1}} + \sum_{n=0}^{\infty} \frac{(-1)^n}{(2n)!} \mu^{2n} \varepsilon^{2n} \zeta^{2n} \frac{\partial^{2n} \hat{w}}{\partial x^{2n}}, \tag{2.8b}$$

and then substituted into the kinematic free surface boundary condition (2.2c) to give

$$\begin{aligned} \frac{\partial \zeta}{\partial t} - \hat{w} + \sum_{n=0}^{\infty} \frac{(-1)^n}{(2n+1)!} \mu^{2n} \varepsilon^{2n+1} \frac{\partial}{\partial x} \Big(\zeta^{2n+1} \frac{\partial^{2n} \hat{u}}{\partial x^{2n}} \Big) + \\ + \sum_{n=0}^{\infty} \frac{(-1)^n}{(2n+2)!} \mu^{2n+2} \varepsilon^{2n+2} \frac{\partial}{\partial x} \Big(\zeta^{2n+2} \frac{\partial^{2n+1} \hat{w}}{\partial x^{2n+1}} \Big) = 0. \end{aligned} \tag{2.9}$$

Equation (2.9) is equivalent to

$$\zeta_t + q_x = 0, \tag{2.10}$$

where

$$\begin{aligned} q = \int_{-h}^{\varepsilon\zeta} u \, \mathrm{d}z^* = \sum_{n=0}^{\infty} \frac{(-1)^n}{(2n+1)!} \mu^{2n} (\varepsilon^{2n+1} \zeta^{2n+1} + h^{2n+1}) \frac{\partial^{2n} \hat{u}}{\partial x^{2n}} + \\ + \sum_{n=0}^{\infty} \frac{(-1)^n}{(2n+2)!} \mu^{2n+2} (\varepsilon^{2n+2} \zeta^{2n+2} - h^{2n+2}) \frac{\partial^{2n+1} \hat{w}}{\partial x^{2n+1}} \end{aligned} \tag{2.11}$$

is the horizontal flux. Using (2.7) and then substituting (2.11) into itself, leads to an approximate explicit expression for $\hat{u}$ in terms of q such that

$$\hat{u} = \frac{q}{h} - \varepsilon \zeta \frac{q}{h^2} + \mu^2 \frac{h^2}{6} \Big(\frac{q}{h} \Big)_{xx} - \mu^2 \frac{h}{2} q_{xx} + O(\varepsilon^2, \varepsilon\mu^2, \mu^4). \tag{2.12}$$

Differentiating the dynamic free surface boundary condition (2.2d) with respect to x leads to

$$\begin{aligned} \sum_{n=0}^{\infty} \frac{\partial}{\partial x} \Bigg(\frac{(-1)^n}{(2n)!} \mu^{2n} \varepsilon^{2n} \zeta^{2n} \frac{\partial^{2n-1}}{\partial x^{2n-1}} \Big(\frac{\partial \hat{u}}{\partial t} \Big) + \frac{(-1)^n}{(2n+1)!} \mu^{2n+2} \varepsilon^{2n+1} \zeta^{2n+1} \frac{\partial^{2n}}{\partial x^{2n}} \Big(\frac{\partial \hat{w}}{\partial t} \Big) \Bigg) + \\ + \frac{\partial \zeta}{\partial x} + \frac{\varepsilon}{2} \frac{\partial \tilde{u}^2}{\partial x} + \frac{\varepsilon\mu^2}{2} \frac{\partial \tilde{w}^2}{\partial x} = 0. \end{aligned} \tag{2.13}$$

All velocity variables can be expressed in terms of q (via (2.7), (2.8) and (2.12)) so that (2.13) becomes

$$q_t + (h + \varepsilon\zeta)\zeta_x + \varepsilon \Big(\frac{q^2}{h} \Big)_x + \mu^2 \frac{h^3}{6} \Big(\frac{q}{h} \Big)_{xxt} - \mu^2 \frac{h^2}{2} q_{xxt} = O(\varepsilon^2, \varepsilon\mu^2, \mu^4). \tag{2.14}$$

(2.14) differs from the corresponding equation found in literature (see Madsen and Schäffer (1999), Madsen and Sørensen (1992) or Dingemans (1997) for example), whereby the term $\varepsilon(\frac{q^2}{h})_x$ is quoted to be $\varepsilon(\frac{q^2}{h+\varepsilon\zeta})_x$. Since $\varepsilon(\frac{q^2}{h+\varepsilon\zeta})_x = \varepsilon(\frac{q^2}{h})_x + O(\varepsilon^2)$, adopting the conventional formulation involves including an $O(\varepsilon^2)$ term. Since the resultant equations are assumed to be suitable for weakly non-linear waves, the $O(\varepsilon^2)$ term will naturally be negligible.

Converting (2.10) and (2.14) back into dimensional variables, using (2.2) and $q' = \frac{1}{a_0\sqrt{gh_0}}q$, leads to

$$\zeta_t + q_x = 0, \tag{2.15a}$$

$$q_t + gd\zeta_x + \Big(\frac{q^2}{d}\Big)_x = -\frac{1}{6}h^3\Big(\frac{q}{h}\Big)_{xxt} + \frac{1}{2}h^2 q_{xxt}. \tag{2.15b}$$

(2.15) are the classical Boussinesq equations of order $O(\varepsilon, \mu^2)$ expressed in (ζ, q). The terms on the right hand side of (2.15b) are referred to as the dispersive terms.

2.2 Enhanced Boussinesq equations

The range of applicability of the classical Boussinesq equations given by (2.15) is extended offshore following the method outlined in Madsen *et al.* (1991) and Madsen and Sørensen (1992).

For a mildly sloping bottom topography, by neglecting terms containing derivatives of h_x or products of h_x, (2.15b) simplifies to

$$q_t + gd\zeta_x + \Big(\frac{q^2}{d}\Big)_x = \frac{1}{3}h^2 q_{xxt} + \frac{1}{3}hh_x q_{xt}. \tag{2.16}$$

By judicious use of linear long wave theory, the dispersive terms in (2.16) can be modified in order to improve the linear dispersion properties of the resultant equations. Such manipulations were first undertaken by Peregrine (1967). Retaining only $O(1)$ terms from (2.14) leads to $q_t + gh\zeta_x = 0$, in dimensional form, which after double derivation with respect to x becomes

$$q_{xxt} + 2gh_x\zeta_{xx} + gh\zeta_{xxx} = 0. \tag{2.17}$$

Note that the mild bottom slope assumption is applied in (2.17). Pre-multiplying (2.17) by Bh^2 and adding to (2.16) gives the enhanced Boussinesq momentum equation

$$q_t + gd\zeta_x + \Big(\frac{q^2}{d}\Big)_x = \Big(B + \frac{1}{3}\Big)h^2 q_{xxt} + Bgh^3\zeta_{xxx} + hh_x\Big(\frac{1}{3}q_{xt} + 2Bgh\zeta_{xx}\Big), \tag{2.18}$$

where the added terms are of order $O(\mu^2)$ and B is the Boussinesq dispersion coefficient. Note that the performed manipulations have no effect on the order of the equation.

To verify the enhancement technique, the embedded linear dispersion relations for equation systems (2.15a) with (2.18) and (2.15a) with (2.16) are derived and compared to the exact linear dispersion relation. Since (2.18) reverts back to (2.16) for $B = 0$, it suffices to analyse (2.18). For a linear model solution $\zeta = a_1 \cos(kx - \omega t)$ and $q = q_1 \cos(kx - \omega t)$ on a horizontal bottom, (2.15a) and (2.18) become

$$\begin{pmatrix} \omega & -k \\ -ghk - Bgh^3k^3 & \omega + \left(B + \frac{1}{3}\right)h^2k^2\omega \end{pmatrix} \begin{pmatrix} a_1 \\ q_1 \end{pmatrix} = \mathbf{0}, \tag{2.19}$$

where k is the wavenumber and ω is the wave frequency of the assumed model solution. Non-linear terms are discarded in (2.19). For a non-trivial solution (ζ, q), the matrix determinant in (2.19) is required to be 0, which gives the embedded linear dispersion

$$\frac{\omega^2}{k^2gh} = \frac{c^2}{gh} = \frac{1 + Bk^2h^2}{1 + \left(B + \frac{1}{3}\right)k^2h^2}, \tag{2.20}$$

where c is the wave celerity. The above dispersion relation can also be derived in a different way: by expressing (2.15a) and (2.18) as a single higher-order equation in a single variable, either ζ or q, then simplifying for a flat bottom and substituting in the model solution. The exact linear dispersion relation (see Dean and Dalrymple (1991) for example) reads as

$$\frac{c^2}{gh} = \frac{\tanh kh}{kh}. \tag{2.21}$$

A [2][2] Padé expansion of (2.21) is given by

$$[2][2]\frac{c^2}{gh} = \frac{1 + \frac{1}{15}(kh)^2}{1 + \frac{2}{5}(kh)^2} + O(\mu^6). \tag{2.22}$$

It is easy to see that by choosing $B = \frac{1}{15}$ the embedded linear dispersion relation (2.20) becomes (2.22). The enhancement technique has effectively doubled the accuracy of the linear dispersion of (2.15a) and (2.18), since the embedded dispersion relation is now $O(\mu^4)$, as can be seen from (2.22). Figure 2.2 shows the deviation of the embedded wave velocities from the exact celerity given by (2.21). The classical Boussinesq equations (2.15a) and (2.16) correspond to $B = 0$. The new enhanced Boussinesq equations (2.15a) and (2.18) correspond to $B = \frac{1}{15}$. It is clear that the linear dispersion characteristics of the new formulation have been significantly improved. Allowing for a 5% error, the dispersion characteristics of the new Boussinesq set are acceptable in water as deep as $kh = 3$.

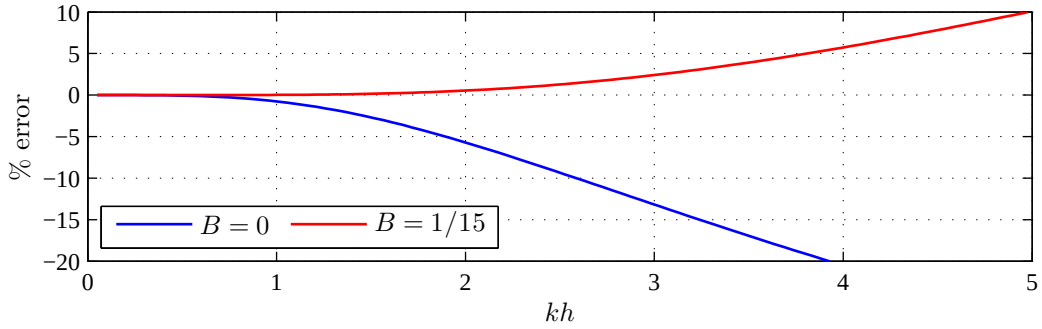

Figure 2.2: Percentage error of the embedded dispersion relation (2.20) for $B = 0$ and $B = 1/15$ from the exact linear dispersion relation (2.21).

2.3 Non-linear shallow water equations

The non-linear shallow water equations are the long wave approximation to the non-linear dispersive water wave problem. Utilising the technique from Section (2.1), the equations can be derived assuming $O(\varepsilon) = 1$ and $\mu \ll 1$ whereby all non-linear terms are retained and all dispersive terms neglected. In dimensional form, the equations are given by

$$\zeta_t + q_x = 0, \tag{2.23a}$$

$$q_t + gd\zeta_x + \left(\frac{q^2}{d}\right)_x = 0. \tag{2.23b}$$

In the non-linear shallow water wave theory it is assumed that the horizontal velocity component u is uniform with depth and the vertical component w varies linearly with elevation above the bed. The pressure distribution p is hydrostatic: $p = \rho g(\zeta - z^*)$, where ρ denotes water density. System (2.23) does not support a smooth solution of a permanent form (other than a uniform flow with undisturbed free surface). Under (2.23) a wave crest travels faster than a trough and as such any wave form involving a hump (a positive elevation above the still water level) continuously steepens, even on a horizontal bottom, leading to shock formation and wave breaking. For a mathematical demonstration of this phenomenon see Section 2.6.1 in Johnson (1997) or Sections 10.4 and 10.10 in Stoker (1957). The use of (2.23) in wave modelling should therefore be restricted to the inner surf zone. In deeper water the modelled waves would be propagated at an incorrect speed, due to lack of frequency dispersion, and wave breaking would also most likely occur prematurely.

Splitting the term $gd\zeta_x$ in (2.23b) such that $gd\zeta_x = \frac{1}{2}g(d^2)_x + gdb_x$, where b is the topography/bathymetry elevation above a prescribed horizontal datum (see Figure

2.1), (2.23) can be rewritten as hyperbolic [1] system of conservation laws $\boldsymbol{u}_t + \boldsymbol{f}_x = \boldsymbol{s}$, where $\boldsymbol{u}$ is the vector of conserved variables, $\boldsymbol{f}$ is the flux vector and $\boldsymbol{s}$ is the vector of source/sink terms. The resultant hyperbolic system on a non-uniformly varying bed is, however, unbalanced when solved within a Godunov-type finite volume framework. Non-physical fluxes are calculated, leading to meaningless results (see Rogers *et al.* (2001, 2003)).

2.4 Inclusion of friction and formulation in terms of (η, q)

Following Liang and Borthwick (2009), the non-linear shallow water equations (2.23) are expressed in a stage-discharge (η, q) formulation, where $\eta = b + h + \zeta$ denotes the free surface level above a prescribed horizontal datum as shown in Figure 2.1. Splitting the $gd\zeta_x$ term such that $gd\zeta_x = \frac{1}{2}g(\eta^2 - 2b\eta)_x + g\eta b_x$ and utilising $\zeta_t = \eta_t$, which holds for a fixed bed, leads to

$$\eta_t + q_x = 0, \tag{2.24a}$$

$$q_t + \left(\frac{q^2}{d} + \frac{1}{2}g(\eta^2 - 2\eta b)\right)_x = -\frac{\tau_b}{\rho} - g\eta b_x, \tag{2.24b}$$

where bottom friction τ_b has been taken into account. It is given empirically by

$$\tau_b = \rho C_f u|u|, \tag{2.25}$$

where C_f denotes the friction coefficient and ρ the water density. The new hyperbolic formulation (2.24) correctly balances the flux gradient and source terms when discretized within a Godunov-type finite volume framework. Additionally, it is particularly well suited to simulations involving wetting and drying as there is no explicit dependence on h and ζ which are difficult to define in dry areas (see Liang and Borthwick (2009)). The equation set is appropriate for modelling wave run-up, overtopping and coastal flooding scenarios.

[1] In order to classify an $m \times m$ system of first-order partial differential equations $\boldsymbol{u}_t + \boldsymbol{f}_x = \boldsymbol{s}$, a quasi-linear form $\boldsymbol{u}_t + \boldsymbol{A}\boldsymbol{u}_x = \boldsymbol{s}$ is utilised, where elements of the Jacobian matrix $\boldsymbol{A}$ are defined by $a_{ij} = \frac{\partial f_i}{\partial u_j}$. A solution of an eigenvalue problem $\det(\boldsymbol{A} - \lambda_i \boldsymbol{I}) = 0$ where $\boldsymbol{I}$ is an $m \times m$ identity matrix and $\lambda_i, i = 1, \ldots, m$ is an eigenvalue, determines the system's classification. For 2×2 systems, a system with 2 distinct real eigenvalues is said to be hyperbolic, a system with one repeated real eigenvalue is parabolic, and a system with complex eigenvalues is elliptic. For higher dimensions, there is no such simple classification. However, an $m \times m$ system is still referred to as hyperbolic, if it has m real eigenvalues and a corresponding set of m linearly independent eigenvectors, according to Toro (1999)

The enhanced Boussinesq equations (2.15a) and (2.18) are also expressed in terms of (η, q), to facilitate joining of the two equation sets in the present hybrid model, to give

$$\eta_t + q_x = 0, \tag{2.26a}$$

$$q_t + \Big(\frac{q^2}{d} + \frac{1}{2}g(\eta^2 - 2\eta b)\Big)_x = -\frac{\tau_b}{\rho} - g\eta b_x + \Big(B + \frac{1}{3}\Big)h^2 q_{xxt} + Bgh^3\eta_{xxx} + hh_x\Big(\frac{1}{3}q_{xt} + 2Bgh\eta_{xx}\Big). \tag{2.26b}$$

Note that the presence of h, the still water depth, in equation (2.26b) is acceptable since the Boussinesq equations are only applied in parts of the domain where h and ζ are well defined (see Section 2.5).

In order to facilitate Runge-Kutta time-stepping when solving (2.26), the momentum equation (2.26b) is recast in the way suggested by Bradford and Sanders (2001) and the system becomes

$$\eta_t = -q_x, \tag{2.27a}$$

$$F(q_t) = -\Big(\frac{q^2}{d} + \frac{1}{2}g(\eta^2 - 2\eta b)\Big)_x - \frac{\tau_b}{\rho} - g\eta b_x + Bgh^3\eta_{xxx} + 2Bgh^2 h_x\eta_{xx}, \tag{2.27b}$$

where

$$F = q_t - \Big(B + \frac{1}{3}\Big)h^2(q_t)_{xx} - \frac{1}{3}hh_x(q_t)_x. \tag{2.27c}$$

2.5 Hybrid model and treatment of wave breaking

The present hybrid model uses 2 sets of governing equations. The enhanced Boussinesq equations (2.27) are used pre-breaking, when the modelled waves are smooth and non-breaking. Once the waves are breaking, the non-linear shallow water equations (2.24) are locally applied, which model broken waves as non-dispersive bores. Energy dissipation associated with wave breaking is naturally handled by (2.24) due to energy loss across a shock (see Section 2.7 in Johnson (1997) or Section 10.6 in Stoker (1957)).

An ad-hoc breaking initiation criterion is based on the local free surface slope η_x. At the beginning of every time step, the domain is separated into individual waves using a down-crossing method. The maximum wave steepness η_x is calculated for every wave. The most offshore wave with $-\eta_x \geq 0.4$ (corresponding to roughly

22°) determines the current breaking location. The switch from the Boussinesq equations (2.27) to the non-linear shallow water equations (2.24) is shifted a quarter of a wavelength offshore from the location of $-\eta_x = 0.4$. Offshore of the switch, the Boussinesq equations are applied, whereas inshore of this point, the non-linear shallow water equations are solved. Switching between the two equation sets is a matter of retaining or neglecting the dispersive terms since the shallow water equations are a subset of the Boussinesq equations. However, to minimize instabilities in the flow which could arise due to the abrupt switch between the two equation sets, the dispersive terms are ramped down smoothly over half a wavelength spatially. The breaking location, if there is any, is then recalculated at the next time step so that the breaking region follows the wave inshore and the Boussinesq equations can be re-established at the original breaking location. In practice, this simple treatment of wave breaking does not require any additional calibration and re-tuning for simulations reproducing a wide variety of laboratory-scale waves. As shown in Chapter 4, a single value of the breaking wave slope $-\eta_x = 0.4$ works well for all the test cases simulated herein, including solitary waves and steep dispersive wave groups.

Additionally, the dispersion/shallowness parameter μ is also considered. The non-linear shallow water equations (2.24) are solved in all sections of the domain where $\mu \leq \frac{1}{20}$ and dispersive effects are therefore negligible. This is mathematically consistent as the non-linear shallow water equations are a non-dispersive approximation of the Boussinesq equations. Bellotti and Brocchini (2002) demonstrate that dispersive $O(\mu^2)$ terms diminish close to the shoreline, unlike dispersive-non-linear terms such as $O(\varepsilon\mu^2)$. However, since the Boussinesq equations of Madsen and Sørensen (1992) are of $O(\varepsilon, \mu^2)$ accuracy, the problem identified by Bellotti and Brocchini (2002) does not apply to the present hybrid model.

Figure 2.3 presents the wave breaking treatment in the numerical model. The switch from the Boussinesq equations to the non-linear shallow water equations is clearly shown. In the top plot, no breaking is taking place and the switch is simply governed by the dispersion parameter μ. In the other three plots, waves can be seen breaking.

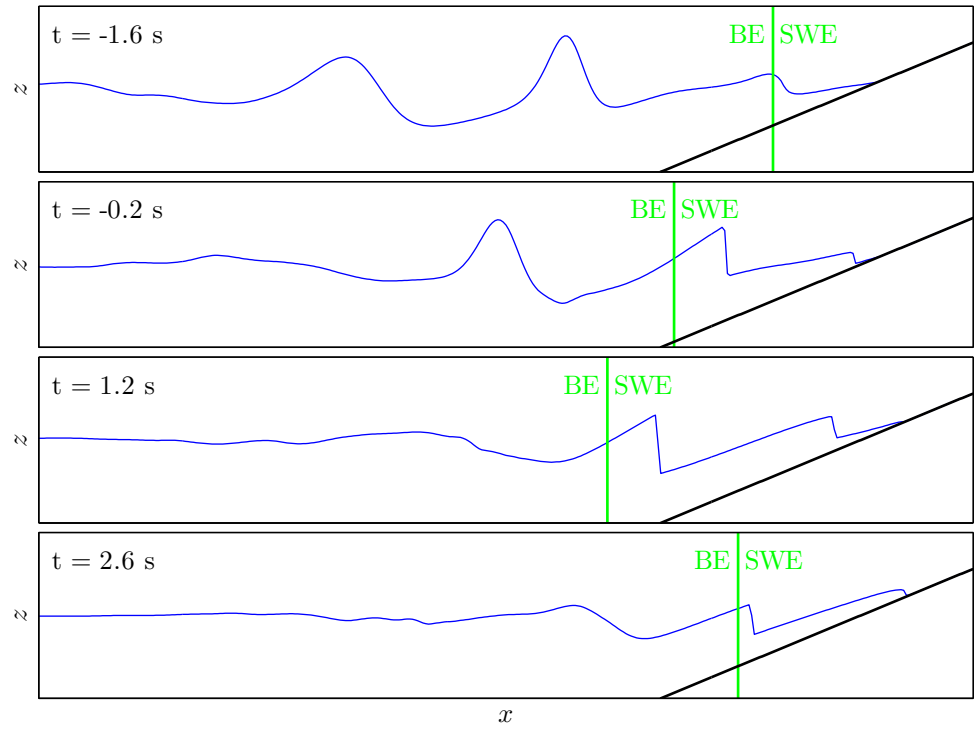

Figure 2.3: Wave breaking treatment. The switch between the Boussinesq equations (BE) and the non-linear shallow water equations (SWE) is plotted in green.

2.6 Wave generation with a piston paddle

In shallow water laboratory flumes, piston paddles are often used for mechanical wave generation (see Figure 2.4). The paddle moves horizontally according to a supplied paddle displacement time series. Sections 2.6.2 and 2.6.3 discuss wavemaker theories and the calculation of such paddle signals. Section 2.6.1 describes a mathematical method for inclusion of the moving paddle into a numerical model.

Image unavailable due to copyright.

Figure 2.4: Example of a piston paddle wavemaker in a wave flume. Photograph from wave generator specialists, Edinburgh Designs (www.edesign.co.uk).

2.6.1 In-built paddle

While the paddle operates, the size of the domain changes. The effective length of the tank reduces when the paddle moves forwards to create a wave crest. Equivalently, the domain lengthens when the paddle moves backwards to create a wave trough. In order to overcome this problem, when building a numerical model of a wave tank with an incorporated paddle, a mathematical transformation T is first employed. T maps the time-varying physical domain in vicinity of the paddle, referred to as the *paddle domain*, onto a fixed computational domain.

As shown in Figure 2.5, the *paddle domain* is defined by $x \in [x_p(t)\ m_0]$ with $x_p(t)$ denoting the paddle displacement from its initial position and m_0 denoting the location of the end of the *paddle domain*. The length of the *paddle domain* is given by $m(t) = m_0 - x_p(t)$. The value of m_0 is calculated at the beginning of each simulation, and is set to the grid point which is nearest to the location of ten times the maximum paddle sweep. By applying the transformation T of the independent variable x, such that

$$T(x) = \tilde{x} = \frac{m_0}{m(t)}\big(x - x_p(t)\big), \tag{2.28}$$

the time-varying *paddle domain* is mapped onto a fixed $\tilde{x} \in [0\ m_0]$ domain.

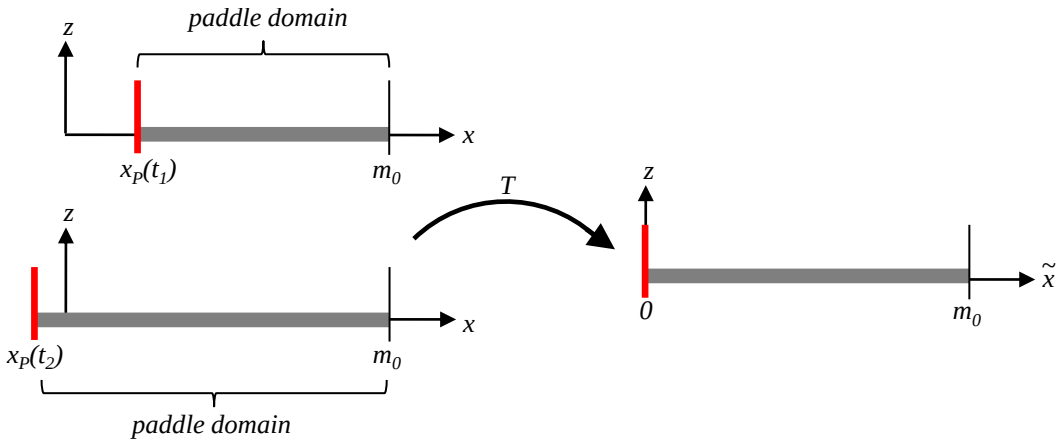

Figure 2.5: Sketch of the domain transformation T.

The mapped governing equations (2.27) become

$$\eta_t = -\frac{1}{m}m_t(m_0-\tilde{x})\eta_{\tilde{x}} - \frac{m_0}{m}q_{\tilde{x}}, \tag{2.29a}$$

$$\begin{aligned} G(q_t) = &-\frac{1}{m}m_t(m_0-\tilde{x})q_{\tilde{x}} - \frac{m_0}{m}\Big(\frac{q^2}{d}+\frac{1}{2}g(\eta^2-2\eta b)\Big)_{\tilde{x}} - \frac{\tau_b}{\rho} - g\eta\frac{m_0}{m}b_{\tilde{x}} \\ &+\Big(B+\frac{1}{3}\Big)h^2\Big(\frac{m_0}{m}\Big)^2\frac{1}{m}m_t\Big((m_0-\tilde{x})q_{\tilde{x}\tilde{x}\tilde{x}}-2q_{\tilde{x}\tilde{x}}\Big) + Bgh^3\Big(\frac{m_0}{m}\Big)^3\eta_{\tilde{x}\tilde{x}\tilde{x}} \\ &+2Bgh^2h_{\tilde{x}}\Big(\frac{m_0}{m}\Big)^3\eta_{\tilde{x}\tilde{x}}+\frac{1}{3}hh_{\tilde{x}}\Big(\frac{m_0}{m}\Big)^2\frac{1}{m}m_t\Big((m_0-\tilde{x})q_{\tilde{x}\tilde{x}}-q_{\tilde{x}}\Big), \end{aligned} \tag{2.29b}$$

where

$$G = q_t - \Big(B+\frac{1}{3}\Big)h^2\Big(\frac{m_0}{m}\Big)^2(q_t)_{\tilde{x}\tilde{x}} - \frac{1}{3}hh_{\tilde{x}}\Big(\frac{m_0}{m}\Big)^2(q_t)_{\tilde{x}}. \tag{2.29c}$$

As discussed in Chapter 3, the transformed governing equations (2.29) are time marched forward to find updated values of η and q, as a function of $\tilde{x}$. This solution is then mapped back onto the physical domain, using the inverse transformation $T^{-1}(\tilde{x}) = x = \tilde{x}\frac{m}{m_0}+x_p$. Although the transformed governing equations (2.29) contain time-varying parameters, these pose minimal additional difficulty for the numerical solver.

2.6.2 First and second order wavemaker theory

Wavemaker theory entails calculation of the required wavemaker motion to generate waves with desired characteristics such as wave amplitude and frequency. Chapter 6 of Dean and Dalrymple (1991) and Chapter 7 of Hughes (1993) provide very good overviews of wavemaker theory, and much of the present section is based on these two sources. Schäffer (1996) is followed for the second order wavemaker calculations. Calculation of the appropriate paddle signal requires understanding of the underlying wave theory. In this Section, first and second order Stokes wave solutions and second order wave-wave interactions are utilised. A very brief review is thus included. Assuming irrotational, inviscid and incompressible flow, the Laplace equation and the associated boundary conditions (2.1) apply. For a horizontal bottom, $h_x = 0$, and therefore the bottom boundary condition simplifies as $\Phi_{z^*} = 0$ on $z^* = -h$. For a periodic solution of a permanent form, $\Phi(x,z,t) = \Phi(\theta,z)$ is additionally assumed, where $\theta = kx - \omega t$, with k being the wave number and ω the angular frequency of the solution wave form. The perturbation method of Stokes expresses ζ and Φ as power series in wave steepness ka or wave non-linearity $\varepsilon = \frac{a}{h}$, where a denotes the wave amplitude [2]. Additionally, the free surface boundary conditions (2.1c) and (2.1d) are

[2] For solutions of order higher than 2, ω is also expressed as a power series.

expanded around $z^* = 0$ using Taylor series. The original non-linear boundary value problem is thus expressed as an infinite set of linear partial differential equations. Solving the first order problem, which is equivalent to the linear small amplitude wave theory, leads to a simple harmonic solution

$$\zeta \approx \zeta_0 = a\cos(\theta), \tag{2.30a}$$

$$\Phi \approx \Phi_0 = -a\frac{g}{\omega}\frac{\cosh(k(h+z^*))}{\cosh(kh)}\sin(\theta), \tag{2.30b}$$

with k and ω related by the linear dispersion relation (2.21). Extending the solution to second order gives rise to additional double frequency terms, and reads as

$$\zeta \approx \zeta_0 + \varepsilon\zeta_1 = a\cos(\theta) + a^2\frac{k}{4}\frac{\cosh(kh)}{\sinh^3(kh)}(2+\cosh(2kh))\cos(2\theta), \tag{2.31a}$$

$$\Phi \approx \Phi_0 + \varepsilon\Phi_1 = -a\frac{g}{\omega}\frac{\cosh(k(h+z^*))}{\cosh(kh)}\sin(\theta) - a^2\frac{3\omega}{8}\frac{\cosh(2k(h+z^*))}{\sinh^4(kh)}\sin(2\theta), \tag{2.31b}$$

with the same dispersion relation given by (2.21). The second order term travels at the same speed as the linear wave, and so the linear term is referred to as a free wave, and the second order term as a bound wave. For more details of the Stokes perturbation method, the reader is recommended to consult Section 2.5 of Johnson (1997) or Section 11.2 of Dean and Dalrymple (1991). For irregular waves, the superposition principle can be applied, and at first order this leads to

$$\zeta \approx \sum_{n=1}^{N} a_n\cos(\theta_n), \tag{2.32}$$

where $\theta_n = k_n x - \omega_n t$ and N is the number of regular wave trains considered. For simplicity the equivalent expression for Φ is omitted. At second order, additionally, wave-wave interactions give rise to both sum and difference frequency terms such that

$$\begin{aligned}\zeta \approx &\sum_{n=1}^{N} a_n\cos(\theta_n) + \sum_{n=1}^{N} a_n^2 A_n\cos(2\theta_n) \\ &+ \sum_{n=1}^{N}\sum_{m=n+1}^{N} a_n a_m B_{nm}^{+}\cos(\theta_n+\theta_m) + a_n a_m B_{nm}^{-}\cos(\theta_n-\theta_m),\end{aligned} \tag{2.33a}$$

where coefficients A_n follow from (2.31a) such that

$$A_n = \frac{k_n}{4}\frac{\cosh(k_n h)}{\sinh^3(k_n h)}(2+\cosh(2k_n h)) \tag{2.33b}$$

and coefficients $B^{\pm}_{nm}$ are given in Dalzell (1999) as

$$\begin{aligned} B^{\pm}_{nm} =& \frac{\omega_n^2+\omega_m^2}{2g} \mp \frac{\omega_n\omega_m}{2g}\Big(1 \mp \frac{1}{\tanh(k_nh)\tanh(k_mh)}\Big) \\ &\times \Big(\frac{(\omega_n \pm \omega_m)^2 + g(k_n \pm k_m)\tanh((k_n \pm k_m)h)}{(\omega_n \pm \omega_m)^2 - g(k_n \pm k_m)\tanh((k_n \pm k_m)h)}\Big) \\ &+ \frac{1}{2g}\Big(\frac{\omega_n \pm \omega_m}{(\omega_n \pm \omega_m)^2 - g(k_n \pm k_m)\tanh((k_n \pm k_m)h)}\Big) \\ &\times \Big(\frac{\omega_n^3}{\sinh^2(k_nh)} \pm \frac{\omega_m^3}{\sinh^2(k_mh)}\Big). \end{aligned} \tag{2.33c}$$

The second order sum and difference terms are also bound waves, whose dynamics is governed by the underlying free waves.

When considering a piston paddle wavemaker problem, a boundary condition is imposed on the wavemaker, which matches the horizontal component of the flow velocity with the speed of the prescribed paddle motion such that

$$\Phi_x = (x_p)_t \qquad\qquad \text{on } x = x_p. \tag{2.34}$$

Using the standard approach, the paddle displacement x_p is expressed as a power series in the perturbation parameter, and a Taylor expansion of (2.34) about $x = 0$ is applied, giving rise to ordered approximations to the original wavemaker problem. To generate a first order regular wave train (2.30), a periodic paddle motion given by

$$x_{p0} = a_p \sin(\omega t), \tag{2.35}$$

where a_p is the amplitude of the paddle oscillation, seems appropriate. At first order, the problem can be solved to give

$$\zeta_0 = \Re\Big\{\sum_{j=0}^{\infty} a_p c_j e^{i(\omega t - k_j x)}\Big\} \tag{2.36a}$$

$$= a_p c_0 \cos(kx - \omega t) + \sum_{j=1}^{\infty} a_p |c_j| e^{-|k_j|x} \sin(\omega t), \tag{2.36b}$$

where the first term in (2.36b) represents a regular progressive wave (with wave number $k_0 = k$) and the summation represents local evanescent waves. The evanescent disturbances arise because the paddle motion is uniform over the depth and does not match the vertical velocity profile of the generated regular wave. In (2.36) k_j is a purely imaginary wave number associated with the j^{th} evanescent mode. It is given by the linear dispersion relation (2.21) generalised to complex wave numbers such that $-\dfrac{j\pi}{h}i < k_j < -\dfrac{(j-\frac{1}{2})\pi}{h}i$, $j = 1, 2, \ldots$ is satisfied. The evanescent disturbances

rapidly decay as the distance from the wavemaker increases (due to $e^{-|k_j|x}$) so away from the wavemaker the target regular wave is generated to first order. In 2.36 c_j is given by

$$c_j = \frac{2\big(\cosh(2k_jh) - 1\big)}{\sinh(2k_jh) + 2k_jh}, \tag{2.37}$$

which for $j = 1, 2, \ldots$ is purely imaginary and such that $c_j = -i|c_j|$. For $j = 0$, on the other hand, c_0 is real and is known as the Biésel transfer function which gives a relation between the amplitude of the paddle motion a_p and the amplitude of the generated wave a such that $a = c_0 a_p$.

The first order paddle wavemaker problem is linear, and therefore for irregular first order wave generation the paddle signal can be calculated from

$$x_{p0} = \sum_{n=1}^{N} \frac{a_n}{c_{0n}} \sin(\omega_n t). \tag{2.38}$$

In laboratory experiments, all finite sized generated waves contain non-linearities. Therefore, when using a first order paddle signal given by (2.35) or (2.38), the boundary condition at the paddle face is not consistent with the second order waves. Consequently various free second order waves are unintentionally generated to compensate for this mis-match. These free waves are often called error, spurious or parasitic waves. They travel with their own dynamics and are not bound to the underlying first order waves. Second order wavemaker theory from Schäffer (1996) suppresses generation of such error waves. At second order, the boundary value wavemaker problem is again linear and thus decomposition and superposition are applicable. Following Barthel *et al.* (1983) and Schäffer (1996), the second order velocity potential Φ_1 is decomposed into three partial velocity potentials each satisfying the Laplace equation and a specific simplified set of boundary conditions. The three subproblems can be solved to ensure that the correct bound second order waves are produced without any second order free waves. For regular waves, only double frequency super-harmonics are present, and the second order paddle signal is given by

$$x_{p0} + \varepsilon x_{p1} = \frac{a}{c_0} \sin(\omega t) + a^2 \Big(\Re\{F^+\} \cos(2\omega t) + \Im\{F^+\} \sin(2\omega t) \Big), \tag{2.39}$$

where F^+ is a complex valued second order transfer function for super-harmonics. For irregular waves, the second order paddle signal has to cater for both the sub- and

the super-harmonic contributions and reads as

$$
\begin{aligned}
x_{p_0} + \varepsilon x_{p_1} = & \sum_{n=1}^{N} \frac{a_n}{c_{0n}} \sin(\omega_n t) \\
& + \sum_{n=1}^{N} a_n^2 \Big(\Re\{F_{nn}^{+}\} \cos(2\omega_n t) + \Im\{F_{nn}^{+}\} \sin(2\omega_n t) \Big) \\
& + \sum_{n=1}^{N} \sum_{m=n+1}^{N} a_n a_m \Big(\Re\{F_{nm}^{+}\} \cos((\omega_n + \omega_m)t) + \Im\{F_{nm}^{+}\} \sin((\omega_n + \omega_m)t) \Big) \\
& + \sum_{n=1}^{N} \sum_{m=n+1}^{N} a_n a_m \Big(\Re\{F_{nm}^{-}\} \cos((\omega_n - \omega_m)t) + \Im\{F_{nm}^{-}\} \sin((\omega_n - \omega_m)t) \Big),
\end{aligned}
\tag{2.40}
$$

where $F_{nm}^{\pm}$ is the second order transfer function for each interacting pair of regular components, with $^{+}$ denoting super-harmonics and $^{-}$ denoting sub-harmonics. The expression for $F_{nm}^{\pm}$ is given by (A.1) in Appendix A. Figures 2.6 and 2.7 show first and second order paddle signals for a regular wave and a bichromatic wave group respectively. These signals are used in Chapter 4. In general, the second order signal requires larger paddle strokes. Both examples are taken from Schäffer (1996) with $a = 0.07$ m, $f = \frac{1}{3}$ Hz and $h = 0.7$ m for the regular wave case; and $a_1 = a_2 = 0.03$ m, $f_1 = 0.495$ Hz, $f_2 = 0.566$ Hz and $h = 0.3$ m for the wave group case.

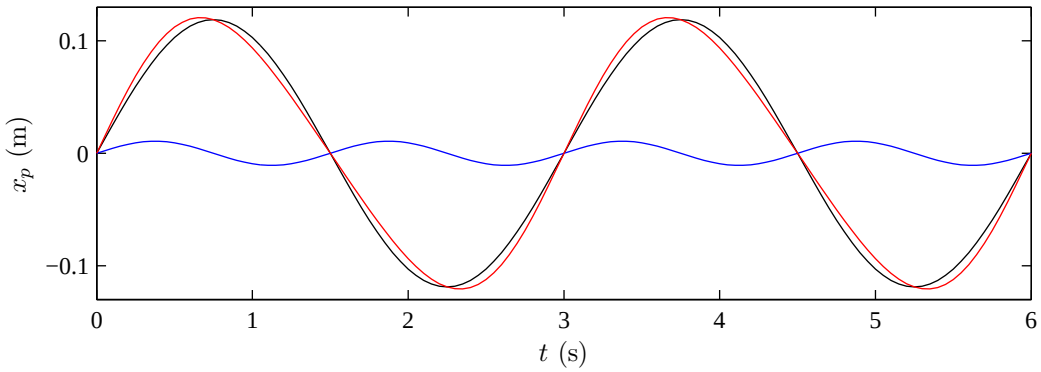

Figure 2.6: Paddle displacement time series x_p for a regular wave. Black line denotes the first order paddle signal x_{p_0}, blue line denotes the second order paddle signal εx_{p_1}, red line denotes the combined paddle signal $x_{p_0} + \varepsilon x_{p_1}$.

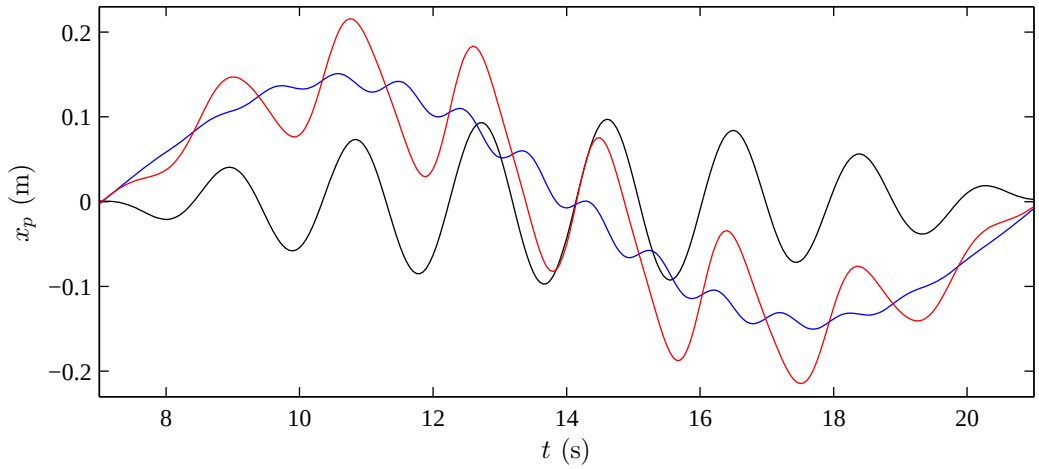

Figure 2.7: Paddle displacement time series x_p for a bichromatic wave group. Black line denotes the first order paddle signal x_{p0}, blue line denotes the second order paddle signal εx_{p1}, red line denotes the combined paddle signal $x_{p0} + \varepsilon x_{p1}$.

2.6.3 Wavemaker theory for solitary waves

A solitary wave is an infinitely long wave form that propagates without change of form. A profile of a solitary wave encompasses a symmetric positive elevation that smoothly tends back to the still water level. It is a shallow water phenomenon. Mathematically, a solitary wave described by ζ and q satisfies

$$\zeta(x,t) = \zeta(x - Ct) = \zeta(\xi) \qquad \text{and} \qquad q(x,t) = q(x - Ct) = q(\xi), \tag{2.41a}$$

where C is the wave celerity and $\xi = x - Ct$ is the moving ordinate. Additionally, ζ and q satisfy

$$\lim_{\xi \to \pm\infty} \zeta^{(n)}(\xi) = 0 \qquad \text{and} \qquad \lim_{\xi \to \pm\infty} q^{(n)}(\xi) = 0, \tag{2.41b}$$

where $n = 0, 1, 2, \ldots$ and subscript $^{(n)}$ denotes the n^{th} derivative with respect to ξ.

Following Goring (1978), in shallow water wavemaker theory the paddle velocity $(x_p)_t$ is matched with the local depth-averaged particle velocity $\overline{u}$ of the wave that is being generated, such that

$$(x_p)_t = \overline{u}(x_p, t). \tag{2.42}$$

Utilising (2.41), the continuity equation (2.15a) simplifies as $-C\zeta + q = 0$ with $q = (h + \zeta)\overline{u}$, and therefore (2.42) can be rewritten in terms of ζ and C as follows

$$(x_p)_t = \frac{C\zeta(x_p, t)}{h + \zeta(x_p, t)}. \tag{2.43}$$

For a sech^2 solitary wave with amplitude A and free surface profile given by

$$\zeta = A\,\text{sech}^2(\kappa(x - Ct)), \tag{2.44a}$$

where

$$\kappa = \sqrt{\frac{3A}{4h^3}} \quad \text{and} \quad C = \sqrt{g(h+A)}, \tag{2.44b}$$

Equation (2.43) can be integrated numerically to find x_p. Since it is a first order ordinary differential equation, an in-built solver in Matlab such as ode113 can be employed. Alternatively, Goring (1978) gives an implicit expression for x_p for a sech^2 solitary wave such that

$$x_p = \frac{A}{\kappa h} \tanh(\kappa(x_p - Ct)), \tag{2.45}$$

which, at every desired time increment, can be solved for x_p iteratively. Figure 2.8 shows the calculated paddle signal x_p for a sech^2 solitary wave with amplitude $A = 0.1$ m on $h = 0.5$ m depth. This paddle signal is used in Chapter 4.

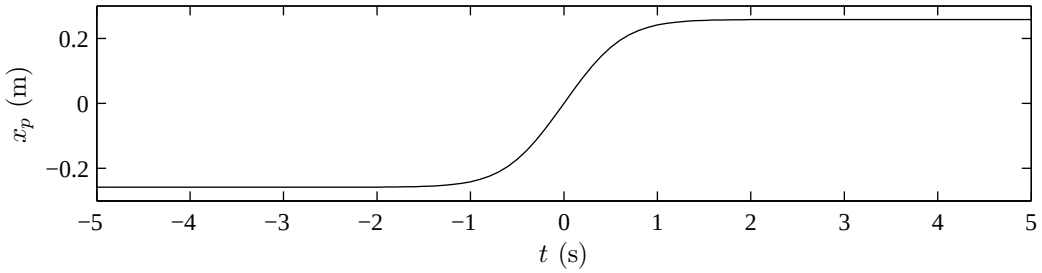

Figure 2.8: Paddle displacement time series x_p for a sech^2 solitary wave.

2.7 Chapter summary

- This chapter presents derivation of the classical Boussinesq equation for one horizontal dimension. The starting point is the Laplace equation, with the associated free surface and bottom boundary conditions. Retaining only $O(\mu^2, \varepsilon)$ terms, the conservation of mass and the conservation of horizontal momentum Boussinesq equations are formulated, whereby the vertical coordinate has been explicitly eliminated.

- Enhancement technique, using linear long wave theory, allows for improved linear dispersion characteristics extending the range of applicability of the new equation set to $kh = 3$. It should be emphasised, that the formal order of the equations has not been raised, and therefore the flow field in the extended region is not accurate.

- The non-linear shallow water equations are introduced, and both of the governing equations are expressed in the stage-discharge (η, q) formulation. Wave

breaking treatment is discussed, where by the governing equations locally switch from the Boussinesq to the non-linear shallow water equations upon the free surface slope satisfying $-\eta_x \geq 0.4$.

- Piston paddle moving boundary is incorporated into the model using a domain transformation in the vicinity of the paddle. The Boussinesq governing equations are solved in the fixed transformed domain. The solution is then mapped back onto the physical domain, which changes in size according to the paddle position. First and second order wavemaker theory is introduced, as well as the non-linear algorithm for solitary waves generation.

Chapter 3

Numerical implementation

This chapter describes the numerical methods applied to solve the governing equations of the present model. The Boussinesq equations are discretised with finite differences, as smooth solutions are expected pre-breaking. A shock-capturing finite volume method is applied to the non-linear shallow water equations in order to resolve the propagating bores. Wave breaking is handled using a single parameter criterion, with a smooth transition between the Boussinesq and the shallow water equations. Treatment of wetting and drying at the moving shoreline is also presented. Due to the moving paddle that is built into the numerical model, special attention is given to the computational grid used for the Boussinesq equations. Figure 3.1 shows a typical domain under consideration with labels for individual sections to visually show how this chapter is organised.

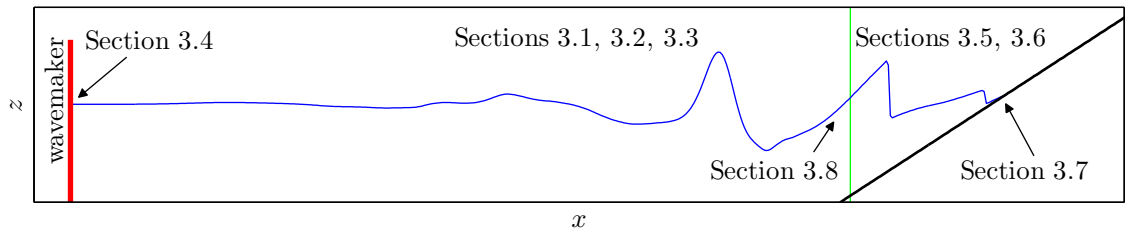

Figure 3.1: Structure of Chapter 3 shown on a typical domain under consideration. Note that the green vertical line denotes the interface between the Boussinesq equations domain and the non-linear shallow water equations domain.

3.1 Computational grids for the Boussinesq equations

Let the physical domain under consideration be defined as $x \in [0\ L]$, where L denotes the length of the flume. Initially, the paddle is at rest such that $x_p(0) = 0$. The initial

underlying uniform computational grid x_i^0 is defined by

$$x_i^0 = (i-1)\Delta x, \text{ where } \Delta x = \frac{L}{(M-1)}, \qquad \text{for } i = 1 \dots M, \tag{3.1}$$

where M is the total number of grid points and Δx is the spacing between any two adjacent grid points x_i^0.

However, as discussed in Section 2.6.1, the size of the domain changes according to the paddle movement. For this reason, the *paddle domain* $x \in [x_p \; m_0]$ is mapped onto a fixed $\tilde{x} \in [0 \; m_0]$ domain. The value of m_0, which defines the end of the *paddle domain*, is given by

$$m_0 = (\widetilde{M} - 1)\Delta x, \text{ where } (\widetilde{M} - 1) \text{ is the nearest integer of } \max_t \frac{10 x_p(t)}{\Delta x}. \tag{3.2}$$

In the transformed *paddle domain* $\tilde{x} \in [0 \; m_0]$, a uniform computational grid $\tilde{x}_i$ is used, such that

$$\tilde{x}_i = (i-1)\Delta \tilde{x}, \text{ where } \Delta \tilde{x} = \frac{m_0}{(\widetilde{M} - 1)} = \Delta x, \qquad \text{for } i = 1 \dots \widetilde{M}, \tag{3.3}$$

where $\widetilde{M}$ is the number of grid points in the transformed *paddle domain* and $\Delta \tilde{x} = \Delta x$ is the spacing between any two adjacent grid points $\tilde{x}_i$ in the transformed domain. At each time step, the updated solution for (η, q) in the fixed transformed domain $\tilde{x} \in [0 \; m_0]$ is calculated from the transformed Boussinesq equations (2.29). It is then mapped onto the physical domain using the inverse transformation $T^{-1}(\tilde{x}) = x = \tilde{x}\frac{m}{m_0} + x_p$. The solution grid of the original time-varying *paddle domain* $x \in [x_p \; m_0]$ is thus recovered via T^{-1} such that

$$x_i = x_p + \frac{m}{m_0}(i-1)\Delta x \qquad \text{for } i = 1 \dots \widetilde{M}. \tag{3.4}$$

It is clear that this solution grid varies in time since $m = m(t)$ and $x_p = x_p(t)$. Spacing between any two grid points x_i is given by $\frac{m}{m_0}\Delta x$, which is a function of time. When the paddle moves forwards such that $x_p > 0$, the *paddle domain* contracts and the grid spacing between individual grids points x_i decreases, since under these circumstances $m < m_0$ and therefore $\frac{m}{m_0}\Delta x < \Delta x$. Equivalently, when the paddle moves backwards such that $x_p < 0$, the *paddle domain* expands and the spacing increases, since in this case $m > m_0$ and therefore $\frac{m}{m_0}\Delta x > \Delta x$. Figure 3.2 shows the adapting solution grid with $m_0 = 1$ m.

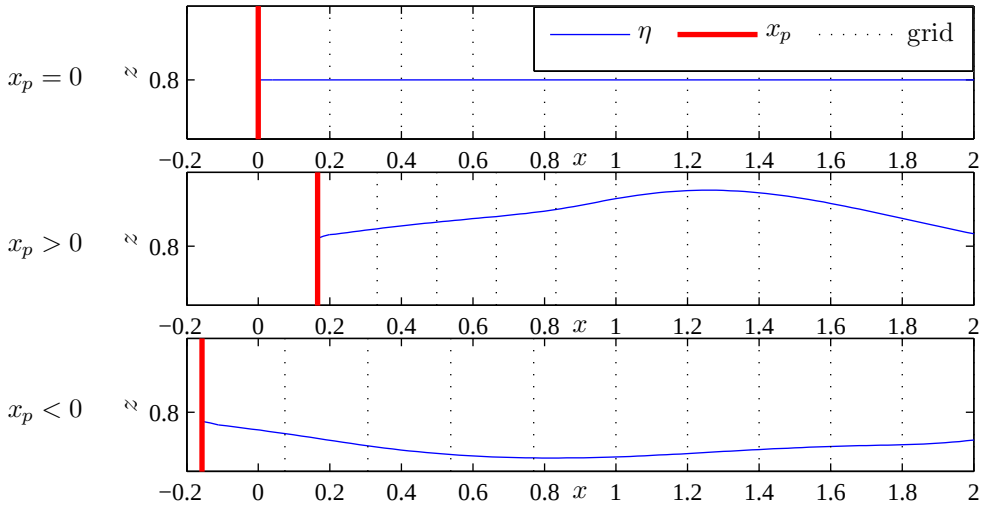

Figure 3.2: Adapting solution grid in the *paddle domain* for $x \leq 1$ m. Fixed computational grid for $x > 1$ m.

The region of the domain, where the original untransformed Boussinesq equations (2.27) are solved, utilizes a uniform grid

$$x_i = (i-1)\Delta x \qquad \text{for } i = \widetilde{M} + 1 \ldots M_{switch}, \tag{3.5}$$

where M_{switch} is the index of the last grid point solved by the Boussinesq equations. As discussed in Section 2.5, the switch between the Boussinesq equations and the shallow water equations is determined at every time step according to the local wave steepness η_x and the dispersion parameter μ; therefore, $M_{switch} = M_{switch}(t)$. Figure 3.2 shows part of the fixed uniform grid for $x > 1$ m.

3.2 Finite difference discretisation for the Boussinesq equations

Both Boussinesq equation sets (2.27) and (2.29) are discretized and solved using finite differences. All spatial derivatives, apart from when very close to the moving paddle, are approximated by 5-point centered stencils. This leads to fourth order accuracy for first and second derivatives, and second order accuracy for third derivatives. As pointed out by Wei and Kirby (1995), this ensures that, in the momentum equations (2.27b) and (2.29b), the truncation error arising from discretising first derivatives is smaller than the dispersive terms with third derivatives. The derivative approximations for an arbitrary function $f = f(x)$ at $x = x_i$ on a uniform grid with Δx

spacing are given below in (3.6), where $f_i = f(x_i)$. Note that x is replaced by $\tilde{x}$ when discretising (2.29).

$$f_x(x_i) \approx \frac{1}{12\Delta x}(f_{i-2} - 8f_{i-1} + 8f_{i+1} - f_{i+2}), \tag{3.6a}$$

$$f_{xx}(x_i) \approx \frac{1}{12(\Delta x)^2}(-f_{i-2} + 16f_{i-1} - 30f_i + 16f_{i+1} - f_{i+2}), \tag{3.6b}$$

$$f_{xxx}(x_i) \approx \frac{1}{2(\Delta x)^3}(-f_{i-2} + 2f_{i-1} - 2f_{i+1} + f_{i+2}). \tag{3.6c}$$

Care has to be taken at the interface between the *paddle domain* and the rest of the Boussinesq domain, as different governing equations and computational grids are used on either side of the grid point $\widetilde{M}$. The *paddle domain* is solved in the transformed ordinate system given by $\tilde{x}$, whereas the rest of the Boussinesq domain is solved in the original ordinate system given by x. When approximating spatial derivatives with respect to $\tilde{x}$ at grid points $\widetilde{M}-1$ and $\widetilde{M}$; and spatial derivatives with respect to x at grid point $\widetilde{M}+1$, the finite difference stencils span both regions. Figure 3.3 shows the grid around the interface, viewed in the transformed $\tilde{x}$ ordinate system in subplot *a)*, and in the original x ordinate system in subplot *b)*.

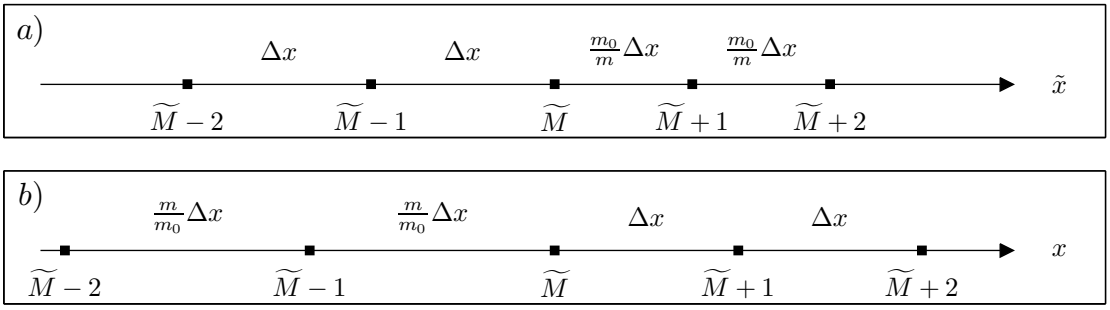

Figure 3.3: Computational grid around grid point $\widetilde{M}$, viewed in ordinate $\tilde{x}$ in subplot *a)* and in ordinate x in subplot *b)*.

Due to the non-uniform spacing between grid points at the interface, the stencil (3.7) is used for discretisation of first order derivatives at grid points $\widetilde{M}-1$, $\widetilde{M}$ and $\widetilde{M}+1$. Equivalent expressions for higher derivatives can be found in Appendix B.

$$\begin{aligned} f_{\tilde{x}}(\tilde{x}_{\widetilde{M}-1}) \approx{}& \frac{1}{\Delta x}\Big(\frac{m+m_0}{6(3m+m_0)}\Big) f_{\widetilde{M}-3} \\ &- \frac{1}{\Delta x}\Big(\frac{m+m_0}{2m+m_0}\Big) f_{\widetilde{M}-2} \\ &- \frac{1}{\Delta x}\Big(\frac{m-m_0}{2(m+m_0)}\Big) f_{\widetilde{M}-1} \\ &+ \frac{1}{\Delta x}\Big(\frac{m+m_0}{3m_0}\Big) f_{\widetilde{M}} \end{aligned}$$

$$- \frac{1}{\Delta x}\Big(\frac{2m^4}{m_0(m+m_0)(2m+m_0)(3m+m_0)}\Big) f_{\widetilde{M}+1} \tag{3.7a}$$

$$\begin{aligned} f_{\tilde{x}}(\tilde{x}_{\widetilde{M}}) \approx{}& \frac{1}{\Delta x}\Big(\frac{m_0^2}{2(m+m_0)(2m+m_0)}\Big) f_{\widetilde{M}-2} \\ &- \frac{1}{\Delta x}\Big(\frac{4m_0^2}{(m+m_0)(m+2m_0)}\Big) f_{\widetilde{M}-1} \\ &- \frac{1}{\Delta x}\Big(\frac{3(m-m_0)}{2m_0}\Big) f_{\widetilde{M}} \\ &+ \frac{1}{\Delta x}\Big(\frac{4m^3}{m_0(m+m_0)(2m+m_0)}\Big) f_{\widetilde{M}+1} \\ &- \frac{1}{\Delta x}\Big(\frac{m^3}{2m_0(m+m_0)(m+2m_0)}\Big) f_{\widetilde{M}+2} \end{aligned} \tag{3.7b}$$

$$\begin{aligned} f_x(x_{\widetilde{M}+1}) \approx{}& \frac{1}{\Delta x}\Big(\frac{2m_0^4}{m(m+m_0)(m+2m_0)(m+3m_0)}\Big) f_{\widetilde{M}-1} \\ &- \frac{1}{\Delta x}\Big(\frac{m+m_0}{3m}\Big) f_{\widetilde{M}} \\ &- \frac{1}{\Delta x}\Big(\frac{m-m_0}{2(m+m_0)}\Big) f_{\widetilde{M}+1} \\ &+ \frac{1}{\Delta x}\Big(\frac{m+m_0}{(m+2m_0)}\Big) f_{\widetilde{M}+2} \\ &- \frac{1}{\Delta x}\Big(\frac{m+m_0}{6(m+3m_0)}\Big) f_{\widetilde{M}+3}. \end{aligned} \tag{3.7c}$$

At grid points $\tilde{x}_1$ and $\tilde{x}_2$, which are the two grid points closest to the moving paddle, a special local discretisation treatment is used, as described in Section 3.4.

3.3 Time integration for the Boussinesq equations

Discretised systems (2.27) and (2.29), via Equations (3.6), (3.7) and (B.1), can be written together as

$$\boldsymbol{\eta}_t = \boldsymbol{a}(\boldsymbol{\eta}, \boldsymbol{q}) \qquad \text{and} \qquad \boldsymbol{M}\boldsymbol{q}_t = \boldsymbol{b}(\boldsymbol{\eta}, \boldsymbol{q}), \tag{3.8}$$

where $\boldsymbol{\eta}$ and $\boldsymbol{q}$ each represent a vector of values of η and q at all grid points with indices $i = 3, \ldots, M_{switch}$, $\boldsymbol{a}$ and $\boldsymbol{b}$ are vectors dependent on values of $\boldsymbol{\eta}$ and $\boldsymbol{q}$, and $\boldsymbol{M}$ is a matrix of coefficients. $\boldsymbol{a}$ follows from the right-hand side of (2.27a) and (2.29a). $\boldsymbol{b}$ follows from the right-hand side of (2.27b) and (2.29b). $\boldsymbol{M}$ follows from discretised functions F and G defined by (2.27c) and (2.29c). System (3.8) is integrated forward in time using a fourth order Runge-Kutta method (RK4), which uses the following

time advancing algorithm:

$$\boldsymbol{\eta}^{n+1} = \boldsymbol{\eta}^n + \frac{1}{6}\Delta t(\boldsymbol{k}^1 + 2\boldsymbol{k}^2 + 2\boldsymbol{k}^3 + \boldsymbol{k}^4), \qquad \boldsymbol{q}^{n+1} = \boldsymbol{q}^n + \frac{1}{6}\Delta t(\boldsymbol{l}^1 + 2\boldsymbol{l}^2 + 2\boldsymbol{l}^3 + \boldsymbol{l}^4),$$

where

$$\begin{aligned}
\boldsymbol{k}^1 &= \boldsymbol{a}(\boldsymbol{\eta}^n, \boldsymbol{q}^n), & \boldsymbol{M}\boldsymbol{l}^1 &= \boldsymbol{b}(\boldsymbol{\eta}^n, \boldsymbol{q}^n),\\
\boldsymbol{k}^2 &= \boldsymbol{a}(\boldsymbol{\eta}^n + \frac{1}{2}\Delta t\boldsymbol{k}^1, \boldsymbol{q}^n + \frac{1}{2}\Delta t\boldsymbol{l}^1), & \boldsymbol{M}\boldsymbol{l}^2 &= \boldsymbol{b}(\boldsymbol{\eta}^n + \frac{1}{2}\Delta t\boldsymbol{k}^1, \boldsymbol{q}^n + \frac{1}{2}\Delta t\boldsymbol{l}^1),\\
\boldsymbol{k}^3 &= \boldsymbol{a}(\boldsymbol{\eta}^n + \frac{1}{2}\Delta t\boldsymbol{k}^2, \boldsymbol{q}^n + \frac{1}{2}\Delta t\boldsymbol{l}^2), & \boldsymbol{M}\boldsymbol{l}^3 &= \boldsymbol{b}(\boldsymbol{\eta}^n + \frac{1}{2}\Delta t\boldsymbol{k}^2, \boldsymbol{q}^n + \frac{1}{2}\Delta t\boldsymbol{l}^2),\\
\boldsymbol{k}^4 &= \boldsymbol{a}(\boldsymbol{\eta}^n + \Delta t\boldsymbol{k}^3, \boldsymbol{q}^n + \Delta t\boldsymbol{l}^3), & \boldsymbol{M}\boldsymbol{l}^4 &= \boldsymbol{b}(\boldsymbol{\eta}^n + \Delta t\boldsymbol{k}^3, \boldsymbol{q}^n + \Delta t\boldsymbol{l}^3),
\end{aligned}$$

where $\boldsymbol{\eta}^{n+1}$ and $\boldsymbol{q}^{n+1}$ denote the newly updated values of η and q calculated from the known values $\boldsymbol{\eta}^n$ and $\boldsymbol{q}^n$; $\boldsymbol{k}^j$ and $\boldsymbol{l}^j$ for $j = 1, \ldots, 4$ denote the intermediate rates of change of η and q at the j^{th} step of the RK4 algorithm and Δt denotes the time stepping interval. It is clear from the above that, at each of the four intermediate steps, a system of equations has to be solved for $\boldsymbol{l}$. Since $\boldsymbol{M}$ is a pentadiagonal matrix, each system can be efficiently solved by an extension of the Thomas algorithm, whereby row operations eliminate non-zero entries from the two sub-diagonals, and back-substitution is used to find $\boldsymbol{l}$.

If at the n^{th} time step, the switch between the Boussinesq equations and the non-linear shallow water equations exists, then the pentadiagonal system under consideration differs in size at every intermediate step of the RK4 algorithm. More details are given in Section 3.8, which explains how the Boussinesq equations and the shallow water equations domains are joined together.

If at the n^{th} time step, the Boussinesq equations are applied in the entire computational domain, the pentadiagonal system is of the same size with $i = 3, \ldots, M$ for all four intermediate steps in the RK4 algorithm.

Boundary conditions are covered in Section 3.4, where calculations of η_i^{n+1} and q_i^{n+1} for $i = 1, 2, M-1, M$ are discussed.

3.4 Boundary conditions for the Boussinesq equations

In order to avoid undesirable oscillations at the paddle arising from higher derivatives, the dispersive terms in (2.29b) and (2.29c) are neglected at the first two grid points closest to the paddle. It is assumed that over such a short distance, the lack of

dispersion is insignificant. The local momentum equation therefore becomes

$$q_t = -\frac{1}{m} m_t (m_0 - \tilde{x}) q_{\tilde{x}} - \frac{m_0}{m}\Big(\frac{q^2}{d} + \frac{1}{2} g(\eta^2 - 2\eta b)\Big)_{\tilde{x}} - \frac{\tau_b}{\rho} - g\eta \frac{m_0}{m} b_{\tilde{x}}. \tag{3.9}$$

The values of η and q at the paddle are calculated as part of the solution while utilizing the known paddle displacement signal x_p. The updated value of η on the paddle, denoted by η_1^{n+1}, is calculated via RK4 as described in Section 3.3, but using forward stencils for discretisation of spatial derivatives in (2.29a). The applied first order derivative approximation is given by Equation (3.10a), whereby grid points with indices $i = 1, \ldots, 5$ are utilised. The updated value η_2^{n+1} is calculated in an equivalent way, using (3.10b) for spatial discretisation.

$$f_{\tilde{x}}(\tilde{x}_1) \approx \frac{1}{12\Delta x}(-25 f_1 + 48 f_2 - 36 f_3 + 16 f_4 - 3 f_5), \tag{3.10a}$$

$$f_{\tilde{x}}(\tilde{x}_2) \approx \frac{1}{12\Delta x}(-3 f_1 - 10 f_2 + 18 f_3 - 6 f_4 + f_5). \tag{3.10b}$$

The updated value of q on the paddle, denoted by q_1^{n+1}, uses the updating formula $q_1^{n+1} = q_1^n + \frac{1}{6}\Delta t(l_1^1 + 2l_1^2 + 2l_1^3 + l_1^4)$, with each of the four intermediate rates of change l_1 calculated from the paddle displacement signal x_p such that $l_1 = (x_p)_t k_1 + d_1 (x_p)_{tt}$, where $(x_p)_t$ is the paddle velocity signal and $(x_p)_{tt}$ is the paddle acceleration signal, both of which are supplied to the numerical code; k_1 denotes the intermediate rates of change of η at the paddle; and d_1 is the total depth at the paddle. The updated value q_2^{n+1} is calculated in a similar way to η_2^{n+1}; applying discretisation from (3.10b) to approximate first order spatial derivatives in (3.9) and using the updating formula $q_2^{n+1} = q_2^n + \frac{1}{6}\Delta t(l_2^1 + 2l_2^2 + 2l_2^3 + l_2^4)$. Note that when calculating l_3 using the RK4 algorithm described in Section 3.3, values of l_1 and l_2 are utilised. Similarly, for calculation of l_4, l_2 is used. Whilst developing the code, numerical tests using fictitious grid points as well as Riemann invariants were carried out for calculation of the updated solution values at the paddle. However, the use of forward stencils and the paddle signal x_p gave the most stable results, and therefore has been implemented in the numerical model.

In simulations where the whole domain is solved by the Boussinesq equations, treatment at the right-hand side boundary is needed. Solid wall conditions are implemented with the use of fictitious grid points, such that

$$\eta_{M+1}^n = \eta_{M-1}^n,\ q_{M+1}^n = -q_{M-1}^n \quad \text{and} \quad \eta_{M+2}^n = \eta_{M-2}^n,\ q_{M+2}^n = -q_{M-2}^n. \tag{3.11}$$

The free surface elevation η_M^{n+1} and η_{M-1}^{n+1} and the flux q_{M-1}^{n+1} can then be calculated as part of the solution following methods from Sections 3.2 and 3.3 . Since there can be no flow through a solid boundary, the flux on the boundary is given by $q_M^{n+1} = q_M^n = 0$.

3.5 Finite volume scheme for the non-linear shallow water equations

The non-linear shallow water equations (2.24) can give rise to discontinuous solutions. For this reason the integral form of (2.24) is used such that

$$\boldsymbol{u}_i^{n+1} = \boldsymbol{u}_i^n - \frac{\Delta t}{\Delta x}(\boldsymbol{f}_{i+1/2} - \boldsymbol{f}_{i-1/2}) + \Delta t \boldsymbol{s}_i, \tag{3.12}$$

where $\boldsymbol{u}_i^{n+1}$ denotes the newly calculated cell-averaged values of η and q in the i^{th} grid cell, $\boldsymbol{u}_i^n$ denotes the known cell-averaged values of η and q in the i^{th} grid cell, $\boldsymbol{f}_{i+1/2}$ and $\boldsymbol{f}_{i-1/2}$ denote the mass and momentum fluxes through the east and west edges of the i^{th} cell respectively, $\boldsymbol{s}_i$ denotes the cell-averaged source terms evaluated at the centre of the i^{th} cell, Δt is the time stepping interval and Δx is the width of the i^{th} grid cell. A uniform grid is applied, whereby the centres of the grid cells are given by

$$x_i = (i-1)\Delta x \qquad \text{for } i = M_{switch} + 1 \ldots M. \tag{3.13}$$

Accurate estimation of the fluxes $\boldsymbol{f}_{i\pm1/2}$ is needed for the updating formula (3.12). In general, at an $(i+\frac{1}{2})^{\text{th}}$ interface between two cells, values of $\boldsymbol{u}_i$ and $\boldsymbol{u}_{i+1}$, or suitably reconstructed values of these at the cells' interface, will vary. Therefore at every interface, a Riemann problem $\boldsymbol{u}_t + \boldsymbol{f}_x = \boldsymbol{0}$ with initial conditions $\boldsymbol{u} = \boldsymbol{u}_L$ for $x < x_{i+1/2}$ and $\boldsymbol{u} = \boldsymbol{u}_R$ for $x > x_{i+1/2}$ such that, in general, $\boldsymbol{u}_L \neq \boldsymbol{u}_R$ can be considered. Several approximate Riemann solvers have been developed (see for example Toro (1999)) for an efficient estimation of the inter-cell fluxes $\boldsymbol{f}_{i\pm1/2}$, in order to use the updating formula (3.12).

Following Liang and Borthwick (2009), the inter-cell fluxes are calculated for the non-linear shallow water equations using the HLL approximate Riemann solver, which has been extended for dry bed scenarios (see Fraccarollo and Toro (1995)). The flux estimates are given by

$$\boldsymbol{f}_{i\pm1/2} = \begin{cases} \boldsymbol{f}_L = \boldsymbol{f}(\boldsymbol{u}_L) & 0 \leq S_L \\ \boldsymbol{f}_{HLL} = \dfrac{S_R\boldsymbol{f}_L - S_L\boldsymbol{f}_R + S_R S_L(\boldsymbol{u}_R - \boldsymbol{u}_L)}{S_R - S_L} & S_L \leq 0 \leq S_R \\ \boldsymbol{f}_R = \boldsymbol{f}(\boldsymbol{u}_R) & S_R \leq 0 \ , \end{cases} \tag{3.14a}$$

where S_L and S_R are the speeds of the left- and right-propagating waves given by

$$S_L = \begin{cases} u_R - 2\sqrt{gd_R} & d_L = 0, d_R > 0 \\ u_L - \sqrt{gd_L} & d_L > 0, d_R = 0 \\ \min(u_L - \sqrt{gd_L}, u^* - \sqrt{gd^*}) & d_L > 0, d_R > 0 \end{cases} \tag{3.14b}$$

$$S_R = \begin{cases} u_R + \sqrt{gd_R} & d_L = 0, d_R > 0 \\ u_L + 2\sqrt{gd_L} & d_L > 0, d_R = 0 \\ \max(u_R - \sqrt{gd_R}, u^* + \sqrt{gd^*}) & d_L > 0, d_R > 0 \end{cases} , \tag{3.14c}$$

where u^* and d^* represent the depth-averaged velocity and total depth in the middle region bounded by the two waves and are given by

$$u^* = \frac{1}{2}(u_L + u_R) + \sqrt{gd_L} - \sqrt{gd_R}, \tag{3.14d}$$

$$\sqrt{gd^*} = \frac{1}{2}(\sqrt{gd_L} + \sqrt{gd_R}) + \frac{1}{4}(u_L - u_R). \tag{3.14e}$$

Slope-limited data reconstruction is used for improved estimates of the cell edge values $\boldsymbol{u}_L$ and $\boldsymbol{u}_R$ such that

$$\boldsymbol{u}_L = \boldsymbol{u}_i + \frac{1}{2}\Psi(r_i)(\boldsymbol{u}_i - \boldsymbol{u}_{i-1}), \tag{3.15a}$$

$$\boldsymbol{u}_R = \boldsymbol{u}_{i+1} - \frac{1}{2}\Psi(r_{i+1})(\boldsymbol{u}_{i+1} - \boldsymbol{u}_i), \tag{3.15b}$$

where $\Psi(r_i)$ represents the slope limiter which restricts the slopes $(\boldsymbol{u}_i - \boldsymbol{u}_{i-1})$ in the vicinity of steep gradients or jumps in the solution. Following Liang and Borthwick (2009), a min-mod limiter is chosen, which is given by

$$\Psi(r_i) = \max(0, \min(r_i, 1)); \tag{3.15c}$$

where r_i represents the gradient ratios, where

$$r_i = \frac{\eta_{i+1} - \eta_i}{\eta_i - \eta_{i-1}} \qquad \text{and} \qquad r_i = \frac{q_{i+1} - q_i}{q_i - q_{i-1}} \tag{3.15d}$$

for the non-linear shallow water equations (2.24).

3.6 Time integration for the non-linear shallow water equations

A predictor-corrector time-stepping MUSCL-Hancock method is adopted, which leads to overall second order accuracy in time and space. The method was originally proposed by van Leer (1984). It consists of the following three steps:

1. Data reconstruction: to find the interface values $\boldsymbol{u}^n_{i\pm1/2}$ via Equation (3.15), namely
$$\boldsymbol{u}^n_{i\pm1/2} = \boldsymbol{u}^n_i \pm \frac{1}{2}\Psi(r_i)\big(\boldsymbol{u}^n_i - \boldsymbol{u}^n_{i-1}\big).$$
2. Evolution: to update the values $\boldsymbol{u}^n_{i\pm1/2}$ over half a time step such that
$$\boldsymbol{u}^{n+1/2}_{i\pm1/2} = \boldsymbol{u}^n_{i\pm1/2} - \frac{1}{2}\frac{\Delta t}{\Delta x}\Big(\boldsymbol{f}(\boldsymbol{u}^n_{i+1/2}) - \boldsymbol{f}(\boldsymbol{u}^n_{i-1/2})\Big) + \frac{1}{2}\Delta t\boldsymbol{s}(\boldsymbol{u}^n_i).$$

3. Riemann problem: to calculate the inter-cell fluxes $\boldsymbol{f}_{i\pm1/2}$ at the $(i \pm \frac{1}{2})^{\text{th}}$ interfaces with the HLL approximate Riemann solver given by (3.14) with initial conditions for the $(i+\frac{1}{2})^{\text{th}}$ interface such that $\boldsymbol{u}_L = \boldsymbol{u}_{i+1/2}^{n+1/2}$ and $\boldsymbol{u}_R = \boldsymbol{u}_{(i+1)-1/2}^{n+1/2}$ and for the $(i-\frac{1}{2})^{\text{th}}$ interface such that $\boldsymbol{u}_L = \boldsymbol{u}_{(i-1)+1/2}^{n+1/2}$ and $\boldsymbol{u}_R = \boldsymbol{u}_{i-1/2}^{n+1/2}$; and finally to update the cell-averaged values of $\boldsymbol{u}_i$ using the updating formula (3.12).

3.7 Boundary conditions and wetting and drying for the non-linear shallow water equations

If the end of the flume is inundated and the non-linear shallow water equations are applied in this section of the domain, fictitious grid cells are used to implement boundary conditions. For a solid wall at the interface between M^{th} and $(M+1)^{\text{th}}$ grid cells, the following values

$$\eta_{M+1} = \eta_M, q_{M+1} = -q_M \qquad \text{and} \qquad \eta_{M+2} = \eta_{M-1}, q_{M+2} = -q_{M-1} \tag{3.16}$$

ensure no flow through the solid boundary.

Wetting and drying at the moving shoreline is calculated as part of the solution. The approach devised by Brufau *et al.* (2002) is adopted, whereby local bed modification at the wet-dry front ensures correct flow features. Dry cells are excluded from the computational domain unless they are about to be flooded. Figure 3.4 depicts two possible scenarios at a left-hand side wet-dry front. When the water level of the left wet cell is below or the same as the bed level of the right dry cell, $\eta_L \leq \eta_R = b_R$, temporarily setting $b_R = \eta_L$ and $q_R = -q_L$ ensures no flow between the two cells, as desired. Alternatively, when the water level of the left wet cell is above the bed level of the right dry cell, $\eta_L > \eta_R = b_R$, the right cell is included in the computational domain. The right face of the dry cell becomes the computational boundary. Temporary adjustment of the bed level and flux in the first cell outside the computation domain as shown in Figure 3.4 prevents spurious flow in the dry area. In order to increase stability of the model, cells with water depth $d < 10^{-5}$ m are dried automatically. The minuscule amount of water is moved across to a neighbouring wet cell to ensure mass conservation. The above treatment allows for separation of water mass into disjoint blocks with each block of water evolving independently. Such a situation can occur during an overtopping event, where the model can simultaneously calculate the solution in front as well as behind the overtoppped structure.

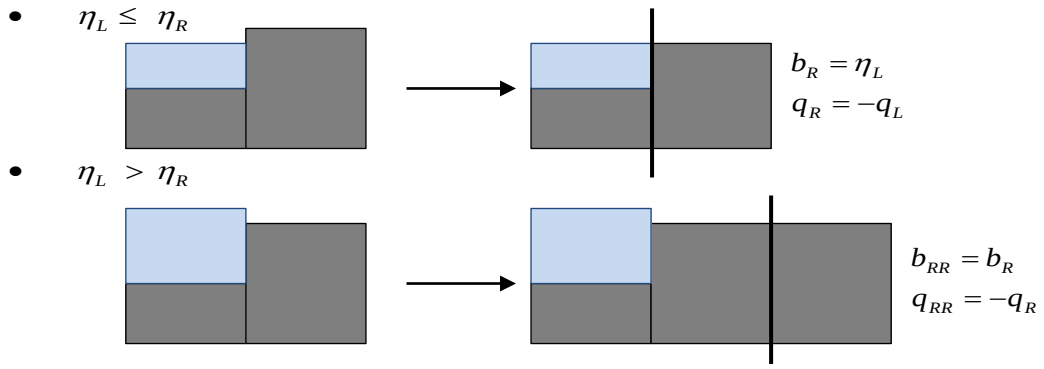

Figure 3.4: Local bed modification at the wet-dry front according to Brufau *et al.* (2002).

3.8 Joining Boussinesq equations and shallow water equations domains

At the interface between the Boussinesq equations domain and the shallow water equations domain, defined by the grid point $x_{M_{switch}}$, artificial treatment is carried out to facilitate a smooth transition between the two domains. The dispersive terms in (2.27) are smoothly ramped down over half a wavelength of the breaking wave such that they vanish at $x_{M_{switch}}$. The ramping function f_r, which pre-multiplies all dispersive terms in (2.27), is given by

$$f_r(x) = \begin{cases} 1 & x < r_s \\ \cos^2\left(\frac{\pi}{2}\frac{x - r_s}{(x_{M_{switch}} - r_s)}\right) & r_s \leq x \leq x_{M_{switch}}, \end{cases} \tag{3.17}$$

where r_s denotes the start of the ramping down zone, which is located quarter of a wavelength offshore from $x_{M_{switch}}$. Applying f_r ensures that the two domains are compatible, because at $x_{M_{switch}}$ the non-linear shallow water equations are solved since the dispersive terms have completely vanished. The above treatment enhances the code's stability. Whilst it is completely artificial, the treatment is only applied in a narrow zone of the overall domain.

Additionally, small adjustments have to be made to the Boussinesq solver described in Section 3.3, if the switch between the Boussinesq equations and non-linear shallow water equations exists. In the RK4 algorithm, the pentadiagonal system $\boldsymbol{Ml} = \boldsymbol{b}$ differs in size at every one of the four intermediate steps. At the first intermediate step, when calculating $\boldsymbol{l}^1$, the system to be solved involves grid points $x_3, \ldots, x_{\widetilde{M}}$ and $x_{\widetilde{M}+1}, \ldots, x_{M_{switch}+6}$. At each successive intermediate step, the system's dimension reduces by two, such that when calculating $\boldsymbol{l}^4$ the system under

consideration involves grid points with indices $3, \ldots, M_{switch}$. This ensures functionality of the algorithm, as the grid point $x_{M_{switch}}$ is in the interior of the computational domain and therefore there is no boundary condition available. Grid points with $i > M_{switch}$ in a way act as fictitious points for the Boussinesq solver. Their values are governed by the non-linear shallow water equations and therefore the entries of matrix $\boldsymbol{M}$ are such that $m_{ij} = 1$ for $i = j$ and $m_{ij} = 0$ for $i \neq j$; and entries of vector $\boldsymbol{b}$, b_i, follow from (2.24b).

Similarly, the grid point $x_{M_{switch}}$ acts as a fictitious point for the shallow water equations solver. The values $\boldsymbol{u}_{M_{switch}}$ are used in data reconstruction given by (3.15) at the edge between cells with indices M_{switch} and $(M_{switch} + 1)$.

3.9 Stability issues

An initial value for a time step Δt is input into the model at the beginning of a simulation. At each time level, the Courant-Friedrichs-Lewy condition is checked and, if need be, the time step Δt is reduced so that

$$\Delta t \leq \Delta t_{CFL} = C \min_i \frac{\Delta x}{|\overline{u}_i| + \sqrt{g d_i}}, \tag{3.18}$$

where C is the Courant number, $\overline{u}_i = \dfrac{q_i}{d_i}$ is the depth-averaged horizontal velocity at the i^{th} grid point and $d_i = \eta_i - b_i$ is the total water depth at the i^{th} grid point. Condition (3.18) is checked at all inundated grid points, including both the Boussinesq equations and the shallow water equations domains. For all calculations performed herein $0.8 \leq C \leq 1$ is used.

In some cases numerical instabilities in the form of rather short waves can arise in simulations carried out by the model. These can grow rapidly and cause a blow-up of the model. In order to improve the stability of the numerical code, optional numerical smoothing can be applied to the newly calculated (η, q) solution to eliminate these undesired oscillations. The applied 5-point filter is given by

$$\eta_i^{filt} = \frac{1}{20}\big(\eta_{i-2} + 4\eta_{i-1} + 10\eta_i + 4\eta_{i+1} + \eta_{i+2}\big), \tag{3.19}$$

where η_i^{filt} represents the newly smoothed value of η. The same filter is used for the flux q. The ratio of the smoothed to unsmoothed amplitudes is refereed to as the filter response function (see Shapiro (1970)). Figure 3.5 shows the filter response function with respect to the ratio of wavelength λ to grid spacing Δx. It can be seen that the filter's response is rather gradual, with a range of shorter waves being

heavily filtered. This is necessary for situations where sharp reflected waves re-enter the finite difference Boussinesq domain, as discussed in Section 5.4 and 5.6. It should be noted, that the use of the filter should be kept to a minimum as the overall energy in the system is reduced every time the filter is applied. In the following chapters, any application of the filter is explicitly commented upon.

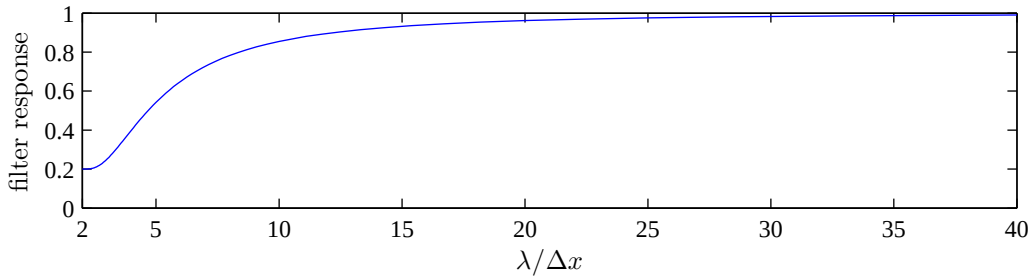

Figure 3.5: Response function of the 5-point filter.

3.10 Chapter summary

- This chapter has presented numerical implementation of the governing equations together with the associated boundary conditions and the wave breaking treatment to create a complete numerical model. The Boussinesq equations are discretised using 5-point central finite different stencils, and are integrated forward in time using a fourth order Runge-Kutta algorithm. The non-linear shallow water equations are solved with the second order MUSCL-Hancock method, with a min-mod limiter used for data reconstruction and the HLL approximate Riemann solver used for estimation of the inter-cell fluxes.

- Due to the moving paddle wavemaker, an adaptive grid is used in the vicinity of the paddle. Non-uniform finite difference stencils are applied at the interface between the *paddle domain* and the rest of the Boussinesq domain.

- The motion of the wetting and drying front is calculated as part of the solution. Dry cells are excluded from the computational domain, unless they are about to be inundated in the next time step. At the shoreline, temporary adjustment to the bed level of the dry cell is applied according to Brufau *et al.* (2002) to ensure that spurious inter-cell fluxes are prevented and that correct flow features are calculated.

- Wave breaking is approximated by switching to the non-linear shallow water equations. The dispersive terms in the Boussinesq momentum equation are

smoothly ramped down, so that at the interface the two equation sets are compatible.

Chapter 4

Model performance tests

In this chapter the numerical model is tested against analytical solutions and experimental measurements.

4.1 Model verification against analytical solutions

First an exact numerical solitary wave solution is derived for the Boussinesq equations by Madsen and Sørensen (1992), with a closed form relation between the solitary wave amplitude and celerity. To the author's knowledge this semi-analytical solution is new. The solution is used to test the model's conservation properties in Section 4.1.1, as well as the numerical paddle wavemaker in Section 4.1.4. A reversibility check in Section 4.1.2 confirms correct discretisation and time-marching of the numerical model, and is also used for calculating the model's convergence rate. The wetting and drying algorithm is tested against an exact solution provided by Sampson *et al.* (2006) for sloshing in a parabolic basin.

4.1.1 Exact solitary wave propagation

For flat bottom topography and no bottom friction, the Boussinesq equations of Madsen and Sørensen (1992) in the (ζ, q) formulation become

$$\zeta_t + q_x = 0, \tag{4.1a}$$

$$q_t + \left(\frac{q^2}{h+\zeta}\right)_x + g(h+\zeta)\zeta_x = \left(B + \frac{1}{3}\right)h^2 q_{xxt} + Bgh^3\zeta_{xxx}. \tag{4.1b}$$

A solitary wave satisfies

$$\zeta(x,t) = \zeta(x - Ct) \equiv \zeta(\xi), \qquad \lim_{\xi\to\pm\infty} \zeta^{(n)}(\xi) = 0, \tag{4.2a}$$

$$q(x,t) = q(x - Ct) \equiv q(\xi), \qquad \lim_{\xi\to\pm\infty} q^{(n)}(\xi) = 0, \tag{4.2b}$$

where C is the wave celerity, $\xi = x - Ct$ is the moving ordinate, $n = 0, 1, 2, \ldots$ and subscript $^{(n)}$ denotes the n^{th} derivative with respect to ξ. Following a direct integration method, also used by Chen *et al.* (2004) and Zhang *et al.* (2004), for a solitary wave solution, the system (4.1) reduces to

$$-C\zeta + q = 0, \tag{4.3a}$$

$$-Cq + \frac{q^2}{h+\zeta} + gh\zeta + \frac{1}{2}g\zeta^2 = -C\Big(B + \frac{1}{3}\Big)h^2 q'' + Bgh^3\zeta'', \tag{4.3b}$$

where the primes denote derivatives with respect to the ordinate ξ. Substituting (4.3a) into (4.3b) results in a second order ordinary differential equation for the flux q

$$q''\Big(-C\Big(B + \frac{1}{3}\Big)h^2 + \frac{Bgh^3}{C}\Big) = \Big(\frac{gh - C^2}{C}\Big)q + \Big(\frac{g}{2C^2}\Big)q^2 + \frac{Cq^2}{Ch + q}, \tag{4.4}$$

Pre-multiplying Equation (4.4) by q' and integrating with respect to ξ symbolically with Matlab® leads to a first order ordinary differential equation for the flux q

$$\frac{1}{2}(q')^2\Big(-C\Big(B + \frac{1}{3}\Big) + \frac{Bgh}{C}\Big) = -\Big(\frac{C^2}{h}\Big)q + \Big(\frac{g}{2Ch}\Big)q^2 + \Big(\frac{g}{6C^2h^2}\Big)q^3 + C^3\ln\Big(\frac{Ch+q}{Ch}\Big), \tag{4.5a}$$

which can be re-arranged as

$$q' = \pm\sqrt{\frac{3Cghq^2 + gq^3 - 6C^4hq + 6C^5h^2(\ln(Ch+q) - \ln(Ch))}{Ch^2(-3C^2B - C^2 + 3Bgh)}} \equiv \pm Z(q). \tag{4.5b}$$

Setting $q' = 0$ in Equation (4.5) provides a relation between the peak flux q_{max} and the wave celerity C. Using Equation (4.3a) it is also possible to derive a relationship between the solitary wave amplitude A and the wave celerity C such that

$$C = \sqrt{\frac{ghA^2(A+3h)}{6h^2(A - h\ln(\frac{h+A}{h}))}} = \sqrt{gh\frac{(1 + \frac{1}{3}\frac{A}{h})}{(1 - \frac{2}{3}(\frac{A}{h}) + \frac{2}{4}(\frac{A}{h})^2 - \frac{2}{5}(\frac{A}{h})^3 + \frac{2}{6}(\frac{A}{h})^4 - ...)}}. \tag{4.6}$$

Equation (4.5b) can be used to give an implicit expression for the flux q at each point along the wave profile, such that

$$\xi = \pm\int_{q_{max}}^{q} \frac{1}{Z(q)}\mathrm{d}q. \tag{4.7}$$

Unfortunately, there appears to be no closed form analytical solution.

Therefore, for a chosen solitary wave amplitude A and still water depth h, Equations (4.6) and (4.3a) give the wave celerity C and the peak flux q_{max} respectively. In order to calculate the flux variation within the wave, Equation (4.5b) with boundary condition $q(0) = q_{max}$ is solved numerically with ode113, an inbuilt ODE solver

in Matlab®. The wave profile is then calculated via (4.3a). This solution can be described as in a semi-analytical form because it is derived from the single ordinary differential equation (4.5b) which has been reduced from the original system of partial differential equations (4.1).

A solitary wave of amplitude $A = 0.6$ m propagating in otherwise still water of depth of $h = 1$ m has been calculated using the above method. The result, in terms of (η, q), is input as the initial condition for the hybrid numerical model. Figure 4.1 shows the initial profile (centered at $x = 30$ m) and the subsequent evolution of the solitary wave. The wave propagates without any change of form as expected, confirming that the governing equations have been correctly discretized and accurately time marched. The profiles are deliberately stacked with vertical spacing of 0.6 m to show clearly the non-changing amplitude of the propagating wave. The whole domain is automatically solved by the Boussinesq equations (2.27) since the breaking threshold criterion has not been reached.

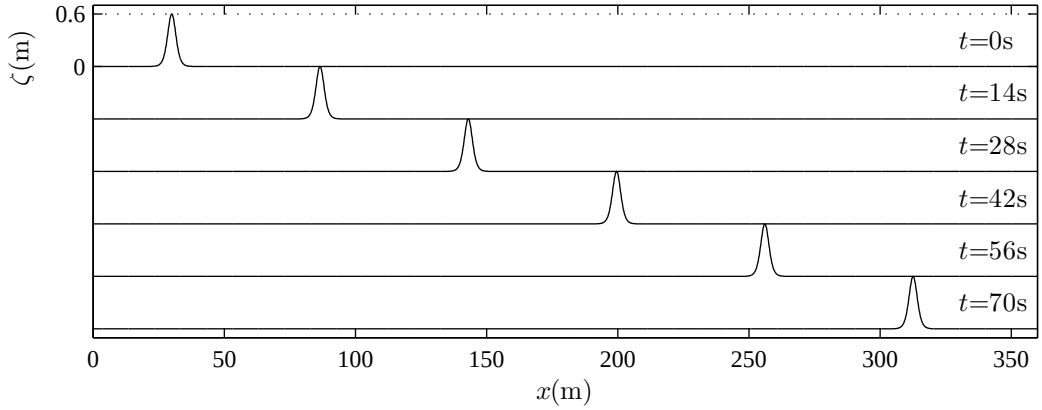

Figure 4.1: Evolution of the exact $A = 0.6$ m solitary wave.

In this case, the wave celerity to 5 significant figures is $C = 4.0373$ ms^{-1}. Figure 4.2 shows the numerically predicted and the semi-analytical wave profiles plotted against the moving coordinate $\xi = x - Ct$ at $t = 70$ s. The two profiles coincide, confirming the ability of the numerical model to propagate information at the correct speed.

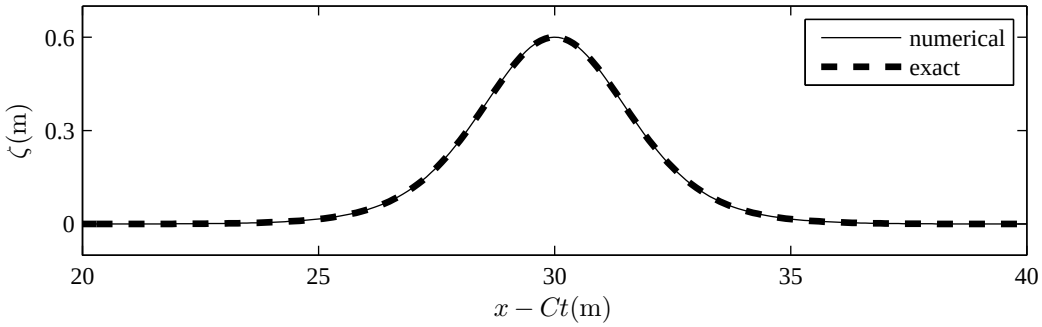

Figure 4.2: Comparison between the exact and the numerically computed solitary wave plotted against $x - Ct$ at $t = 70$ s.

4.1.2 Reversibility check

The overall reversibility of the model is verified with the following test. A solitary wave of amplitude $A = 0.2$ m, derived following Section 4.1.1, is input as the initial condition on otherwise still water of depth $h = 1$ m. The solitary wave then propagates onto a shelf where the still water depth is reduced to $h = 0.5$ m. The domain configuration is presented in Figure 4.3.

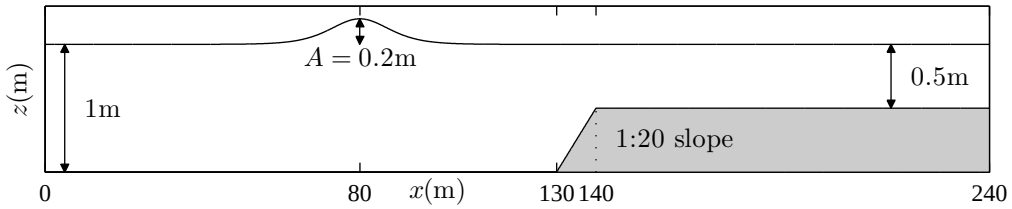

Figure 4.3: Definition sketch for the submerged shelf reversibility check.

The solitary wave propagates unperturbed in the deep water. When it reaches the shelf, it adjusts to the reduced water depth by splitting into three solitary waves, ordered by size, and trailing wiggles. Also, a reflected wave is generated, which travels backwards from the shelf. Figure 4.4 shows stacked spatial profiles of the evolving free surface. The grid spacing is $\Delta x = 0.1$ m and the time step is $\Delta t = 0.019$ s.

The final flux and free surface elevation profiles, at $t = 50$ s, are taken as the initial conditions for a reverse simulation, which runs backwards until $t = 0$ s with a negative time step of $\Delta t = -0.019$ s. The shed waves and wiggles, as well as the reflected wave, are absorbed back into the single wave and the original solitary wave is recovered, as shown in Figures 4.5 and Figure 4.6. This reversibility test is a very sensitive check on the accuracy of the numerical scheme as it corresponds to a complex interaction over a net run time of 100 s and a combined propagation distance of almost 300 m.

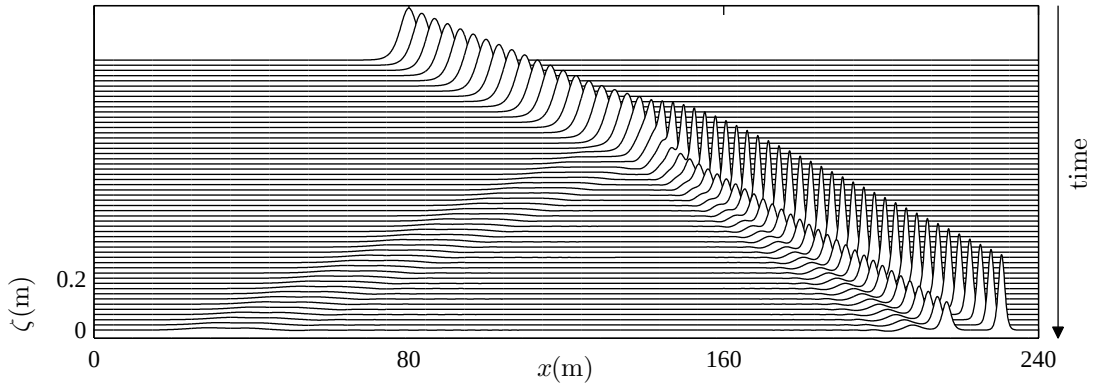

Figure 4.4: Splitting of a solitary wave. Stacked spatial profiles with time running from the top to bottom.

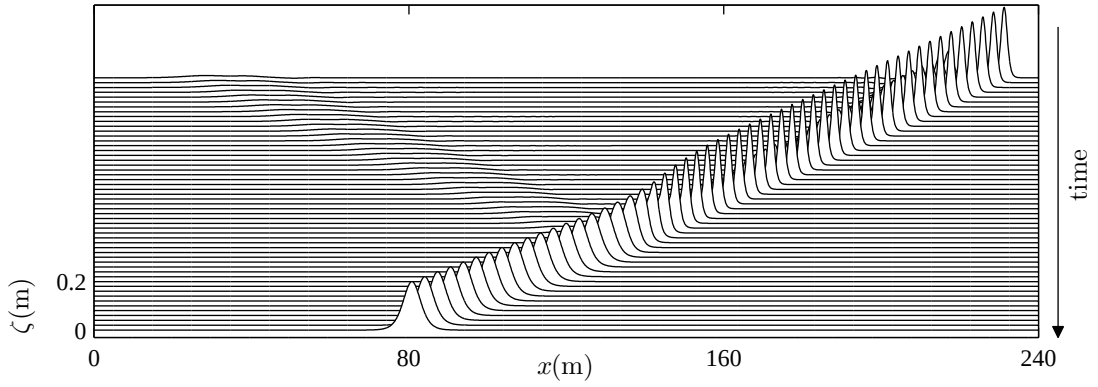

Figure 4.5: Reverse simulation of a solitary wave splitting. Stacked spatial profiles with time running from the top to bottom.

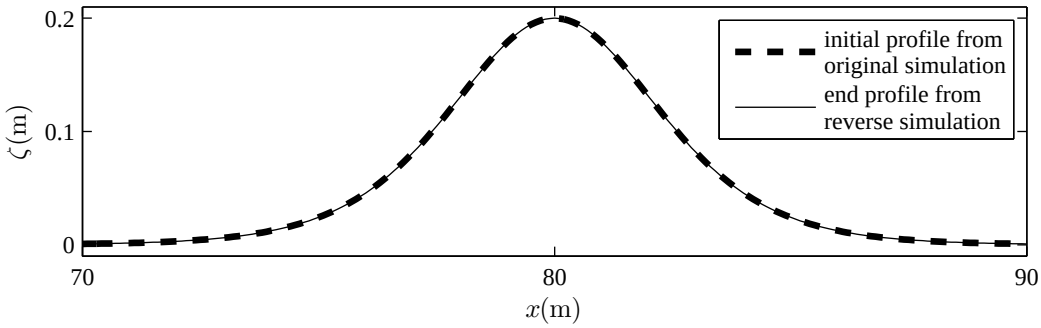

Figure 4.6: Reversibility comparison - end profile of the reversed simulation superimposed on the initial condition of the original simulation.

The reversibility test is additionally used to assess the accuracy and convergence of the numerical model. For simplicity, a sech^2 solitary wave, given by (2.44), is used here as the initial conditions. Five different grids are considered, with $\Delta x = 0.8$ m being

the coarsest and $\Delta x = 0.05$ m the finest. The corresponding time steps are adjusted accordingly to keep the Courant condition constant. The error $\boldsymbol{E}$ associated with each grid resolution is calculated by comparing the end free surface elevation profile from the reverse simulation $\boldsymbol{\eta}_{end}$ with the initial profile of the original simulation $\boldsymbol{\eta}_{init}$, such that

$$\boldsymbol{E} = \boldsymbol{\eta}_{end} - \boldsymbol{\eta}_{init} \ . \tag{4.8a}$$

The size of the error is expressed using three different norms as

$$\|\boldsymbol{E}\|_1 = |E_1| + \cdots + |E_M|, \tag{4.8b}$$

$$\|\boldsymbol{E}\|_2 = \sqrt{|E_1|^2 + \cdots + |E_M|^2}, \tag{4.8c}$$

$$\|\boldsymbol{E}\|_\infty = \max(|E_1|, \ldots, |E_M|). \tag{4.8d}$$

For every grid refinement the observed intermediate convergence rate c_r is calculated from

$$c_r = \frac{\ln(\|\boldsymbol{E}_{fine}\|) - \ln(\|\boldsymbol{E}_{coarse}\|)}{\ln(\Delta x_{fine}) - \ln(\Delta x_{coarse})}. \tag{4.9}$$

The calculated errors are collated in Table 4.1, and the $\|\boldsymbol{E}\|_2$ are graphically presented in Figure 4.7. As expected, for every grid refinement, the global error reduces. For the coarse grids, the spatial resolution is not sufficient to capture the simulated phenomena leading to low accuracy. Overall, the numerical model exhibits a roughly fourth order accuracy, which agrees with the theoretical accuracy of the model due to the fourth order RK4 time-stepping algorithm and fourth order discretisation stencils for first and second spatial derivatives.

Table 4.1: Accuracy and convergence of the numerical model using the reversibility test.

Δx	$\|E\|_1$	c_r	$\|E\|_2$	c_r	$\|E\|_\infty$	c_r
0.8	1.5078e-1	-	2.9369e-2	-	1.2016e-2	-
0.4	5.7894e-2	1.3810	7.7980e-3	1.9131	2.2762e-3	2.4003
0.2	5.7698e-3	3.3268	5.4819e-4	3.8304	1.1288e-4	4.3338
0.1	3.8624e-4	3.9009	2.5956e-5	4.4005	3.7777e-6	4.9011
0.05	2.4407e-5	3.9841	1.1596e-6	4.4843	1.1934e-7	4.9843

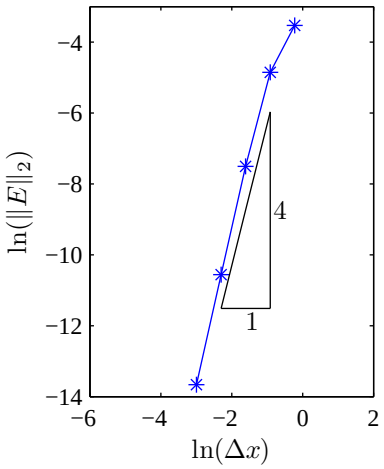

Figure 4.7: Accuracy and convergence of the numerical model using the reversibility test - logarithm of the error $\|E\|_2$ plotted against logarithm of the grid resolution Δx, together with an example 4:1 slope.

4.1.3 Wetting and drying algorithm check

The analytical solution of the non-linear shallow water equations for sloshing in a parabolic basin derived by Sampson *et al.* (2006) is used to validate the wetting and drying treatment in the model. In their solution, the bottom topography is given by

$$b = \frac{h_0}{a^2}(x - 0.5L)^2, \tag{4.10}$$

where L is the length of the domain, h_0 is the still water depth at $x = 0.5L$ and $2a$ is the width of the basin at elevation $z = h_0$. Following Sampson *et al.* (2006), for an initial sloping free surface in the wetted region given by

$$\eta(x,0) = h_0 + \frac{a^2B^2}{8g^2h_0}\Big(\frac{\tau^2}{4} - s^2\Big) - \frac{B^2}{4g} - \frac{Bs}{g}(x - 0.5L), \tag{4.11}$$

the solution in the wetted region for $t > 0$ reads

$$\begin{aligned}\eta(x,t) &= h_0 + \frac{a^2B^2e^{-\tau t}}{8g^2h_0}\Big(-s\tau\sin(2st) + \Big(\frac{\tau^2}{4} - s^2\Big)\cos(2st)\Big) \\ &- \frac{B^2e^{-\tau t}}{4g} - \frac{e^{-\tau t/2}}{g}\Big(Bs\cos(st) + \frac{\tau B}{2}\sin(st)\Big)(x - 0.5L),\end{aligned} \tag{4.12}$$

where τ is a fixed friction parameter, B is a velocity constant, and s is a constant given by $s = 0.5\sqrt{8gh_0/a^2 - \tau^2}$. Note that B in Equation (4.12) is unrelated to the Boussinesq dispersion enhancement coefficient, but the notation is used here for consistency with Sampson *et al.* (2006). Sampson *et al.* (2006) assume linearized friction in the derivation of the above solution; therefore in order to simulate this test

case with the present numerical model (which uses a quadratic friction formulation), the friction coefficient C_f in Equation (2.25) satisfies $C_f = \tau \frac{d}{|u|}$.

The computational domain chosen for this validation simulation is 220 m long with resolution of $\Delta x = 1.76$ m. The coefficients are $a = 80$ m, $B = 10$ ms^{-1}, $h_0 = 80$ m and $\tau = 0.1$ s^{-1}. The simulation is run for 80 s with time step $\Delta t = 0.04$ s. Figure 4.8 shows the very satisfactory agreement between the analytical solution and the model predictions for the free surface throughout the evolution. The moving shoreline is correctly calculated, validating the wetting and drying algorithm.

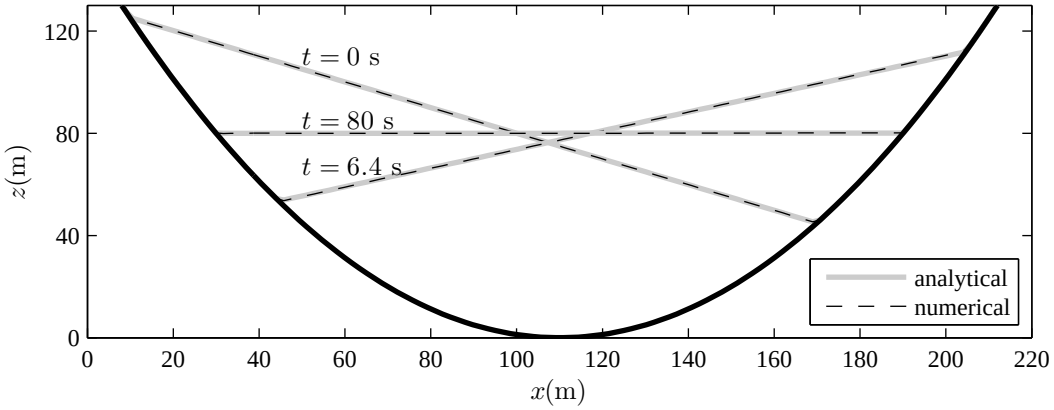

Figure 4.8: Sloshing in a parabolic basin.

4.1.4 Paddle wave generation test

The exact solitary wave solution derived in Section 4.1.1 is used to test the ability of the numerical piston paddle to generate solitary waves of desired amplitude. To find the appropriate paddle displacement time series x_p, one needs to solve Equation (2.42), which is repeated below for clarity.

$$(x_p)_t = \overline{u}(x_p, t). \tag{4.13}$$

The depth-averaged velocity $\overline{u} = \frac{q}{\zeta + h}$ for the exact solitary wave is calculated by the method outlined in Section 4.1.1. Equation (4.13) is solved forwards and backwards in time from $x_p(0) = 0$ using the ode113 solver in Matlab®. The calculated paddle displacement signal x_p is then fed into the model. The simulation is run for 30 s with timestep $\Delta t = 0.018$ s. The length of the computational domain is 100 m with grid spacing $\Delta x = 0.1$ m. Figure 4.9 shows the generation process for a solitary wave of amplitude $A = 0.6$ m. The correct wave is generated. The profiles are deliberately stacked with vertical spacing of 0.6 m to highlight the correct amplitude of the generated wave.

Closer examination of the generated wave in Figure 4.9 reveals very small wiggles trailing the main solitary wave. These could be the consequence of the finite length of the paddle displacement time series or the fact that the solution at the first two grid points adjacent to the paddle is determined from the non-linear shallow water equations rather than the full Boussinesq equations.

This test additionally confirms non-reflective transition of waves between the *paddle domain* and the rest of the Boussinesq domain. For the above case, the interface between the two domains lies at $x = 24.8$ m. From Figure 4.9 it is clear that the solitary wave propagates unaffected as it passes between the two domains, thus confirming correct implementation of non-uniform stencils at grid points $x_{\widetilde{M}-1}$, $x_{\widetilde{M}}$ and $x_{\widetilde{M}+1}$ as described in Section 3.2. Numerical tests carried out without the non-uniform stencils implemented in the code showed partial reflection of the solitary wave as it crossed the interface between the two domains.

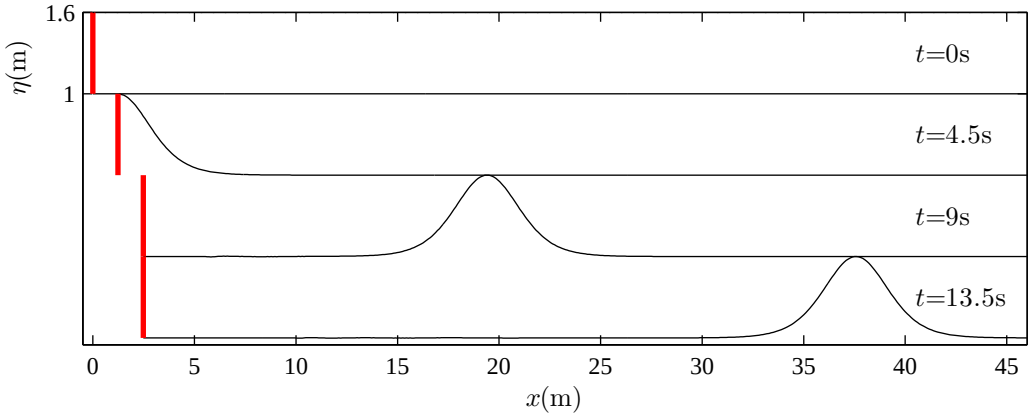

Figure 4.9: Solitary wave generation using the numerical piston paddle.

4.2 Model validation against experimental data

The model is used to simulate a number of shallow water laboratory experiments of solitary wave run-up on a plane beach and solitary wave overtopping of a laboratory seawall. The in-built piston paddle wavemaker is utilised for wave generation. Whenever available, the recorded experimental paddle signals are fed into model. Otherwise, the appropriate paddle displacement time series x_p are calculated using the same methods as were used in the laboratory experiments. Bed friction is calibrated for one wave case in each experimental facility; and is subsequently kept constant for all other cases from the same facility.

Generation and propagation over flat bed of regular waves and bi-chromatic wave groups is also simulated with the numerical model, using both first and second order

paddle displacement signals. Separation of harmonics is carried out to analyse the second order sub- and super-harmonics.

4.2.1 Solitary wave run-up at a plane beach

Hsiao *et al.* (2008) performed a series of experiments on breaking solitary wave run-up at a plane beach in the supertank at the Tainan Hydraulics Laboratory, Taiwan. The supertank is 300 m long, 5.2 m deep and 5 m wide. A plane 1:60 beach was constructed 50 m from the wave paddle. Figure 4.10 shows the layout of the supertank. The free surface elevation was measured by 80 wave gauges. The reference gauge, used for defining the incoming offshore solitary wave amplitude A, was located at $x = 24$ m. Two offshore (paddle) mean water depths were considered: $h_0 = 1.2$ m and $h_0 = 2.2$ m. The horizontal and vertical run-ups of the waves were also recorded.

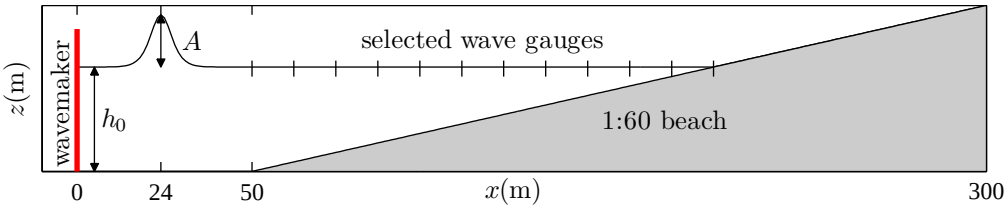

Figure 4.10: Flume setup for the Tainan supertank experiments reported by Hsiao *et al.* (2008).

Three experimental runs, covering small to very large solitary wave heights, were reproduced with the present numerical model. Paddle displacement signals for these sech^2 solitary waves were calculated according to Goring (1978), as described in Section 2.6.3. The friction coefficient was set to $C_f = 0.003$ by tuning one of the runs. The computational grid had spatial resolution of $\Delta x = 4$ cm, and the time step was $\Delta t = 0.01$ s. Each simulation was run for 150 s and took about 14 minutes to complete on a standard PC (Intel Xeon 2.93 GHz processor, 6 GB RAM). Figure 4.11 shows stacked non-dimensionalised free surface time series along the beach; the top series corresponding to the beach toe location and the bottom series to the initial location of the shoreline. The non-dimensionalised variables are indicated by an asterix, and are calculated from $t^* = t/\sqrt{(g/h_0)}$, $\zeta^* = \zeta/h_0$ and $h^* = h/h_0$. From Figure 4.11 it is obvious that the wave evolution is well predicted by the model. Wave shoaling and breaking, and subsequent bore formation are properly captured. Apart from the maximum crest height being slightly underpredicted, there is very good agreement with the gauge measurements at most locations. For the most non-linear case, the predicted bore is also slightly larger than measured.

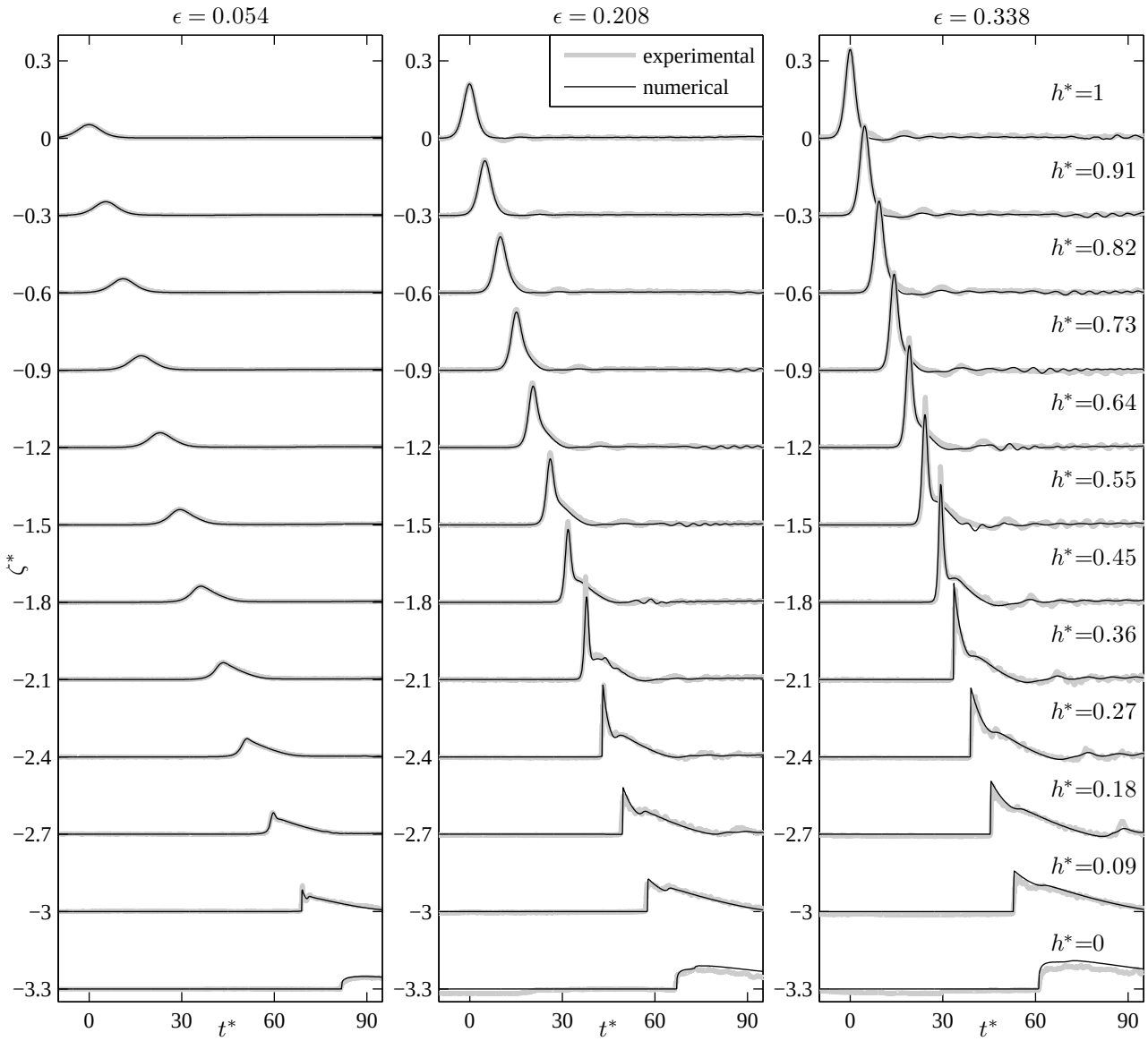

Figure 4.11: Non-dimensionalised free surface stacked time series. Comparison between the model predictions and the measurements from Hsiao *et al.* (2008).

Table 4.2 presents measured and predicted values of the non-dimensionalised vertical run-up scaled using $R^* h_0 = R$. There is excellent agreement. Repeated simulations on a coarser grid with $\Delta x = 8$ cm confirm that the presented results have converged and that a sufficiently refined grid has been used.

Table 4.2: Non-dimensionalised vertical run-up. Comparison between the model predictions and the Tainan supertank measurements reported by Hsiao *et al.* (2008).

ε	A (m)	h_0 (m)	R^* measured	R^* predicted ($\Delta x = 4$ cm)	R^* predicted ($\Delta x = 8$ cm)
0.054	0.119	2.2	0.111	0.1156	0.1154
0.208	0.249	1.2	0.208	0.2115	0.2108
0.338	0.406	1.2	0.261	0.2614	0.2598

4.2.2 Solitary wave overtopping a seawall

Hunt (2003), Hunt-Raby *et al.* (2011) and Borthwick *et al.* (2006) report on a large programme of run-up and overtopping laboratory experiments in the UK Coastal Research Facility (UKCRF). The basin was 36 m long and 27 m wide, with a segmented piston paddle array for wave generation. A plane 1:20 beach was constructed with its toe located a distance of 8.33 m from the paddles. Additionally, for the overtopping experiments, a laboratory seawall was mounted on the beach at a distance of 8.125 m from the beach toe. The slope of the front face of the seawall was 1 : 2.18 and the width of the flat top of the seawall was 0.215 m. Free surface elevation was measured by wave gauges placed along the centre line of the basin, including the beach as well as the seawall, if present. The wave gauges on the seawall were sunk in small PVC tubes set into the seawall. Horizontal run-up and overtopped volume were also recorded. The basic geometry is shown in Figure 4.12, with a detailed diagram of the seawall shown in Figure 4.13.

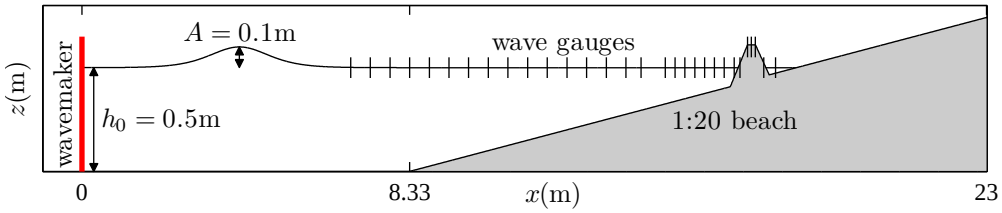

Figure 4.12: Basin setup for the UKCRF overtopping experiments reported by Hunt (2003).

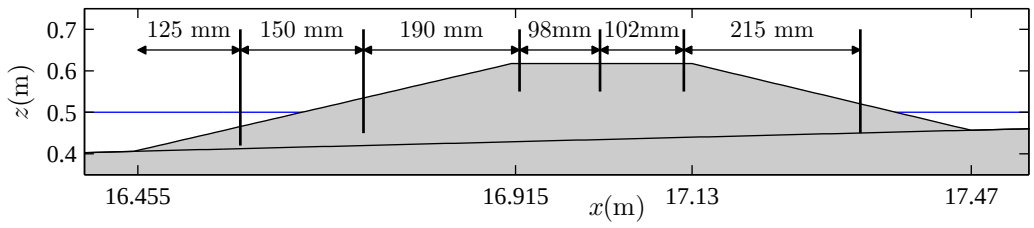

Figure 4.13: Detailed sketch of the seawall and the sunk wave gauges for the UKCRF overtopping experiments reported by Hunt (2003).

Here a case is simulated of a solitary wave overtopping with offshore wave amplitude $A = 0.1$ m and offshore mean water depth $h_0 = 0.5$ m, as also depicted in Figure 4.12. The experiment was replicated with the numerical model on a computational grid of spacing $\Delta x = 1$ cm and time step $\Delta t = 0.0035$ s. The simulation was run for 40 s and took about 6 minutes to complete on a standard PC (Intel Xeon 2.93 GHz processor, 6 GB RAM). The friction coefficient was $C_f = 0.008$ throughout the basin. Note that this is larger than the friction coefficient value used in the supertank simulations. This is expected as the UKCRF facility is smaller and therefore the cement floor is relatively rougher. The sech^2 solitary wave was generated with the numerical paddle using the recorded paddle signal taken directly from the experiment. The paddle signal is reproduced in Figure 2.8.

Figure 4.14 shows snapshots of the overtopping process. The model correctly captures the wave evolution, including the run-up and run-down on the seawall. After the overtopping has taken place, the water body has separated into two blocks either side of the seawall, which poses no difficulty to the numerical model.

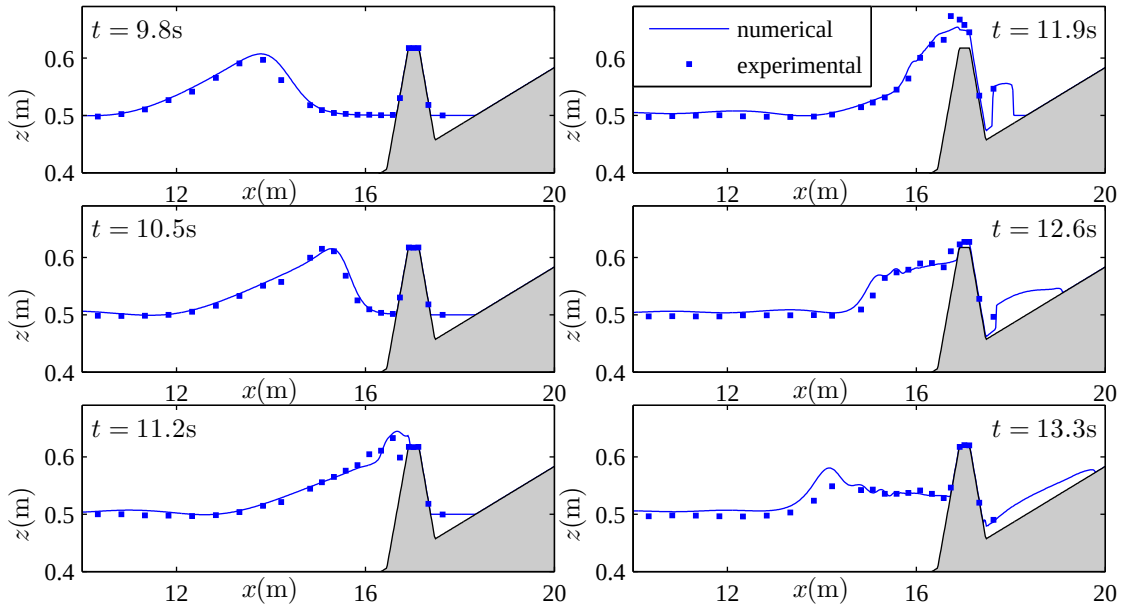

Figure 4.14: Solitary wave overtopping. Comparison between the model prediction and the UKCRF measurements reported by Hunt (2003).

The overtopped volume per unit length of the seawall calculated by the model was 37.51 l/m, whereas the measured volume was 30.6 l/m. The simulation was also repeated on computational grids of spatial resolution of $\Delta x = 0.5$ cm and $\Delta x = 2$ cm (with time steps appropriately adjusted). Overtopped volumes were calculated to be 37.04 l/m and 37.69 l/m, indicating converged results. The present measured

and calculated volumes correspond to the total overtopped volume after $40s$, which includes secondary overtopping from the reflected wave. Figure 4.15 shows free surface time series at five locations along the beach, starting at the beach toe ($x = 8.33$ m) and finishing at the seawall crest ($x = 16.92$ m).

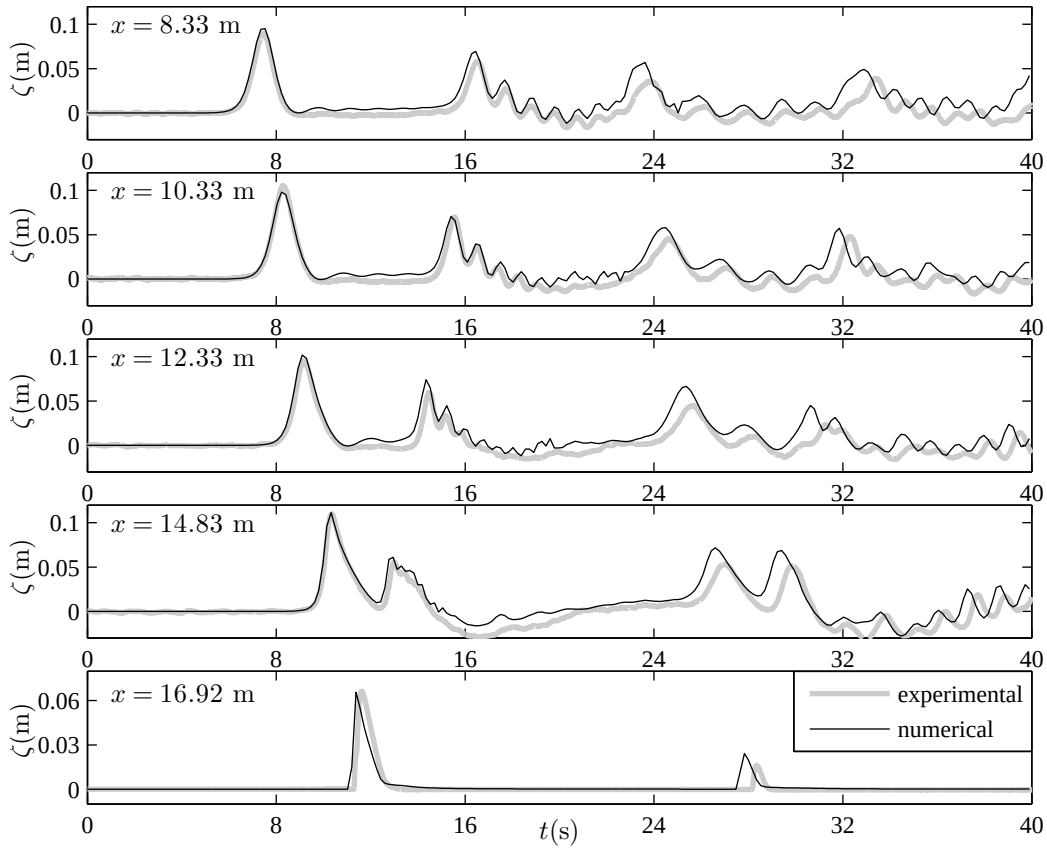

Figure 4.15: Solitary wave overtopping. Free surface time series comparison between the model prediction and the UKCRF measurements reported by Hunt (2003). Note the vertical scale for the wave gauge on top of the seawall (bottom plot) is magnified.

The structure of the leading wave is accurately predicted at all locations. However, there is a small but visible difference in the water levels at all initially submerged locations well after the passage of the first solitary wave. It is believed that this is due to volume conservation in the experimental facility, whereby the empty space left behind the paddles as they move forward to generate the solitary wave slowly fills with water from the basin. For a stroke length of around 0.516 m and a still water depth at the paddles of 0.5 m, the displaced volume of water per unit width is roughly 0.25 m^2. Dividing this by the wetted length of the basin (of around 16.5 m) gives a drop of 1.5 cm of the mean water level in the basin after the flow to behind the paddles is complete. This leakage is not accounted for in the model. One could

argue that the lower experimental still water levels, after the leak is finished, lead to the mismatch in the secondary overtopping (see Figure 4.15, location $x = 16.92$ m, $t = 27 - 29$ s) as well as the slight phase difference of the reverberating waves in the basin (see Figure 4.15, any location, $t > 16$ s). Repeating the simulation with $h_0 = 0.485$ m indeed improves the prediction of the secondary overtopping and the phase of the reflected waves.

4.2.3 Regular wave generation, propagation and analysis

Full second order wavemaker theory was developed by Schäffer (1996). In his paper, Schäffer reports on laboratory experiments using regular waves and bi-chromatic waves groups generated by a piston-type wavemaker using first order and second order paddle displacement signals. The experimental flume was 20 m long, 1 m deep and 0.6 m wide. A passive absorber was positioned at the end of the flume to minimise wave reflection. The bottom was flat. For the experiments involving regular waves, wave gauges measuring surface elevation were positioned at locations 1.0 m, 4.4 m, 4.4 m and 8.7 m from the wavemaker.

Here a case is simulated of generation and propagation of a regular wave with an amplitude of $a = 0.07$ m and a frequency of $f = \frac{1}{3}$ Hz on a depth of $h = 0.7$ m. The numerical code reproduces the experiment on a computational grid of spacing $\Delta x = 10$ cm with time step $\Delta t = 0.03$ s. The length of the computational domain is 120 m to avoid wave reflection from the end of the numerical flume. The simulation is run for 50s (taking about 4 minutes to complete on a standard PC with Intel Xeon 2.93 GHz processor and 6 GB RAM). In the first simulation, the regular wave is generated with the numerical paddle using a first order paddle signal. In the second simulation, a second order paddle signal, computed as per Schäffer (1996), is used. Both signals are reproduced in Figure 2.6.

Figure 4.16 shows the calculated surface elevation time series, generated with a paddle signal correct to first order. The presence of free error super-harmonics is evident due to the varying shape of the propagating wave. It appears that at the first location ($x = 1$ m) the error super-harmonics and the natural bound super-harmonics cancel out resulting in an almost sinusoidal profile. At the final location ($x = 8.7$ m) constructive interference of the free and the bound super-harmonics leads to very flat troughs and steep crests. Schäffer (1996) reports on the presence of secondary peaks within the troughs in the experimental time series recorded by the last wave gauge ($x = 8.7$ m). These are marginally detectable in the predicted results, when zoomed in sufficiently. Figure 4.17 shows the calculated surface elevation time series

generated with a second order paddle signal. The homogeneous wave field indicates that the generation of the free second order error waves has been suppressed through the use of the second order paddle signal.

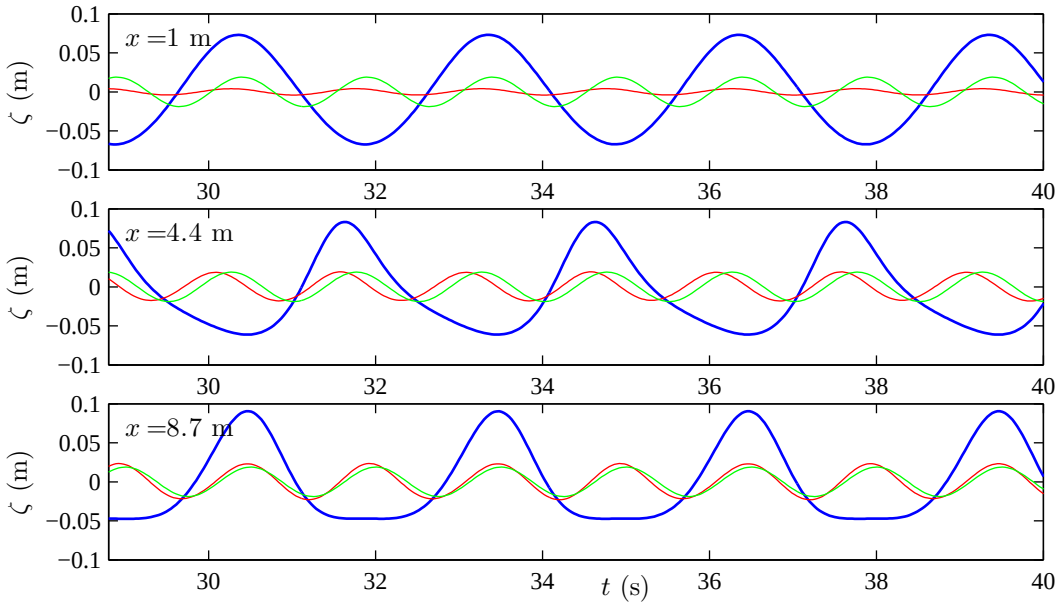

Figure 4.16: Regular waves generated with a first order paddle signal. Blue (thick) line denotes the calculated free surface elevation ζ. Red line denotes the filtered-out second order super-harmonics (both error and bound waves). Green line denotes the theoretical bound second order super-harmonics.

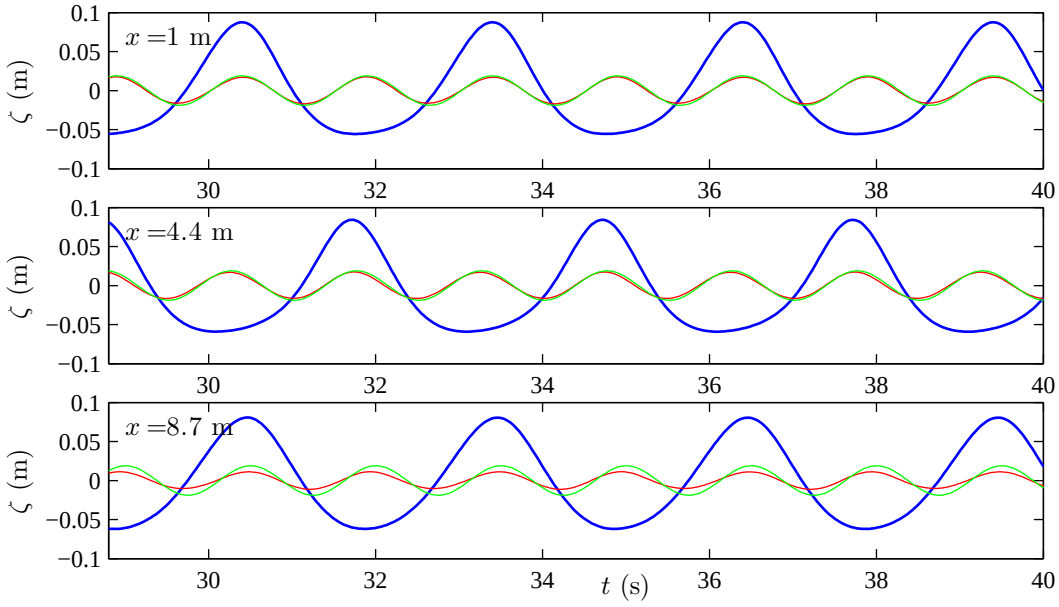

Figure 4.17: Regular waves generated with a second order paddle signal. Blue (thick) line denotes the calculated free surface elevation ζ. Red line denotes the filtered-out second order super-harmonics. Green line denotes the theoretical bound second order super-harmonics.

Further analysis is carried out to evaluate and compare the calculated super-harmonics from the model's output and the theoretical bound super-harmonics as per Stoke's regular wave theory. The bound second order super-harmonics are calculated using Equation (2.31a) together with the linear dispersion relation. In order to extract the super-harmonics from the calculated ζ time series, inverted waves are used. It should be noted that for regular waves, the super-harmonics could simply be filtered out, as explained at the end of this section, due to the clear separation between individual harmonics. However, the use of inverted waves will be necessary when analysing wave groups in Chapter 5, and is therefore performed here too. Inverted waves are defined by linear wave amplitude of opposite sign and equal magnitude of the wave amplitude of the original wave (i.e. a is replaced by $-a$). The same principle applies to inverted wave groups, whereby a_n is replaced by $-a_n$ for all $n = 1, \ldots, N$. This is of course equivalent to applying a phase shift of π radians to each wave component. Two further simulations have been carried out. Simulation 3 is run with a first order paddle signal for an inverted regular wave train (where the new paddle signal is simply given from the original first order signal by pre-multiplying it by -1). Simulation 4 is carried out with a second order paddle signal for an inverted regular wave train (where the new paddle signal is calculated according to Schäffer (1996) with a replaced by $-a$). The original surface elevation time series calculated by the numerical model are denoted by ζ_c and the inverted calculated time series by ζ_t. Now, judicious addition and subtraction of ζ_c and ζ_t allows for separation of harmonics as follows:

- Addition $\frac{1}{2}(\zeta_c + \zeta_t)$ gives the even order harmonics as the linear components and all the odd order harmonics cancel out.

  This cancellation and retention applies to both natural bound waves and free error waves present in the time series, meaning that a resultant addition time series calculated from ζ_c and ζ_t, which were generated (numerically or experimentally) using first order paddle signals, will contain second order error waves, but no third order error waves, etc.

  For regular waves, even super-harmonics are solely present in the addition time series. For wave groups, both even super-harmonics and even sub-harmonics are present.

- Subtraction $\frac{1}{2}(\zeta_c - \zeta_t)$ gives the linear components and all the odd order harmonics, whereas the even order harmonics cancel out.

As with addition, this cancellation and retention applies to both natural bound waves and free error waves present in the time series.

For regular waves, odd super-harmonics are solely present in the subtraction time series. For wave groups, both odd super-harmonics and odd sub-harmonics are present.

Filters can be applied in the frequency domain to completely isolate the individual harmonics (for example to isolate second order super-harmonics from the fourth and higher order super-harmonics in the addition time series). The considered time series is first transformed into the frequency domain by application of the Fourier transform. A suitable cut-off frequency is found and the truncated spectrum is subject to the inverse Fourier transform resulting in a suitably filtered time series. In this work, discrete Fourier transforms are performed with an in-built FFT algorithm in Matlab®.

In Figures 4.16 and 4.17 the filtered-out second order super-harmonics and the theoretically derived natural bound second order super-harmonics are superimposed on the surface elevation time series. As expected, in Figure 4.16 there is a mis-match between the curves. In Figure 4.17, the two curves almost coincide, confirming correct implementation of the second order wavemaker theory in the numerical model.

4.2.4 Bi-chromatic wave group generation and propagation

The second set of experiments reported by Schäffer (1996) involved bi-chromatic wave groups. The flume setup was identical to that for the regular waves experiments described in Section 4.2.3. Wave gauges measuring free surface elevation were positioned at locations 1.95 m, 3.0 m, 6.0 m, 6.4 m and 12.0 m from the wavemaker.

The numerical model is used to reproduce a generation and propagation test involving a bi-chromatic wave group composed of two primary regular wave trains with $a_1 = a_2 = 0.03$ m, $f_1 = 0.495$ Hz and $f_2 = 0.566$ Hz propagating on otherwise still water depth of $h = 0.3$ m. As in the regular wave test, the length of the computational domain is chosen to be 120 m to avoid wave reflection from the end of the numerical flume. The simulation is performed for 50 s with time step $\Delta t = 0.05$ s on a computational grid of spacing $\Delta x = 10$ cm (taking a couple of minutes to complete on a standard PC with Intel Xeon 2.93 GHz processor and 6 GB RAM). Four simulations are carried out in total, with first and second order paddle signals for both the original wave group and its inverted counterpart. Figure 2.7 shows the applied, first and second order, paddle displacement time series for the original wave group.

In order to check whether the generation of second order sub-harmonic error waves is suppressed with the second order paddle signal, the long waves are filtered from the calculated addition time series (with a low-pass filter; see Section 4.2.3 for more details) and compared to the naturally occurring second order bound sub-harmonics. The bound waves are given by the difference terms in Equation (2.33). Figures 4.18 and 4.19 present the calculated free surface elevation time series generated with first and second order paddle signals. The filtered-out long waves and the theoretically derived bound difference frequency waves are also plotted. In Figure 4.18 the bound and the error long waves are almost out of phase, so for the first order paddle signal, the net time history at this location is rather small. In Figure 4.19, it can be seen that when the second order paddle signal is used, the low frequency set-down is correctly reproduced. This confirms correct implementation of the second order wavemaker theory of Schäffer (1996) in the numerical model.

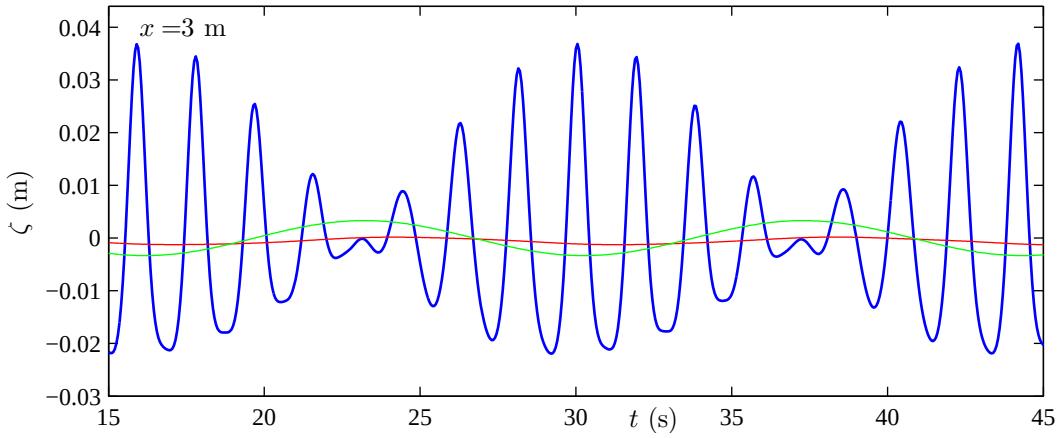

Figure 4.18: Bi-chromatic wave group generated with a first order paddle signal. Blue (thick) line denotes the calculated free surface elevation ζ. Red line denotes the filtered-out sub-harmonics (both error and bound waves). Green line denotes the theoretical bound second order sub-harmonics.

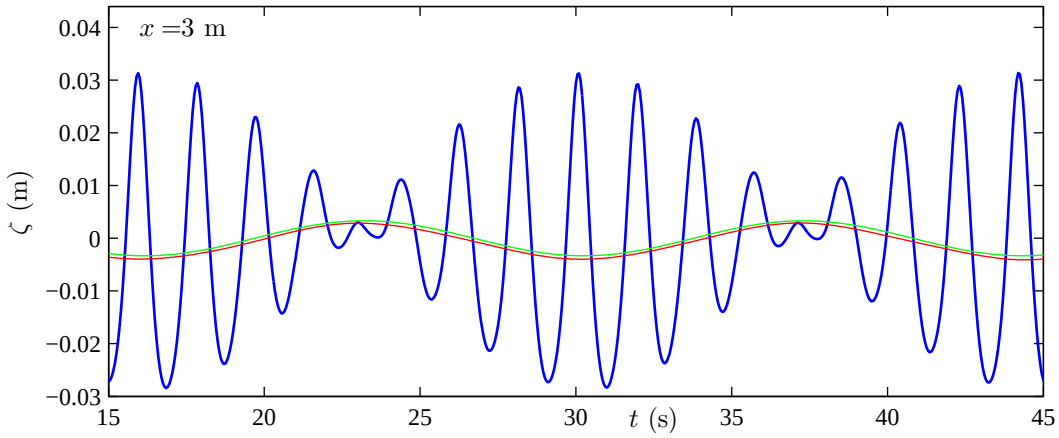

Figure 4.19: Bi-chromatic wave group generated with a second order paddle signal. Blue (thick) line denotes the calculated free surface elevation ζ. Red line denotes the filtered-out sub-harmonics. Green line denotes the theoretical bound second order sub-harmonics.

4.3 Chapter summary

- This Chapter has presented numerical simulations of test cases designed to verify correct implementation of various aspects of the present numerical model. Solitary wave propagation over a flat bed is used to check conservation properties of the model. The simulation results agree very well with the derived solution. The solitary wave undergoes no transformation or damping over a long distance. A reversibility test, involving solitary wave interaction over a submerged reef, confirms correct discretisation and time-marching in the model. The test is also used to calculate a roughly fourth order convergence rate of the Boussinesq part of the present solver. Implementation of the paddle wavemaker and the wetting and drying treatment are also satisfactorily tested against known analytical solutions.

- Simulations of shallow water experiments of solitary wave run-up and overtopping are used for validation of the complete model, including wave generation, propagation, treatment of wave breaking, and wetting and drying. Excellent agreement between the model prediction and high quality experimental data is achieved for solitary wave run-up on a plane beach. Satisfactory agreement is found for solitary wave overtopping a seawall, and a physically based explanation is given for the relatively small differences in overtopped volume and phase lag of the reverberating wave.

- Regular wave and bi-chromatic wave group tests are also used to validate the numerical model. Analyses of the second order super-harmonics (for the regular waves test) and sub-harmonics (for the bi-chromatic wave group test) are carried out using inverted waves, Fourier transform and filters. The second order wavemaker theory by Schäffer (1996) is correctly implemented, as second order error wave generation is suppressed when second order paddle displacement signals are fed into the model.

Chapter 5

Numerical study of NewWave

In this chapter the numerical model is used to simulate run-up and overtopping experiments involving NewWave focused wave groups. The model is also used to assess the effect of using second order paddle signals on run-up distances and overtopping volumes.

5.1 NewWave theoretical model

A focused wave group is a wave group composed of a number of individual sinusoidal wave components which come into phase at one point in time and space. The surface elevation, using linear wave theory, at any time and any point in space can be described by

$$\zeta(x,t) = \sum_{n=1}^{N} a_n \cos(k_n(x - x_f) - \omega_n(t - t_f) + \phi), \tag{5.1}$$

where a_n is the wave amplitude, k_n the wave number, and ω_n the angular frequency of the n^{th} component; ϕ is the phase angle at focus; x_f and t_f the focus location and focus time, and N is the number of the Fourier components. Indeed, at $x = x_f$ and $t = t_f$ all wave components are in phase.

In the laboratory, it is possible to create a focused wave group with desired focus location and focus time by correctly offsetting individual wave components at the paddle to account for their different propagation speeds down the tank. Using Equation (5.1), a phase shift of $-k_n x_f + \phi$ is applied to each n^{th} component, assuming that the wave maker is located at $x = 0$ m and that $t_f = 0$ s. When focused, constructive interference between individual components occurs and the wave group produces a large energetic event. Due to frequency dispersion, away from focus, the wave group is less compact and less violent. A crest-focused wave group is given by $\phi = 0$, whereby wave crests come into phase at the focus point. A trough-focused

wave group is defined by $\phi = \pi$, such that wave troughs align at the focus location. Chapter 6 investigates the influence of different values of the phase angle of the wave components on the group propagation and run-up.

Additionally, the NewWave focused wave group is consistent with the mathematical description of the expected shape of extreme wave events in a linear random sea, as shown by Jonathan and Taylor (1997) and Taylor and Williams (2004). The underlying statistical theory originates from Lindgren (1970) and Boccotti (1983), however it is rather difficult to grasp. More readable accounts are given by Tromans *et al.* (1991) and in Section 5.4 of Tucker and Pitt (2001). According to the theory, an average shape of the free surface near an arbitrary crest is given by the normalised autocorrelation function pre-multiplied by the crest height. The NewWave time history, for a crest-focused wave, therefore reads as

$$\zeta(t) = \frac{A_{\mathcal{N}}}{\sum_n S_n(\omega)\Delta\omega_n} \sum_n S_n(\omega)\Delta\omega_n \cos(\omega_n(t - t_f)), \tag{5.2}$$

where $A_{\mathcal{N}}$ is the linear amplitude of the NewWave group at focus, S_n is the discretised underlying energy spectrum and $\Delta\omega_n$ is the angular frequency resolution. In Equation (5.2) the second summation represents the autocorrelation function, given by the inverse Fourier transform of the underlying spectrum, and the first summation (the denominator) normalises the autocorrelation function. In the NewWave representation, the individual wave amplitudes a_n are thus given by

$$a_n = \frac{A_{\mathcal{N}} S_n(\omega)\Delta\omega_n}{\sum_n S_n(\omega)\Delta\omega_n}. \tag{5.3}$$

In Equation (5.3), the summation contains terms with indices $n = 1, \ldots, N$, but the simplified notation is used for brevity. Note that the choice of $A_{\mathcal{N}}$ is arbitrary as it represents the amplitude of the largest wave from a sea surface time series of $\mathcal{N}$ waves in a narrow-banded linear random sea. Following Chapter 7 in Dean and Dalrymple (1991) and Section 5.3.2 in Tucker and Pitt (2001), $A_{\mathcal{N}}$ can be thought of as the amplitude exceeded by only one out of the $\mathcal{N}$ waves present, and is given by

$$A_{\mathcal{N}} = \left(2\sigma^2 \ln \mathcal{N}\right)^{1/2}, \tag{5.4}$$

where σ^2 denotes the variance of the free surface time series.

Much of ocean engineering research is aimed at extreme physical events, be it calculating loads on coastal structures or predicting maximum run-up and overtopping

from severe storms. Laboratory experiments and numerical simulations involving focused wave groups benefit from the complete spectral information contained in the single wave group, so compared to random wave time domain experiments/simulations are quick and inexpensive. Additionally, due to the transient nature of the wave groups, the experiments/simulations avoid issues of wave reflection and absorption at the boundaries of the tank and at the wavemaker.

5.2 Analysis of NewWave using first and second order paddle displacement signals

In this Section, NewWave focused wave group propagation on a flat bed is investigated, using first and second order paddle displacement signals. The effect of second order error waves on the group shape is assessed, and the effectiveness of second order paddle signals in eliminating the error waves is commented upon.

The laboratory experiments reported by Hunt (2003), Hunt-Raby *et al.* (2011) and Borthwick *et al.* (2006) also involved NewWave focused wave groups. Run-up on a plane beach and overtopping of a laboratory seawall associated with these wave groups are examined in Sections 5.3 - 5.6. In the experimental programme, 8 normally-incident NewWave focused wave groups were considered, involving 4 crest-focused and 4 trough-focused wave groups, covering a range of group amplitudes and focus locations. The underlying energy spectrum used in the UKCRF experiments was a Pierson-Moskowitz spectrum given by

$$S(\omega) = \Big(\frac{\omega_p}{\omega}\Big)^5 \exp\Big(-1.25\Big(\frac{\omega_p}{\omega}\Big)^4\Big), \tag{5.5}$$

with peak angular frequency $\omega_p \approx 2.91$ rad s^{-1}. The truncated spectrum ($\omega_{min} \approx 2.07$ rad s^{-1}, $\omega_{max} \approx 6.06$ rad s^{-1}) was discretised into $N = 53$ components with a uniform angular frequency resolution of $\Delta\omega \approx 0.077$ rad s^{-1}.

In the experiments, linear paddle displacement signals calculated according to Equation 2.38 were used, with the Biesel paddle transfer function c_0 replaced by an experimentally derived paddle transfer function. For more details on the experimental paddle calibration procedure, see the section on Calibration of the UKCRF in the thesis by Hunt (2003). For a pair of wave groups WG2 and WG6 (see Table 5.1 in Section 5.3), the experimental paddle signals are fed into the present numerical model to investigate the group propagation on a flat bed. Additionally, the simulations are repeated with corresponding second order paddle displacement signals calculated according to Schäffer (1996). Schäffer's second order wavemaker theory has been

introduced in Section 2.6.2; and for irregular waves and wave groups the paddle signal is calculated according to Equation 2.40. Figure 5.1 shows the first and the second order paddle displacement time series for the WG2 and WG6 pair of wave groups. The second order signal requires a much larger paddle sweep. Due to the finite number of frequency components ($N = 53$ for the present wave groups), the paddle signals have a finite repeat period given by $\frac{1}{\Delta f}$, with Δf being the frequency resolution. The repeat period for the present wave groups is 81.92 s. The second order paddle signals are truncated at $x_p = 0$ to contain a single repeat period. For the wave groups considered here, the truncation points are around $t = -3$ to -1 s and $t = 78$ to 81 s (not shown in Figure 5.1). The larger the number of frequency components, the longer the signal repeat period. In the limit as $\Delta f \to 0$, the repeat period becomes infinite and the second order paddle displacement signal tends to 0 away from the main wave packet asymptotically slowly. Figure 5.2 presents the resolved second order paddle displacement time series x_p and paddle velocity time series $(x_p)_t$. The short and the long corrections to the first order signals are clearly visible. From the paddle velocity plot, it appears that sufficient frequency components are used, as the paddle motion associated with re-setting the position (resulting from the finite repeat period) is significantly slower than the paddle motion necessary for the actual wave group generation. This is demonstrated by the fact that the second order long paddle velocity contribution is minimal away from the wave packet (i.e. at $t = 25$ to 35 s and $t = 45$ to 55 s).

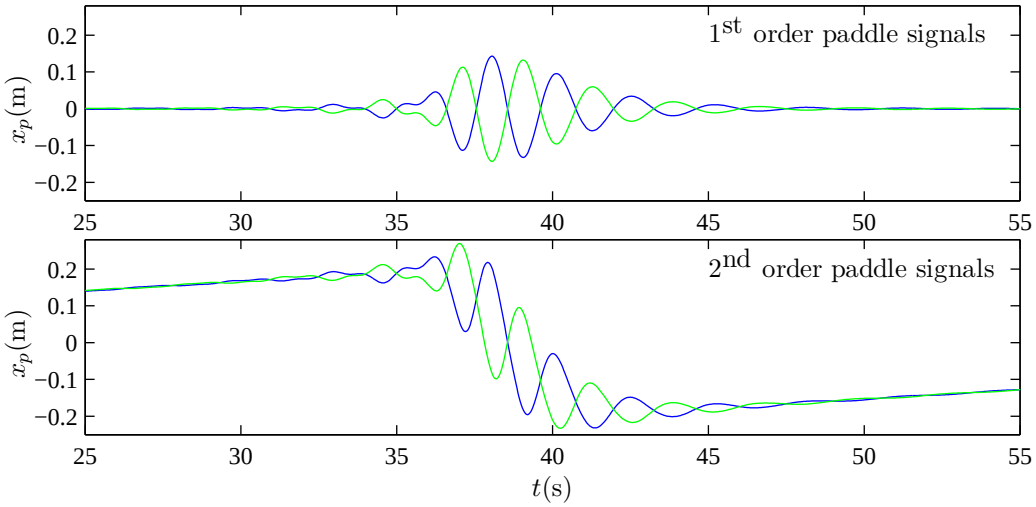

Figure 5.1: Paddle displacement time series for the WG2 crest-focused wave group (blue line) and the WG6 trough-focused wave group (green line). First order paddle signals are shown in the top plot. Corresponding second order paddle signals are shown in the bottom plot.

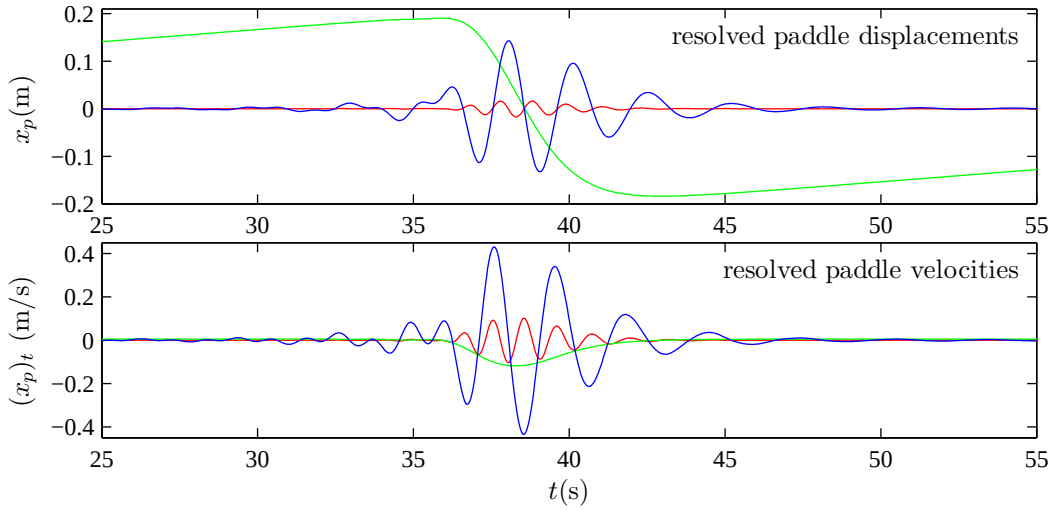

Figure 5.2: Paddle displacement (top plot) and paddle velocity (bottom plot) time series for the WG2 crest-focused wave. The first order paddle displacement/velocity is shown in blue. The second order long correction to the paddle displacement/velocity is shown in green. The second order sum frequency correction to the paddle displacement/velocity is shown in red.

Before looking at the numerical simulation results, it is useful to recall that the second order wavemaker theory by Schäffer (1996) is based on second order solutions to the full Laplace equation water wave problem given by Equations (2.1), together with the paddle boundary condition (2.34), rather than the Boussinesq equation set used in the present numerical model, which was derived by Madsen and Sørensen (1992) and is given by Equation (2.26). As shown in Sections 2.1 and 2.2, the Boussinesq equations are a weakly dispersive and weakly non-linear approximation of the full water wave problem, so for mild wave heights in shallow water the second order paddle signals calculated according to Schäffer (1996) should satisfactorily eliminate the spurious second order error waves. Indeed, in Sections 4.2.3 and 4.2.4, the use of second order signals have been shown to create successfully second order bound sub-harmonic and super-harmonic wave components and suppress second order error waves. Figure 5.3 shows the time series of the theoretically derived bound sub-harmonics and super-harmonics for the WG2 crest-focused wave group. The time series are calculated at the paddle ($x = 0$ m) in the absence of the evanescent modes. Both the Laplace equation and the Boussinesq equations second order bound solutions are shown. Note that the second order bound components for the Boussinesq equations are calculated according to Madsen and Sørensen (1993). In order to suppress formation of second order error waves, the bound harmonics need to be correctly created at the paddle. From Figure 5.3 it follows that the Laplace super-harmonic components are larger

than the Boussinesq super-harmonic components. Therefore, it might be expected that some small excess double frequency waves will be generated and propagate as free waves when the calculated second order signal is fed into the present Boussinesq model. On the other hand, the Laplace sub-harmonic components are marginally smaller than the Boussinesq long components, suggesting that the long error wave will not be quite perfectly eliminated. For reference, the percentage error associated with the largest difference between the Laplace and Boussinesq second order components is around 25 % for the super-harmonic components and about 12 % for the sub-harmonics.

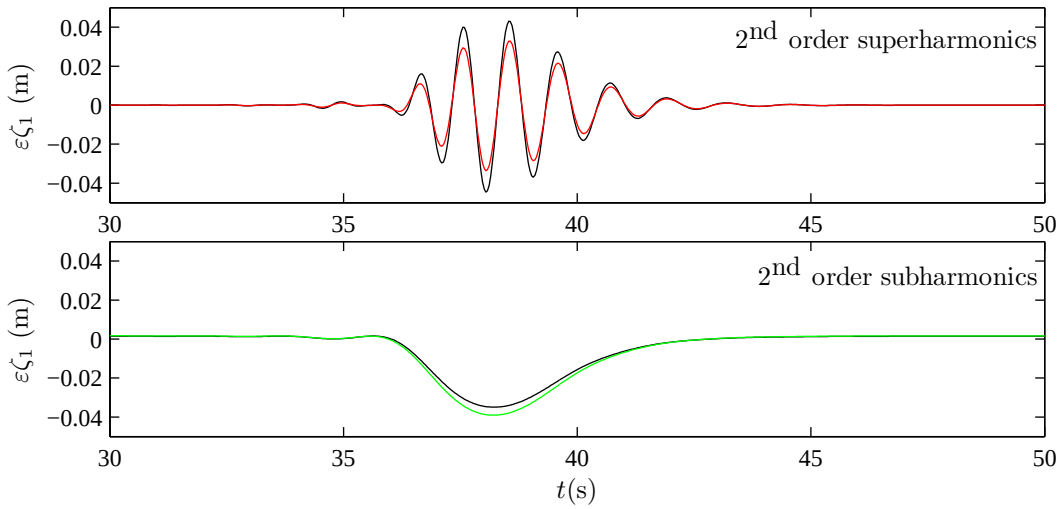

Figure 5.3: Second order bound super-harmonic (top plot) and sub-harmonic (bottom plot) time series at $x = 0$ for the WG2 crest-focused wave group. Comparison between the second order components for the Laplace equation (black line) and the Boussinesq equations (red line for super-harmonics, green line for sub-harmonics).

Figures 5.4 to 5.10 present a comparison between using first (left plot) and second order paddle signals (right plot) for wave groups WG2 and WG6 propagating on a flat bed. Each figure comprises an $x - t$ contour plot of stacked free surface time series calculated by the model. The free surface deviation from the still water level is expressed by the colour, whereby positive elevation is shown by yellow, orange and red; and depression is shown by different shades of blue.

Figure 5.4 presents the $x - t$ propagation plot for the WG2 crest-focused wave group. In both cases, the group is initially compact around the focus and spans roughly 7 s. As it propagates further away from the paddles, the group disperses, expanding over the remaining 20 s shown. However, there are stark visual differences between using a first and a second order paddle signal. The left and the central crests

are higher in the first order case for the entire propagation. On the other hand, the left trough is deeper in the second order case throughout the record shown.

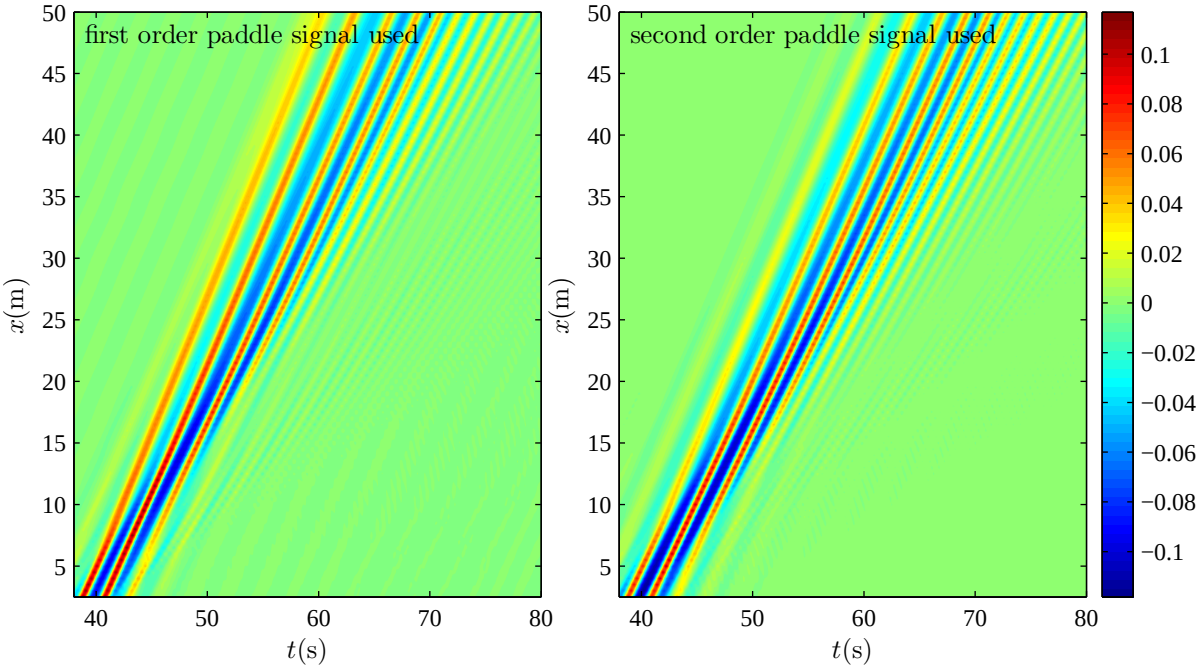

Figure 5.4: NewWave propagation on a flat bed for the WG2 crest-focused wave group. Calculated **total free surface** time series using a first order paddle signal (left plot) and a second order paddle signal (right plot).

Figure 5.5 shows the stacked time series for the WG6 trough-focused wave group. Group dispersion is again clearly visible. In the second order case, the left and the central troughs are deeper, and the two left crests are less pronounced. In both plots, high frequency waves can be seen trailing the main wave packet.

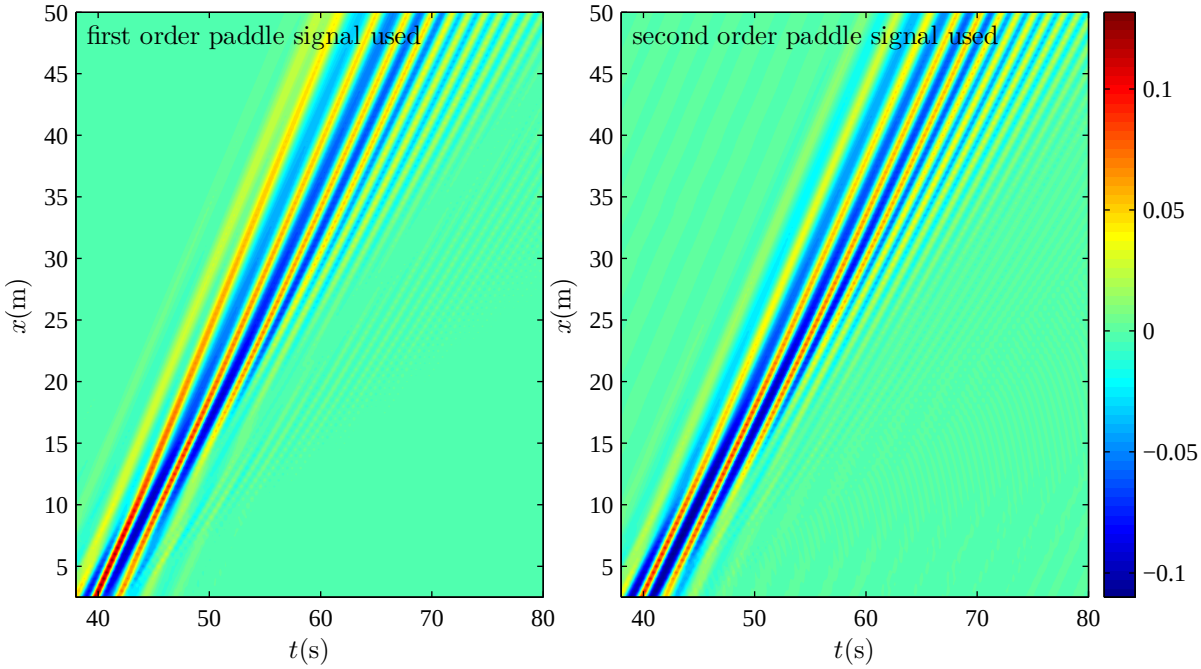

Figure 5.5: NewWave propagation on a flat bed for the WG6 trough-focused wave group. Calculated **total free surface** time series using a first order paddle signal (left plot) and a second order paddle signal (right plot).

As discussed in Section 4.2.3, addition and subtraction of the free surface time series with suitable frequency filtering can reveal detailed features of the wave groups. Denoting the crest-focused free surface by ζ_c and the trough-focused free surface by ζ_t, addition $\frac{1}{2}(\zeta_c + \zeta_t)$ gives the even order harmonics as the linear components and all the odd order harmonics cancel out. Subtraction $\frac{1}{2}(\zeta_c - \zeta_t)$ results in the linear components and all the odd order harmonics. Filtering can be used on the addition and subtraction time series. Suitable cut-off frequencies for the applied high-pass and low-pass filters can be found from the frequency spectra. Figure 5.6 displays the amplitude spectra associated with the crest-focused time series (top plot), the addition time series (middle plot) and the subtraction time series (bottom plot) from $x = 8.33$ m, which is the location of the beach toe in the run-up and overtopping studies presented in the subsequent sections. Amplitude spectra are shown for the wave group generated with the first order paddle signal (black line) and the second order paddle signal (red line). From the Figure, it follows that for the addition time series, which contains the even harmonics, a cut-off frequency of 0.5 Hz can be used to separate the sub-harmonics (denoted by 2^-) from the super-harmonics (denoted by 2^+). For the subtraction time series, which contains the odd harmonics, a cut-off frequency of 1 Hz is used to separate the linear terms (denoted by 1) from the

third (denoted by 3^+) and higher order odd harmonics. The spectra were obtained by applying a Fast Fourier Transform (FFT) algorithm to the time series. After frequency filtering is performed, the inverse transform recovers the filtered time series.

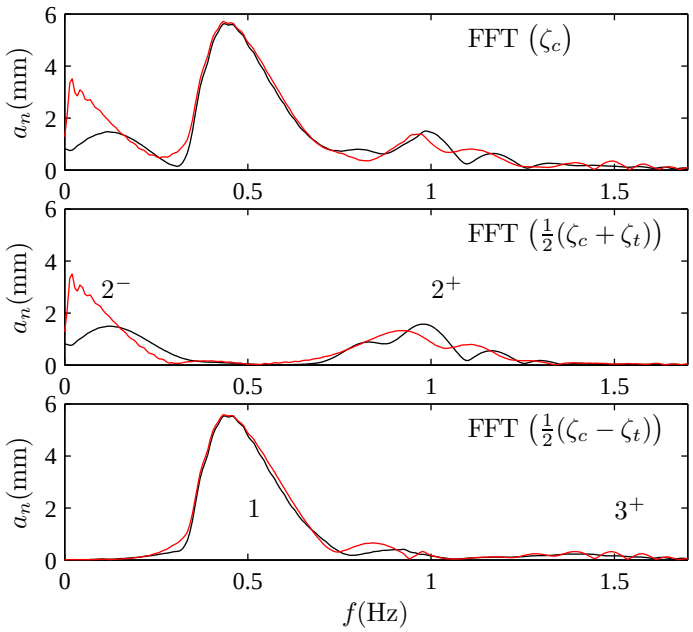

Figure 5.6: Amplitude spectra associated with the total free surface elevation time series (top plot), the addition time series (middle plot) and the subtraction time series (bottom plot) shown for the WG2 and WG6 pair of wave groups generated with the first order paddle signal (black line) and the second order paddle signal (red line).

Figure 5.7 shows the free surface subtraction time series, low-pass filtered at 1 Hz to isolate the linear terms. The two contour plots are rather similar, apart from small discrepancies at the left crest, suggesting that the use of second order paddle signals does not affect the primary frequency components.

Figure 5.8 shows the free surface addition time series, low-pass filtered at 0.5 Hz to isolate the difference frequency components. As can be seen from the two plots, the use of the second order paddle signal substantially alters the structure of the long wave components. In the first order plot, the long error wave manifests itself as a hump (positive elevation shown in orange and red). It is governed by its own dynamics and can be seen propagating ahead of the group due to its long wavelength. In the second order plot, the long error wave is eliminated and the bound long waves can be clearly seen as a depression underneath the main wave group (shown in blue). These long wave plots help to explain observations from Figures 5.4 and 5.5, where higher left crests and shallower left troughs were identified in the first order cases. A very faint yellow elevation can be seen ahead of the bound long wave in the second order

plot (at $t > 50$ s), suggesting that the long error wave is not perfectly suppressed. This is most likely due to the second order wavemaker theory from Schäffer (1996) being applied to the Boussinesq numerical solver. Nevertheless, the release of the long error wave is minimal.

Figure 5.9 shows the free surface addition time series, high-pass filtered at 0.5 Hz to extract the second order sum components (and any other higher order even harmonics). The bound second order super-harmonics (denoted by b) can be seen in both plots, travelling with the speed of the main group, thus reaching $x = 50$ m at $t = 60 - 70$ s. The free error double frequency harmonics (denoted by e) can be seen lagging behind the main group. When using the second order paddle signal, these error waves are weakened but not fully eliminated. As discussed earlier, this is probably due to the different second order bound solution of the Laplace equation and the Boussinesq equations. In Sections 5.5 and 5.6, the influence of using second order paddle signals on run-up distances and overtopping volumes is investigated. Even though the double frequency error waves are not successfully eliminated, since they travel behind the main wave packet, it is clear that their presence will not spoil the investigation.

Figure 5.10 displays the free surface subtraction time series, high-pass filtered at 1 Hz to isolate the third order super-harmonics (and any other higher order odd harmonics). In both plots, the triple frequency bound waves (denoted by b) can be seen, again travelling with the main wave packet. In the second order case, very small free error waves (denoted by e) can be seen travelling far behind the bound waves. It is not clear why these free triple frequency waves arise when the second order paddle signal is used.

Figure 5.11 shows spatial profiles of the WG2 crest-focused wave group at 3 different times. The profiles generated by the first order paddle signal are shown on the left, and the wave group generated by the second order paddle signal is shown on the right. In the first order plots, the long error wave (denoted by 2^-) can be seen dramatically changing the front of the wave packet, increasing wave heights of the first few crests and flattening the leading troughs. Also in the first order plots, the free second order sum components can be seen following the main wave group (denoted by 2^+). In the second order plots, the weakened residual free second order sum components can be seen (denoted by 2^+), which are additionally followed by triple frequency free waves (denoted by 3^+).

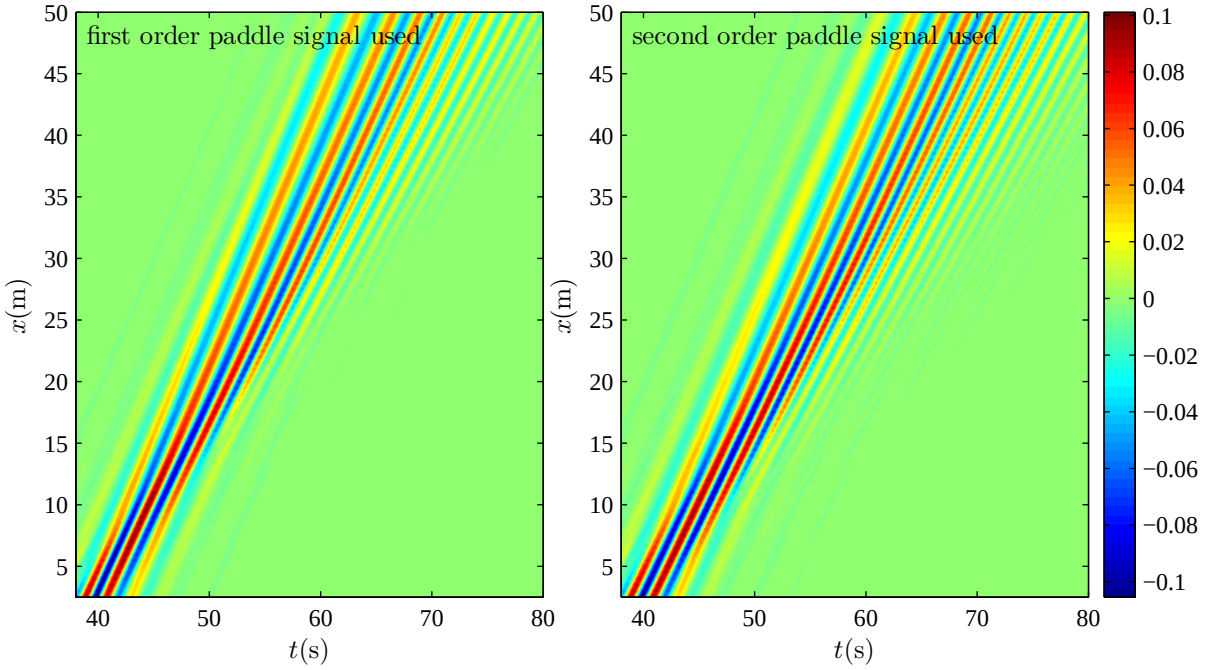

Figure 5.7: NewWave propagation on a flat bed for the subtraction of crest- and trough-focused wave groups (WG2 and WG6). **Linear terms** only - subtraction time series low-pass filtered at 1 Hz. Model predictions using a first order paddle signal shown in the left plot. Model predictions using a second order paddle signal shown in the right plot.

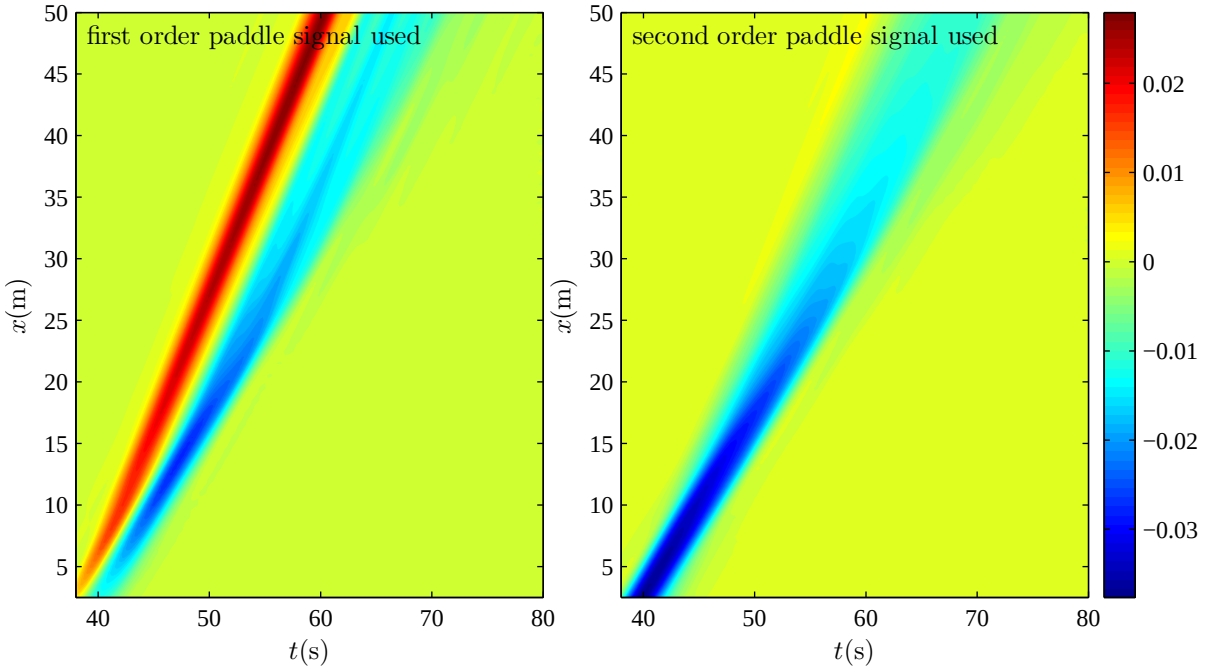

Figure 5.8: NewWave propagation on a flat bed for the addition of crest- and trough-focused wave groups (WG2 and WG6). **Long waves** only - addition time series low-pass filtered at 0.5 Hz. Model predictions using a first order paddle signal shown in the left plot. Model predictions using a second order paddle signal shown in the right plot.

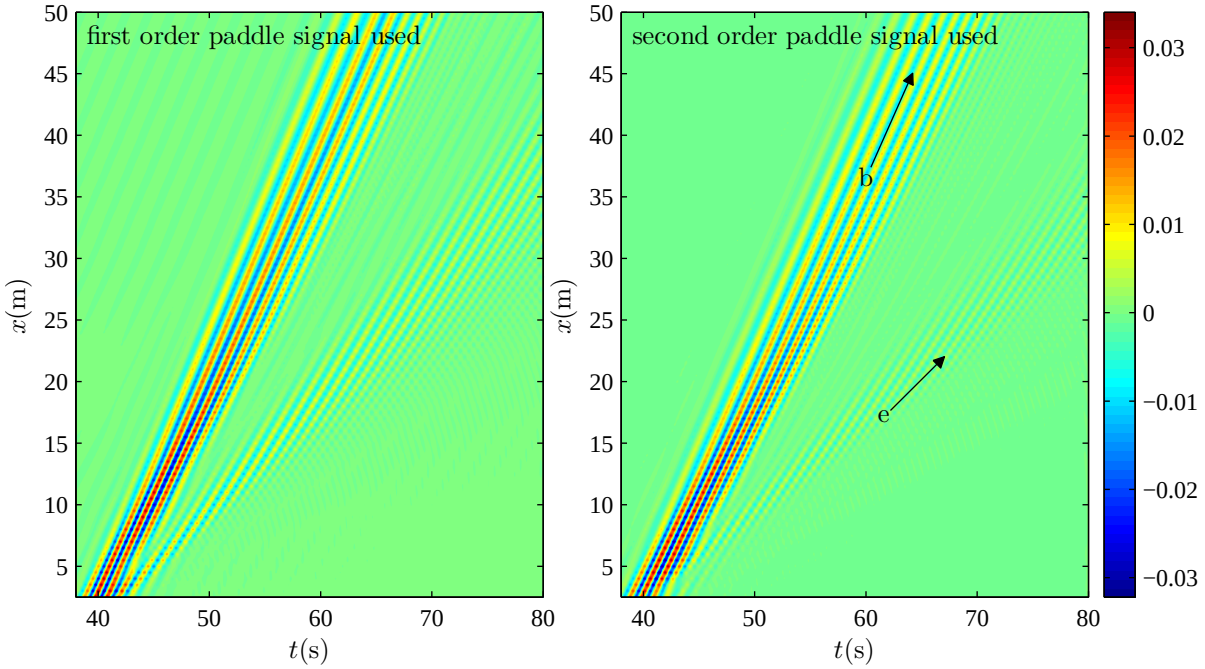

Figure 5.9: NewWave propagation on a flat bed for the addition of crest- and trough-focused wave groups (WG2 and WG6). **Even order super-harmonics** only - addition time series high-pass filtered at 0.5 Hz. Model predictions using a first order paddle signal shown in the left plot. Model predictions using a second order paddle signal shown in the right plot.

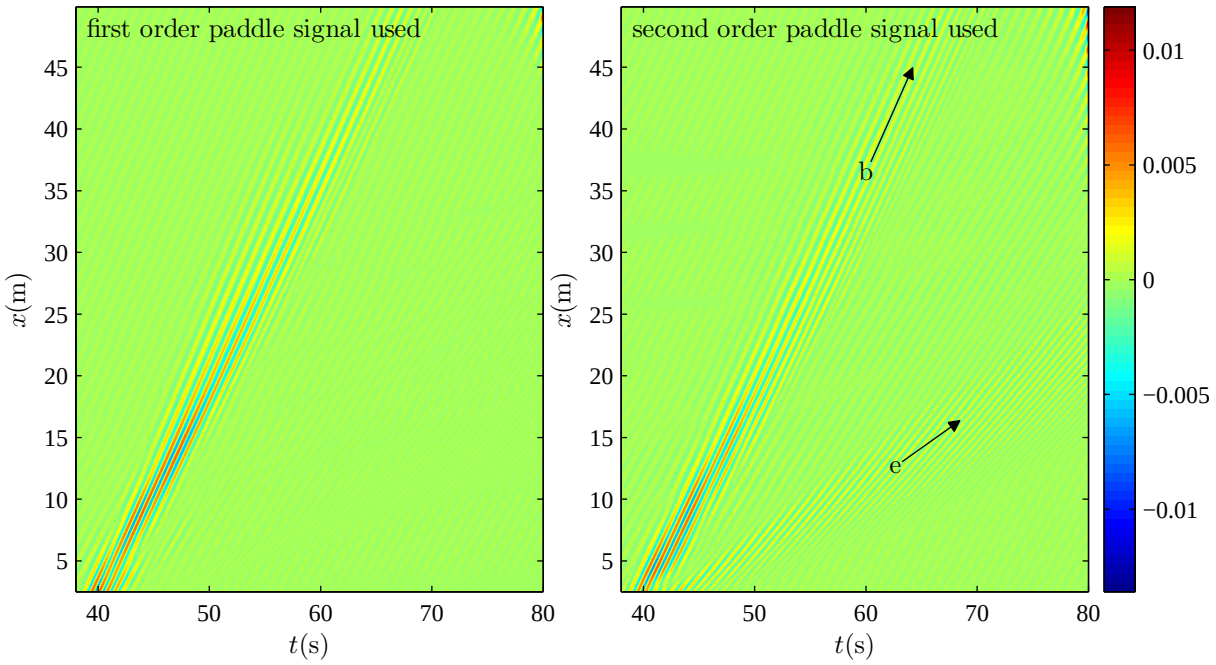

Figure 5.10: NewWave propagation on a flat bed for the subtraction of crest- and trough-focused wave groups (WG2 and WG6). **Odd order super-harmonics** only - subtraction time series high-pass filtered at 1 Hz. Model predictions using a first order paddle signal shown in the left plot. Model predictions using a second order paddle signal shown in the right plot.

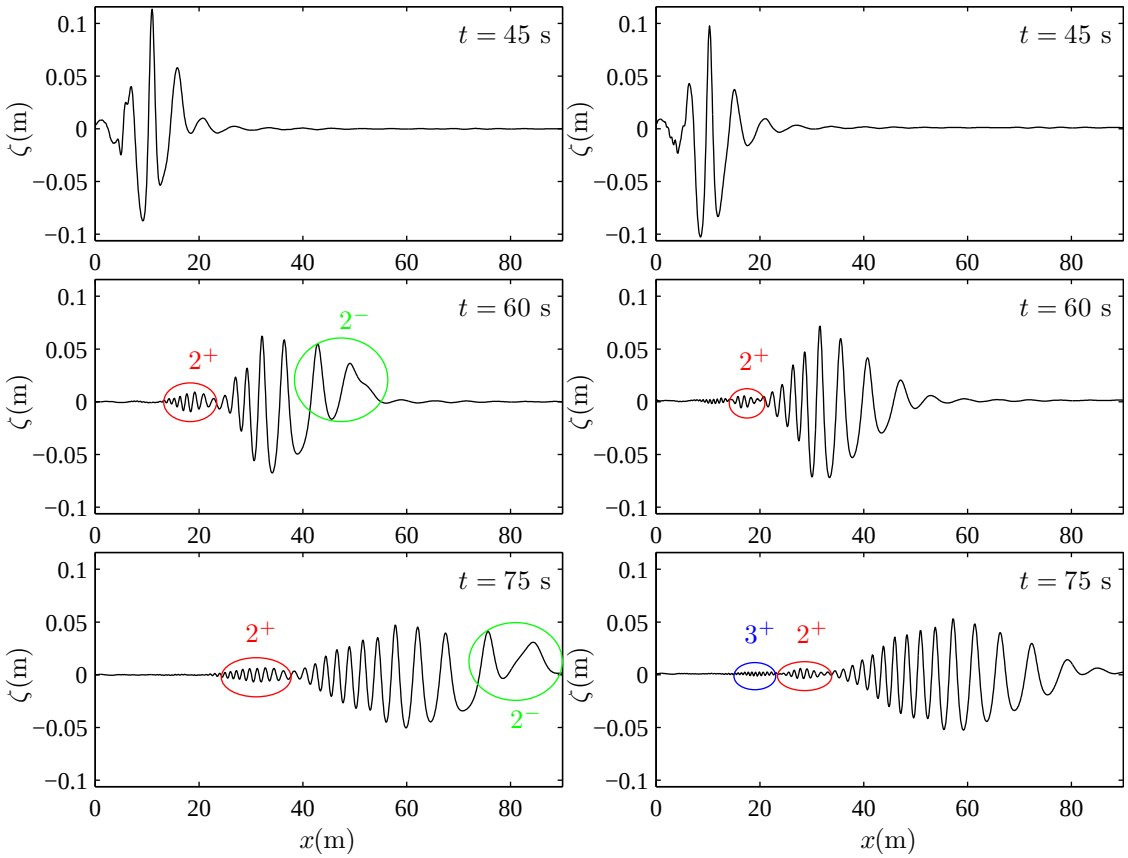

Figure 5.11: NewWave propagation on a flat bed for the WG2 crest-focused wave group. Spatial profiles of the wave group when using a first order paddle signal (left plot) and a second order paddle signal (right plot).

5.3 NewWave run-up at a plane beach

The laboratory experiments reported by Hunt (2003), Hunt-Raby *et al.* (2011) and Borthwick *et al.* (2006) are again considered, this time to investigate run-up by NewWave focused wave groups on a plane beach. The UKCRF experimental basin, where the experiments were performed, had a bed topography as follows: 8.33 m of flat bed from the paddles, followed by a plane 1:20 beach, which extended to well above the still water level. The still water depth at the paddles was 0.5 m. For the NewWave run-up tests, 44 wave gauges, measuring free surface elevation, were deployed at 0.25 m intervals starting at a distance of 6.83 m from the paddles (which is 1.5 m offshore of the beach toe; and where the still water depth was 0.5 m) and finishing at a distance of 17.58 m (which is 0.75 m offshore of the still water line; and where the still water depth was 0.0375 m). Figure 5.12 shows the basin setup.

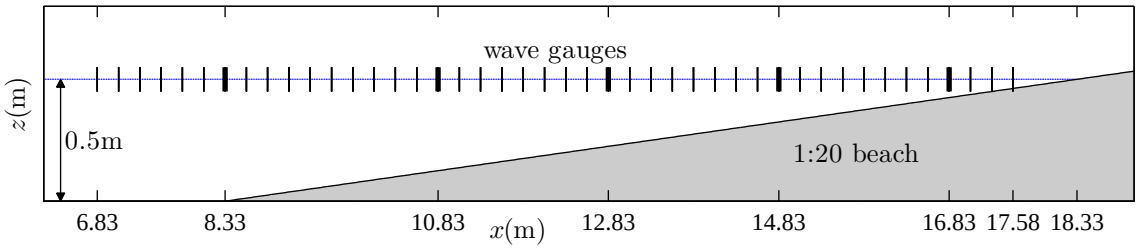

Figure 5.12: Basin setup and wave gauge placement for the UKCRF run-up experiments reported by Hunt (2003). Note that the gauge locations shown in bold are used in Figures 5.19 and 5.35.

In total, 8 normally-incident NewWave run-up experiments were performed, involving 4 crest-focused and 4 trough-focused wave groups, covering a range of group amplitudes and focus locations. Table 5.1 summarises the wave group properties. There is a shift in the observed focus location away from the input focus location predicted by linear theory. Note that in the experiments, focus location was defined as the point in space where the troughs either side of the central crest, for a crest-focused wave group, are of equal depth. Cases WG1 and WG4, where focusing occurs before the bathymetry changes, exhibit an upstream shift of the focus location, which increases with the group's nonlinearity. This behaviour is qualitatively similar to the observations by Baldock *et al.* (1996).

Table 5.1: Properties of the normally-incident NewWave focused wave groups reported by Hunt (2003).

Wave group	Input amplitude $A_{\mathcal{N}}$ (m)	Input focus location x_f (m)	Observed focus location in the UKCRF (m)	Phase angle ϕ (rad)
WG1	0.114	9.00	8.33 (beach toe)	0
WG2	0.114	10.90	10.83 (3/4 depth)	0
WG3	0.090	12.90	13.33 (1/2 depth)	0
WG4	0.057	8.80	8.33 (beach toe)	0
WG5	0.114	9.00	8.33 (beach toe)	π
WG6	0.114	10.90	10.83 (3/4 depth)	π
WG7	0.090	12.90	13.33 (1/2 depth)	π
WG8	0.057	8.80	8.33 (beach toe)	π

The present numerical model has been used to simulate the UKCRF experimental results. The computational grid is uniform, with resolution $\Delta x = 2$ cm; the time step is $\Delta t = 0.007$ s. First order paddle displacement signals recorded directly from the laboratory experiments are used for simulations presented in this section. Figures

5.13 to 5.18 present the numerical (left plot) and experimental results (right plot) for cases WG2 and WG6. Each figure comprises an $x-t$ contour plot determined from the 44 stacked free surface time series (corresponding to the locations of the wave gauges), where the colour represents the free surface deviation from still water depth.

Figure 5.13 shows the $x-t$ propagation of the WG2 crest-focused group. Initially, the group is rather compact, with three main crests (shown in red, orange and yellow) and two troughs (shown in blue). As it propagates up the beach, the group disperses and becomes less well defined. High-frequency waves can be seen trailing the main group. Shoaling is also evident, for example by looking at the first crest at $x = 14$ m to $x = 17$ m. Wave breaking can also be deduced, for example from the sudden loss of amplitude of the central crest (around $x = 14.5 - 15$ m in the numerical plot, or around $x = 14$ m in the experimental plot). Long waves can be seen, reverberating across the flume/basin. The numerical model appears to capture all the main features of this propagating and evolving wave group.

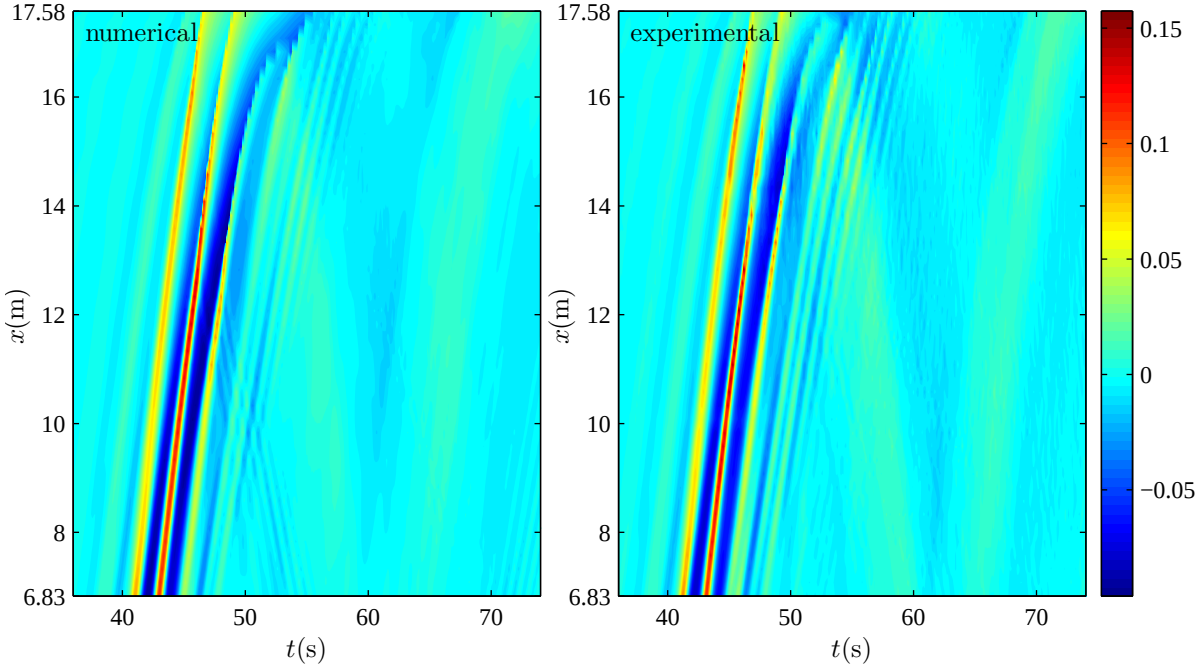

Figure 5.13: NewWave run-up on a plane beach for the WG2 crest-focused wave group. **Total free surface** time series using the model predictions (left plot) and the UKCRF measurements reported by Hunt (2003) (right plot).

Figure 5.14 presents the $x-t$ propagation of the WG6 trough-focused wave group. The central trough (shown in blue) and two surrounding crests (shown in red, orange and yellow) are clearly visible, with the group focusing near $x = 11$ m. The second

crest appears to break around $x = 13$ m. High frequency trailing waves and reverberating long waves are again visible. As with the crest-focused wave group, there is generally good agreement between the model predictions and the measured data.

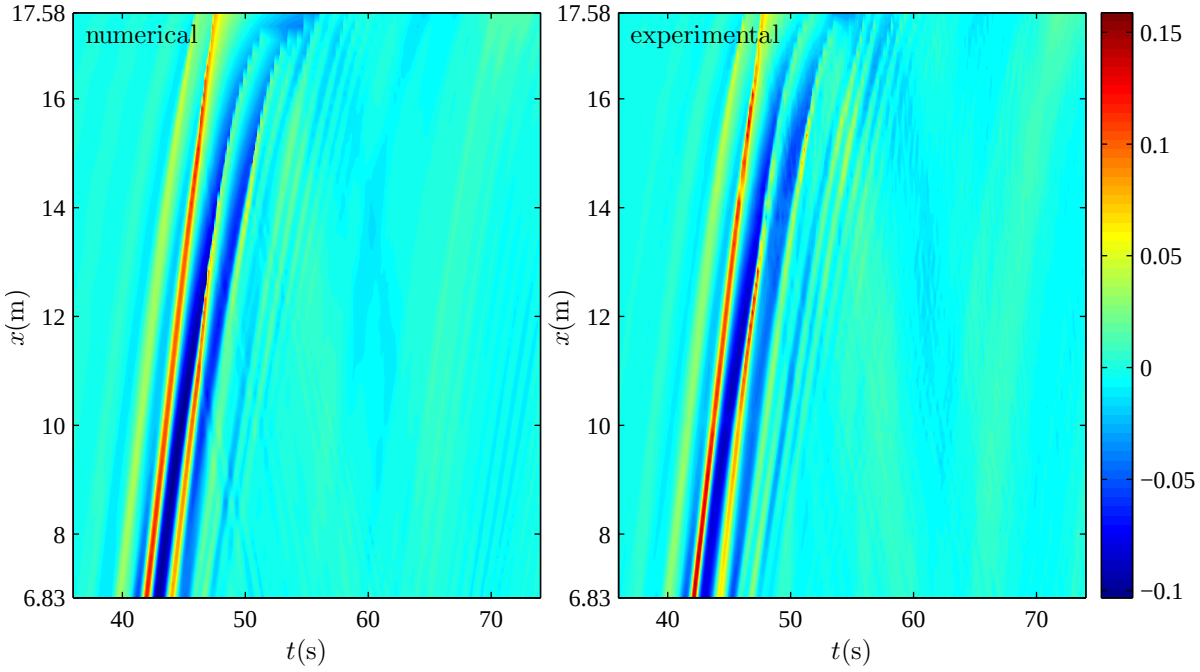

Figure 5.14: NewWave run-up on a plane beach for the WG6 trough-focused wave group. **Total free surface** time series using the model predictions (left plot) and the UKCRF measurements reported by Hunt (2003) (right plot).

Addition, subtraction and filtering are used again to isolate different frequency components. Strictly speaking, these manipulations are not well defined inshore beyond wave breaking or in very shallow water due to mis-alignment of crests and troughs. However, such analysis can still be useful and is therefore performed at all 44 gauge locations.

Figure 5.15 shows the free surface subtraction time series, low-pass filtered at 1 Hz to isolate the linear terms. Group dispersion can be seen. There are no visible reflected waves, suggesting that the linear components are dissipated on the beach.

Figure 5.16 shows the free surface addition time series, low-pass filtered at 0.5 Hz. The resultant long waves are now clearly visible, propagating across the basin. The second order long error wave can be seen as a positive elevation (shown in yellow, orange and red) propagating at the front of the main wave packet. The second order bound waves, the set down underneath the group, can be seen as a depression (shown in blue). The initially bound long waves and the free long error waves are not dissipated at the beach and can be seen reverberating across the flume throughout the

entire record, with the bound waves being released at the beach and then propagating as free components. The significant influence of the low frequency error wave on the wave group run-up is investigated in Section 5.5.

Figure 5.17 shows the free surface addition time series, high-pass filtered at 0.5 Hz. These high frequency waves, predominantly second order sum components, are dissipated at the beach as there are no significant reflected waves coming back from the beach to the paddles. Both bound and free error double frequency harmonics are present in both the numerical results and the experiments. The free error waves (denoted by e) can be seen following the bound waves (denoted by b) as they propagate more slowly than the main group. In the numerical plot, there is an evidence of small wave reflection around $x = 11 - 12$ m. This arises due to the treatment of wave breaking in the model by switching from the Boussinesq to the shallow water equations (see Sections 2.5 and 3.8).

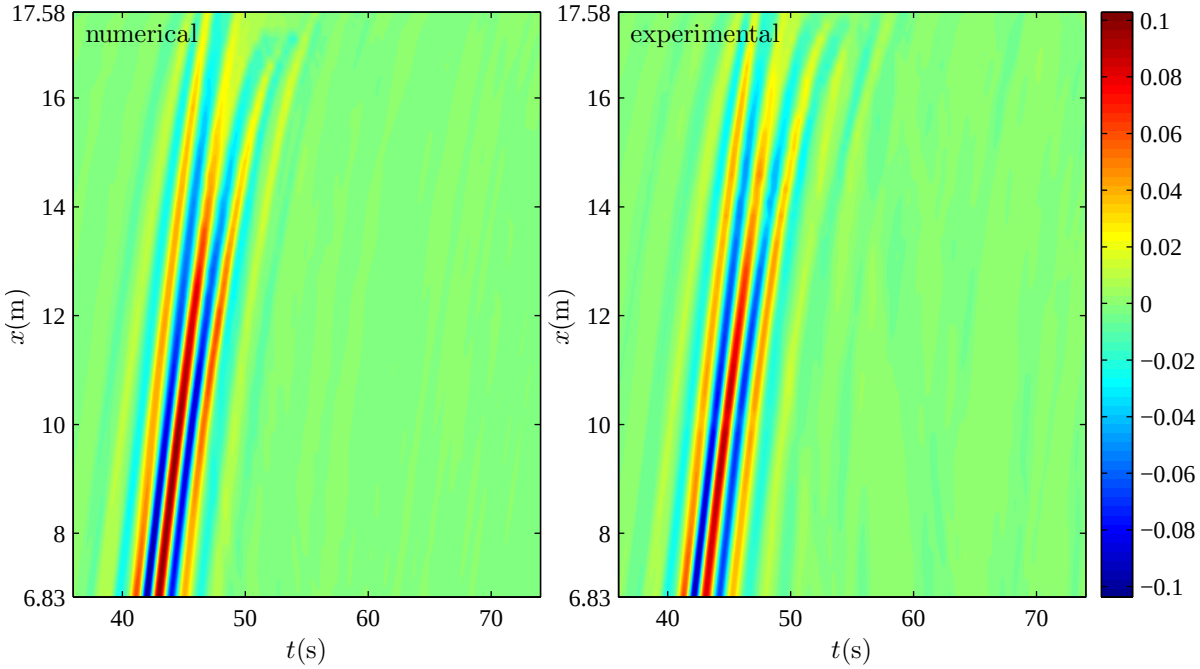

Figure 5.15: NewWave run-up on a plane beach for the subtraction of crest- and trough-focused wave groups (WG2 and WG6). **Linear terms** only - subtraction time series low-pass filtered at 1 Hz. Model predictions shown in the left plot. UKCRF measurements shown in the right plot.

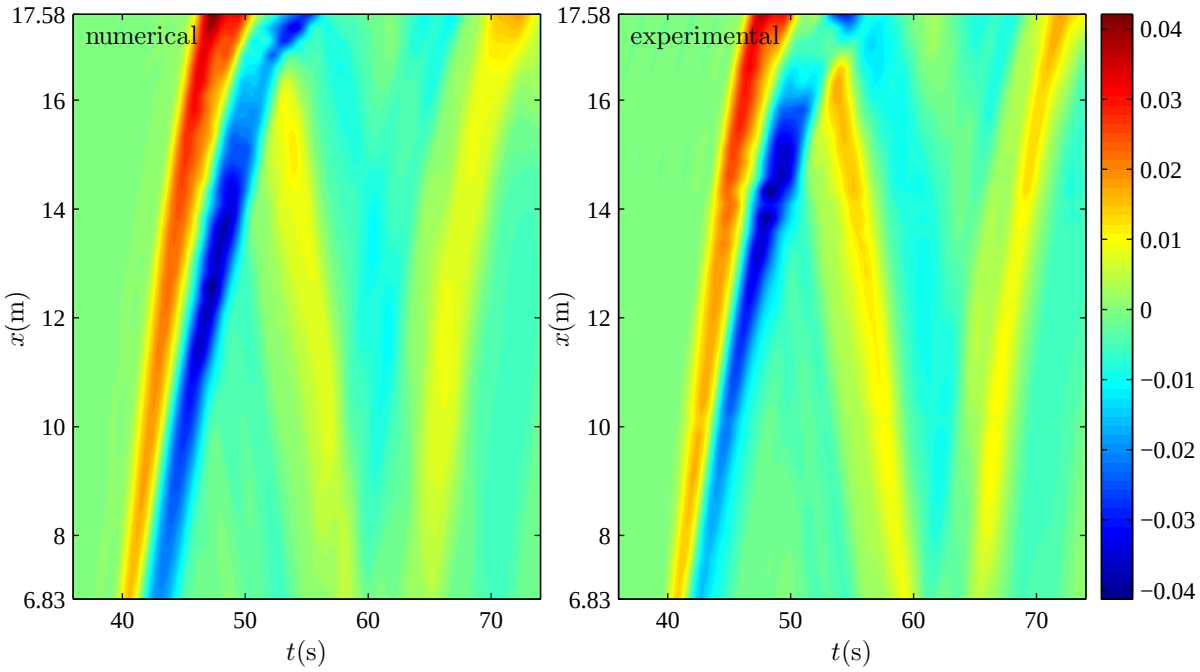

Figure 5.16: NewWave run-up on a plane beach for the addition of crest- and trough-focused wave groups (WG2 and WG6). **Long waves** only - addition time series low-pass filtered at 0.5 Hz. Model predictions shown in the left plot. UKCRF measurements shown in the right plot.

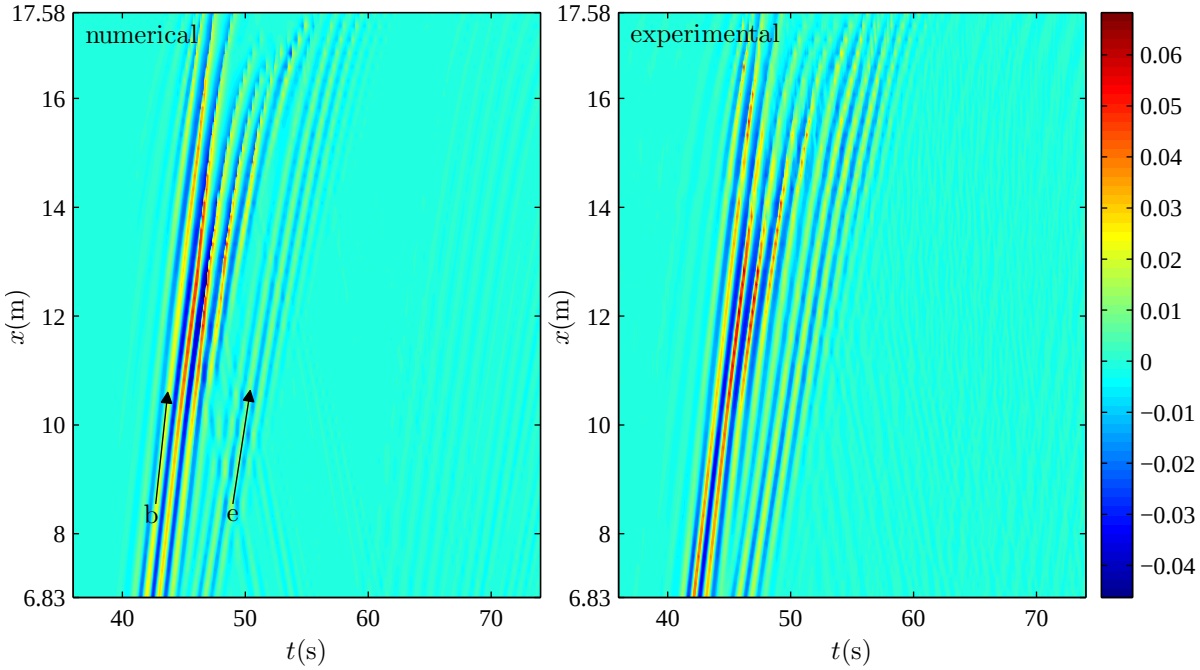

Figure 5.17: NewWave run-up on a plane beach for the addition of crest- and trough-focused wave groups (WG2 and WG6). **Even order super-harmonics** only - addition time series high-pass filtered at 0.5 Hz. Model predictions shown in the left plot. UKCRF measurements shown in the right plot.

Figure 5.18 displays the free surface subtraction time series, high-pass filtered at 1 Hz to isolate the third order super-harmonics (and any other higher order odd harmonics). As with second order harmonics, these waves are fully absorbed at the beach. In the numerical plot, however, very weak waves can again be seen reflected from around $x = 12$ m, which are then re-reflected from the numerical paddle reaching the first gauge at around 70 s. These are purely numerical and are associated with the switch of the governing equations in the model. Numerical tests have been carried out with different values of the breaking initiation criterion such that $-\eta_x = 0.3, 0.5$ and 0.6. The small wave reflection detected is further inshore for higher values of $-\eta_x$.

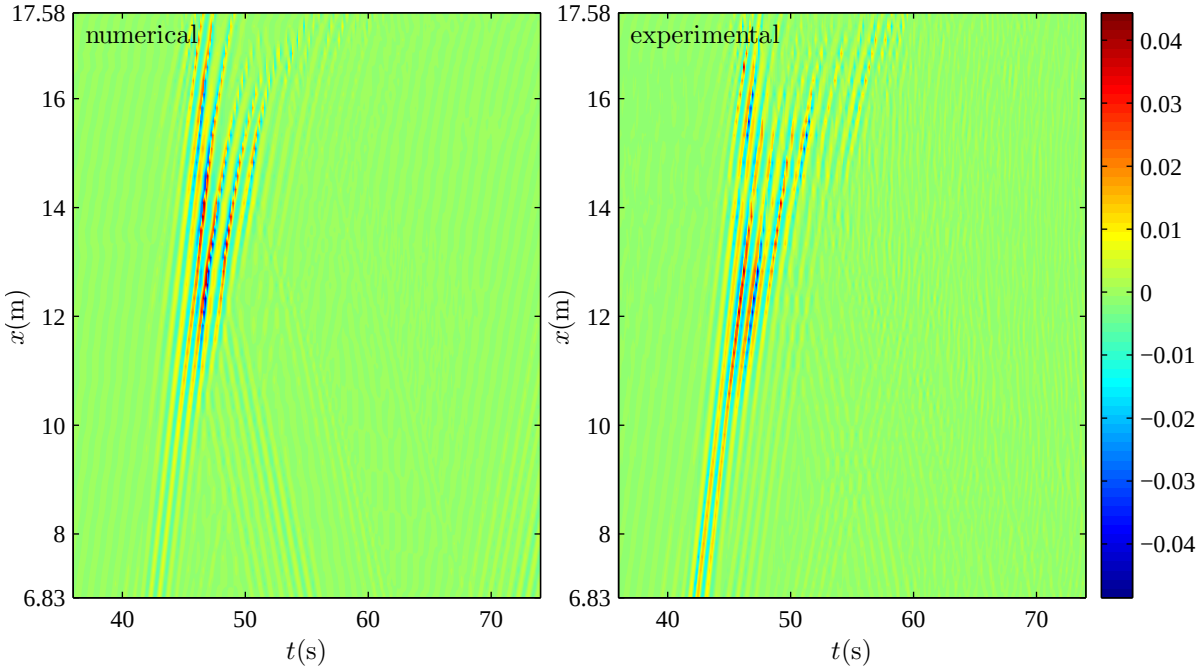

Figure 5.18: NewWave run-up on a plane beach for the subtraction of crest- and trough-focused wave groups (WG2 and WG6). **Odd order super-harmonics** only - subtraction time series high-pass filtered at 1 Hz. Model predictions shown in the left plot. UKCRF measurements shown in the right plot.

A more direct comparison between the model output and the experimental measurements is presented in Figure 5.19. Experimental and numerical time series are shown at 5 different locations, providing information on the detailed structure of the focused wave groups. For reference, the 5 chosen gauge locations have been highlighted, with bold lines, in Figure 5.12. In the crest-focused case, there is a mis-match between the predicted and measured values of the central crest height and the second trough depth at the first two locations. Wave breaking and bore formation appear

to be well captured by the model, apart from a slight time shift in some of the broken waves. In the trough-focused case, there is a mis-match in the predicted and measured values of the first crest height and the central trough depth at the first location. Overall, although there are small differences, it is clear that the numerical model properly reproduces the evolution of both the crest-focused and trough-focused wave groups as they propagate up the beach.

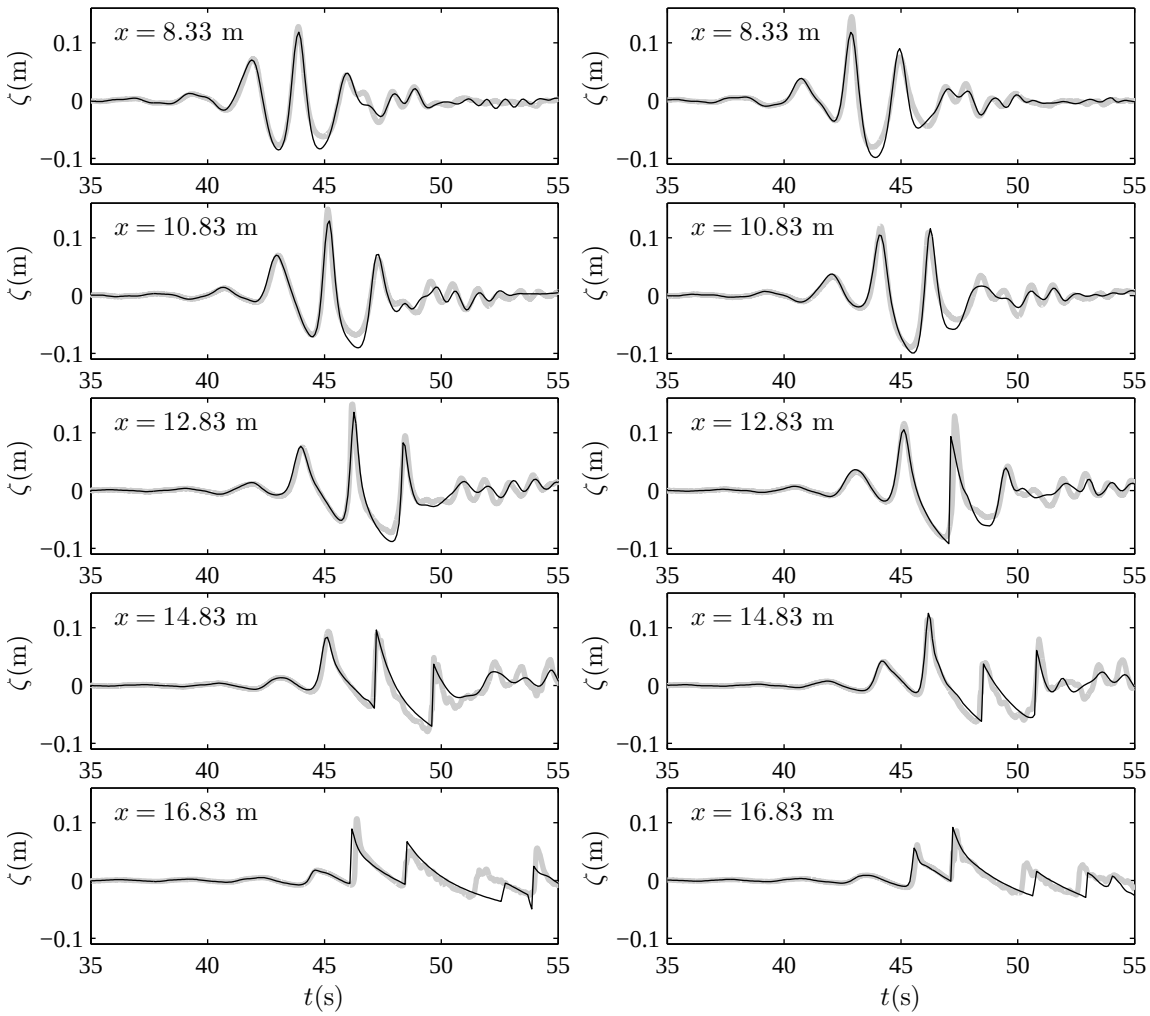

Figure 5.19: NewWave run-up on a plane beach, with the WG2 crest-focused wave shown on the left and the WG6 trough-focused wave shown on the right. Free surface time series comparison between the model predictions (thin black line) and the UKCRF measurements reported by Hunt (2003) (thick grey line).

Table 5.2 summarises the measured and calculated horizontal run-up for all of the 8 NewWave cases. In general, run-up increases with linear amplitude of the wave group, with crest-focused waves producing smaller values of run-up compared to their trough-focused counterparts. The numerical model mirrors this behaviour. All the

predicted run-up values are slightly larger than those measured, as can be seen in Figure 5.20. The maximum error in the model run-up prediction is about 15 %, while the average error (of the 8 simulations) is about 6 %. It should be noted that the inferred experimental error in the measured run-up values is about 5 %. This was estimated from repeat measurements of run-up from this experimental programme.

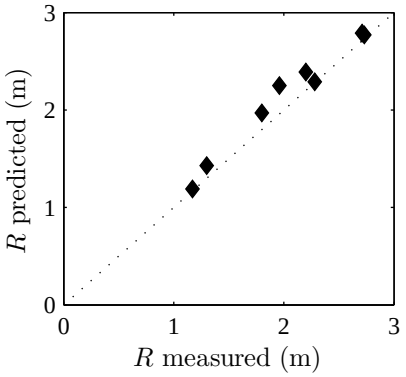

Wave group	Horizontal R measured (m)	Horizontal R predicted (m)	% error
WG1	1.96	2.25	14.8
WG2	2.20	2.39	8.6
WG3	1.80	1.97	9.4
WG4	1.17	1.19	1.7
WG5	2.71	2.79	3.0
WG6	2.73	2.77	1.5
WG7	2.28	2.29	0.4
WG8	1.30	1.43	10.0

Figure 5.20 and Table 5.2: Horizontal run-up of NewWave. Comparison between the model predictions and the UKCRF measurements reported by Hunt (2003).

5.4 NewWave overtopping a seawall

The 8 NewWave focused wave tests from Table 5.1 were repeated for the same offshore bathymetry but now with a laboratory seawall mounted on the 1 : 20 plane beach. The offshore toe of the seawall was constructed at a distance of 8.125 m from the beach toe where the still water depth was approximately 9.4 cm. Figure 4.13 in Section 4.2.2 presents details of the seawall dimensions.

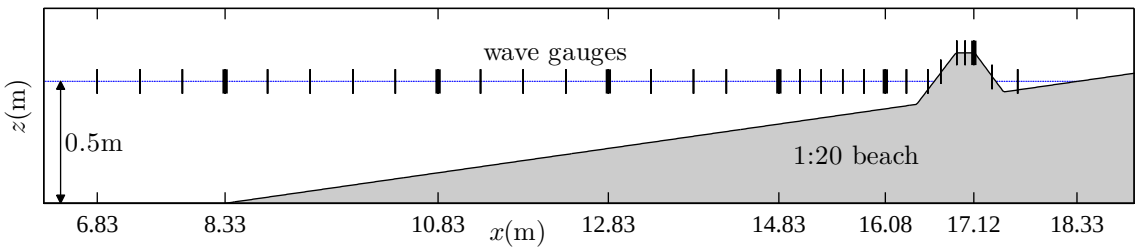

Figure 5.21: Basin setup and wave gauge placement for the UKCRF overtopping experiments reported by Hunt (2003). Note that the gauge locations shown in bold are used in Figures 5.26 and 5.43.

For the overtopping tests, wave gauges were placed along the centre line of the basin at 0.5 m intervals in the deeper sections of the beach and at smaller intervals directly

in front of and across the seawall. Figure 5.21 shows the basin setup with the gauge layout for the overtopping experiments.

In the simulations of the overtopping experiments using the numerical model, sharp reflected (off the seawall) waves re-entering the Boussinesq domain pose difficulty to the finite difference solver, resulting in erroneous generation of short waves. For this reason, a numerical filter is applied to the calculated solution spatially (over a wavelength around the interface between the Boussinesq and the shallow water equations domains) and temporarily (for up to twenty times, at every other time step, as each of the largest 1-3 waves re-enters the Boussinesq domain). The smoothing algorithm is described in Section 3.9. The application of the smoothing filter increases the stability of the model and allows for completion of each simulation. Note in passing that without applying the filter, most of the simulations would run for long enough to compute overtopping volumes from the incoming waves. However, the available laboratory measurements contain total overtopped volumes at the end of each run, which can also contain water from additional overtopping from reflected waves. It is therefore desirable to calculate the overtopping volume at the end of the simulation. Additionally, the complete simulation allows for a comparison of the free surface evolution with the entire experimental record from the wave gauges.

Figures 5.22 to 5.25 present the numerical (left plot) and experimental results (right plot) for Cases WG4 and WG8 as $x - t$ contour plots of stacked free surface time series. The presented time series cover locations from 6.83 m to 15.08 m from the paddles. In order to allow a visual comparison with results presented in Section 5.3, which relate to a different wave gauge spacing, the data shown in Figures 5.22 to 5.25 are presented to align with the gauge locations from the run-up experiments. Since there are less data available in these overtopping experiments (due to sparser wave gauge distribution), the contour plots in Figures 5.22 to 5.25 exhibit an artificial modulation in the crest heights and trough depths. This is particularly visible for waves of higher frequencies; and herein the linear and the super-harmonic plots suffer from this synthetic visual defect.

Figure 5.22 shows the propagation of the WG4 crest-focused group. Three main crests (shown in red, orange and yellow) separated by two troughs (shown in blue) are clearly visible. Significant reflections and re-reflections, at a large range of frequencies, can be seen throughout the entire record, unlike in the run-up case presented in Figure 5.13. The corresponding plot of the trough-focused wave is very similar and so has been omitted for brevity.

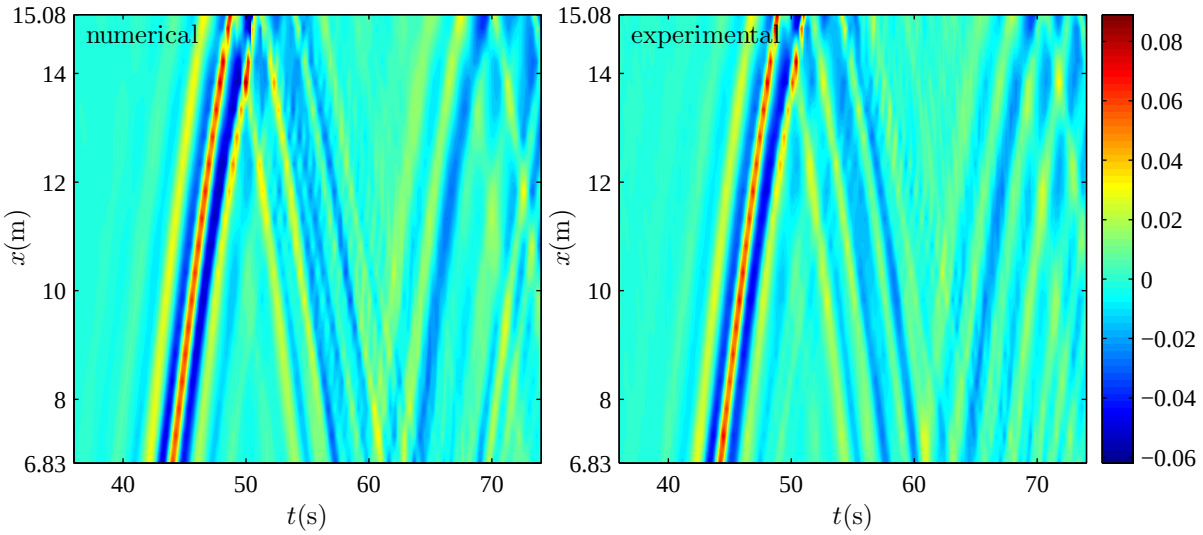

Figure 5.22: NewWave overtopping a seawall for the WG4 crest-focused wave group. **Total free surface** time series using the model predictions (left plot) and the UKCRF measurements reported by Hunt (2003) (right plot).

Figure 5.23 shows the free surface subtraction time series, low-pass filtered at 1 Hz to isolate the linear terms. Unlike the run-up case, the linear terms undergo considerable reflection from the beach and the seawall. The plot of the high-pass filtered subtraction time series is omitted as the third and higher odd harmonics are very small for the two cases WG4 and WG8.

Figure 5.24 shows the free surface addition time series, low-pass filtered at 0.5 Hz. Reverberating long waves are again evident. As in Section 5.3, the long error wave comprises a hump ahead of the group (shown in red) and the bound long wave is a depression underneath the group (shown in blue). In the experiments, the long waves are slowly dissipated as they travel up and down the basin. This is, however, not the case in the numerical simulation, where the long waves do not appear to experience significant energy loss. The influence of the low frequency error wave on the wave group overtopping volume is investigated in Section 5.6.

Figure 5.25 shows the free surface addition time series, high-pass filtered at 0.5 Hz. Both bound and free error double frequency harmonics are evident. It is clear that these high frequency waves are not dissipated at the seawall, as was the case for the run-up tests. The free error waves (denoted by e) propagate more slowly than the bound waves (denoted by b) and can be seen lagging further and further behind the bound waves (see 45 to 70 s of the record).

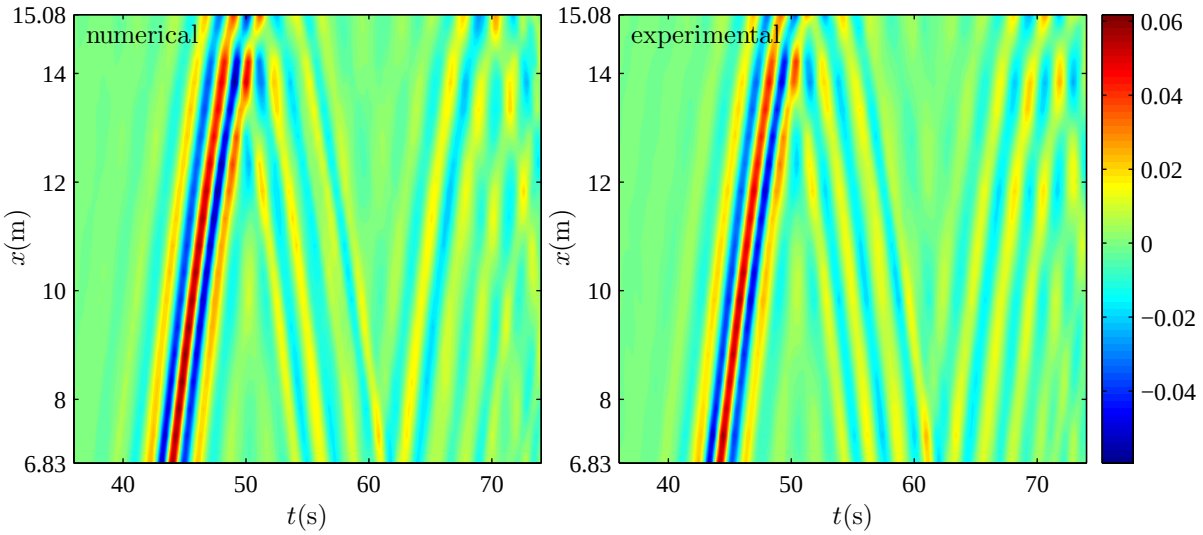

Figure 5.23: NewWave overtopping a seawall for the subtraction of crest- and trough-focused wave groups (WG4 and WG8). **Linear terms** only - subtraction time series low-pass filtered at 1 Hz. Model predictions shown in the left plot. UKCRF measurements shown in the right plot.

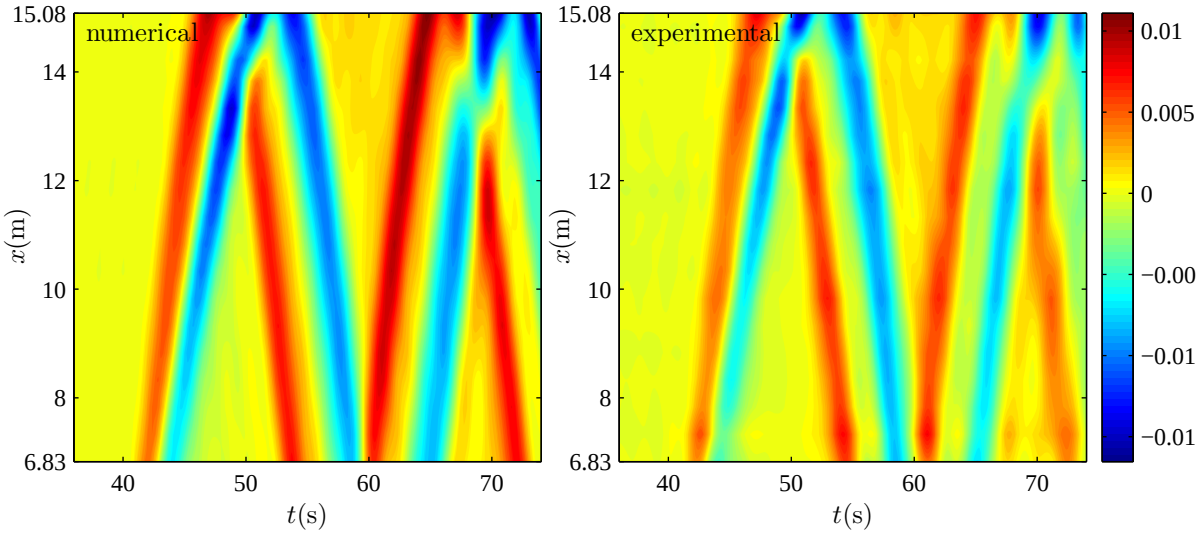

Figure 5.24: NewWave overtopping a seawall for the addition of crest- and trough-focused wave groups (WG4 and WG8). **Long waves** only - addition time series low-pass filtered at 0.5 Hz. Model predictions shown in the left plot. UKCRF measurements shown in the right plot.

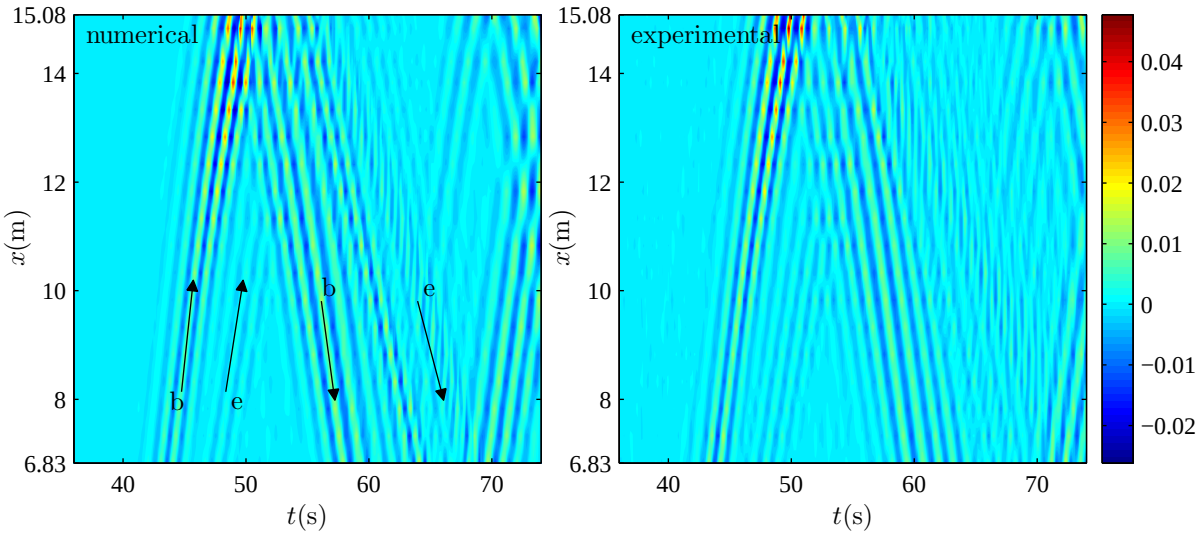

Figure 5.25: NewWave overtopping a seawall for the addition of crest- and trough-focused wave groups (WG4 and WG8). **Even order super-harmonics** only - addition time series high-pass filtered at 0.5 Hz. Model predictions shown in the left plot. UKCRF measurements shown in the right plot.

Figure 5.26 provides an explicit comparison between the numerical and experimental time series at 6 different locations, starting at the beach toe ($x = 8.33$ m) and finishing at the seawall crest ($x = 17.12$ m). For reference, the 6 chosen gauge locations have been highlighted, by bold lines, in Figure 5.21. The initial stages of group propagation appear to be well captured by the model. Agreement during the breaking process is not particularly good, but the broken waves are modelled relatively well. Water elevation on the seawall crest associated with overtopping flow is captured in the bottom plots. The initial overtopping (resulting from the central crest for the WG4 crest-focused wave group; and from the left crest for the WG8 trough-focused wave group) is satisfactorily predicted. However, any subsequent overtopping is much less accurately forecast by the model. Note that the model prediction of overtopping volume (per unit length of the seawall) is the worst for the pair WG4 and WG8, as can be seen in Table 5.3. The maximum error in overtopping volume prediction is about 43 %, whereas the average error (for the 8 simulations) is about 14 %. Values in Table 5.3 represent the overall overtopped volumes (per unit length of the seawall) after 90 s, and therefore in some cases contain additional overtopping from re-reflected waves. It should also be noted that the inferred experimental error in the measured values of overtopping volume is about 5 %. This was calculated from repeat measurements of volumes from this experimental program.

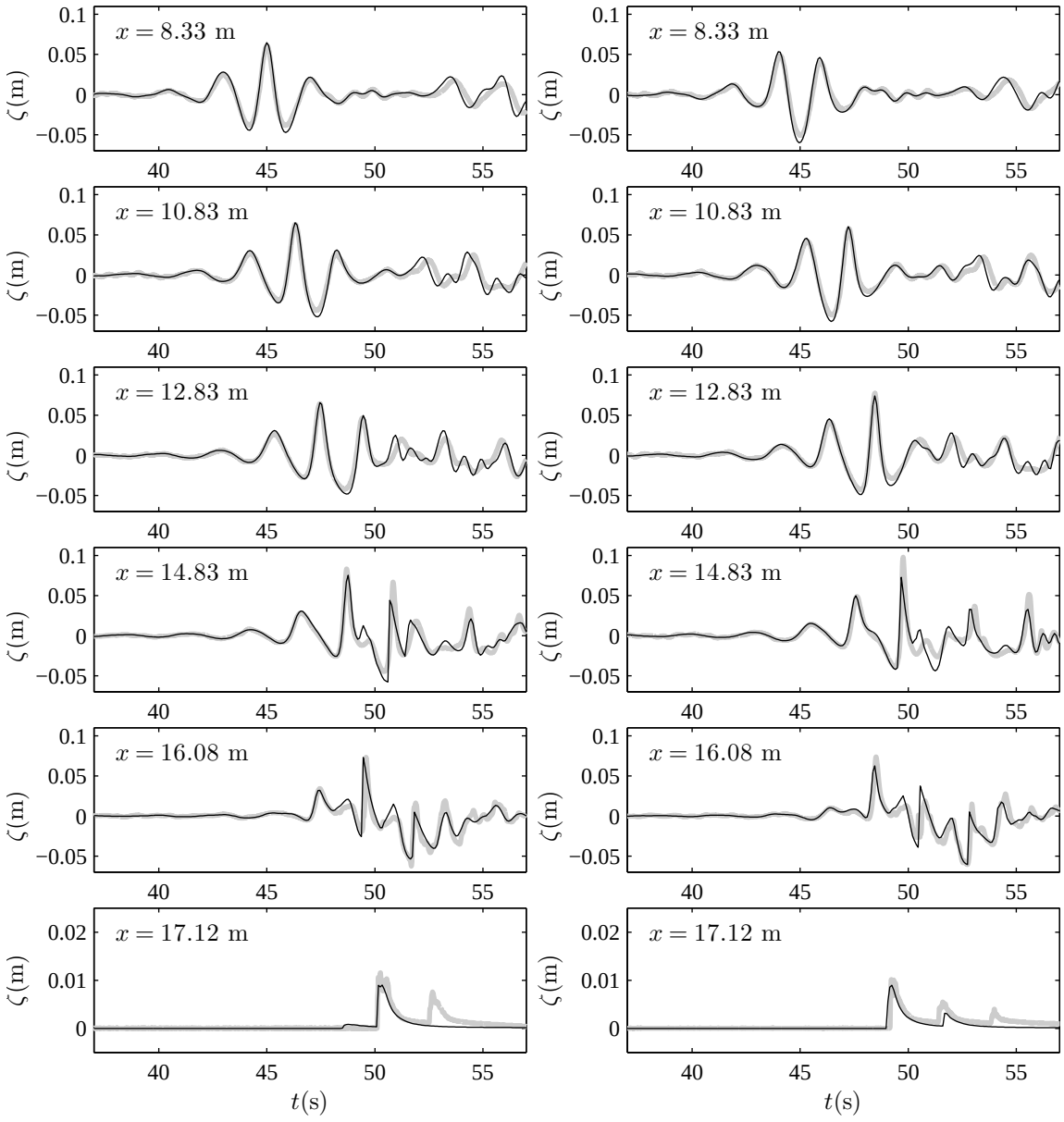

Figure 5.26: NewWave overtopping a seawall, with the WG4 crest-focused wave shown on the left and the WG8 trough-focused wave shown on the right. Free surface time series comparison between the model predictions (thin black line) and the UKCRF measurements reported by Hunt (2003) (thick grey line). Note the vertical scale for the gauge located on top of the seawall (bottom plot) is magnified.

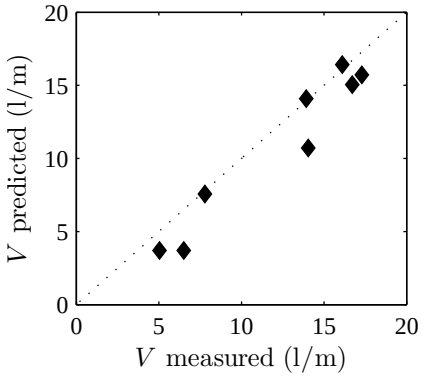

Wave group	V measured (l/m)	V predicted (l/m)	% error
WG1	16.10	16.41	1.9
WG2	13.92	14.10	1.3
WG3	7.78	7.57	-2.7
WG4	6.51	3.71	-43.0
WG5	16.71	15.05	-9.9
WG6	17.29	15.71	-9.1
WG7	14.05	10.71	-23.7
WG8	5.04	3.70	-26.6

Figure 5.27 and Table 5.3: NewWave overtopping volume per unit length of the seawall. Comparison between the model predictions and the UKCRF measurements reported by Hunt (2003).

Figure 5.28 displays the water elevation on the seawall crest associated with the overtopping flow for all the 8 NewWave tests and allows for a visual comparison of wave-by-wave overtopping. In all cases, the model captures the main features of the overtopping flow, but at times fails to predict some of the smaller successive overtopping events. As shown in Table 5.3 and Figure 5.27, the large volume overtopping cases are well predicted numerically, with the biggest percentage errors occurring for the smaller overtopping groups.

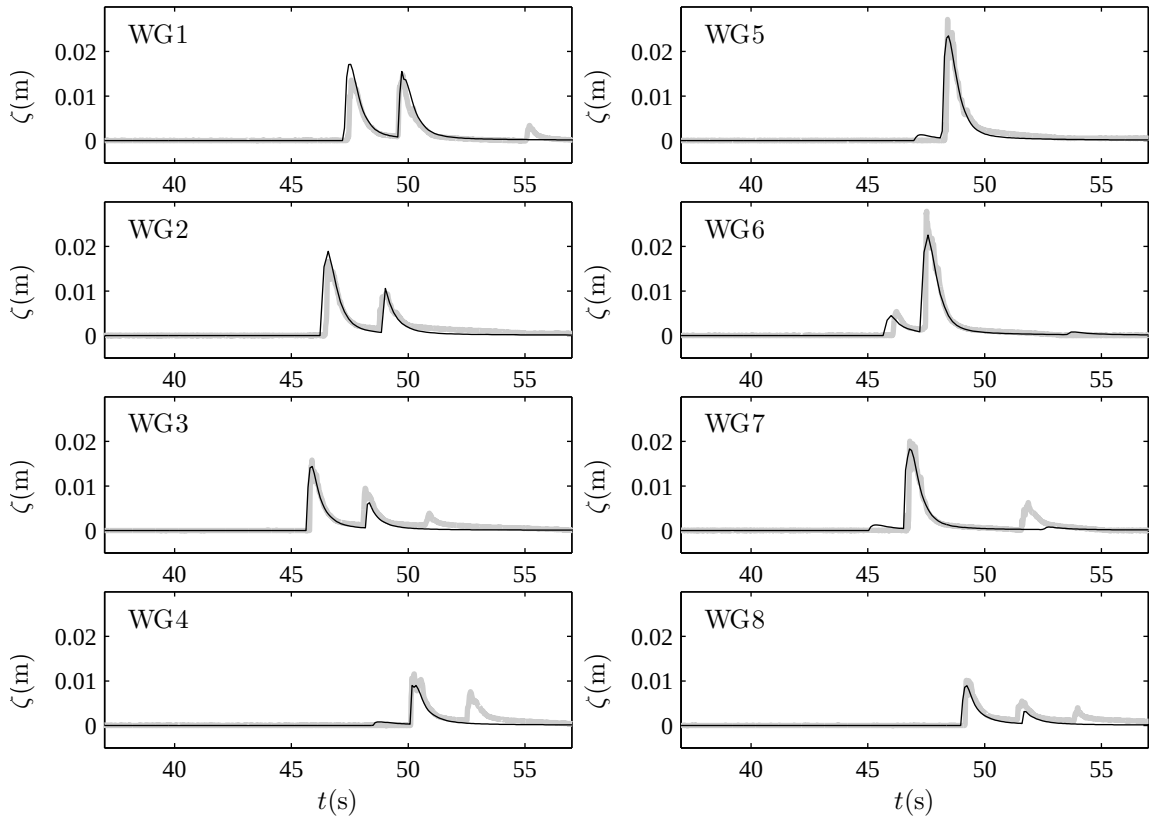

Figure 5.28: NewWave overtopping a seawall. Time variation of the water elevation on the seawall crest ($x = 17.12$ m) associated with the overtopping flow for all 8 NewWave groups. Comparison between the model predictions (thin black line) and the UKCRF measurements reported by Hunt (2003) (thick grey line).

5.5 NewWave run-up revisited with second order paddle signals

The influence of the spurious error waves on the run-up of NewWave focused wave groups is investigated numerically. The error waves have been described in previous sections: a low-frequency hump travelling ahead of the main group and high-frequency waves trailing the main group. As shown in Section 5.2 the long second order error wave can be almost completely eliminated and the second order sum frequency error waves can be partially weakened by the use of a second order paddle displacement signal calculated according to Schäffer (1996). The 8 run-up simulations involving NewWave groups, as presented in Table 5.1, are reproduced again, this time using paddle signals correct to second order.

Figures 5.29 to 5.34 present a comparison between using a first (left plot) and a second order paddle signal (right plot) for wave groups WG2 and WG6. Each figure

comprises an $x - t$ contour plot of the numerically calculated free surface deviation from still water depth. The figures are centred on the propagating wave group to investigate the effect of the error waves on the resulting wave form, which ultimately influences the run-up distance.

Figure 5.29 shows the $x - t$ propagation of the WG2 crest-focused group. The difference between using a first and a second order paddle signal is evident. In the first order case, the left crest is much more pronounced throughout the entire record and breaks further inshore. The central crest, similarly, is higher in the first order case, and propagates further up the beach. The right crest and the high frequency waves trailing the main group do not appear to be significantly affected by the use of the second order paddle signal.

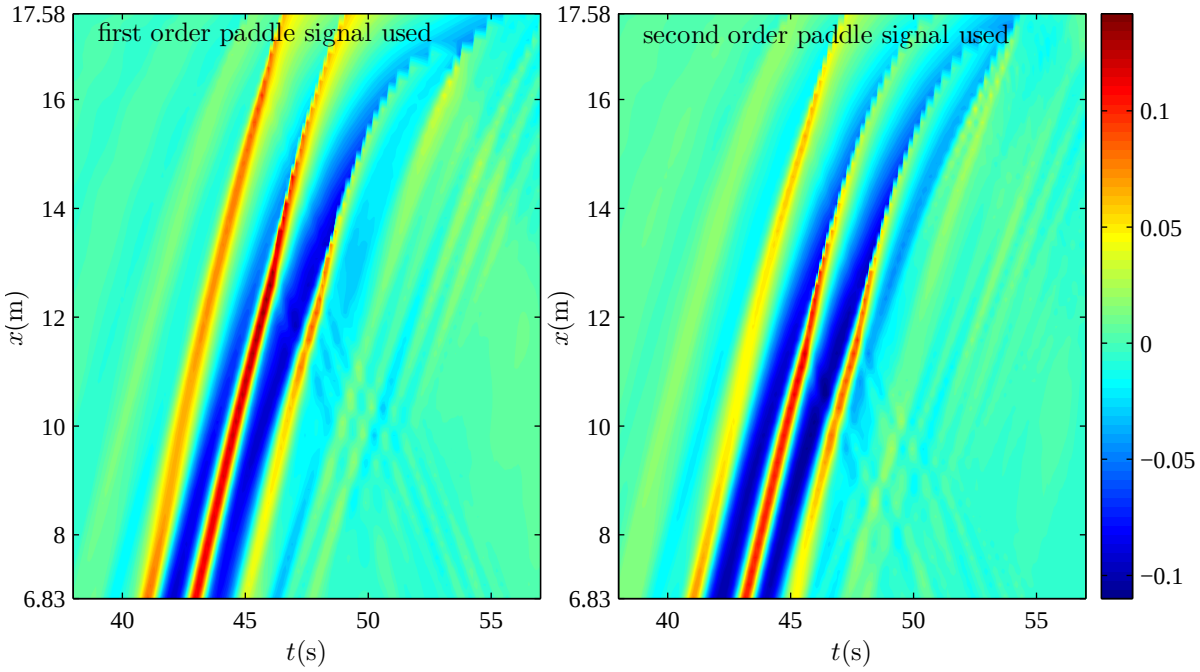

Figure 5.29: NewWave run-up on a plane beach for the WG2 crest-focused wave group. Calculated **total free surface** time series using a first order paddle signal (left plot) and a second order paddle signal (right plot).

Figure 5.30 shows the stacked time series for the WG6 trough-focused group. The two wave profiles are again visibly different. The left trough in the second order case is more pronounced. In the first order case, the left crest is notably higher, propagates and breaks further inshore on the beach. Also, the central trough appears marginally deeper and the right crest appears to break slightly earlier in the second order case.

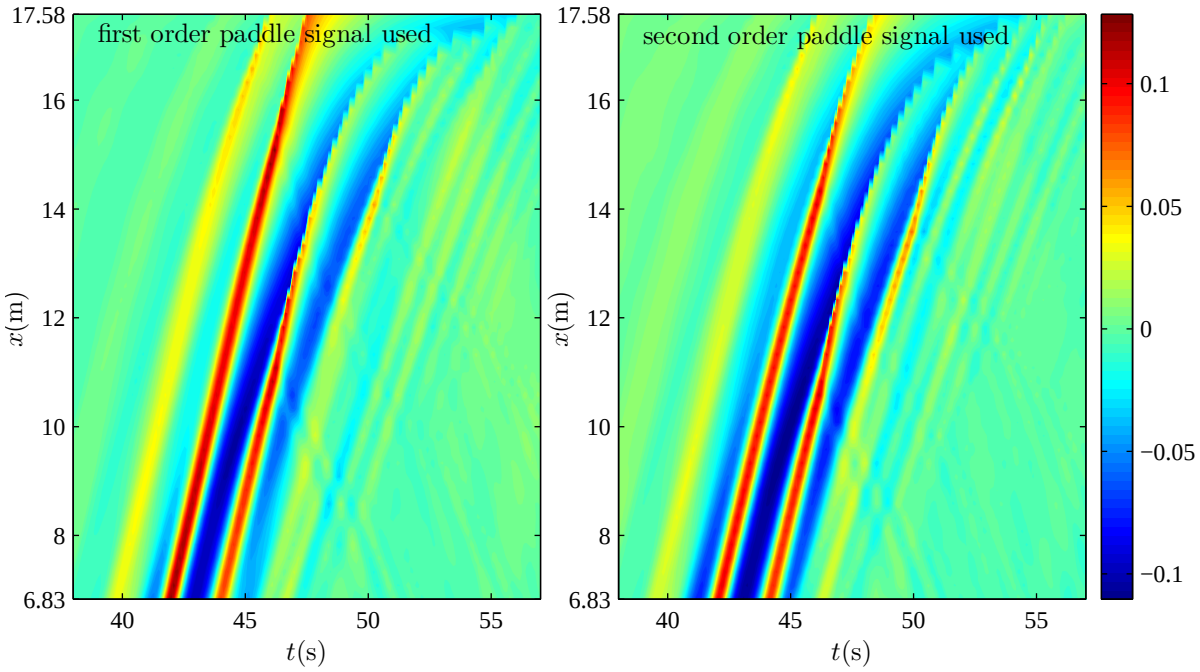

Figure 5.30: NewWave run-up on a plane beach for the WG6 trough-focused wave group. Calculated **total free surface** time series using a first order paddle signal (left plot) and a second order paddle signal (right plot).

As already discovered in Section 5.2, there are obvious visual differences between the numerical simulations of nominally the same wave group caused by using second order instead of linear wave generation. These differences are much greater than those discussed earlier between simulations and physical experiments, and are now explored in detail using addition, subtraction and frequency filtering.

Figure 5.31 shows the free surface subtraction time series, low-pass filtered at 1 Hz to isolate the linear terms. The two contour plots are very similar, confirming that the second order correction to the paddle signal does not alter the linear free waves, as of course it should not.

Figure 5.32 shows the free surface addition time series, low-pass filtered at 0.5 Hz, to extract the long wave components. Use of the second order paddle signal has a profound effect on the long waves. The free wave, previously travelling ahead of the group, is eliminated when second order signal is used. The bound long wave can now be clearly seen as a depression underneath the main wave packet. It is clear that the pronounced left crests and flatter left troughs observed in the first order cases in Figures 5.29 and 5.30 were due to the spurious long wave hump.

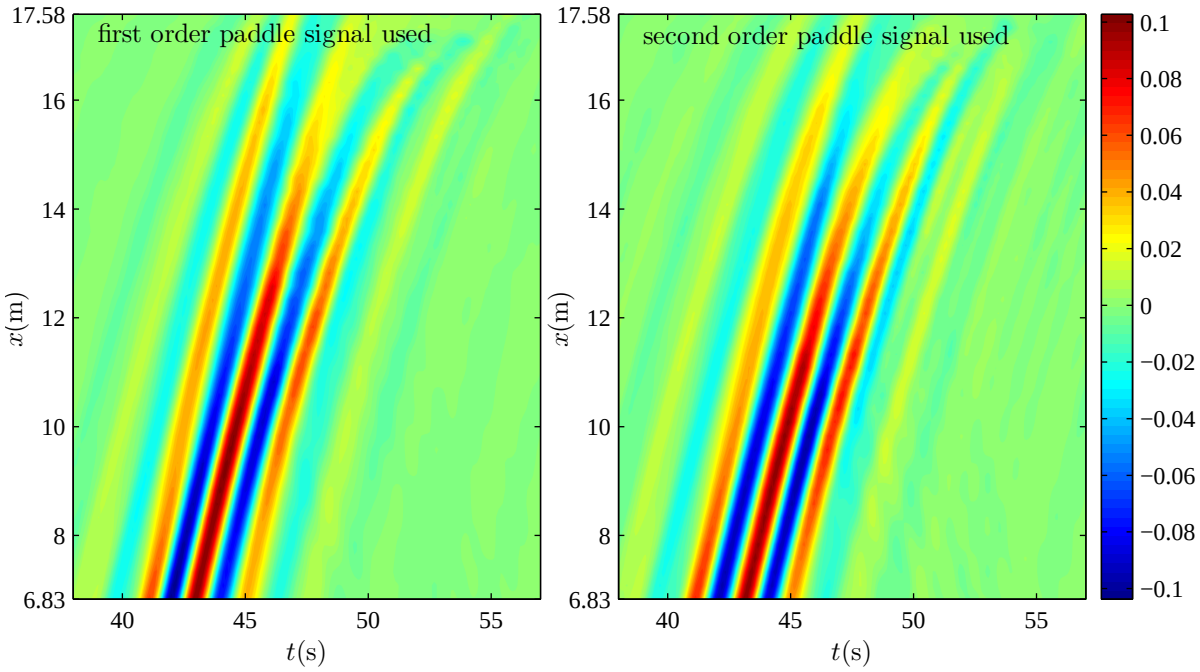

Figure 5.31: NewWave run-up on a plane beach for the subtraction of crest- and trough-focused wave groups (WG2 and WG6). **Linear terms** only - subtraction time series low-pass filtered at 1 Hz. Model predictions using a first order paddle signal shown in the left plot. Model predictions using a second order paddle signal shown in the right plot.

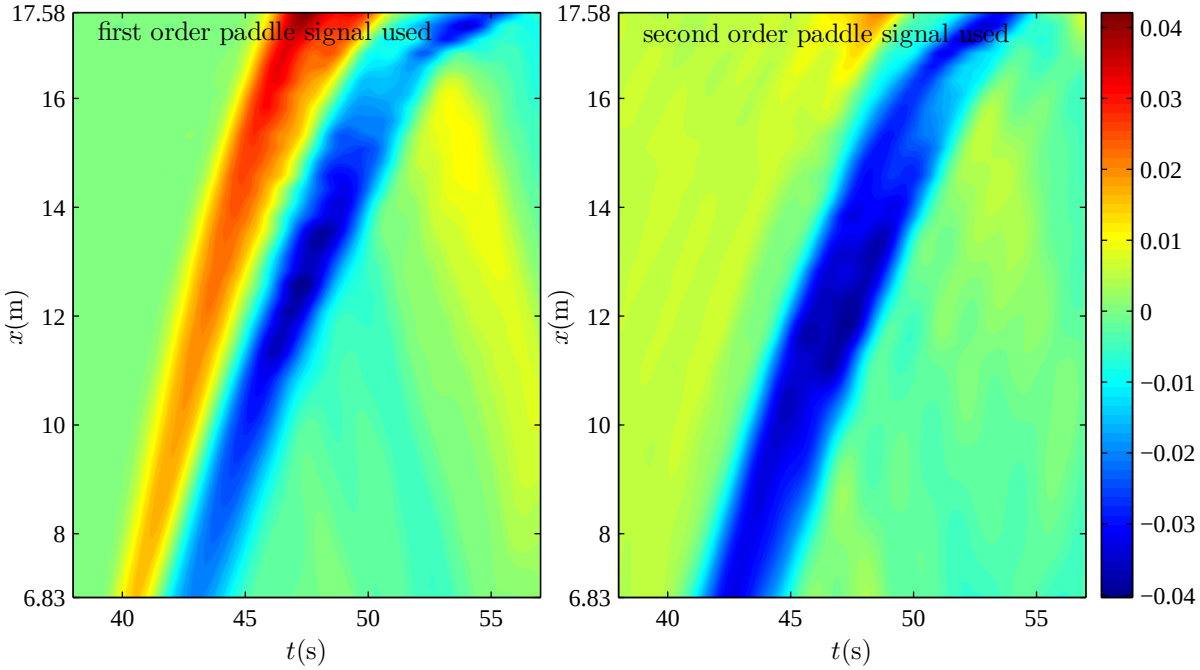

Figure 5.32: NewWave run-up on a plane beach for the addition of crest- and trough-focused wave groups (WG2 and WG6). **Long waves** only - addition time series low-pass filtered at 0.5 Hz. Model predictions using a first order paddle signal shown in the left plot. Model predictions using a second order paddle signal shown in the right plot.

Figure 5.33 displays the free surface addition time series, high-pass filtered at 0.5 Hz. The double frequency waves are visible. The second order paddle signal fails to sufficiently eliminate the error super-harmonics, which can be seen in both plots trailing the main group. As explained in Section 5.2 this may be because the second order wavemaker theory from Schäffer (1996) is based on solutions to the full Laplace equation water wave problem rather than the shallow water Boussinesq equation set of Madsen and Sørensen (1992).

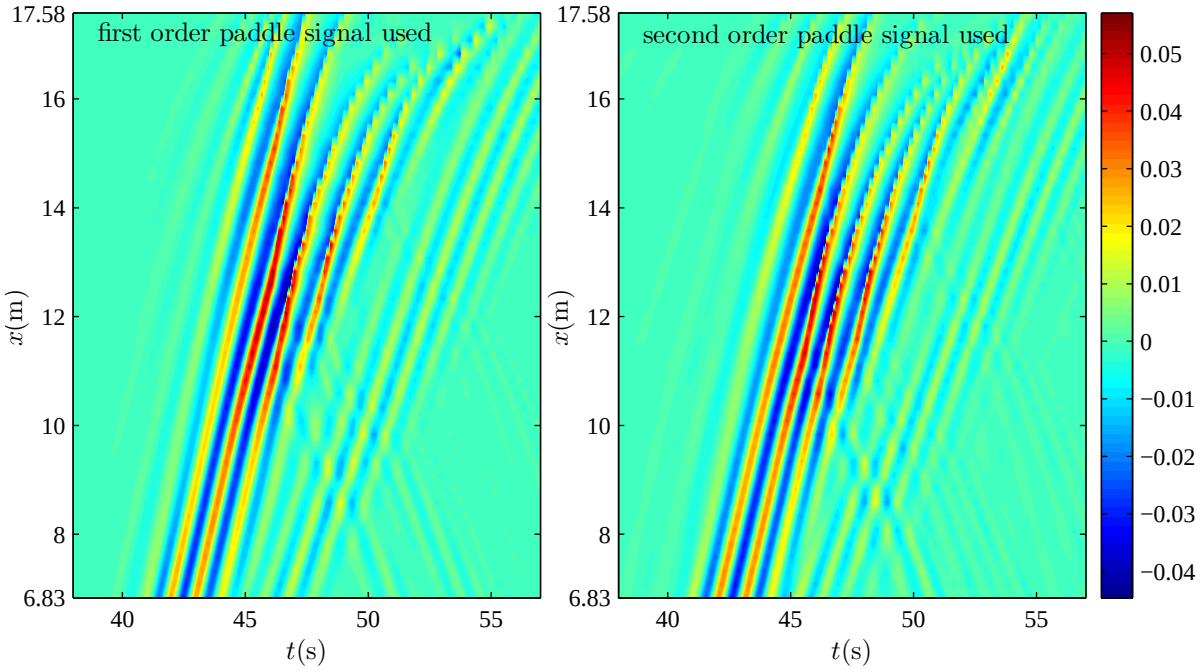

Figure 5.33: NewWave run-up on a plane beach for the addition of crest- and trough-focused wave groups (WG2 and WG6). **Even order super-harmonics** only - addition time series high-pass filtered at 0.5 Hz. Model predictions using a first order paddle signal shown in the left plot. Model predictions using a second order paddle signal shown in the right plot.

Figure 5.34 shows the free surface subtraction time series, high-pass filtered at 1 Hz to isolate the third order super-harmonics (and any other higher order odd harmonics). The two plots appear similar, suggesting that the use of second order paddle signal does not significantly alter the third harmonic structure of the wavefield.

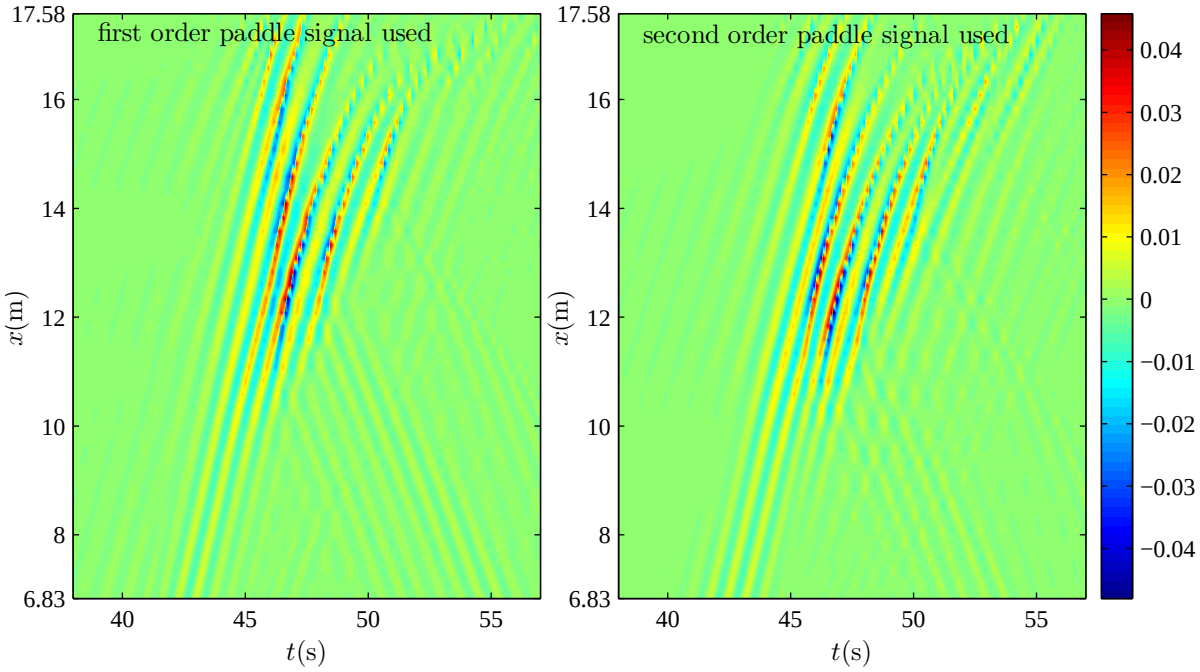

Figure 5.34: NewWave run-up on a plane beach for the subtraction of crest- and trough-focused wave groups (WG2 and WG6). **Odd order super-harmonics** only - subtraction time series high-pass filtered at 1 Hz. Model predictions using a first order paddle signal shown in the left plot. Model predictions using a second order paddle signal shown in the right plot.

Figure 5.35 presents free surface time series at 5 different locations along the beach when using first and second order paddle signals. The WG2 crest-focused wave group is shown on the left, and the WG6 trough-focused group on the right. Evolution of the groups resulting from using a first order signal and a second order signal are plotted simultaneously to allow for a comparison. Additionally, the measured time series from experiments using first order paddle signals are also displayed. Locations of the 5 chosen time series can be seen in Figure 5.12. When using a second order signal, the crest-focused wave group at the first two locations has a smaller left crest and deeper left and right troughs. Also, the crests appear to be delayed, when compared to the first order case, in which the wave group is deformed by the long error wave. As the group propagates further up the beach, the left crest is consistently smaller and the central crest breaks earlier. For this reason, in the second order case, the waves reaching the top of the beach are considerably smaller. This leads to a reduced run-up as shown in Table 5.4. The trough-focused wave group generated with a second order paddle signal also exhibits deeper troughs and delayed crests. The left crest,

which in the first order case leads to the maximum run-up, is smaller throughout the propagation process, resulting in a much shorter run-up distance.

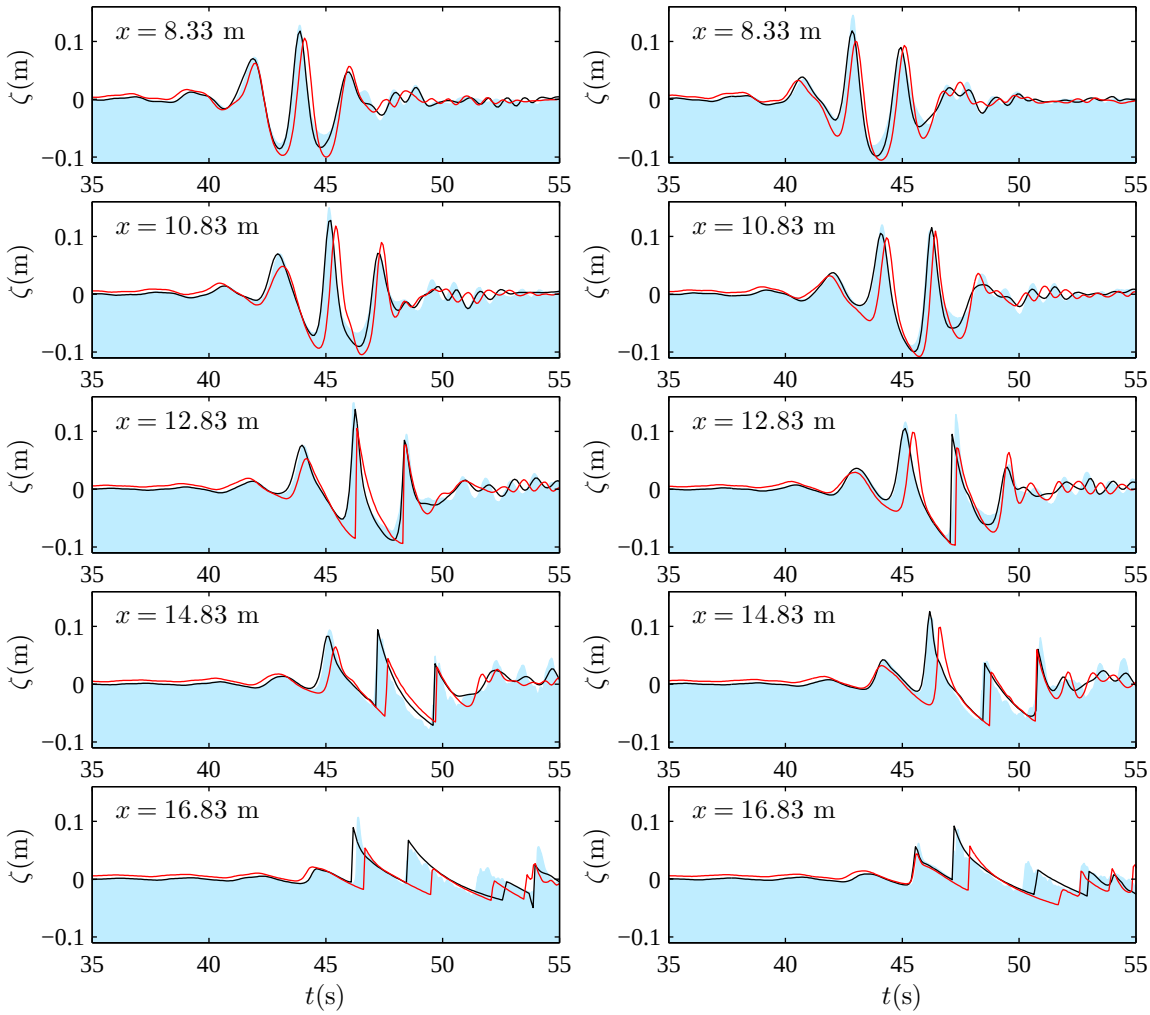

Figure 5.35: NewWave run-up on a plane beach, with the WG2 crest-focused wave shown on the left and the WG6 trough-focused wave shown on the right. Free surface time series comparison between the model predictions when using a first order paddle signal (black line) and a second order paddle signal (red line). For reference, the measured free surface time series, from experiments using first order paddle signals, are plotted in blue.

Table 5.4 summarises the horizontal run-up values for the 8 NewWave focused wave groups. The calculated run-up resulting from using second order paddle displacement signals is compared to the measured and calculated run-up from using first order paddle signals. The run-up values from simulations with the corrected paddle signals are on average around 40 % smaller. This is a significant difference, even when the imperfections of the present numerical model are taken into account, as can be clearly seen in Figure 5.36. For reference, as shown in Section 5.3, the average error

(for the 8 cases) between the numerical simulation and the physical experiment for the prediction of run-up values using first order paddle signals was 6 %. Clearly, as a simulation of what happens in the field, wave groups driven by linear paddle signals leave much to be desired.

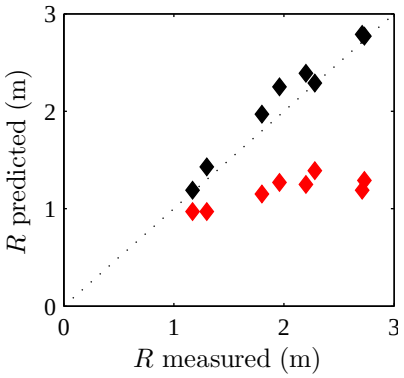

Wave group	Horizontal R (m) using 1st order x_p measured, predicted	Horizontal R (m) using 2nd order x_p predicted	predicted % difference between using 1st and 2nd order x_p
WG1	1.96, 2.25	1.27	-43.6
WG2	2.20, 2.39	1.25	-47.7
WG3	1.80, 1.97	1.15	-41.6
WG4	1.17, 1.19	0.97	-18.5
WG5	2.71, 2.79	1.19	-57.3
WG6	2.73, 2.77	1.29	-53.4
WG7	2.28, 2.29	1.39	-39.3
WG8	1.30, 1.43	0.97	-32.2

Figure 5.36 and Table 5.4: Horizontal run-up of NewWave. Comparison between using first and second order paddle displacement signals. In the Figure, black markers denote predicted run-up values using first order paddle signals; and red markers denote predicted run-up values using second order paddle signals.

5.6 NewWave overtopping revisited with second order paddle signals

The effect of the second order error waves on overtopping volumes is investigated numerically. The 8 NewWave overtopping simulations are repeated with second order paddle displacement signals. Note in passing that similar amounts of numerical filtering are applied, as discussed in Section 5.4. Figures 5.37 to 5.42 present comparisons of the resulting wave groups generated by the first order signals and the second order signals. These are $x-t$ contour plots (composed of stacked time series from different

locations along the beach) for wave groups WG1 and WG5. Since only numerical data are shown, there are no restrictions on data availability imposed by sparse wave gauge spacing. For this reason, the number of the displayed time series can be greatly increased to improve the resolution of the plots and to avoid the artificial modulation encountered in Figures 5.22 to 5.25.

Figure 5.37 shows the evolution of the WG1 crest-focused wave group. The difference between using a first and a second order paddle signal is apparent. When using a second order signal, the left crest is smaller and the central crest breaks further offshore. Also, the left and the right troughs are deeper. At the last location shown ($x = 15.08$ m), which is 1.375 m offshore of the seawall, the wave group generated by the second order signal is considerably smaller.

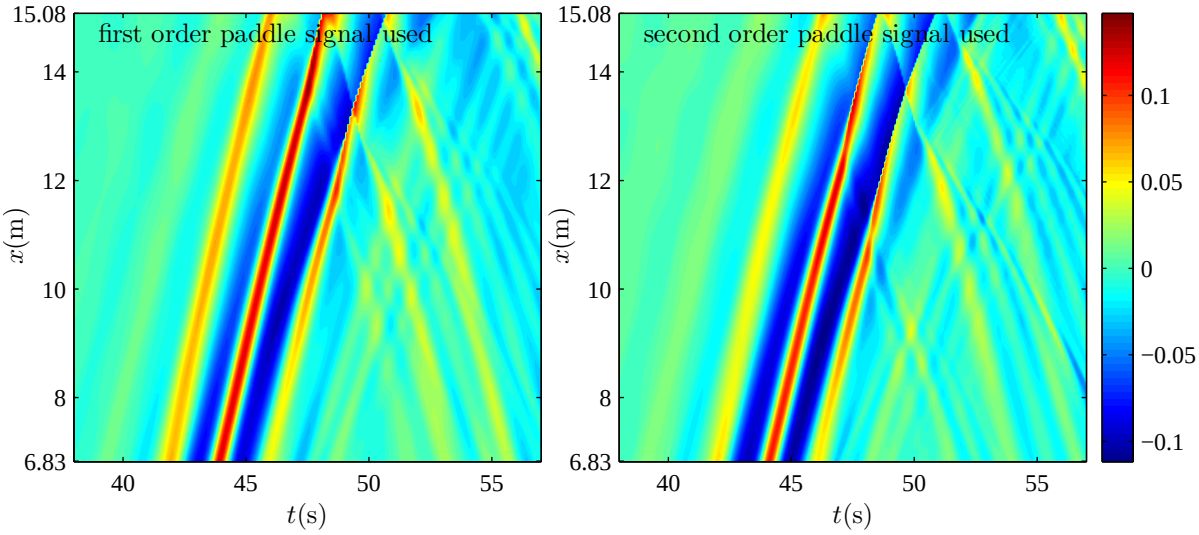

Figure 5.37: NewWave overtopping a seawall for the WG1 crest-focused wave group. Calculated **total free surface** time series using a first order paddle signal (left plot) and a second order paddle signal (right plot).

Figure 5.38 shows the $x - t$ propagation of the WG5 trough-focused wave group. The second order paddle signal results in a wave form with deeper troughs (left, central and right) and lower crests (left and right). Complex interference patterns between the incoming and the reflected waves can be seen in both plots.

Figure 5.39 shows the free surface subtraction time series, low-pass filtered at 1 Hz, to extract the linear components. As expected, the two contour plots exhibit very similar patterns.

Figure 5.40 shows the free surface addition time series, low-pass filtered at 0.5 Hz, to isolate the long wave components. Similarly to the run-up case, the long error wave is eliminated when the second order paddle signal is used. However, a low positive

elevation, shown in orange, can be seen far ahead of the bound long wave. This is a result of the gentle forward motion of the paddle prior to generating the main wave packet (for reference see the second order paddle displacement signal in Figure 5.1), which is due to the finite repeat length of the signal. Since this build up of fluid is very small, it is believed not to affect subsequent overtopping volumes.

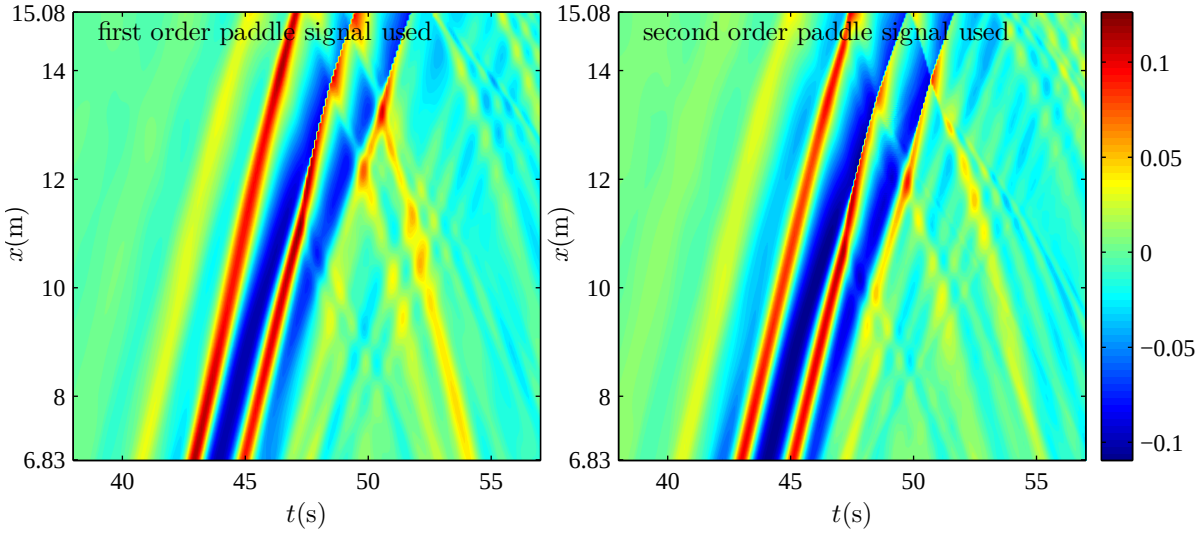

Figure 5.38: NewWave overtopping a seawall for the WG5 trough-focused wave group. Calculated **total free surface** time series using a first order paddle signal (left plot) and a second order paddle signal (right plot).

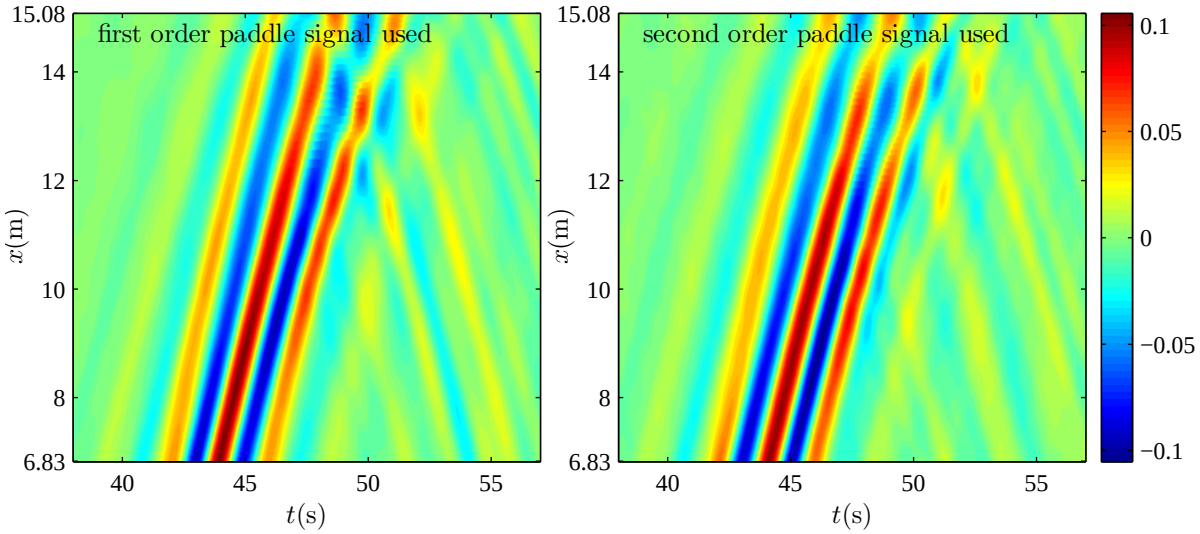

Figure 5.39: NewWave overtopping a seawall for the subtraction of crest- and trough-focused wave groups (WG1 and WG5). **Linear terms** only - subtraction time series low-pass filtered at 1 Hz. Model predictions using a first order paddle signal shown in the left plot. Model predictions using a second order paddle signal shown in the right plot.

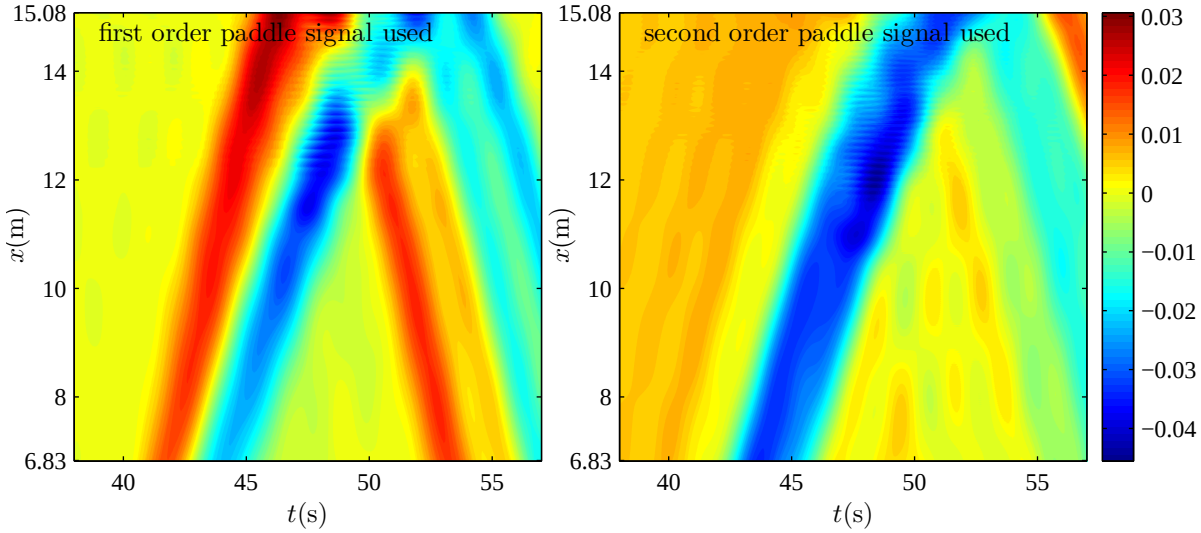

Figure 5.40: NewWave overtopping a seawall for the addition of crest- and trough-focused wave groups (WG1 and WG5). **Long waves** only - addition time series low-pass filtered at 0.5 Hz. Model predictions using a first order paddle signal shown in the left plot. Model predictions using a second order paddle signal shown in the right plot.

Figure 5.41 displays the free surface addition time series, high-pass filtered at 0.5 Hz, to separate the double frequency waves. The use of the second order paddle signal does not suppress the free error super-harmonics, as they can be seen following the ingoing bound waves in both plots.

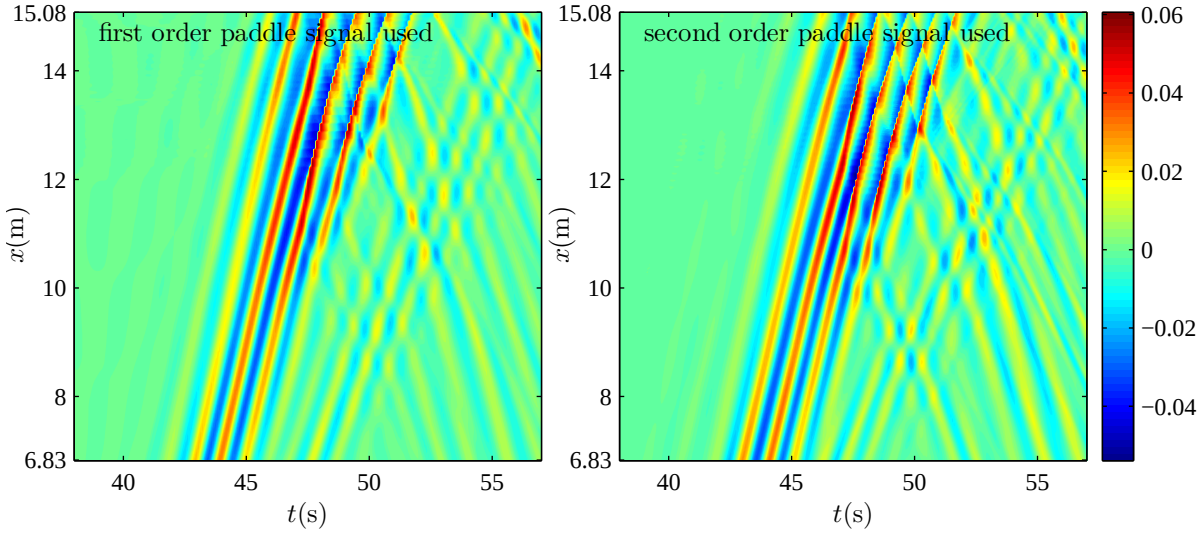

Figure 5.41: NewWave overtopping a seawall for the addition of crest- and trough-focused wave groups (WG1 and WG5). **Even order super-harmonics** only - addition time series high-pass filtered at 0.5 Hz. Model predictions using a first order paddle signal shown in the left plot. Model predictions using a second order paddle signal shown in the right plot.

Figure 5.42 shows the free surface subtraction time series, high-pass filtered at

1 Hz. The triple frequency waves are clearly visible. The two plots seem similar, with the bound third harmonics becoming more obvious in the upper half of the beach. It is difficult to see on the shown scale, but in the second order case, there appear to be triple frequency waves trailing the bound waves.

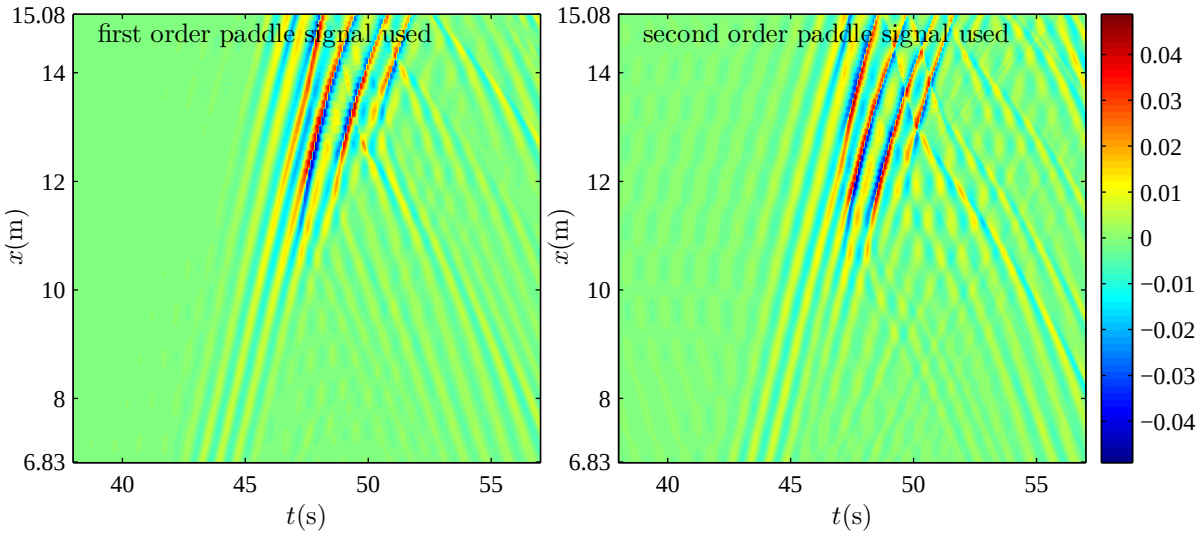

Figure 5.42: NewWave overtopping a seawall for the subtraction of crest- and trough-focused wave groups (WG1 and WG5). **Odd order super-harmonics** only - subtraction time series high-pass filtered at 1 Hz. Model predictions using a first order paddle signal shown in the left plot. Model predictions using a second order paddle signal shown in the right plot.

Figure 5.43 presents a more direct comparison between using first and second order paddle signals. Free surface time series (at 6 different locations) of the WG1 crest-focused wave group are shown on the left, and of the WG5 trough-focused group on the right. For reference, the 6 chosen locations have been highlighted, using bold lines, in Figure 5.21. For each wave group, numerical results when using a second order paddle signal, and numerical and experimental results when using a first order paddle signal are plotted. When using a second order signal, the crest-focused wave group has deeper troughs. At all shown locations, the left crest is smaller. The central crest looks narrower and delayed, when compared to the first order case. It breaks earlier. At the location $x = 16.08$ m, which is 0.375 m offshore of the seawall, the waves are significantly lower in the second order case, ultimately leading to a limited overtopping flow over the seawall (see the location $x = 17.12$ m which is on the seawall crest). The trough-focused wave group generated with a second order paddle signal also exhibits delayed crests and deeper troughs. The left crest is thinner (meaning it contains less volume) and breaks considerably earlier. Understandably,

it results in a much lower overtopping surge over the seawall. For both wave groups, the underlying long error wave, when using first order paddle signals, greatly deforms the wave groups and produces much larger overtopping.

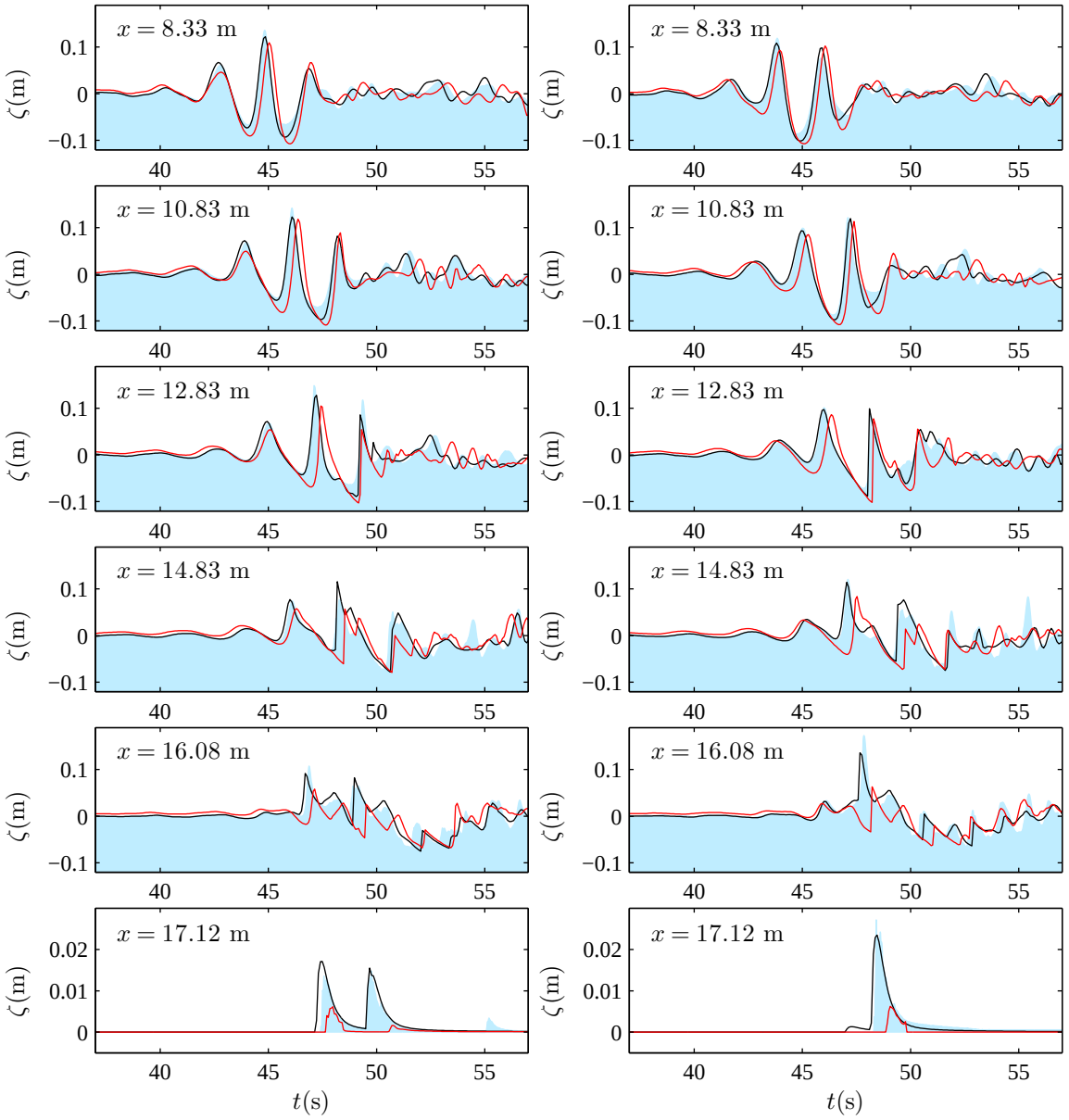

Figure 5.43: NewWave overtopping a seawall, with the WG1 crest-focused wave shown on the left and the WG5 trough-focused wave shown on the right. Free surface time series comparison between the model predictions when using a first order paddle signal (black line) and a second order paddle signal (red line). For reference, the measured free surface time series, from experiments using first order paddle signals, are plotted in blue.

Figure 5.44 displays the wave-by-wave overtopping flow at the seawall crest for all the 8 NewWave tests. For each wave group, numerical results when using a second

order paddle signal, and numerical and experimental results when using a first order paddle signal are plotted. It is clear that when using second order paddle signals, which eliminate the long error wave, the overtopping flow is substantially smaller.

Table 5.5 summarises the overtopping volume per unit length of the seawall for the 8 NewWave focused wave groups. The predicted volumes resulting from using second order paddle displacement signals are compared to the measured and calculated volumes from using first order paddle signals. The volumes from simulations with the corrected paddle signals are on average 60-70 % smaller (depending on whether the comparison is performed against first order numerical or experimental volumes). From Figure 5.45 it is apparent that, when second order paddle signals are used, there is much less variation in the resulting overtopping volumes amongst the 8 wave groups .

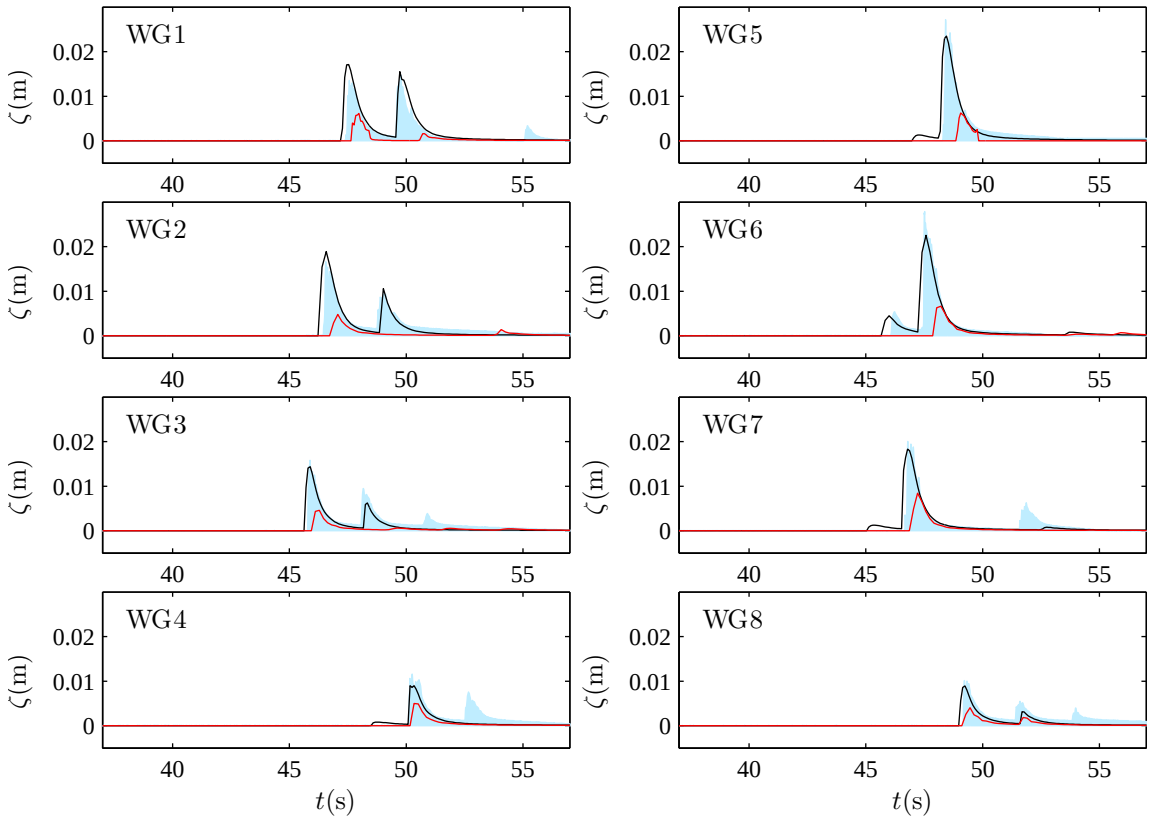

Figure 5.44: NewWave overtopping a seawall. Time variation of the water elevation on the seawall crest (x = 17.12 m) associated with the overtopping flow for all 8 NewWave groups. Comparison between the calculated overtopping when using a first order paddle signal (black line) and a second order paddle signal (red line). For reference, the measured free surface time series, from experiments using first order paddle signals, is plotted in blue.

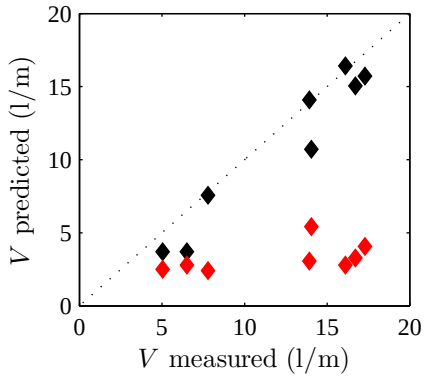

Wave group	Overtopping V (l/m) using 1st order x_p measured, predicted	Overtopping V (l/m) using 2nd order x_p predicted	% difference between using 1st and 2nd order x_p
WG1	16.10, 16.41	2.79	-82.7, -83.0
WG2	13.92, 14.10	3.07	-77.9, -78.2
WG3	7.78, 7.57	2.41	-69.0, -68.1
WG4	6.51, 3.71	2.79	-57.2, -24.8
WG5	16.71, 15.05	3.28	-80.4, -78.2
WG6	17.29, 15.71	4.07	-76.4, -74.1
WG7	14.05, 10.71	5.43	-61.4, -49.3
WG8	5.04, 3.70	2.51	-50.2, -32.2

Figure 5.45 and Table 5.5: NewWave overtopping volume per unit length of the seawall. Comparison between using first and second order paddle displacement signals. In the Figure, black markers denote predicted volumes using first order paddle signals; and red markers denote predicted volumes using second order paddle signals.

5.7 Chapter summary

- Validation of the numerical model against laboratory experiments involving NewWave focused wave group run-up on a plane beach and overtopping of a laboratory seawall, with very close agreement in prediction of run-up distances and a reasonable agreement in prediction of overtopping volumes.

- Implementation of second order paddle displacement signals according to Schäffer (1996) with successful elimination of second order long error wave and partial suppression of second order sum frequency error waves.

- Investigation of the effect of second order error waves on NewWave focused wave group run-up distances and overtopping volumes leading to conclusions that the error waves significantly increase run-up and overtopping due to the presence of the long error wave ahead of the main group.

- For realistic simulation of incoming waves in the field, the use of second order paddle signals is essential. In order to prevent the released reflected long wave from re-reflecting at the paddles back into the flow, active absorption of long waves at the paddle is also required, unless very short experimental runs such as those involving NewWave focused wave groups are being carried out.

Chapter 6

Parameter study of run-up from NewWave groups

In this chapter a parameter study of NewWave focused wave group run-up is carried out using the numerical model. The effect of three parameters is examined: linear focus amplitude $A_{\mathcal{N}}$, linear focus location x_f, and phase angle of the group at focus ϕ. The study investigates the general sensitivity of the wave group run-up to the three varying parameters, and also identifies circumstances leading to extreme run-up events.

6.1 Parameter study setup

The parameter study builds upon results from Chapter 5, where the NewWave run-up laboratory experiments of Hunt (2003) and their subsequent reproduction with the numerical model are presented. The same bathymetry setup is therefore utilised here, with 8.33 m of flat bed followed by a plane 1 : 20 beach. The still water depth is kept at 0.5 m. The underlying Pierson-Moskowitz type wave energy spectrum, from which the studied NewWave groups are derived, is also retained, and is given by Equation (5.5). Five different linear focus amplitudes $A_{\mathcal{N}}$, ranging from 0.0285 m to 0.1425 m, are selected. For each of these, a high resolution full phase ϕ variation for eleven different focus locations x_f is carried out. In total, there are 1980 cases considered. Table 6.1 summarises the parameter values investigated.

Table 6.1: Chosen values of the linear focus amplitude $A_{\mathcal{N}}$, the linear focus location x_f and the group phase at focus ϕ for the parameter study.

Parameter	Values
$A_{\mathcal{N}}$ (m)	0.0285, 0.0570, 0.0855, 0.114, 0.1425
x_f (m) relative to the paddles	5.83, 8.33, ... increasing by 2.5 ..., 28.33, 30.83
relative to the beach toe	-2.5, 0, ... increasing by 2.5 ..., 20, 22.5
relative to the shoreline	-12.5, -10, ... increasing by 2.5 ..., 10, 12.5
ϕ (degrees)	10, 20, ... increasing by 10 ..., 350, 360

Figure 6.1 illustrates the setup for the parameter study simulations. The investigated linear focus locations x_f are indicated. Note that several of these are beyond the initial shoreline position on the dry beach. Of course, in such cases, the wave group will never actually focus, and no waves may ever reach the focus location due to the presence of the beach. This does not matter for the purpose of the parameter study. As explained in Section 5.1, the NewWave theory gives the expected shape of an extreme event. Such an event, created by individual wave components coming into phase at one point in time and space, is equally likely to occur at any location in the domain. The focus location is simply a free parameter and the whole purpose of the parameter study is to investigate the dependence of run-up on choice of linear focus location.

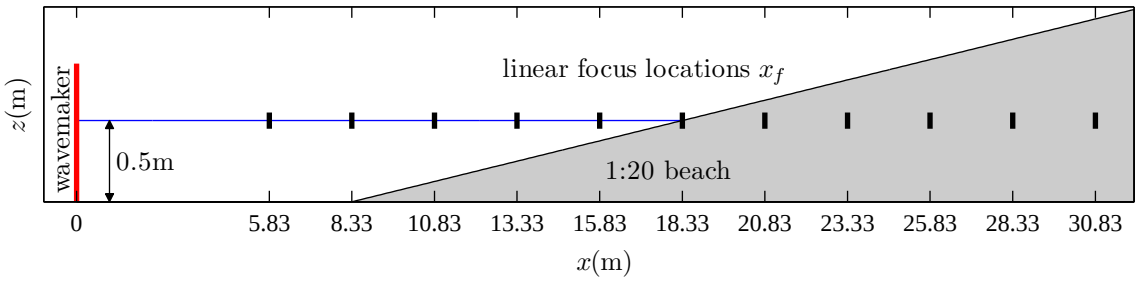

Figure 6.1: Setup for the NewWave parameter study investigating run-up on a plane beach. The chosen focus locations x_f are shown by vertical marks.

Each of the tests summarised in Table 6.1 is simulated with the numerical model on a computational grid of resolution $\Delta x = 2$ cm. Each simulation is run for 65 s with time step of $\Delta t = 0.007$ s. Each run takes about 5 minutes to complete on a standard PC (Intel Xeon 2.93 GHz processor, 6 GB RAM) so the entire parameter study can be completed in a week using a single PC. Use of parallel processing by employing multiple machines, since the individual runs are independent of each other, would of course reduce the completion time.

As demonstrated in Chapter 5, the use of second order paddle signals for wave generation is crucial for trustworthy run-up and overtopping investigations involving focused wave groups. For this reason, in this parameter study all paddle signals are calculated according to the second order wavemaker theory of Schäffer (1996). The calculated paddle signals for $-45 \text{ s} \leq t \leq 20 \text{ s}$ (assuming focus time $t_f = 0$ s) are fed into the numerical model. Figure 6.2 provides an example of such paddle displacement time series for a family of NewWave groups with $A_{\mathcal{N}} = 0.0855$ m, $x_f = 15.83$ m over the full variation in phase ϕ. Each curve (corresponding to a different value of the group phase at focus ϕ) is plotted in a different shade of grey, with smaller values of ϕ plotted in darker colour. Also, the crest-focused ($\phi = 0 \equiv 2\pi$), the trough-focused ($\phi = \pi$), and the wave groups with $\phi = \frac{1}{2}\pi,\ \frac{3}{2}\pi$ are highlighted. The envelope of the paddle motion for this family of wave groups is clearly visible.

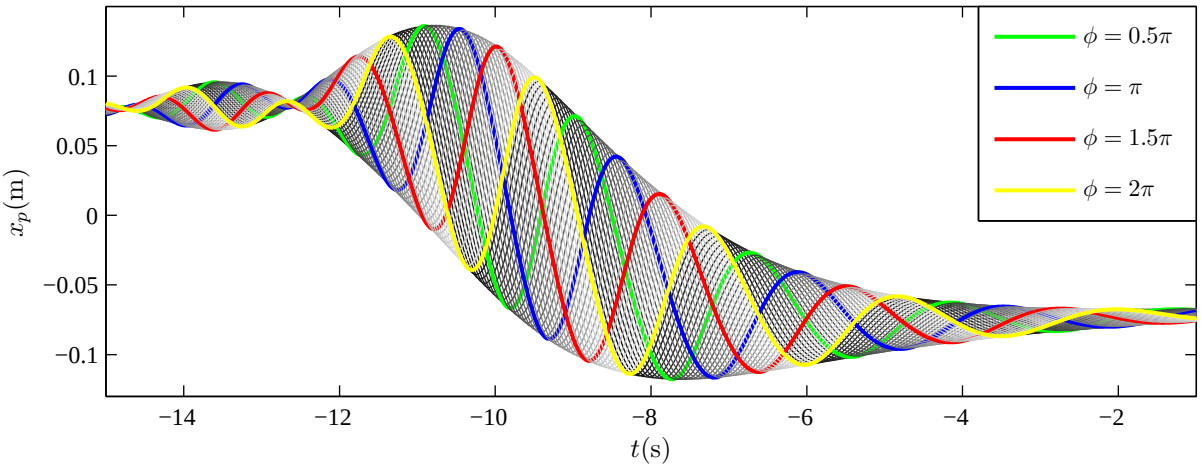

Figure 6.2: Paddle displacement signals for a family of 36 NewWave focused wave groups with $A_{\mathcal{N}} = 0.0855$ m, $x_f = 15.83$ m and $\phi = \frac{k}{36}2\pi$ for $k = 1, \ldots, 36$. Each signal is plotted in a different shade of grey, with $\phi = 0.5\pi$ highlighted in green, $\phi = \pi$ (trough-focused wave) in blue, $\phi = 1.5\pi$ in red and $\phi = 2\pi$ (crest-focused wave) in yellow.

6.2 Visualisation and discussion of results

For all simulations, spatial profiles of the free surface and the horizontal flux at sparse time intervals are outputted. The maximum vertical run-up R produced by each wave group, together with the time when it was attained, are also saved. Note that in all simulations, the time t is defined relative to $t_f = 0$ s, where t_f is the linear focus time.

6.2.1 Results for a specific linear focus location

Figures 6.3 - 6.5 show snapshots of wave group propagation and run-up calculated by the numerical model. Each figure presents five spatial profiles of an evolving wave group family, given by a complete loop of phase at focus ϕ. The smallest, the medium and the largest wave group families ($A_{\mathcal{N}} = 0.0285,\ 0.0855,\ 0.1425$ m) with $x_f = 15.83$ m are plotted, all on the same scale. Using the same colour convention as before, each wave group profile is displayed in a different shade of grey, with the crest-focused, the trough-focused, and the wave groups with $\phi = \frac{1}{2}\pi,\ \frac{3}{2}\pi$ highlighted in colour and bolder lines.

Figure 6.3 shows the computed results for the smallest of the investigated wave group families ($A_{\mathcal{N}} = 0.0285$ m). In the first subplot ($t = -1.6$ s) a smooth wave group family envelope is evident, with the beach having little effect on the individual waves. As the groups move further towards the shore ($t = -0.2$ s), the waves start to become distorted due to the decreasing depth. Small bore formation is also evident close to the shoreline ($x > 17$ m). Note in passing that this time instant almost coincides with the linear focus time $t_f = 0$ s (in the absence of the beach). At $t = 1.2$ s, wave breaking can be seen at the front of the wave packet for all of the wave groups. Small loss of amplitude is also evident from the jump downwards in the wave envelope moving inshore. The two remaining snapshots show the wave run-up as the wave groups diminish due to further breaking and energy dissipation.

Figure 6.4 presents the evolution of the medium wave group family ($A_{\mathcal{N}} = 0.0855$ m). The first snapshot reveals wave asymmetry in the main wave packet due to the different propagation speeds of crests and troughs in this decreasing water depth. The smaller waves at the front of the wave packets are steepening up and breaking. At the next time instant shown ($t = -0.2$ s), wave breaking can be seen in all of the wave groups, with the envelope indicating the associated wave amplitude loss. More breaking and bore formation follows, as the waves move further inshore. In the last two plots, the surging waves are climbing up the beach and the wave groups essentially collapse.

The evolution of the largest wave group family ($A_{\mathcal{N}} = 0.1425$ m) is presented in Figure 6.5. Due to their larger amplitudes, the waves are breaking earlier and further offshore. Already in the first snapshot shown ($t = -1.2$ s), the middle waves of the wave group packets are breaking with considerable energy dissipation. By comparing the first two plots and tracking individual wave crests, the broken waves, now as bores, can be seen moving along the beach and further decreasing in height. Small instabilities in the numerical code can be seen developing in some of the cases

($t = -0.2$ s, 12 m $\leq x \leq$ 14 m). In order to suppress these sufficiently so that the stability of the numerical model is not compromised, very limited amount of numerical smoothing is applied to the updated solution in the solver. A five-point smoothing algorithm, as described in Section 3.9, is used everywhere offshore of the breaking point at 5 instances between $t = 1$ s and $t = 20$ s (at every 600^{th} time step, which corresponds to every 4.2 s). This has very little effect on the naturally present waves in the system and the overall wave energy. Yet, the stability of the code is maintained so that a large number of simulations can be run successively without interruption. At $t = 1.2$ s, further reduction in the wave height, and bore run-up on the beach can be seen. The last two plots display the increased extent of the wave run-up on the beach as well as an almost complete dissipation of the wave groups.

Figure 6.6 shows the calculated vertical run-up R as a function of wave phase at focus ϕ (i.e. for each ϕ, the maximum run-up attained by that wave group is shown). Results are displayed for the three wave group families discussed above. The same presentation convention is used, with each shade of grey corresponding to a particular value of ϕ, and $\phi = \frac{1}{2}\pi,\ \pi,\ \frac{3}{2}\pi$ and 2π highlighted in colour. It should be noted that, as expected, the largest run-up value in each wave group family is consistent with the results displayed in the bottom plots ($t = 4$ s) of Figures 6.3 - 6.5. For example, for the smallest wave group family ($A_{\mathcal{N}} = 0.0285$ m), the largest run-up is generated by the blue trough-focused group ($\phi = \pi$), and indeed in Figure 6.3 the wave profile shown in blue can be seen extending the furthest inshore at $t = 4$ s. Similarly, the largest run-up in the medium wave group family ($A_{\mathcal{N}} = 0.0855$ m) is given by the green wave group ($\phi = \frac{1}{2}\pi$); and by the yellow crest-focused group ($\phi = 2\pi$) in the largest wave group family ($A_{\mathcal{N}} = 0.0855$ m). Therefore for this particular linear focus location ($x_f = 15.83$ m) there is a shift observed from trough-focused ($\phi = \pi$) to crest-focused ($\phi = 0$) wave group associated with the maximum run-up (within a wave group family) as the wave group amplitude increases. Similar phase shift can be seen at other focus locations, as is shown later.

In the three wave group families, and in fact in all the fifty-five families investigated, the run-up curves have similar characteristics. Each curve exhibits a hump and a dip, as seen in Figure 6.6. It is unclear why the depression in the run-up curve for the largest wave group family is more pronounced (top right plot in Figure 6.6). However, the sharp transition in this run-up curve around $\phi = 0.3\pi$ can be traced back to the corner-like feature on the wave group envelope seen around $x = 15$ m in the top plot ($t = -1.6$ s) of Figure 6.5. Also shown in Figure 6.6 are the time instants when these maximum run-ups R occur in the simulations (again plotted against ϕ).

For all wave group families, the minimum run-up values (corresponding to the dip in the run-up curve) correlate with a jump in the time curve (with a reduction in time across the discontinuity). The values of ϕ at which such a discontinuity in the time curve occurs correspond to wave groups with two successive waves, both of which lead to the same run-up value. In the wave group to the right of the discontinuity, the first of the two successive waves produces the maximum run-up, whereas in the wave group to the left of the discontinuity it is the second wave that generates the largest run-up. From Figure 6.6, it follows that for the smallest wave group family, the discontinuity occurs around $\phi = 1.75\pi$, which is between the yellow and the red wave group. Going back to Figure 6.3 and tracking the individual red and yellow crests in the snapshots, it is clear that the maximum run-up for the yellow wave group (which occurs just before $t = 4$ s) is produced by the first wave in the wave packet (located at $x = 15$ m on the $t = -1.2$ s plot). On the other hand, for the red wave group, the largest run-up (which occurs roughly at $t = 5$ s) is generated by the middle wave of the wave packet (located at $x = 13$ m on the $t = -1.2$ s plot). Therefore, one of the wave groups plotted in light grey (between the yellow and the red wave group) necessarily has both the first and the second wave generating roughly equal run-ups, which appears to be linked to the smallest run-up value in the wave group family.

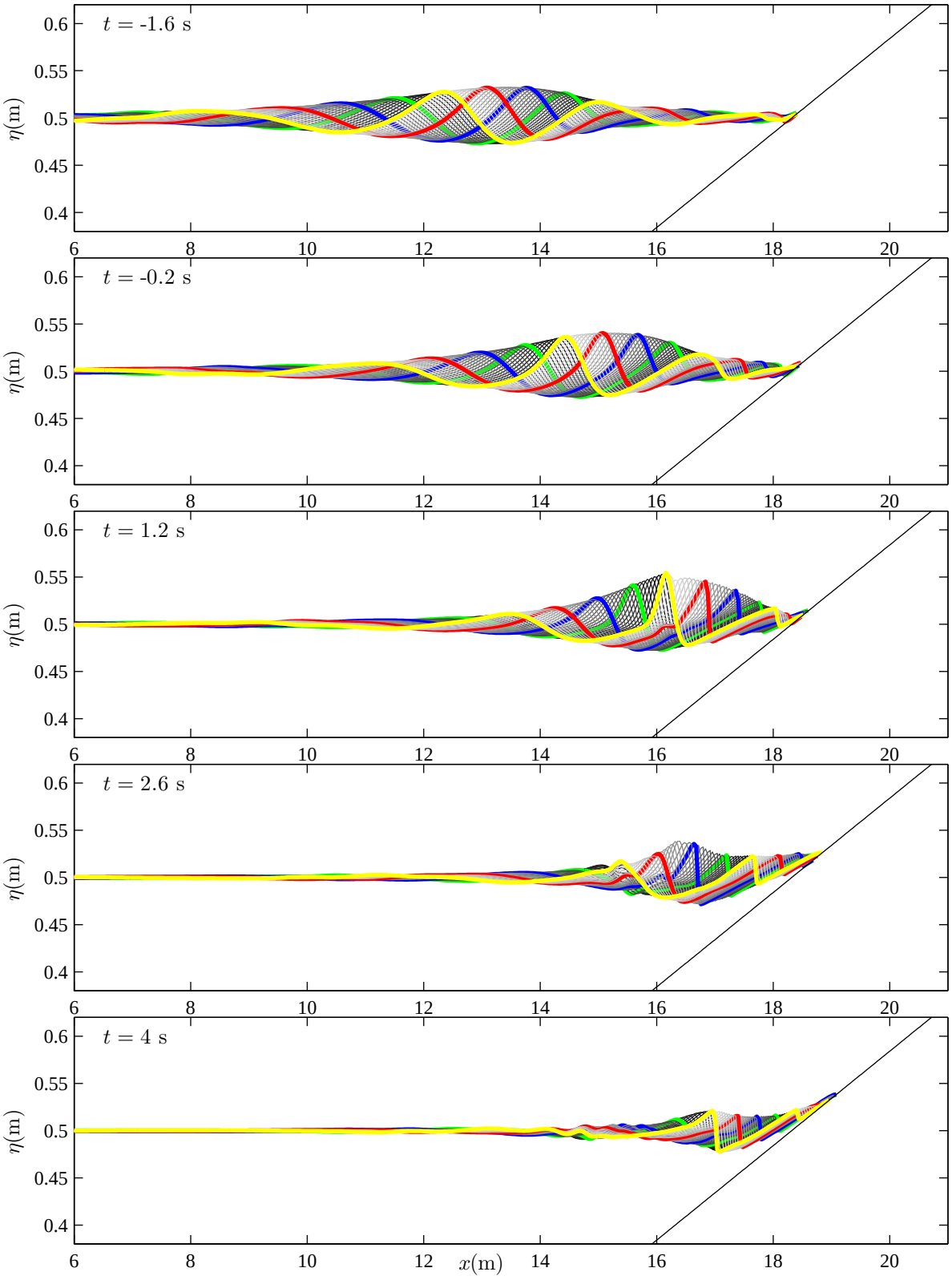

Figure 6.3: Free surface spatial profiles for a family of 36 NewWave focused wave groups with $A_{\mathcal{N}} = 0.0285$ m, $x_f = 15.83$ m and $\phi = \frac{k}{36}2\pi$ for $k = 1, \ldots, 36$. Each profile is plotted in a different shade of grey, with $\phi = 0.5\pi$ highlighted in green, $\phi = \pi$ (trough-focused wave) in blue, $\phi = 1.5\pi$ in red, and $\phi = 2\pi$ (crest-focused wave) in yellow.

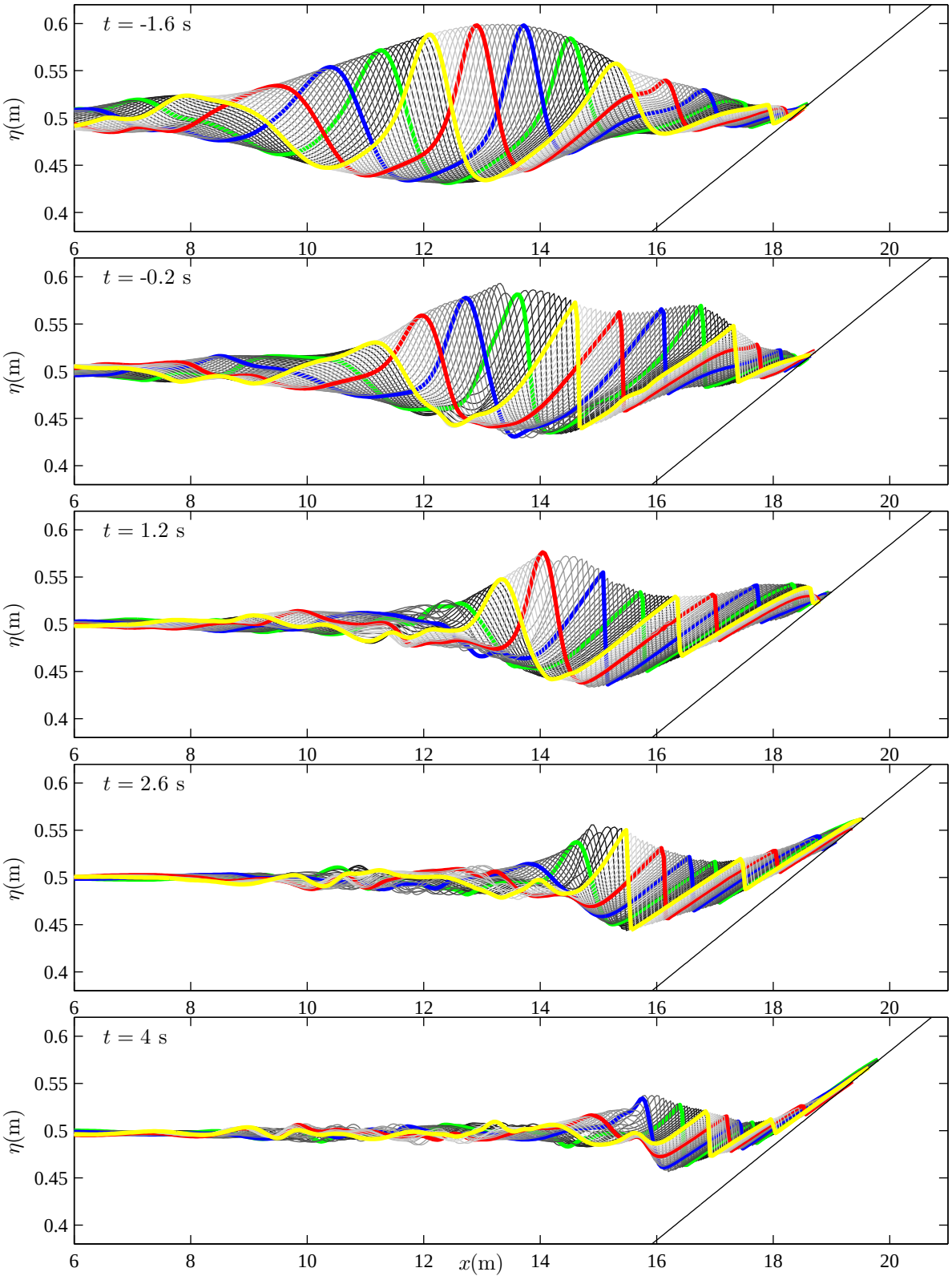

Figure 6.4: Free surface spatial profiles for a family of 36 NewWave focused wave groups with $A_{\mathcal{N}} = 0.0855$ m, $x_f = 15.83$ m and $\phi = \frac{k}{36}2\pi$ for $k = 1, \ldots, 36$. Each profile is plotted in a different shade of grey, with $\phi = 0.5\pi$ highlighted in green, $\phi = \pi$ (trough-focused wave) in blue, $\phi = 1.5\pi$ in red, and $\phi = 2\pi$ (crest-focused wave) in yellow.

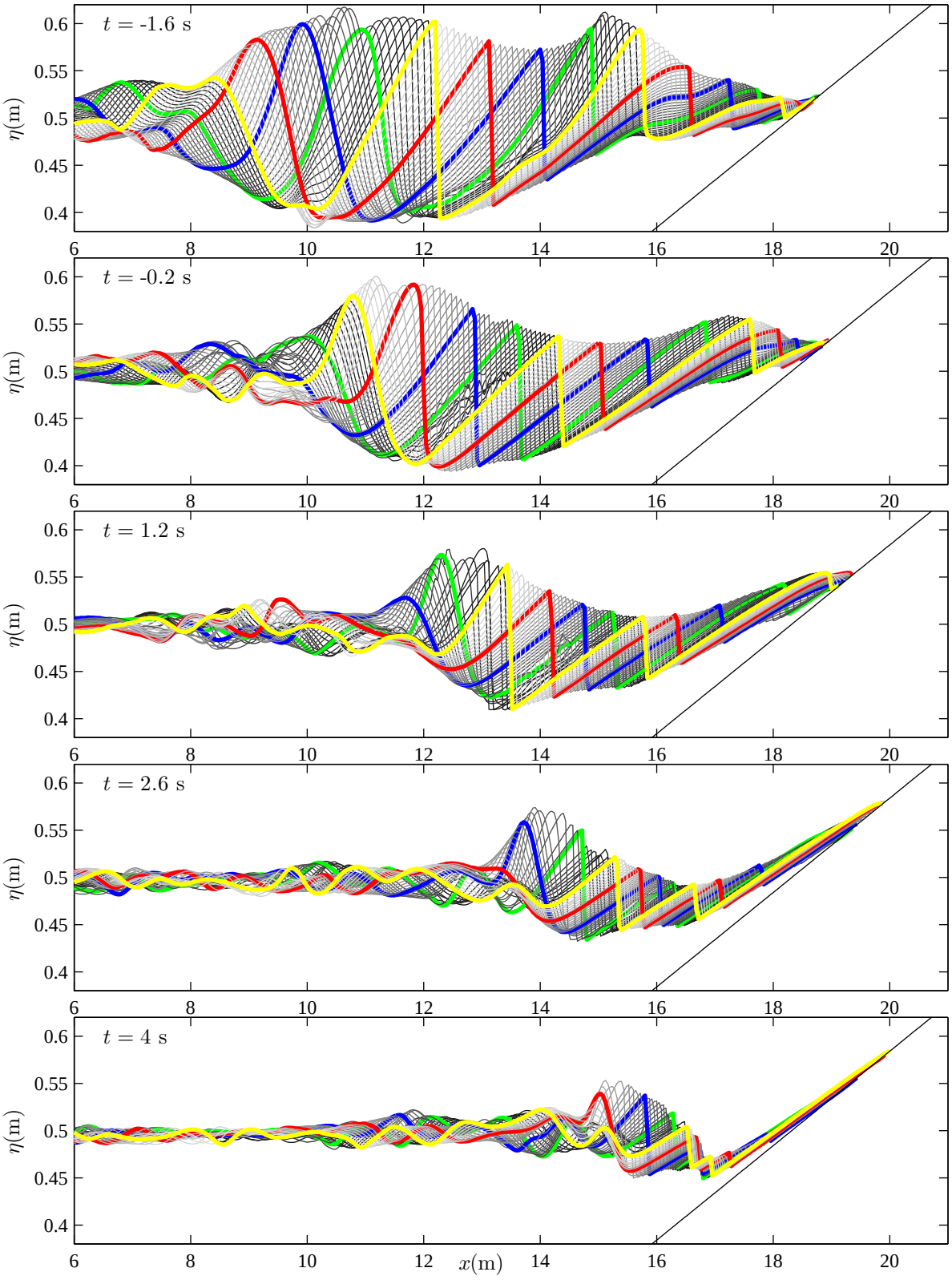

Figure 6.5: Free surface spatial profiles for a family of 36 NewWave focused wave groups with $A_{\mathcal{N}} = 0.1425$ m, $x_f = 15.83$ m and $\phi = \frac{k}{36}2\pi$ for $k = 1, \ldots, 36$. Each profile is plotted in a different shade of grey, with $\phi = 0.5\pi$ highlighted in green, $\phi = \pi$ (trough-focused wave) in blue, $\phi = 1.5\pi$ in red, and $\phi = 2\pi$ (crest-focused wave) in yellow.

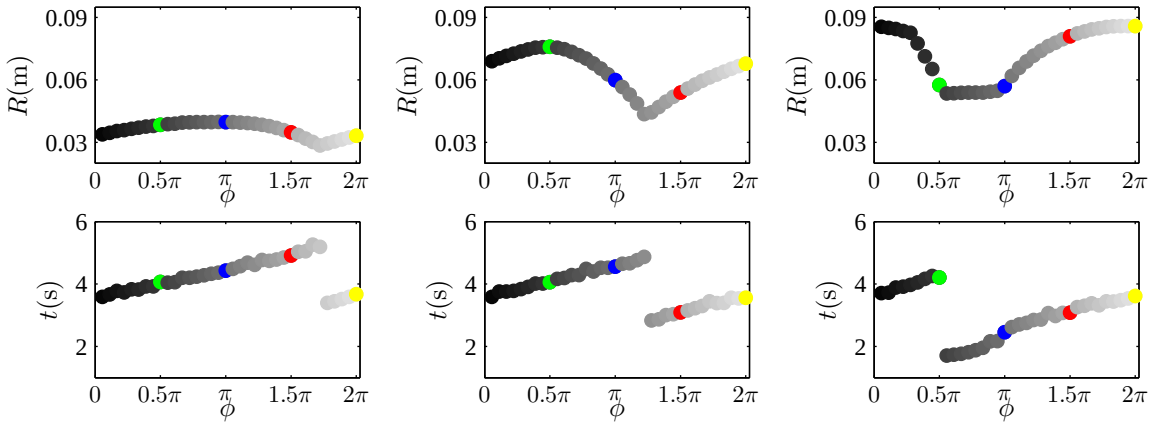

Figure 6.6: Top row - variation of the vertical run-up R with the group phase ϕ for three families of NewWave focused wave groups with linear focus location $x_f = 15.83$ m and linear focus amplitudes $A_{\mathcal{N}} = 0.0285$ m (left plot), $A_{\mathcal{N}} = 0.0855$ m (middle plot) and $A_{\mathcal{N}} = 0.1425$ m (right plot). Bottom row - times when these maximum run-ups occur as a function of phase ϕ. The three wave group families correspond to those presented in Figures 6.3 - 6.5. Using the same presentation, each run-up value/run-up time is plotted in a different shade of grey, with $\phi = 0.5\pi$ highlighted in green, $\phi = \pi$ (trough-focused wave) in blue, $\phi = 1.5\pi$ in red, and $\phi = 2\pi$ (crest-focused wave) in yellow.

6.2.2 The complete result set

Results from multiple focus locations are presented in Figure 6.7. The top row of the figure consists of contour plots, each for a given focus location x_f, of the wave group run-up R as a function of the group phase at focus ϕ and the linear focus amplitude $A_{\mathcal{N}}$. Results for six focus locations, out of the investigated eleven, are displayed. The plots share common features. In general there is a positive correlation between the run-up R and the amplitude $A_{\mathcal{N}}$. However, varying the group phase at focus ϕ has a significant effect on the run-up. In each plot, there are certain values of ϕ leading to a much reduced run-up, creating a valley-like feature. Note that the localised depressions in these 'valleys' (indicated by blue and green islands) are artifacts arising because only five amplitudes $A_{\mathcal{N}}$ are investigated. It is expected that if a higher number of $A_{\mathcal{N}}$ were to be chosen, the contour plots would be smoother. However, this is not deemed necessary, as the chosen number of amplitudes is sufficient to detect the main features in the run-up response.

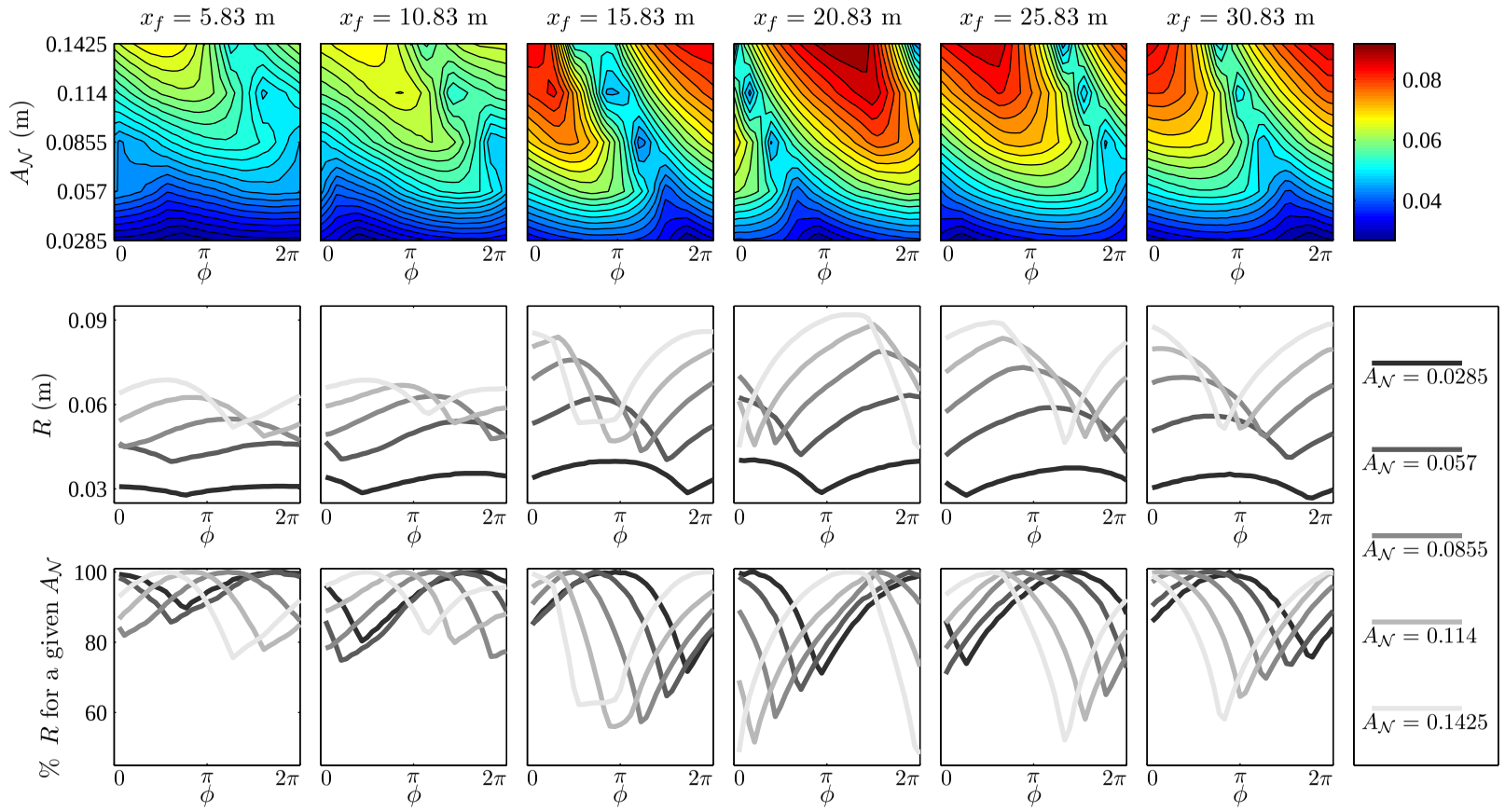

Figure 6.7: Contour plots of vertical run-up R as a function of the group phase at focus ϕ and the linear focus amplitude $A_\mathcal{N}$ for six different linear focus locations x_f (top row). Individual line plots (for each amplitude $A_\mathcal{N}$) of the run-up dependency on the phase for six different focus locations (middle row). Percentage variation of run-up with phase (for each amplitude $A_\mathcal{N}$) for six different focus locations (bottom row).

The middle row of Figure 6.7 contains line plots of run-up variation with the phase ϕ for each wave amplitude $A_{\mathcal{N}}$, as if created by taking horizontal slices through the contour plots above them. The characteristic hump and dip shape of the run-up curves becomes evident. Note also the aforementioned phase shift, where by the wave group phase ϕ associated with the maximum (or minimum) run-up values (within a wave group family) changes as the amplitude $A_{\mathcal{N}}$ increases.

When interested in the maximum run-up response, as important for engineering applications, it appears that the chosen resolution for phase sampling (by 10°, so 36 different values between 0 and 2π) is slightly excessive. Halving the sampling resolution, would obviously halve the parameter study completion time. Yet, it would not significantly compromise the accuracy of the maximum run-up prediction, as the run-up curves pass through the maximum value relatively slowly and smoothly, as seen in the middle row of Figure 6.7. Alternatively, in similar parameter studies, a rough phase variation could be carried out first, followed by more refined phase sampling in the region of the larger run-up values.

The bottom row of Figure 6.7 contains line plots of percentage run-up variation with the phase for each wave amplitude. These were created from each run-up curve in the plots above, by assigning 100 % to the maximum run-up, and then expressing the other run-up values (within that wave group family) as a percentage of this maximum. The influence of phase on the run-up value is considerable; up to 50 % difference can be seen in the middle right plot ($x_f = 20.83$ m) for the largest amplitude wave group family ($A_{\mathcal{N}} = 0.1425$ m).

Figure 6.8 provides a compact and an intuitive way of presenting the results from all the 1980 simulations undertaken for this parameter study. The top row consists of contour plots, one for each linear focus amplitude $A_{\mathcal{N}}$, of the calculated vertical run-up R as a function of the linear focus location x_f and the wave group phase at focus ϕ. These are plotted using the same colour scaling for the run-up, given by the colour bar on the right hand side. The difference in colour between the individual plots is immediately obvious. Note that the localised depressions (indicated by blue islands) and the localised peaks (indicated by red and orange islands) coincide with the focus locations investigated, and are an artifact of using a too crude sampling resolution for x_f. However, the plots are sufficiently resolved to show the main features. All of the contour plots appear to contain sharp valley-like and smooth ridge-like features, indicating that different combinations of x_f and ϕ can lead to much lower (within a valley) and higher (within a ridge) run-ups.

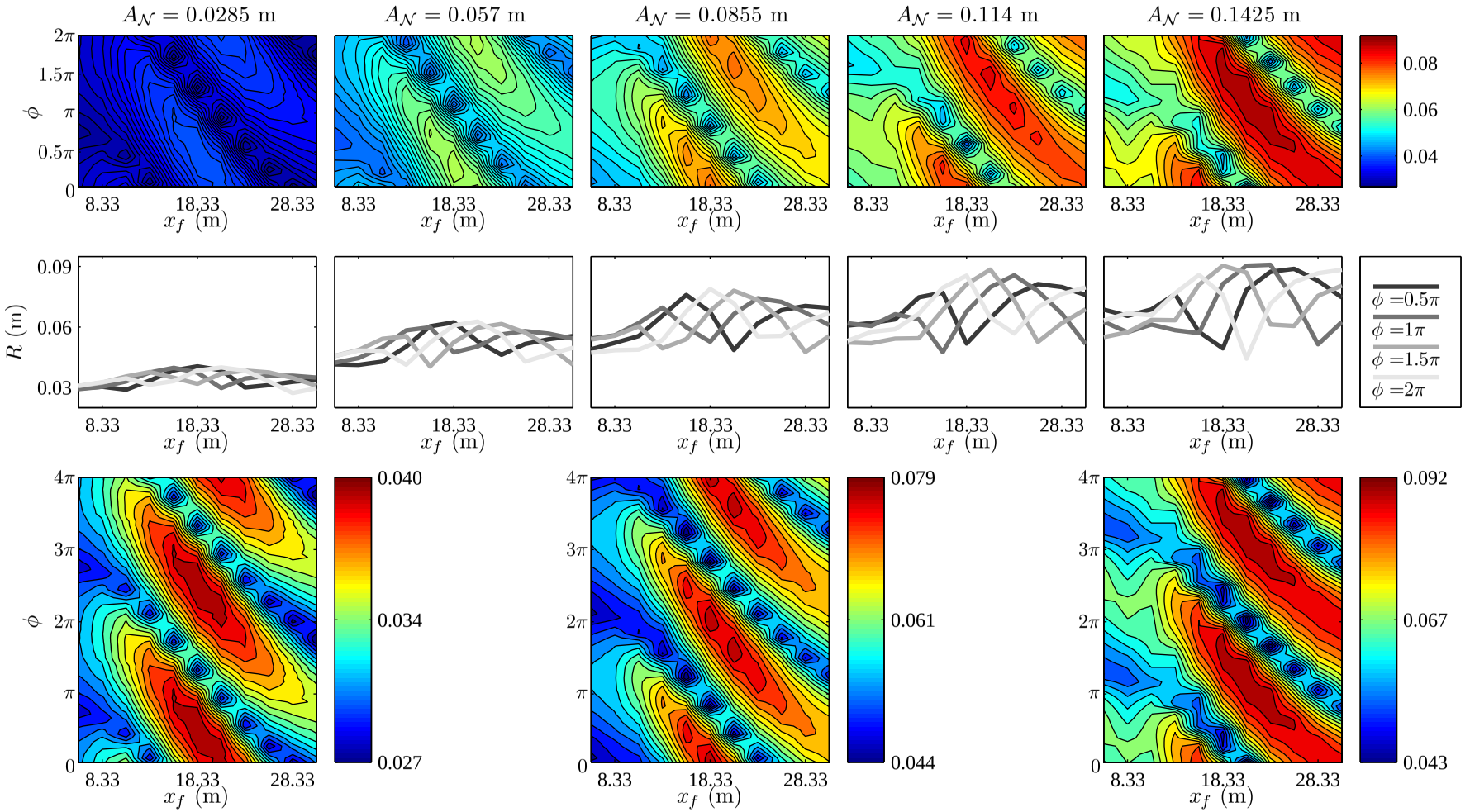

Figure 6.8: Contour plots of vertical run-up R as a function of linear focus location x_f and group phase at focus ϕ for a given linear focus amplitude $A_{\mathcal{N}}$ (top row). Individual line plots (for four selected phases) of the run-up dependency on the focus location for a given focus amplitude (middle row). Contour plots of run-up variation with focus location and repeated phase ($\phi \in [0\ 2\pi] \equiv [2\pi\ 4\pi]$) for the smallest, the medium and the largest amplitude (bottom row).

The detailed dependence of the run-up on the focus location, for four selected phases, is displayed in the middle row of Figure 6.8. These line plots correspond to horizontal slices taken through the contour plots above them. Each of the displayed run-up curves exhibits two crests and two troughs, which is in contract to the phase-dependent run-up curves shown in the middle row of Figure 6.7. For each $A_{\mathcal{N}}$, the run-up curves are consistent with an envelope for the maximum run-up variation with the focus location. The envelope appears to indicate that for a given $A_{\mathcal{N}}$ there is one overall maximum value of run-up produced by a specific combination of x_f and ϕ.

Three of the contour plots, for the smallest, the medium and the largest $A_{\mathcal{N}}$, are reproduced again in the bottom row of Figure 6.8, but this time plotted over a doubled range of values of ϕ and each with its own run-up colour scaling. Due to the 2π periodicity of ϕ, each of these contour plots is simply generated by vertically stacking two copies of the original contour plot. What becomes clear is that the 'ridges' seen on the original contour plots, are in fact rather elongated 'hills' with a well-defined peak area, which then drops off. These plots confirm that a clear maximal response in terms of run-up is produced for each given $A_{\mathcal{N}}$, as already shown by the line plots above. Additional simulations with input values of x_f and ϕ taken from the dark red regions in the contour plots, could further pin-point the worst-case conditions as well as enhance the accuracy of the most severe run-up value. However, considering the inherent error of the model's run-up predictions and the fact that the variation of the peak run-up along the backbone of the 'hills' is rather flat, this is not worthwhile for the present parameter study.

For reference, the calculated peak run-up values for each linear focus amplitude $A_{\mathcal{N}}$ are summarised in Table 6.2, together with the optimal wave group characteristics in terms of x_f and ϕ. From the table it follows that, in this parameter study, the linear focus location x_f leading to the largest run-ups is in the vicinity of the still water position on the beach ($x = 18.33$ m). For the smaller waves, the optimal value of x_f coincides with the initial shoreline location, and for the larger wave groups it moves slightly inshore (to the next investigated value of x_f). The optimal values of phase ϕ vary considerably for the investigated values of $A_{\mathcal{N}}$. There appears to be a negative correlation between the amplitude $A_{\mathcal{N}}$ and the optimal phase ϕ. This can also be easily identified in the contour plots in Figure 6.8, by noticing a downwards movement (along the ϕ axis) of the 'hills' across the different contour plots of increasing $A_{\mathcal{N}}$.

Table 6.2: Calculated values of the maximum run-up R for each linear focus amplitude $A_{\mathcal{N}}$, together with the associated wave group characteristics in terms of the linear focus location x_f and the group phase at focus ϕ.

$A_{\mathcal{N}}$ (m)	Maximum run-up R (m)	x_f (m)	ϕ (degrees)	ϕ (radians)
0.0285	0.0405	18.33	$90 \equiv 450$	$0.50\pi \equiv 2.50\pi$
0.0570	0.0636	18.33	$50 \equiv 410$	$0.2\overline{7}\pi \equiv 2.2\overline{7}\pi$
0.0855	0.0788	20.83	280	$1.5\overline{5}\pi$
0.1140	0.0885	20.83	270	1.50π
0.1425	0.0919	20.83	220	$1.2\overline{2}\pi$

6.2.3 Further discussion

In this parameter study, a peak run-up scenario has been identified for each investigated wave group amplitude $A_{\mathcal{N}}$. One fundamental question remains to be answered: whether, for each $A_{\mathcal{N}}$, the study provides a global maximum for all possible values of x_f and ϕ, or a local maximum meaning that different values of ϕ and x_f (not included in this study) could lead to higher values of R. Due to its periodicity, a full range of possible values of ϕ has been investigated. On the other hand, the range of possible focus locations x_f is unbounded. However, a practical range for x_f can be established, as has been achieved in this parameter study. From Figure 6.8, it appears unlikely that, for a given $A_{\mathcal{N}}$, any wave group from a wave group family focused further offshore than $x_f = 5.83$ m (the most offshore focus location investigated) would generate larger response than the maximum already identified. Essentially such wave groups would be more dispersed upon reaching the beach (whether broken or un-broken), therefore ultimately leading to smaller run-up. Similarly, for a given $A_{\mathcal{N}}$, any wave group from a wave group family focused further inshore than $x_f = 30.83$ m (the most inland focus location investigated) would again reach the beach less concentrated (less focused), leading to lower run-up. It therefore appears that the identified extreme run-up with the optimal values of x_f and ϕ are indeed global maxima, for each $A_{\mathcal{N}}$.

Figure 6.9 presents the overall optimised peak run-up R as a function of the linear wave group amplitude at focus $A_{\mathcal{N}}$. It follows that the maximum run-up increases with the incident wave amplitude, but with wave breaking being increasingly important for larger waves. However, in this study there has not been identified an upper limit on the wave group induced run-up. As explained in Section 5.1, the NewWave focused wave group amplitude $A_{\mathcal{N}}$ is directly related to the probability of

occurrence of an event of such size. This follows from

$$A_{\mathcal{N}} = \left(2\sigma^2 \ln \mathcal{N}\right)^{1/2}, \tag{6.1}$$

where $A_{\mathcal{N}}$ denotes the amplitude of the largest wave, out of $\mathcal{N}$ waves, in the free surface time series with assumed Rayleigh distribution, and σ is the standard deviation (the root-mean-square) of that sea state. Thus, if a laboratory scale $A_{\mathcal{N}} = 0.114$ m is assumed to correspond to a one in three hour extreme wave amplitude (roughly 1 in 10^3 waves, assuming an 11 s wave period at field scale), then $A_{\mathcal{N}} = 0.1425$ m corresponds roughly to a 1 in 50×10^3 waves for the same assumed storm severity. Put simply, such an event has a probability of occurrence of around 2 % in the same three hour storm, and produces run-up only 4 % larger. So in this assumed scenario (with a fixed storm severity), the increased run-up (associated with a larger $A_{\mathcal{N}} = 0.1425$ m) is relatively unlikely, even for a storm of significantly longer duration. Realistically, a more severe storm is needed to generate notably enhanced run-up.

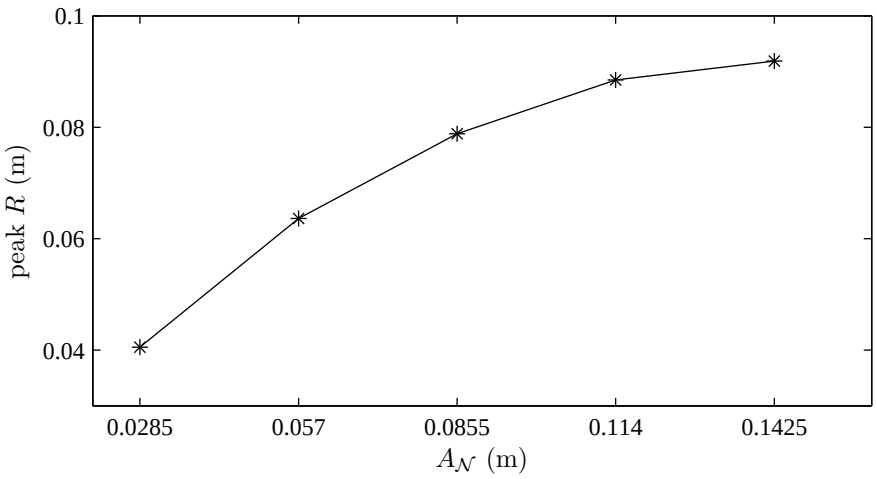

Figure 6.9: Dependence of the peak vertical run-up R on the linear focus amplitude $A_{\mathcal{N}}$ found in this parameter study.

The chosen method of presenting the results of the parameter study used in Figure 6.8, whereby $A_{\mathcal{N}}$ is fixed in each case and then the run-up is displayed as a function of x_f and ϕ, is the most natural way of splitting the three-dimensional parameter space. Even though the linear focus amplitude $A_{\mathcal{N}}$ is treated as a free parameter in this study, as explained previously, its value is related to the probability of occurrence of such a wave. Therefore using the methodology of this parameter study at a particular location with known wave spectrum characteristics, the investigated values of $A_{\mathcal{N}}$

can be chosen specifically to represent for example the largest winter storm waves or milder more frequently encountered waves. Due to the present numerical model being one-dimensional, there are limitations as to where this kind of parameter study can be applied: the prevailing waves would need to be normally incident, and the topography of the sea bed and beach would need to be mainly uniform in the long-shore direction. Under these assumptions, this procedure can be used by engineering practitioners wishing to determine the maximum run-up due to storm-induced wave groups. Using NewWave focused wave groups and varying the linear focus location x_f and the group phase at focus ϕ to find the overall maximum response, could provide a real alternative to using repeated random wave simulations for extreme run-up analysis. It should be noted, however, that this approach needs further validation.

6.3 Chapter summary

- This chapter has described the successful completion of around 2000 successive simulations involving NewWave focused wave group run-up on a plane beach for a parameter study investigating five different values of the linear focus amplitude $A_{\mathcal{N}}$, eleven different linear focus locations x_f and thirty-six different values of the wave group phase at focus ϕ.

- The results of the parameter study have been presented in meaningful ways, allowing for a straightforward interpretation of the effects of wave phase ϕ and focus location x_f on run-up. Typical shapes of the ϕ-dependent and x_f-dependent run-up curves have also been established.

- A methodology has been presented for identifying NewWave conditions, in terms of x_f and ϕ, leading to peak wave run-up. It has been found that in this parameter study, the optimal x_f is close to the still water location for all $A_{\mathcal{N}}$, whereas the optimal ϕ varies for each $A_{\mathcal{N}}$. A physically-sound argument has been given for these worst-case scenarios being unique for a given $A_{\mathcal{N}}$.

- The chapter provides a successful demonstration of the numerical code as a useful analysis tool for extreme run-up prediction. The generally-applicable methodology for extreme run-up studies involving NewWave focused wave groups has been laid out and the approach could be of considerable value to practicing coastal engineers.

Chapter 7

Conclusions and recommendations

This chapter provides a concluding summary of the work carried out in the thesis. Possible extensions to the present work are also discussed.

7.1 Conclusions

This thesis presents a one-dimensional numerical model of a shallow-water wave flume with an in-built piston paddle wavemaker. The model is suitable for simulating the propagation of breaking and non-breaking weakly dispersive waves and can additionally model any associated inundation, overtopping or inland flooding within the same simulation. The model is designed for run-up and overtopping studies.

Structure of the model

The underlying governing equations in the model are the weakly non-linear and weakly dispersive Boussinesq equations of Madsen and Sørensen (1992) and the non-linear shallow water equations. The model is suitable for breaking and non-breaking waves. Wave breaking is approximated by locally switching to the non-linear shallow water equations, which can inherently model wave breaking and the associated energy losses using shallow-water shock theory. A wave breaking initiation criterion has been proposed in terms of the free surface slope, whereby the shallow water equations are applied onshore of a point with $-\eta_x \geq 0.4$ (first shifted a quarter of a wavelength offshore). This treatment of breaking using a single value of the breaking criterion works well for all the simulated cases in this work. To facilitate joining of the two equation sets, the dispersive terms in the Boussinesq momentum equation are smoothly reduced over half a wavelength, so that at the interface the two sets are compatible. Both of the governing equation sets are formulated in terms of (η, q), where η represents the free surface elevation measured above a prescribed horizontal datum and q

is the horizontal flux. This allows for a straightforward application of the model in wetting and drying scenarios.

The Boussinesq equations in the present numerical model are discretised using a central finite difference scheme, as smooth solutions are expected in this region of the domain. The discretised equations are time marched forwards using the fourth order Runge Kutta method. In order to incorporate neatly the moving paddle into the model, a local domain transformation is applied, which maps the time-varying region in the vicinity of the paddle onto a fixed region. Therefore, close to the paddle, the transformed Boussinesq equations are solved on a fixed uniform grid in the mapped domain. The newly calculated solution is then mapped back onto the physical domain, where an adapting grid is used that mimics the paddle motion. Pre-calculated time series of the paddle displacements, which govern the wave generation, are fed into the model. For regular and irregular waves, the displacement can be computed according to first or second order wavemaker theory. For solitary waves, a fully non-linear algorithm can be used. The non-linear shallow water equations are solved using a finite volume MUSCL-Hancock scheme to allow modelling of sharp and discontinuous features such as bores. An HLL approximate Riemann solver is employed to resolve intercell fluxes and is extended for dry-bed scenarios. Using the wetting and drying algorithm of Brufau *et al.* (2002), the model is capable of simulating the movement of the shoreline during run-up, run-down and overtopping.

Verification and validation

The individual components of the model have each been carefully verified against analytical solutions, and the complete model has been validated against laboratory experiments involving solitary waves and dispersive wave groups. A new semi-analytical solitary wave solution of the Boussinesq equations has been derived, together with a closed form relation between the solitary wave amplitude and celerity. This solution form is used to confirm reversibility and conservation properties of the model, as well as the correct implementation of the paddle wavemaker. The non-linear shallow water equations and the treatment of the moving shoreline are successfully verified against analytical solution of a sloshing motion in a parabolic basin derived by Sampson *et al.* (2006).

When reproducing laboratory experiments with the numerical code, the same wave breaking criterion is used for all tests regardless of the modelled wave form. The applied value of friction coefficient C_f has to be calibrated for each experimental

setup. Once determined, an identical value of C_f is used for all runs from the same experimental facility.

Simulations of the Tainan supertank experiments of solitary wave run-up reported by Hsiao *et al.* (2008) are used for initial validation of the complete model. The agreement in run-up values is excellent. The calculated free surface time series also match well the measured data from the wave gauges, apart from the model under-predicting crest heights during the shoaling process just prior to breaking. Further validation is carried out using UKCRF laboratory data reported by Hunt (2003), where the recorded paddle displacement signals taken directly from the experiments are fed into the numerical model. Reproduction of experimental data of a solitary wave overtopping a laboratory-scale seawall shows that the model captures all the main features of the process, including run-up and run-down on the seawall, the overtopping flow over the seawall and the reverberation of reflected waves in the basin. Satisfactory agreement is achieved in terms of free surface time series and overtopping volume. Run-up on a plane beach involving a range of NewWave focused wave groups has also been simulated, with good agreement obtained between calculated and measured run-up distances. The maximum error in the model run-up prediction is 15 %, while the average error for the 8 cases simulated is around 6 %. The same NewWave experiments have been repeated for a bathymetry involving a seawall present on the beach. Wave-by-wave overtopping has been succesfully simulated, with generally good estimates of the free surface elevation at the seawall associated with the overtopping flow. Satisfactory agreement is achieved in terms of the overtopping volumes, with an average error of about 14 %, and a maximum discrepancy of 43 %.

Importance of second order wave generation

The UKCRF NewWave focused wave group experiments and their simulations use first order accurate paddle signals. Addition and subtraction of the crest-focused and trough-focused time series, together with suitable filtering in the frequency domain, allow separation of individual harmonics. Using this technique, second order waves can be isolated, and the presence of second order error waves becomes evident in both the experimental and numerical results. The difference frequency error wave arises in the absence of the set-down at the paddle, and constitutes a positive elevation travelling ahead of and underneath the front of the main group. Its effect on the NewWave run-up distances and overtopping volumes has been investigated using the numerical model by repeating the NewWave simulations with second order accurate paddle signals calculated according to Schäffer (1996). It is found that the

presence of the long error wave deforms the waves in the wave packet in such a way that they travel further inshore before breaking, thus generating larger run-up and overtopping. The predicted run-up values, when second order paddle signals are used, are on average 40 % smaller compared to corresponding cases with first order paddle signals. A similar trend is found for the overtopping volumes, whereby an average reduction of 60-70 % is observed. Therefore first order wavemaker theory, using piston paddles, should be avoided as otherwise the experiments/simulations will be severely contaminated by the second order error waves. Additionally, active absorption at the paddle of reflected waves returning offshore should be carried out throughout the experiment/simulation as the released waves will affect any subsequent ingoing waves unless they are allowed to exit the domain. As seen in Chapter 5, long waves are difficult to dissipate naturally on a beach, and are reflected back into the flume. If not absorbed at the wavemaker, the long waves will bounce back and significantly affect the flow field, as was demonstrated with incoming long error waves in Sections 5.5 and 5.6. For steeper beaches/structures, wave reflection occurs over a wider range of frequencies (as seen in Sections 5.4 and 5.6 where the seawall was present on the beach) so active absorption becomes unavoidable for such studies. Fortunately, active wave absorption is not needed for the NewWave experiments/simulations considered in this thesis due to their transient nature.

Application of the model - optimised wave group run-up

The numerical model has been used to conduct a parameter study investigating the optimal linear focus location x_f and group phase at focus ϕ for the largest run-up induced by NewWave focused wave groups on a 1:20 plane beach. Nearly 2000 successive simulations were undertaken with the model for eleven values of x_f along the beach extending to the dry part of the domain, thirty-six values of ϕ between 0 and 2π, and five values of the linear focus amplitude $A_{\mathcal{N}}$. From the results, it follows that all ϕ-dependent run-up curves (for fixed $A_{\mathcal{N}}$ and x_f) exhibit a hump and a sharp dip. The smallest run-up values in each ϕ-dependent run-up curve (associated with the dip in the curve) are linked to wave groups with two successive waves producing equal run-up distances. The variation of run-up with the phase ϕ can be significant, up to 50 % in some of the cases considered. For each $A_{\mathcal{N}}$ investigated, the maximum response is identified for a specific combination of x_f and ϕ (see Table 6.2). The optimal focus location x_f is in the vicinity of the still water line on the beach for all $A_{\mathcal{N}}$. The optimal phase ϕ varies systematically with $A_{\mathcal{N}}$. Given the range of values of x_f and ϕ investigated in the parameter study, it seems that the identified

maximum run-up response is global for each $A_{\mathcal{N}}$. In the present study, the overall optimised run-up increases with the wave amplitude $A_{\mathcal{N}}$, but appears to almost saturate for the largest amplitudes considered, as wave breaking becomes increasingly important. The approach taken here, which uses varying NewWave focused wave groups for extreme run-up determination and statistics, could be of considerable value to practicing coastal engineers. It provides an alternative method to repeated random wave experiments/simulations, whereby the parameters can be varied systematically, as opposed to randomly. Further validation is required but this seems to be a promising approach.

7.2 Recommendations for future work

This section discusses areas of future research following on from the work presented in this thesis, including improvements and new extensions to the present model.

2D and governing equations

The most obvious improvements to the present work include extension of the numerical model to two horizontal dimensions and replacing the weakly non-linear and weakly dispersive Boussinesq equations with a fully non-linear version. Creation of a two-dimensional model would require a multi-element paddle system, whereby each grid point on the moving boundary could move independently. Special attention would need to be paid to the treatment of wave breaking at an angle to the beach/structure. The non-linearity breaking criterion of Tonelli and Petti (2009) or the energy dissipation criterion of Bonneton *et al.* (2011) might be more appropriate. As seen in comparisons between the measured solitary wave data of Hsiao *et al.* (2008) and the model predictions, the weak non-linearity of the governing Boussinesq equations of Madsen and Sørensen (1992) leads to under-prediction of the highest waves. Fully non-linear formulations such as those derived by Wei and Kirby (1995) or Zou (1999) could remedy this shortcoming.

Active absorption

Active absorption of reflected waves at the wavemaker is crucial in experiments/simulations, unless very short experiments/simulations such as those involving NewWave focused wave groups are performed. The method of Schäffer and Skourup (1996) could be useful for incorporating simultaneous generation and absorption at the numerical paddle.

Improved stability

As discussed in Section 5.4, steep reflected waves re-entering the Boussinesq domain (as can happen in presence of a seawall) can cause the model to become unstable as the finite difference solver used in the Boussinesq domain cannot handle these sharp wave profiles. In the present work, in order to proceed with the simulations, numerical smoothing is applied locally and temporarily. This is not an attractive option for longer simulations or studies involving a large number of successive simulations. Instead, applying finite volume methods, naturally suitable for steep-fronted and discontinuous wave forms, to solve the Boussinesq equations could provide a neat way to circumvent this problem. Finite volume methods are already used in the model to solve the non-linear shallow water equations, so it would be relatively straightforward to use them in the Boussinesq domain too. Note that fourth order spatial accuracy is needed for the present Boussinesq set and therefore a fourth order reconstruction technique would be necessary (the second order data reconstruction used in the MUSCL-Hancok method would not be sufficient). In the vicinity of the paddle in the *paddle domain*, where the transformed Boussinesq equations are solved, finite differencing could be kept for simplicity. It is unlikely that in any sensible tests, the reflecting structure would be so close to the paddles that the broken reflected waves would have insufficient time to re-form before reaching the *paddle domain*. During code development, numerical tests were carried out for the Boussinesq equations solved by finite differencing and finite volume methods. Finite differences performed better (in a solitary wave propagation test) and were therefore selected for the Boussinesq part of the domain.

Improved efficiency

Additionally, as already suggested by reviewers of the JCP paper Orszaghova *et al.* (2012), investigation of second order time integration techniques for the Boussinesq equations, such as the second order leapfrog method, could be worthwhile in order to make the numerical model more efficient. Shiach and Mingham (2009) demonstrate that using a second order time marching method instead of a fourth order one in their Boussinesq code also based on equations by Madsen and Sørensen (1992), produces indistinguishable results and a speed up of 2 - 3 times.

Implementation of a numerical flume for experimental design

One attractive application of this work would be the creation of a dedicated version

of the numerical code matching an experimental flume. This would inevitably require further validation and calibration of the code. Once suitably linked, preliminary numerical simulations of the proposed physical experiments could be carried out with the model to help guide the experimental test programme. The numerical flume could also be used to carry out further simulations after the experimental programme is finished.

Additionally, for studies of very long tsunami-like waves, the lengths of present-day experimental facilities are simply not sufficient. Therefore, although the very near-shore and immediate on-land flow regions can be modelled physically, the remainder of the wave (or series of long waves) must be modelled numerically. A simulation on a numerical domain covering the experimental flume and extending much further offshore could be used to determine the necessary behaviour of the laboratory wave-maker (for simultaneous generation and absorption), as has been proposed for the flume housing HR Wallingford's new tsunami generator (see Rossetto *et al.* (2011)).

Wave group optimisation - an approach to extreme response in the coastal zone

Other immediate extensions of the work relate to the parameter study designed for extreme run-up analysis. Repeating the method for different values of beach slope (other than the 1:20 slope investigated) could be carried out and the results compared to see if similar trends are observed for example in terms of the typical features present in the run-up contour plots such as those in Figure 6.8 or in the almost limiting peak run-up variation with $A_{\mathcal{N}}$ as shown in Figure 6.9. Further validation would be desirable at this point against laboratory measurements of free surface elevation and run-up involving various NewWave focused wave groups. Also, results from prolonged random wave simulations derived from the same input wave spectra as the NewWaves would be extremely useful for comparison. Graphs could then be produced, similar to the one in Figure 6.9, presenting the peak optimised run-up as a function of the number of waves in the random wave time series $\mathcal{N}$, since $A_{\mathcal{N}}$ and $\mathcal{N}$ are linked via Equation (6.1). Comparison could be made between the maximum run-up induced by NewWave focused wave groups and waves from random wave experiments. Once suitably validated, the numerical code set up specifically for the parameter studies could be a very useful engineering design tool for coastal flood prediction. It would also be very interesting to vary the underlying spectral characteristics in terms of different values of the peak frequency f_p. One could then non-dimensionalise the run-up problem and investigate whether the maximum optimised run-up variation with $A_{\mathcal{N}}$

for wave groups with different periods collapses onto a single curve. A suitable length scale for this non-dimensionalisation could be the deep water wavelength associated with the peak frequency f_p (from the deep water dispersion relation $c^2 = \frac{g}{k}$ so that ${\omega_p}^2 = gk$).

It is recommended that the parameter study methodology be applied to overtopping scenarios for extreme overtopping analysis, which could then lead onto an optimisation tool for seawall assessment and design.

Coastal morphology

So far only impermeable and fixed bathymetry has been considered in this work. However, real coastal regions are covered by sand, pebbles or other movable sediments. It would certainly be worthwhile to account for infiltration at beaches in the numerical model by roughly approximating this flow through a porous medium. In the first instance it could be assumed that this medium is fixed. It would be unrealistic to attempt to capture all the features of such percolating flows, but it ought to be possible to account for them perhaps using a distributed mass and momentum sink along the beach or by means of another equally simplistic method. Extending this even further could lead to integrated morphology modelling, whereby sediment would be moved under the action of waves, either suspended in the water or as bedload. Even though the vertical profiles and particle motion in the governing equations are not exact, it should be possible to calibrate a sediment transport model. Such a combined model could be valuable in long term sandbank movement or beach profile change studies, due to its relative efficiency, even if the detailed physics is only approximated.

Appendix A

Second order paddle transfer function

The second order transfer function $F^{\pm}_{nm}$, as given by Schäffer (1996), reads as

$$\begin{aligned} F^{\pm}_{nm} = E^{\pm}_{nm}\Big\{ &\mp \frac{g}{2\omega_n}\sum_{j=0}^{\infty} c_{jn}\frac{k_{jn}^2}{k_{jn}^2-(K_0^{\pm})^2}\Big(\omega_n^2-(\omega_n\pm\omega_m)^2\Big) \\ &\mp \frac{g}{2\omega_m}\sum_{l=0}^{\infty} c_{lm}^{-:*}\frac{(k_{lm}^{-:*})^2}{(k_{lm}^{-:*})^2-(K_0^{\pm})^2}\Big(\omega_m^2-(\omega_n\pm\omega_m)^2\Big) \\ &+\sum_{j=0}^{\infty}\sum_{l=0}^{\infty} c_{jn}c_{lm}^{-:*}\frac{k_{jn}\pm k_{lm}^{-:*}}{(k_{jn}\pm k_{lm}^{-:*})^2-(K_0^{\pm})^2}H^{\pm}_{jnlm}\Big\}, \end{aligned} \tag{A.1a}$$

where the superscript $^{-:*}$ is given by

$$z^{-:*} = \begin{cases} z & \text{for superharmonics} \\ z^* & \text{for subharmonics,} \end{cases} \tag{A.1b}$$

meaning that when calculating F^+ the superscript is ignored, and when calculating F^- the superscript denotes a complex conjugate of the variable it is associated with.

In (A.1a) $E^{\pm}_{nm}$ is given by

$$E^{\pm}_{nm} = \frac{\delta_{nm}(K_0^{\pm})^2}{c_{0n}c_{0m}(\omega_n\pm\omega_m)^3}, \tag{A.1c}$$

with

$$\delta_{nm} = \begin{cases} \frac{1}{2} & \text{for } n=m \\ 1 & \text{for } n\neq m, \end{cases} \tag{A.1d}$$

and $K_0^{\pm}$ being the unique real solution of the linear dispersion relation

$$(\omega_n\pm\omega_m)^2 = gK_0^{\pm}\tanh(K_0^{\pm}h). \tag{A.1e}$$

Finally, $H^{\pm}_{jnlm}$ reads as

$$H^{\pm}_{jnlm} = (\omega_n\pm\omega_m)\Big(\pm\omega_n\omega_m - \frac{g^2k_{jn}k_{lm}^{-:*}}{\omega_n\omega_m}\Big) + \frac{\omega_n^3\pm\omega_m^3}{2} - \frac{g^2}{2}\Big(\frac{k_{jn}^2}{\omega_n}\pm\frac{k_{lm}^2}{\omega_m}\Big). \tag{A.1f}$$

Appendix B

Finite difference approximations

$$
\begin{aligned}
f_{\tilde{x}\tilde{x}}(\tilde{x}_{\widetilde{M}-1}) \approx & -\frac{1}{(\Delta x)^2}\Big(\frac{m}{3(3m+m_0)}\Big) f_{\widetilde{M}-3} \\
& + \frac{1}{(\Delta x)^2}\Big(\frac{3m+m_0}{2m+m_0}\Big) f_{\widetilde{M}-2} \\
& - \frac{1}{(\Delta x)^2}\Big(\frac{3m+2m_0}{m+m_0}\Big) f_{\widetilde{M}-1} \\
& + \frac{1}{(\Delta x)^2}\Big(\frac{m+3m_0}{3m_0}\Big) f_{\widetilde{M}} \\
& - \frac{1}{(\Delta x)^2}\Big(\frac{2m^4}{m_0(m+m_0)(2m+m_0)(3m+m_0)}\Big) f_{\widetilde{M}+1}, \qquad \text{(B.1a)} \\
f_{\tilde{x}\tilde{x}\tilde{x}}(\tilde{x}_{\widetilde{M}-1}) \approx & -\frac{1}{(\Delta x)^3}\Big(\frac{m+m_0}{3m+m_0}\Big) f_{\widetilde{M}-3} \\
& + \frac{1}{(\Delta x)^3}\Big(\frac{3m_0}{2m+m_0}\Big) f_{\widetilde{M}-2} \\
& + \frac{1}{(\Delta x)^3}\Big(\frac{3(m-m_0)}{m+m_0}\Big) f_{\widetilde{M}-1} \\
& - \frac{1}{(\Delta x)^3}\Big(\frac{2m-m_0}{m_0}\Big) f_{\widetilde{M}} \\
& + \frac{1}{(\Delta x)^3}\Big(\frac{12m^4}{m_0(m+m_0)(2m+m_0)(3m+m_0)}\Big) f_{\widetilde{M}+1}, \qquad \text{(B.1b)} \\
f_{\tilde{x}\tilde{x}}(\tilde{x}_{\widetilde{M}}) \approx & -\frac{1}{(\Delta x)^2}\Big(\frac{m_0(3m-2m_0)}{2(m+m_0)(2m+m_0)}\Big) f_{\widetilde{M}-2} \\
& + \frac{1}{(\Delta x)^2}\Big(\frac{4m_0(3m-m_0)}{(m+m_0)(m+2m_0)}\Big) f_{\widetilde{M}-1} \\
& + \frac{1}{(\Delta x)^2}\Big(\frac{2m^2-9mm_0+2m_0^2}{2m_0^2}\Big) f_{\widetilde{M}} \\
& - \frac{1}{(\Delta x)^2}\Big(\frac{4m^3(m-3m_0)}{m_0^2(2m+m_0)(m+m_0)}\Big) f_{\widetilde{M}+1}
\end{aligned}
$$

$$+\frac{1}{(\Delta x)^2}\Big(\frac{m^3(2m-3m_0)}{2m_0^2(m+m_0)(m+2m_0)}\Big)f_{\widetilde{M}+2}, \tag{B.1c}$$

$$\begin{aligned}
f_{\tilde{x}\tilde{x}\tilde{x}}(\tilde{x}_{\widetilde{M}}) \approx{}& \frac{1}{(\Delta x)^3}\Big(\frac{3m(m-3m_0)}{2(2m+m_0)(m+m_0)}\Big)f_{\widetilde{M}-2}\\
&-\frac{1}{(\Delta x)^3}\Big(\frac{6m(2m-3m_0)}{(m+m_0)(m+2m_0)}\Big)f_{\widetilde{M}-1}\\
&+\frac{1}{(\Delta x)^3}\Big(\frac{9m(m-m_0)}{2m_0^2}\Big)f_{\widetilde{M}}\\
&-\frac{1}{(\Delta x)^3}\Big(\frac{6m^3(3m-2m_0)}{m_0^2(2m+m_0)(m+m_0)}\Big)f_{\widetilde{M}+1}\\
&+\frac{1}{(\Delta x)^3}\Big(\frac{3m^3(3m-m_0)}{2m_0^2(m+m_0)(m+2m_0)}\Big)f_{\widetilde{M}+2},
\end{aligned} \tag{B.1d}$$

$$\begin{aligned}
f_{xx}(x_{\widetilde{M}+1}) \approx{}& -\frac{1}{(\Delta x)^2}\Big(\frac{2m_0^4}{m(m+m_0)(m+2m_0)(m+3m_0)}\Big)f_{\widetilde{M}-1}\\
&+\frac{1}{(\Delta x)^2}\Big(\frac{3m+m_0}{3m}\Big)f_{\widetilde{M}}\\
&-\frac{1}{(\Delta x)^2}\Big(\frac{2m+3m_0}{m+m_0}\Big)f_{\widetilde{M}+1}\\
&+\frac{1}{(\Delta x)^2}\Big(\frac{m+3m_0}{m+2m_0}\Big)f_{\widetilde{M}+2}\\
&-\frac{1}{(\Delta x)^2}\Big(\frac{m_0}{3(m+3m_0)}\Big)f_{\widetilde{M}+3},
\end{aligned} \tag{B.1e}$$

$$\begin{aligned}
f_{xxx}(x_{\widetilde{M}+1}) \approx{}& -\frac{1}{(\Delta x)^3}\Big(\frac{12m_0^4}{m(m+m_0)(m+2m_0)(m+3m_0)}\Big)f_{\widetilde{M}-1}\\
&-\frac{1}{(\Delta x)^3}\Big(\frac{m-2m_0}{m}\Big)f_{\widetilde{M}}\\
&+\frac{1}{(\Delta x)^3}\Big(\frac{3(m-m_0)}{m+m_0}\Big)f_{\widetilde{M}+1}\\
&-\frac{1}{(\Delta x)^3}\Big(\frac{3m}{m+2m_0}\Big)f_{\widetilde{M}+2}\\
&+\frac{1}{(\Delta x)^3}\Big(\frac{m+m_0}{m+3m_0}\Big)f_{\widetilde{M}+3}.
\end{aligned} \tag{B.1f}$$

Bibliography

Agnon, Y., Madsen, P. A., and Schäffer, H. A. (1999). A new approach to high-order Boussinesq models. *Journal of Fluid Mechanics*, *399*, 319 – 333.

Baldock, T. E., Swan, C., and Taylor, P. H. (1996). A laboratory study of nonlinear surface waves on water. *Philosophical Transactions of the Royal Society of London. Series A: Mathematical, Physical and Engineering Sciences*, *354*, 649 – 676.

Barthel, V., Mansard, E. P. D., Sand, S. E., and Vis, F. C. (1983). Group bounded long waves in physical models. *Ocean Engineering*, *10*, 261 – 294.

Battjes, J. (1974). Surf similarity. *Proceedings of the International Conference on Coastal Engineering*, *1*, 466 – 480.

Bellotti, G., and Brocchini, M. (2002). On using Boussinesq-type equations near the shoreline: a note of caution. *Ocean Engineering*, *29*, 1569 – 1575.

Boccotti, P. (1983). Some new results on statistical properties of wind waves. *Applied Ocean Research*, *5*, 134 – 140.

Bonneton, P., Chazel, F., Lannes, D., Marche, F., and Tissier, M. (2011). A splitting approach for the fully nonlinear and weakly dispersive Green-Naghdi model. *Journal of Computational Physics*, *230*, 1479 – 1498.

Borthwick, A. G. L., Ford, M., Weston, B. P., Taylor, P. H., and Stansby, P. K. (2006). Solitary wave transformation, breaking and run-up at a beach. *Proceedings of the Institution of Civil Engineers - Maritime Engineering*, *159*, 97 – 105.

Bradford, S. F., and Sanders, B. F. (2001). Finite volume schemes for the Boussinesq equations. In B. L. Edge, and J. M. Hemsley (Eds.), *Proceedings of the Fourth International Symposium on Ocean Wave Measurement and Analysis* (pp. 953 – 962). ASCE volume 273.

Brufau, P., Vázquez-Cendón, M. E., and García-Navarro, P. (2002). A numerical model for the flooding and drying of irregular domains. *International Journal for Numerical Methods in Fluids*, *39*, 247 – 275.

Chen, C.-L., Lou, S.-Y., and Li, Y.-S. (2004). Solitary wave solutions for a general Boussinesq type fluid model. *Communications in Nonlinear Science and Numerical Simulation*, *9*, 583 – 601.

Dalrymple, R. A., and Rogers, B. D. (2006). Numerical modeling of water waves with the SPH method. *Coastal Engineering*, *53*, 141 – 147.

Dalzell, J. F. (1999). A note on finite depth second-order wave-wave interactions. *Applied Ocean Research*, *21*, 105 – 111.

Dean, R. G. (2009). Chapter 1: Wave setup. Handbook of Coastal and Ocean Engineering (pp. 1 – 23). World Scientific.

Dean, R. G., and Dalrymple, R. A. (1991). *Water Wave Mechanics for Engineers and Scientists*. Advanced Series on Ocean Engineering, Volume 2. Singapore: World Scientific.

Dingemans, M. W. (1997). *Water Wave Propagation over Uneven Bottoms, Part 2-Non-linear Wave Propagation*. Advanced Series on Ocean Engineering, Volume 13. River Edge, NJ: World Scientific.

Fraccarollo, L., and Toro, E. F. (1995). Experimental and numerical assessment of the shallow water model for two-dimensional dam-break type problems. *Journal of Hydraulic Research*, *33*, 843 – 864.

Fuhrman, D. R., and Madsen, P. A. (2008). Simulation of nonlinear wave run-up with a high-order Boussinesq model. *Coastal Engineering*, *55*, 139 – 154.

Gobbi, M. F., Kirby, J. T., and Wei, G. (2000). A fully nonlinear Boussinesq model for surface waves. Part 2. Extension to $O(kh)^4$. *Journal of Fluid Mechanics*, *405*, 181 – 210.

Goring, D. G. (1978). *Tsunamis- The Propagation of Long Waves Onto a Shelf*. Ph.D. thesis California Institute of Technology Rep. No. KH-R-38, W.M. Keck Laboratory of Hydraulics and Water Resources, Pasadena, California.

Hsiao, S.-C., Hsu, T.-W., Lin, T.-C., and Chang, Y.-H. (2008). On the evolution and run-up of breaking solitary waves on a mild sloping beach. *Coastal Engineering*, *55*, 975 – 988.

Hu, K., Mingham, C. G., and Causon, D. M. (2000). Numerical simulation of wave overtopping of coastal structures using the non-linear shallow water equations. *Coastal Engineering*, *41*, 433 – 465.

Hubbard, M. E., and Dodd, N. (2002). A 2D numerical model of wave run-up and overtopping. *Coastal Engineering*, *47*, 1 – 26.

Hughes, S. A. (1993). *Physical Models and Laboratory Techniques in Coastal Engineering*. Advanced Series on Ocean Engineering, Volume 7. Singapore ; River Edge, NJ: World Scientific.

Hunt, A. C. (2003). *Extreme Waves, Overtopping and Flooding at Sea Defences*. Ph.D. thesis University of Oxford, UK.

Hunt, I. A. J. (1959). Design of seawall and breakwaters. *Journal of Waterway, Port, Coastal, and Ocean Engineering*, *85*, 123 – 152.

Hunt-Raby, A., Borthwick, A. G. L., Stansby, P. K., and Taylor, P. H. (2011). Experimental measurement of focused wave group and solitary wave overtopping. *Journal Hydraulics Research*, *Accepted*.

Johnson, R. S. (1997). *A Modern Introduction to the Mathematical Theory of Water Waves*. Cambridge Texts in Applied Mathematics, Volume 19. Cambridge: Cambridge University Press.

Jonathan, P., and Taylor, P. H. (1997). On irregular, nonlinear waves in a spread sea. *Journal of Offshore Mechanics and Arctic Engineering*, *119*, 37 – 41.

Karambas, T. V., and Koutitas, C. (1992). A breaking wave propagation model based on the Boussinesq equations. *Coastal Engineering*, *18*, 1 – 19.

Kennedy, A. B., Chen, Q., Kirby, J. T., and Dalrymple, R. A. (2000). Boussinesq modeling of wave transformation, breaking and run-up. I: One dimension. *ASCE Journal of Waterway, Port, Coastal and Ocean Engineering*, *126*, 48 – 56.

Kobayashi, N. (1999). Wave runup and overtopping on beaches and coastal structures. *Advances in Coastal and Ocean Engineering*, *5*, 95 – 154.

van Leer, B. (1984). On the relation between the upwind-differencing schemes of Godunov, Engquist-Osher and Roe. *SIAM Journal on Scientific and Statistical Computing*, *5*, 1 – 20.

Liang, Q., and Borthwick, A. G. L. (2009). Adaptive quadtree simulation of shallow flows with wet-dry fronts over complex topography. *Computers & Fluids*, *38*, 221 – 234.

Lindgren, G. (1970). Some properties of a normal process near a local maximum. *The Annals of Mathematical Statistics*, *41*, 1870 – 1883.

Liu, P. L. F., Lin, P. Z., Chang, K. A., and Sakakiyama, T. (1999). Numerical modelling of wave interaction with porous structures. *ASCE Journal of Waterways, Port, Coastal, and Ocean Engineering*, *125*, 322 – 330.

Losada, I. J., Lara, J. L., Guanche, R., and Gonzalez-Ondina, J. M. (2008). Numerical analysis of wave overtopping of rubble mound breakwaters. *Coastal Engineering*, *55*, 47 – 62.

Lynett, P. J., Melby, J. A., and Kim, D.-H. (2010). An application of Boussinesq modeling to Hurricane wave overtopping and inundation. *Ocean Engineering*, *37*, 135 – 153.

Madsen, P. A., Bingham, H. B., and Liu, H. (2002). A new Boussinesq method for fully nonlinear waves from shallow to deep water. *Journal of Fluid Mechanics*, *462*, 1 – 30.

Madsen, P. A., Bingham, H. B., and Schäffer, H. A. (2003). Boussinesq-type formulations for fully nonlinear and extremely dispersive water waves: derivation and analysis. *Proceedings of the Royal Society of London. Series A: Mathematical, Physical and Engineering Sciences*, *459*, 1075 – 1104.

Madsen, P. A., Murray, R., and Sørensen, O. R. (1991). A new form of the Boussinesq equations with improved linear dispersion characteristics. *Coastal Engineering*, *15*, 371 – 388.

Madsen, P. A., and Schäffer, H. A. (1998). Higher-order Boussinesq-type equations for surface gravity waves: derivation and analysis. *Philosophical Transactions of the Royal Society of London. Series A: Mathematical, Physical and Engineering Sciences*, *356*, 3123 – 3184.

Madsen, P. A., and Schäffer, H. A. (1999). A review of Boussinesq-type equations for surface gravity waves. *Advances in Coastal and Ocean Engineering*, *5*, 1 – 94.

Madsen, P. A., and Sørensen, O. R. (1992). A new form of the Boussinesq equations with improved linear dispersion characteristics. Part 2. A slowly-varying bathymetry. *Coastal Engineering*, *18*, 183 – 204.

Madsen, P. A., and Sørensen, O. R. (1993). Bound waves and triad interactions in shallow water. *Ocean Engineering*, *20*, 359 – 388.

Madsen, P. A., Sørensen, O. R., and Schäffer, H. A. (1997). Surf zone dynamics simulated by a Boussinesq type model. Part I. Model description and cross-shore motion of regular waves. *Coastal Engineering*, *32*, 255 – 287.

McGranahan, G., Balk, D., and Anderson, B. (2007). The rising tide: assessing the risks of climate change and human settlements in low elevation coastal zones. *Environment and Urbanization*, *19*, 17 – 37.

van der Meer, J. W., and Janssen, J. P. F. M. (1995). Chapter 1: Wave run-up and overtopping at dikes. Wave forces on inclined and vertical wall structures (pp. 1 – 27). ASCE.

van der Meer, J. W., and Stam, C. J. M. (1992). Wave runup on smooth and rock slopes of coastal structures. *Journal of Waterway, Port, Coastal, and Ocean Engineering*, *118*, 534 – 550.

van der Meer, J. W., Verhaeghe, H., and Steendam, G. J. (2009). The new wave overtopping database for coastal structures. *Coastal Engineering*, *56*, 108 – 120. The CLASH Project - Crest Level Assessment of Coastal Structures by Full-scale Monitoring, Neural Network Prediction and Hazard Analysis on Permissible Wave Overtopping (CLASH).

Nwogu, O. (1993). Alternative form of Boussinesq equations for nearshore wave propagation. *Journal of Waterway, Port, Coastal, and Ocean Engineering*, *119*, 618 – 638.

Orszaghova, J., Borthwick, A. G., and Taylor, P. H. (2012). From the paddle to the beach - A Boussinesq shallow water numerical wave tank based on Madsen and Sørensen's equations. *Journal of Computational Physics*, *231*, 328 – 344.

Orszaghova, J., Borthwick, A. G. L., and Taylor, P. H. (2011). Boussinesq modelling of solitary wave propagation, breaking, runup and overtopping. *Proceedings of the International Conference on Coastal Engineering*, *1*.

Peregrine, D. H. (1967). Long waves on a beach. *Journal of Fluid Mechanics*, *27*, 815 – 827.

Pullen, T., Allsop, W., Bruce, T., Kortenhaus, A., Schuettrumpf, H., and van der Meer, J. (2007). *EurOtop - Wave Overtopping of Sea Defences and Related Structures: Assessment Manual*. http://www.overtopping-manual.com/eurotop.pdf.

Rogers, B., Fujihara, M., and Borthwick, A. G. L. (2001). Adaptive Q-tree Godunov-type scheme for shallow water equations. *International Journal for Numerical Methods in Fluids*, *35*, 247 – 280.

Rogers, B. D., Borthwick, A. G. L., and Taylor, P. H. (2003). Mathematical balancing of flux gradient and source terms prior to using Roe's approximate Riemann solver. *Journal of Computational Physics*, *192*, 422 – 451.

Rossetto, T., Allsop, W., Charvet, I., and Robinson, D. I. (2011). Physical modelling of tsunami using a new pneumatic wave generator. *Coastal Engineering*, *58*, 517 – 527.

Sampson, J., Easton, A., and Singh, M. (2006). Moving boundary shallow water flow above parabolic bottom topography. In A. Stacey, B. Blyth, J. Shepherd, and A. J. Roberts (Eds.), *Proceedings of the 7th Biennial Engineering Mathematics and Applications Conference, EMAC-2005* (pp. 373 – 387). volume 47 of *ANZIAM Journal*.

Sarpkaya, T., and Isaacson, M. (1981). *Mechanics of wave forces on offshore structures*. Van Nostrand Reinhold Co.

Schäffer, H., and Skourup, J. (1996). Active absorption of multidirectional waves. *Proceedings of the International Conference on Coastal Engineering*, *1*.

Schäffer, H. A. (1996). Second-order wavemaker theory for irregular waves. *Ocean Engineering*, *23*, 47 – 88.

Schäffer, H. A., Madsen, P. A., and Deigaard, R. (1993). A Boussinesq model for waves breaking in shallow water. *Coastal Engineering*, *20*, 185 – 202.

Shao, S., Ji, C., Graham, D. I., Reeve, D. E., James, P. W., and Chadwick, A. J. (2006). Simulation of wave overtopping by an incompressible SPH model. *Coastal Engineering*, *53*, 723 – 735.

Shapiro, R. (1970). Smoothing, filtering, and boundary effects. *Reviews of Geophysics and Space Physics*, *8*, 359 – 387.

Shiach, J. B., and Mingham, C. G. (2009). A temporally second-order accurate Godunov-type scheme for solving the extended Boussinesq equations. *Coastal Engineering*, *56*, 32 – 45.

Stansby, P. K. (2003). Solitary wave run up and overtopping by a semi-implicit finite-volume shallow-water Boussinesq model. *Journal of Hydraulic Research*, *41*, 639 – 647.

Stoker, J. J. (1957). *Water waves : the mathematical theory with applications*. Pure and applied mathematics, Volume 4. New York: Interscience Publishers.

Taylor, P. H., and Williams, B. A. (2004). Wave statistics for intermediate depth water - NewWaves and symmetry. *Journal of Offshore Mechanics and Arctic Engineering*, *126*, 54 – 59.

Tonelli, M., and Petti, M. (2009). Hybrid finite volume - finite difference scheme for 2DH improved Boussinesq equations. *Coastal Engineering*, *56*, 609 – 620.

Toro, E. F. (1999). *Riemann solvers and numerical methods for fluid dynamics : a practical introduction*. Berlin: Springer.

Tromans, P. S., Anaturk, A. R., and Hagemeijer, P. (1991). A new model for the kinematics of large ocean waves application as a design wave. In *Proceedings of the First International Offshore and Polar Engineering Conference* (pp. 64 – 71). volume 3.

Tucker, M. J., and Pitt, E. G. (2001). *Waves in ocean engineering*. Elsevier Ocean Engineering Book Series, Volume 5. Amsterdam; New York: Elsevier.

Turnbull, M. S., Borthwick, A. G. L., and Eatock Taylor, R. (2003). Numerical wave tank based on a σ-transformed finite element inviscid flow solver. *International Journal for Numerical Methods in Fluids*, *42*, 641 – 663.

Wei, G., and Kirby, J. T. (1995). Time-dependent numerical code for extended Boussinesq equations. *Journal of Waterway, Port, Coastal, and Ocean Engineering*, *121*, 251 – 261.

Wei, G., Kirby, J. T., and Grill, S. T. (1995). A fully nonlinear Boussinesq model for surface waves. I. Highly nonlinear unsteady waves. *Journal of Fluid Mechanics*, *294*, 71 – 92.

Wright, J., Colling, A., Park, D., and Open University Oceanography Course Team (1999). *Waves, tides, and shallow-water processes*. Oceanography series. Butterworth-Heinemann, in association with the Open University.

Zelt, J. A. (1991). The run-up of nonbreaking and breaking solitary waves. *Coastal Engineering*, *15*, 205 – 246.

Zhang, J. E., Chen, C., and Li, Y. (2004). On Boussinesq models of constant depth. *Physics of Fluids*, *16*, 1287 – 1296.

Zou, Z. L. (1999). Higher order Boussinesq equations. *Ocean Engineering*, *26*, 767 – 792.